

https://dspace.org/

The structure study of low-temperature rhombohedral bismuth oxide-based electrolytes

Morrison, Caitlin Audrey

2025-06

University of the Witwatersrand, Johannesburg

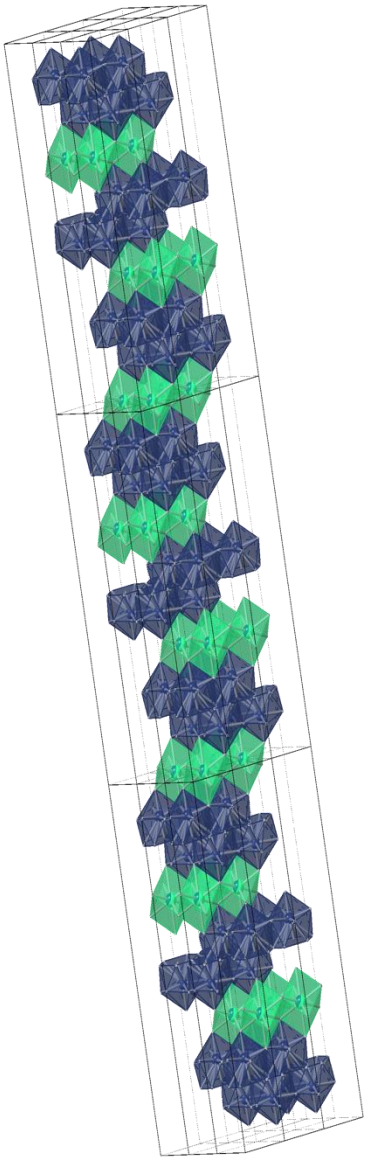
https://hdl.handle.net/10539/47716

Morrison, Caitlin Audrey. (2025). The structure study of low-temperature rhombohedral bismuth oxide-based electrolytes. [Master's dissertation, University of the Witwatersrand, Johannesburg]. WIReDSpace. https://hdl.handle.net/10539/47716

Downloaded from a DSpace repository. https://dspace.org/

THE STRUCTURE STUDY OF LOW-TEMPERATURE RHOMBOHEDRAL BISMUTH OXIDE-BASED ELECTROLYTES

Caitlin Audrey Morrison

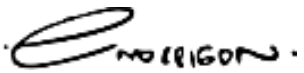


A dissertation submitted to the Faculty of Science, University of the Witwatersrand, Johannesburg, in fulfilment of the requirements for the degree of Master of Science.

2025

Candidate Declaration

I declare that this dissertation is my own, unaided work. It is being submitted for the Degree of Master of Science at the University of the Witwatersrand, Johannesburg. It has not been submitted before any degree or examination at any other University.



Caitlin Morrison

Supervisor: Professor Dave Billing

Co-supervisor: Professor Caren Billing

Co-supervisor: Professor Rudolph Erasmus

9th day of June 2025

Abstract

Solid oxide fuel cells (SOFCS) are high-temperature devices, that operate from 800 to 1000 °C. In this work, stabilized bismuth oxide (Bi_2O_3) is investigated as a potential solid electrolyte for SOFCs. When doping Bi_2O_3 with suitable metals, an unnatural phase known as the rhombohedral phase can form at intermediate temperatures between 450 and 650 °C. The overall aim of this study was to investigate the formation and conductive properties of the rhombohedral phase of doped Bi_2O_3. The dopants included lanthanum (La), samarium (Sm) and gadolinium (Gd) at concentrations between 15 mol and 25 mol%. The citric sol-gel method was used for synthesis of materials that were characterized using laboratory and synchrotron powder X-ray diffraction, Raman spectroscopy and Electrochemical impedance spectroscopy.

Substitution of Bi_2O_3 with 25 mol% La, Sm or Gd confirmed that all three substituents predominantly formed the rhombohedral phase at this concentration. However, La has distinct conductive behaviour compared to the other two substituents with a significant conductivity jump at 700 °C. Varying the substituent concentration in $Bi_{(1-x)}Sm_xO_{1.5}$ from 15 to 25 mol% revealed that the least substituted material had the highest conductivity, but was not stable and underwent a phase change at 550 °C. Annealing duration of $Bi_{0.75}Sm_{0.25}O_{1.5}$ was varied between 5 and 15 hours at 750 °C, which revealed that the time-length of annealing does not have a significant influence on phase or conductivity behaviour. Annealing this same material at two different temperatures, 610 °C and 750 °C, formed different phase compositions at room temperature and had different conductive behaviour.

This work provides further insight on how to leverage synthetic and structural conditions to successfully form the rhombohedral phase and improve its conductive behaviour.

Acknowledgements

The completion of this degree was achieved with the valuable assistance from the following individuals and institutions. I would like to humbly thank everyone who provided all kinds of support that allowed me to submit my Masters Dissertation. I hereby acknowledge the significant contributions to this degree:

1. The NRF and Wits University for their financial assistance towards my Master of Science degree.
2. My supervisors, Professor Dave Billing and Professor Caren Billing, for their valuable guidance, time, exciting opportunities and great memories.
3. My co-supervisor, Professor Rudolph Erasmus, for his continued assistance in understanding and investigating Raman spectroscopy in this project.
4. Dr Mathias Kiefer for always being willing to assist during my project, with advice, proof-reading or even just a great conversation.
5. Darren Fynn for his significant contribution to my understanding of x-ray diffraction, providing his TOPAS input file generator software TIGr for this project and major assistance with the TOPAS programme and python. I can't wait to see you achieve all your dreams, you inspire me everyday.
6. Emileo Naicker, for all the laughs and questionable comments, I can't imagine this journey without you!
7. The rest of the Energy Materials group, for creating a positive environment filled with great support and valuable friendships.
8. My parents, Earl and Samantha Morrison, for their unwavering confidence in what I can achieve. Thank you for believing in me to the extent I started to believe in me too.

The completion of this degree would not be possible without the Most High God!
"I give thanks to you, O Lord my God, with my whole heart, and I will glorify your name forever"

Contents

List of Figures ..... ***viii***

List of Tables ..... ***xiii***

List of Abbreviations ..... ***xv***

Chapter 1- Introduction ***1***

1.1 General Overview **1**

1.2 Fuel Cells **2**

1.3 Solid Oxide Fuel Cells **6**

1.4 Solid oxide ion electrolytes **10**

1.5 Pure Bi_2O_3 ..... **13**

1.5.1 The electrical properties of Bi_2O_3 16

1.6 Doped Bi_2O_3 ..... **17**

1.6.1 The Y_2O_3 - Bi_2O_3 system 18

1.7 The rhombohedral phase of doped Bi_2O_3 ..... **20**

1.7.1 Structure 20

1.7.2 Crystallographic Structure 22

1.7.3 Phase formation 25

1.7.4 Properties 28

1.8 Aims and Objectives **30**

1.9 References **32**

Chapter 2 - Experimental Methodology ***37***

2.1 Sol-gel synthesis **37**

2.2 X-ray Diffraction **38**

2.2.1. Laboratory X-ray tubes 39

2.2.2. Synchrotron radiation 42

2.2.3. Single atom X-ray scattering 44

2.2.4. Bragg's Law and Ewald's sphere 46

2.2.5. Detectors 51

2.2.6. Bragg-Brentano and Debye-Scherrer 51

2.2.7. Rietveld refinement 52

2.2.8. Pair Distribution Function 55

2.3 Raman Spectroscopy **59**

2.3.1 Factors determining vibrational frequencies 60

2.3.2 Selection Rules for Infrared and Raman Spectra 60

2.3.3 Instrumentation 62

2.4 Electrochemical Impedance Spectroscopy **65**

2.4.1 The impedance of an electric circuit 66

2.4.2 Graphical representations of EIS data 67

2.4.3 Electric circuit components 67

2.5 Experimental Procedure **73**

2.5.1 Synthesis Method 73

2.5.2 Laboratory X-ray diffraction 76

2.5.3 Synchrotron X-ray diffraction and total scattering 76

2.5.4 Raman Spectroscopy 77

2.5.5 Electrochemical Impedance Spectroscopy 78

2.6 References 81

Chapter 3 - An X-ray diffraction study of the average and local structure of rhombohedral bismuth oxide 85

3.1 Literature Review 85

3.2 Results and Discussion 95

3.2.1 Laboratory powder X-ray Diffraction 95
3.2.2 Synchrotron powder X-ray Diffraction 104
3.2.3 Pair Distribution Function (PDF) 107

3.3 Conclusion 111

3.4 References 113

Chapter 4 – The local structure of rhombohedral substituted bismuth oxide using Raman Scattering 114

4.1 Literature Review 114

4.1.1 Group Theory and Selection rules 114
4.1.2 Empirical relation – Raman stretching frequencies and bond lengths 117
4.1.3 Raman scattering of bismuth oxide materials 119

4.2 Results and Discussion 122

4.2.1 Substituent Type 122
4.2.2 Substituent concentration and annealing duration 126
4.2.3 Annealing temperature 127
4.2.4 Variable temperature Raman measurements 132

4.3 Conclusion 134

4.4 References 137

Chapter 5 - The ionic conductivity of rhombohedral substituted bismuth oxide using Electrochemical Impedance Spectroscopy 138

5.1 Literature Review 138

5.1.1 Conductivity Mechanism 138
5.1.2 Structural and Synthetic effects 145

5.2 Results and Discussion 150

5.2.1 EIS of $Bi_{0.75}Sm_{0.25}O_{1.5}$ at low temperatures (250 °C – 400 °C) 151
5.2.2 EIS of $Bi_{0.75}Sm_{0.25}O_{1.5}$ at low – intermediate temperatures (450 °C – 600 °C) 152
5.2.3 EIS of $Bi_{0.75}Sm_{0.25}O_{1.5}$ at intermediate - high temperatures (650 °C – 700 °C) 153
5.2.4 EIS of $Bi_{0.75}Sm_{0.25}O_{1.5}$ at high temperatures (750 °C) 154
5.2.5 Effect of substituent type on oxide conductivity 155
5.2.6 Effect of substituent concentration on oxide conductivity 158
5.2.3 Structure - property relationship 160

5.3 Conclusion 163

5.4 References 167

Chapter 6 – General Conclusion 169

6.1 Substituent type 169

6.2 Substituent concentration 171

6.3 Annealing Duration 171

6.4 Annealing Temperature 172

List of Figures

Figure 1.1: Ragone Plot comparing the specific energy and specific power of common energy conversion and storage devices.[9] 2

Figure 1.2: Toyota Mirai electric vehicle which is powered by a hydrogen fuel cell.[18] 5

Figure 1.3: Bloom Energy Server powered by SOFCs.[18] 5

Figure 1.4: The hydrogen fuel cells used by Microsoft as backup generators for data center servers.[19] 6

Figure 1.5: The Coradia iLint train in Germany is the first passenger train powered by a hydrogen fuel cell.[16] 6

Figure 1.6: Schematic diagram of a Solid Oxide Fuel Cell (SOFC) illustrating the typical working principle.[27] 7

Figure 1.7: SEM image showing the cross section of a Scandium stabilized zirconia (ScSZ) and Ni supported film, ScSZ electrolyte, and Lanthanum strontium scandium manganate (LSSM) cathode of a SOFC.[33] 9

Figure 1.8: SEM image showing the cross section of a solid oxide fuel cell where layer delamination has occurred due to thermal expansion mismatch.[35] 10

Figure 1.9: The defect fluorite structure of $Bi2O3$ crystallized in the Fm3m structure. 11

Figure 1.10: Arrhenius plots comparing the conductivities of common electrolytes used in SOFCs over 350-1000 °C. YSZ = yttria stabilized zirconia, $Ce0.9Gd0.1O1.95$ = 10 mol% doped ceria, (La,Sr)(Mg,Ga)$O3$ = LSGM = Strontium-Magnesium doped lanthanium gallium oxide.[5] 12

Figure 1.11: Arrhenius plots comparing the conductivities of bismuth oxide-based electrolytes with electrolytes commonly used in SOFCs; DWSB = Dysprosium-tungsten stabilized bismuth, 20ESB = 20 mol% erbium stabilized bismuth, SNDC= Samarium-Neodymium doped ceria, 10GDC = 10 mol% gadolinium doped ceria, 8YSZ = 8 mol% yttria stabilized zirconia.[8] 13

Figure 1.12: Various phase change behavior of pure Bi_2O_3 during heating and cooling regimes.[45] 16

Figure 1.13: Arrhenius plot comparing the conductivities of the pure Bi_2O_3 polymorphs from 650 °C to 1100 °C.[21] 17

Figure 1.14: Arrhenius plots showing the conductivity of $(Bi2O3)1-x(Y2O3)x$ materials measured in air. 1: x = 0.0 , 2: x = 0.05 , 3: x = 0.20 , 4: x = 0.25 , 5: x = 0.33 , 6: x = 0.425 , 7: x= 0.50, 8: x = 0.60.[55] 19

Figure 1.15: The $\beta 2$ rhombohedral structure of lanthanide stabilized bismuth oxide, determined using x-ray diffraction.[45] 21

Figure 1.16: The structural relationship between (a) the ε-monoclinic, (b) $\beta 1$ or $\beta 2$-hexagonal and (c) δ-cubic cells.[44] 25

Figure 1.17: Relationship between the ε- and $\beta 2$-$Bi1-xLnxO1.5$ composition domains versus Ln^{3+} radius.[44] 27

Figure 1.18: Formation ranges of the rhombohedral and fcc phases related to ionic radius (of $Ln3+$) versus $Bi1-xLnxO1.5$ composition plot.[47] 28

Figure 1.19: Faradaic outputs of the ε, $\beta 2$ and $\beta 1$ phases of $Bi0.7La0.3O1.5$.[45] 29

Figure 1.20: Conductivities of various rhombohedral stabilized Bi_2O_3 systems that are 8% cation doped. (e.g. Ca8 represents 8% Ca doped Bi_2O_3) The conductivities were measured at 500 °C.[70] 30
Figure 2.1: Schematic diagram showing the solution transformation during the Sol-gel method.[2] 38
Figure 2.2: Graphical representation of the electromagnetic spectrum.[14] 38
Figure 2.3: Schematic diagaram of a sealed laboratory X-ray tube with key components indicated.[12] 39
Figure 2.4: Atomic levels involved in $K\beta$ and $K\alpha$ emissions. [13] 40
Figure 2.5: Typical x-ray emission spectra of a copper anode produced with with varying accelerating voltages.[12] 41
Figure 2.6: Schematic illustration of a synchrotron storage ring.[13] 42
Figure 2.7: (a) Tangential fan of radiation emitted from a bending magnet (b) Fan of radiation emitted by a wiggler (c) Collimated beam emitted by an undulator.[14] 43
Figure 2.8: A schematic illustration of X-ray scattering by electrons of an atom.[13] 44
Figure 2.9: X-ray Scattering factor for selection atoms as a function of 2θ and $\sin\theta/\lambda$.[19] 45
Figure 2.10: Diagram illustrating (a) a unit cell and (b) a crystal lattice.[12] 46
Figure 2.11: (a) Single crystal diffraction and (b) powder diffraction.[12] 47
Figure 2.12: Schematic diagram illustraring the Bragg equation.[19] 48
Figure 2.13: The intereference of two sinusoidal waves in the lower diagarams that results in (a) constructive wave interference and (b) complete destructive wave interference.[2] 49
Figure 2.14: Geometrical construction of the Ewald circle. The “0” marks the origin of recirpocal space. The vectors are defined in the text.[13] 50
Figure 2.15: Comaprison between the scattered beams originating from a single crystal (a) and a powder (b). For the latter, Debye-Scherrer cones are drawn.[16] 51
Figure 2.16: Schematic of (a) Bragg-Brentano and (b) Debye-Scherrer diffractometers. Photographs of a (c) Bragg-Brentano diffractometer and (d) Debye-Scherrer diffractometer, courtesy of Bruker.[12]. 52
Figure 2.17: A PDF pattern G(r) illustrating the structural information contained in the function.[46] 58
Figure 2.18: A schematic diagarm illustrating the experimental set-up for PDF measurements at a synchrotron.[31] 59
Figure 2.19: Schematic diagram illustrating the Raman Principle where irradiated photons results in Rayliegh and Raman scattering. [47] 60
Figure 2.20: A mechanical model illustrating the stretching vibrations in a CO_2 molecule.[48] 61
Figure 2.21: Diagram of a standard Raman spectrometer.[48] 63
Figure 2.22: Diagram of the basic components of a noble gas ion laser.[57] 64
Figure 2.23: A plot representing a typical current-voltage relationship for an electrochemical cell.[60] ... 65
Figure 2.24: (a): A typical Nyquist plot. (b): Typical Bode plots separated into the modulus of impedance and phase plots.[59] 67
Figure 2.25: (a) and (b) resistor symbols as represented in electric circuits diagrams. 68
Figure 2.26: Phase diagram for v(t) and i(t) sinusoidal waveforms when an alternating voltage is applied to a resistor.[59] 68
Figure 2.27: Capacitor symbol as represented in electric circuit diagrams.[59] 68

Figure 2.28: Phase diagram for v(t) and i(t) sinusoidal waveforms when an alternating voltage is applied to a capacitor.[59] 69
Figure 2.29: A constant phase element symbol as represented in electric circuits diagrams.[59] 69
Figure 2.30: (a) The Randles equivalent circuit and (b) the corresponding Bode and Nyquist plots of the Randles circuit.[59] 70
Figure 2.31: (a) The Randles equivalent electric circuit over a wide frequency range; (b) the Bode and Nyquist plots of the Randles equivalent circuit.[59] 71
Figure 2.32: The labelled Nyquist plot in correlation with the Randles equivalent circuit over a wide frequency range.[62] 71
Figure 2.33: A representative Nyquist plot representing different mass transfer mechanisms at low frequencies. [60] 73
Figure 2.34: Final powders after the annealing step: $Bi0.75Sm0.25O1.5$ and $Bi0.85O1.5Sm0.15O1.5$ from left to right. 74
Figure 2.35: A schematic representation of the citrate sol-gel synthesis method. 75
Figure 2.36: Bruker D2-Phaser desktop diffractometer at the School of Chemistry, University of the Witwatersrand. 76
Figure 2.37: Beamline ID31 at ESRF.[13] 77
Figure 2.38: Horiba LabRAM HR (Evolution) Raman spectrometer at the Biology School, University of the Witwatersrand. 78
Figure 2.39: 13 mm $Bi1 - xLnxO1.5$ pellets in a boat before sintering at 750 °C for 12 hours. 79
Figure 2.40: Bio-Logic MTZ-35 impedance analyzer coupled with a HF-1100 furnace and HT-1100 sample holder at the School of Chemistry, University of the Witwatersrand. 80
Figure 3.1: Correlation between $Bi_{0.775}Ln_{0.225}O_{1.5}$ lattice constants and $Ln3+$ radii at room temperature.[4] 87
Figure 3.2: The variable temperature evolution of $Bi_{0.775}La_{0.225}O_{1.5}$ lattice parameters from 0 to 900 °C. [4] 88
Figure 3.3: The R3m rhombohedral crystal structure of $Bi_{0.775}Ln_{0.225}O_{1.5}$ materials presented in a ball and stick model, determined using powder x-ray diffraction by Drache et al. [4] 89
Figure 3.4: Rietveld refinement of the neutron diffraction pattern of $Bi_{0.775}Pr_{0.225}O_{1.5}$.[7] 92
Figure 3.5: The proposed R3m rhombohedral crystal structure of $Bi_{0.775}Ln_{0.225}O_{1.5}$ materials presented in a ball and stick model determined using powder neutron diffraction by Obbade et al.[7] 93
Figure 3.6: Superimposed laboratory XRD patterns for $Bi0.75Ln0.25O1.5$ materials where Ln = La, Sm or Gd. 95
Figure 3.7: Rietveld Refinement of the laboratory XRD patterns of (a) $Bi0.75La0.25O1.5$, (b) $Bi0.75Sm0.25O1.5$ and (c) $Bi0.75Gd0.25O1.5$. 97
Figure 3.8: Superimposed laboratory XRD patterns of $Bi(1 - x)Smx\ O1.5$ where x ranges from 15 to 25 mol% 98
Figure 3.9: Rietveld Refinement of the laboratory XRD patterns of (a) $Bi0.85Sm0.15O1.5$ and (b) $Bi0.85Sm0.20O1.5$. 99

Figure 3.10: Superimposed laboratory XRD patterns of $Bi0.75Sm0.25O1.5$ subjected to 5-, 10- and 15-hour annealing treatments. 100
Figure 3.11: Rietveld Refinement of the laboratory XRD pattern of $Bi0.85Sm0.25O1.5$ annealed for (a) 10 hours and (b) 15 hours 102
Figure 3.12: Superimposed laboratory XRD patterns of $Bi0.75Sm0.25O1.5$ subjected to annealing at 610 °C and 750 °C 102
Figure 3.13: Rietveld Refinement of the laboratory XRD pattern of $Bi0.75Sm0.25O1.5$ annealed at (a) 610 °C and (b) 750 °C 104
Figure 3.14: Superimposed synchrotron XRD patterns of $Bi0.75Ln0.25O1.5$ materials where Ln = La, Sm or Gd 105
Figure 3.15: Rietveld Refinement of the synchrotron XRD patterns of (a) $Bi0.75La0.25O1.5$, (b) $Bi0.75Sm0.25O1.5$ and (c) $Bi0.75Gd0.25O1.5$. 107
Figure 3.16: Superimposed PDFs of $Bi0.75Ln0.25O1.5$ materials where Ln = La, Sm and Gd 108
Figure 3.17: Experimental PDF of $Bi0.75Sm0.25O1.5$ superimposed on the calculated partial PDF functions of the R3m rhombohedral structure. 109
Figure 3.18: Refinement of the PDF data for $Bi0.75Sm0.25O1.5$ 110
Figure 4.1: Linear chain model illustrating the Raman and FTIR modes.[4] 115
Figure 4.2: Raman spectrum, measured under polarizing conditions, of pure Bi_2Se_3. The upper trace is the xx Raman tensor component and the lower trace is the xy Raman tensor component. [4] 116
Figure 4.3: The empirical correlation between bismuth – oxygen bond lengths and Raman stretching frequencies.[5] 117
Figure 4.4: The empirical correlation between Pauling bond strength and Raman stretching frequencies.[6] 118
Figure 4.5: Raman spectra of orthorhombic $Bi_{17}Ln_7O_{36}$ (Ln = Tm, Yb, Lu). [7] 119
Figure 4.6: Raman spectra of triclinic $BiLnO_3$ (Ln = Tm, Yb, Lu). [7] 120
Figure 4.7: Raman spectrum of cubic $Bi_{0.7}Yb_{0.3}O_{1.5}$. [7] 120
Figure 4.8: Raman spectra showing the low frequency range (0 – 350 cm^{-1}) for ytterbium substituted bismuth oxides. [7] 121
Figure 4.9: Raman Spectra of $Bi0.75Ln0.25O1.5$ where Ln = La, Sm, Gd. 123
Figure 4.10: Raman spectra of (a) $BixSm(1-x)O1.5$ with x ranging between 0.15 and 0.25 and (b) $Bi0.75Sm0.25O1.5$ with varying annealing durations. 127
Figure 4.11: Raman spectra of $Bi0.75Gd0.25O1.5$ annealed at different temperatures for 5 hours each; 610 °C and 750 °C. 128
Figure 4.12: Multi-point sample square created on $Bi0.75Gd0.25O1.5$ powder sample annealed at 610 °C by selecting 8 x 8 points over an area of 500 μ x 500 μ. The blue dots represent the 64 sample points. 130
Figure 4.13: Raman spectra of the multipoint measurement of $Bi0.75Gd0.25O1.5$, sample points 1 – 64. 131

Figure 4.14: Variable temperature Raman spectra of $Bi0.75Sm0.25O1.5$ annealed at 750 °C for 5 hours. 133
Figure 4.15: Rescaled view of the variable temperature measureent Raman spectra in Figure 4.94. 133
Figure 4.16: Comparison between Raman spectra of $Bi0.75Sm0.25O1.5$ before and after the variable temperature measurement, at 23 °C and 30 °C respectively. 134
Figure 5.1: The R3m structure: CIF obtained from the measurement of $Bi_{0.765}Sr_{0.235}O_{1.383}$ at 300K.[2] 140
Figure 5.2: (a) Thermal evolution of the position of oxide ions with respect to the M(2) layers (positive Δz values correspond to ions within the intersheet space and negative Δz values correspond to ions within the fluorite-like sheets, where Δz represents the displacement of anions from their original positions). (b) The occupancies of oxide ions with increasing temperature. $\sum OI$ refers to the sum of intersheet oxide ions and $\sum OF$ refers to the sum of fluorite-like sheet oxide ions.[1] 141
Figure 5.3: An illustration of the proposed migration pathways in the R3m structure measured at 300K. 142
Figure 5.4: Graphical representation of the components of the R3m structure used to describe anion pathways. 143
Figure 5.5: Unit cell occupation numbers for oxide ions as a function of temperature. $\sum OI$ refers to the sum of intersheet oxide ions and $\sum OF$ refers to the sum of fluorite-like sheet oxide ions.[10] 145
Figure 5.6: Arrhenius plot for $Bi_{0.775}La_{0.225}O_{1.5}$ and $Bi_{0.775}Dy_{0.225}O_{1.5}$ (during the second heating regime).[7] 146
Figure 5.7: Evolution of Ln^{3+} radius with (a) activation energy and (b) isothermal conductivity at 400 °C.[7] 148
Figure 5.8: Arrhenius plots of sintered disks of the $Bi(1-x)LaxO1.5$ system. 149
Figure 5.9: Isothermal conductivity of the $Bi(1-x)LaxO1.5$ system at (a) 800 °C and (b) 600 °C. 150
Figure 5.10: (a) The equivalent electric circuit and (b) the Nyquist plot for $Bi0.75Sm0.25O1.5$ at 250 °C. 152
Figure 5.11: (a) The equivalent electric circuit and (b) the Nyquist plot for $Bi0.75Sm0.25O1.5$ at 550 °C. 153
Figure 5.12: (a) The equivalent electric circuit and (b) the Nyquist plot for $Bi0.75Sm0.25O1.5$ at 600 °C. 154
Figure 5.13: (a) The equivalent electric circuit and (b) the Nyquist plot for $Bi0.75Sm0.25O1.5$ at 750 °C. 154
Figure 5.14: The Arrhenius plots of $Bi0.75Ln0.25O1.5$, $Bi0.75Sm0.25O1.5$ and $Bi0.75Gd0.25O1.5$ displayed as their corresponding (a) heating curves and (b) cooling curves. 156
Figure 5.15: The Arrhenius plots of $Bi0.85Sm0.15O1.5$, $Bi0.8Sm0.2O1.5$ and $Bi0.75Sm0.25O1.5$ displayed by their corresponding (a) heating curves and (b) cooling curves. 159
Figure 5.16: The Arrhenius plots of $Bi0.75Sm0.25O1.5$ that were subjected to 5, 10 and 15 hour annealing time as displayed by their (a) heating curves and (b) cooling curves. 161
Figure 5.17: The Arrhenius plots of $Bi0.75Sm0.25O1.5$ that were subjected to annealing at 610 °C and 750 °C as displayed by their (a) heating curves and (b) cooling curves. 162

List of Tables

Table 1.1: Comparison of the structural characteristics and properties of the five main types of fuel cells.[15] 4
Table 1.2: The structural and chemical characteristics of cell components in SOFCs. 8
Table 1.3: Crystal structure details of the pure Bi_2O_3 polymorphs. [41] 15
Table 1.4: The atomic sites and occupancies of rhombohedral Bi_2O_3 - Lni_2O_3 systems. 22
Table 1.5: The hexagonal crystal family and its crystal systems, bravais lattices and unit cells. Images adapted from.[63] 24
Table 1.6: Unit cell parameters and synthetic conditions for the ε, $\beta 1$/ $\beta 2$ and δ phases.[45] 26
Table 1.7: Relationship between lanthanide (and yttrium) ionic radii and rhombohedral $\beta 2$ composition domain.[45] 26
Table 2.1: Characteristics of anode materials in x-ray diffractometers [17] 39
Table 2.2: The character table of the D_{3d} point group. 62
Table 3.1: Structural information of the rhombohedral R3m Bi – Sr - O structural model 86
Table 3.2: The refined parameters of $Bi_{0.775}Ln_{0.225}O_{1.5}$ materials reported by Drache and co-workers [4]. 87
Table 3.3:Neutron coherent scattering lengths of selected elements [8]. 90
Table 3.4: Summarized information from the Rietveld refinements of $Bi_{0.775}Ln_{0.225}O_{1.5}$ materials. Displacement parameters and site occupancies are included for the representative Pr substituted material 91
Table 3.5:Interatomic distances between metal and oxygen in the mixed bismuth-lanthanide layer and the bismuth only layer for selected lanthanides. 92
Table 3.6 Parameters obtained from Rietveld refinements for the $Bi0.75Ln0.25O1.5$ materials. 98
Table 3.7: Parameters obtained from Rietveld refinements for the $Bi1 - xSmxO1.5$ materials 100
Table 3.8: The refined lattice parameters of $Bi0.75Sm0.25O1.5$ subjected to 5-, 10- and 15-hour annealing treatments 101
Table 3.9: The refined lattice parameters of $Bi0.75Sm0.25O1.5$ subjected to annealing temperatures of 610 °C and 750 °C 103
Table 3.10: Parameters obtained from Rietveld refinements for the $Bi0.75Ln0.25O1.5$ materials. 106
Table 4.1:Key to the representative pattern arrangement for the materials studied by Richter et al. [4] 115
Table 4.2: Positions of Raman bands of the spectra in Figure 4.9 that were determined by fitting with a Gaussian-Lorentzian function. 123
Table 4.3:Character table of the D_{3d} point group. 124
Table 4.4:The estimated stretching frequencies for the R3m rhombohedral phase determined using the empirical relation of Hardcastle and Wachs [5]. 125
Table 4.5:Comparison of the actual stretching frequencies in the Raman spectra to the estimated frequencies from the empirical relation. 126
Table 4.6: The Raman bands of the spectra in Figure 4.91 that were fitted with a Gaussian-Lorentzian function. 128

Table 5.1: The oxide ions occupancies determined by single crystal neutron diffraction at 300 K, 600 K and 1500 K.[1] 140
Table 5.2: The values of electrical elements obtained by fitting Nyquist plots with a calculated fit. ... 155
Table 5.3: Conductivities of materials at 750 °C in this work in comparison to commonly used solid electrolytes. 166

List of Abbreviations

SOFCS: Solid Oxide Fuel Cells

XRD: X-ray Diffraction

EIS: Electrochemical Impedance Spectroscopy

LSSM: Lanthanum strontium scandium manganate

LSGM: Lanthanum gallium oxide

YSZ: Yttria-Stabilized Zirconia

PDF: Pair Distribution Functions

MW: Megawatts

HFCEVs: Hydrogen Fuel Cell Electric Vehicles

PEMFC: Proton Exchange Membrane Fuel Cell

AFC: Alkaline Fuel Cell

PAFC: Phosphoric Acid Fuel Cell

MCFC: Molten Carbonate Fuel Cell

SEM: Scanning Electron Microscopy

CHP: Combined heat and power

DWSB: Dysprosium-tungsten stabilized bismuth

ESB: Erbium stabilized bismuth

SNDC: Samarium-Neodymium doped ceria

GDC: Gadolinium doped ceria

STP: Standard temperature and pressure

TEM: Transmission Electron Microscopy

fcc: Face-centered cubic

LSPD: Linear position sensitive detector

CW: Continuous wave

CPE: Constant phase element

ESRF: European Synchrotron Radiation Facility

Chapter 1 - Introduction

1.1 General Overview

The global energy crisis is a major driving force of alternative energy sources that are renewable and clean. Fossil fuels remain dominant due to high accessibility, convenience, and efficiency and this has hindered the widespread adoption of renewable energy. Between 2016 and 2022, South Africa was ranked 7th in the world in terms of overall coal consumption, with roughly 202 million tons being used per year.[1] South Africa has large coal reserves, accounting for approximately 3% of the world's total reserves.[2] While international efforts have been aimed at addressing South Africa's coal-driven energy industry, the continuous use of fossil fuel usage has placed South Africa as the 13th largest emitter of carbon globally in 2022.[3] Alternative renewable energy sources, with performance and efficiency comparative to that of fossil fuel-based sources, are urgently required. Consequently, energy storage and conversion devices have gained popularity as research on improving the efficiency of renewable energy sources has become widespread.

Alternative energy sources can be compared using Ragone plots, which allow for a direct comparison of the performance of energy storage and conversion devices.[4] A typical Ragone plot depicts the relationship between specific energy and specific power of several energy conversion and storage devices, as illustrated in Figure 1.1 [5] Specific energy quantifies the energy available per unit mass, while the specific power indicates the available power per unit mass.[6] Figure 1.1 compares the performance of various energy devices, including batteries, fuel cells and internal combustion engines. Among these, fuel cells have relatively high specific energy, and solid oxide fuel cells (SOFCs) have both high specific power and high specific energy (Figure 1.1). SOFCs also produce comparatively less emissions depending on the fuel used, and can generate additional electricity via co-generation techniques that improves the overall device efficiency.[6–8] The attractive qualities of SOFCs have drawn significant attention from researchers, and these devices will be further explored in this work.

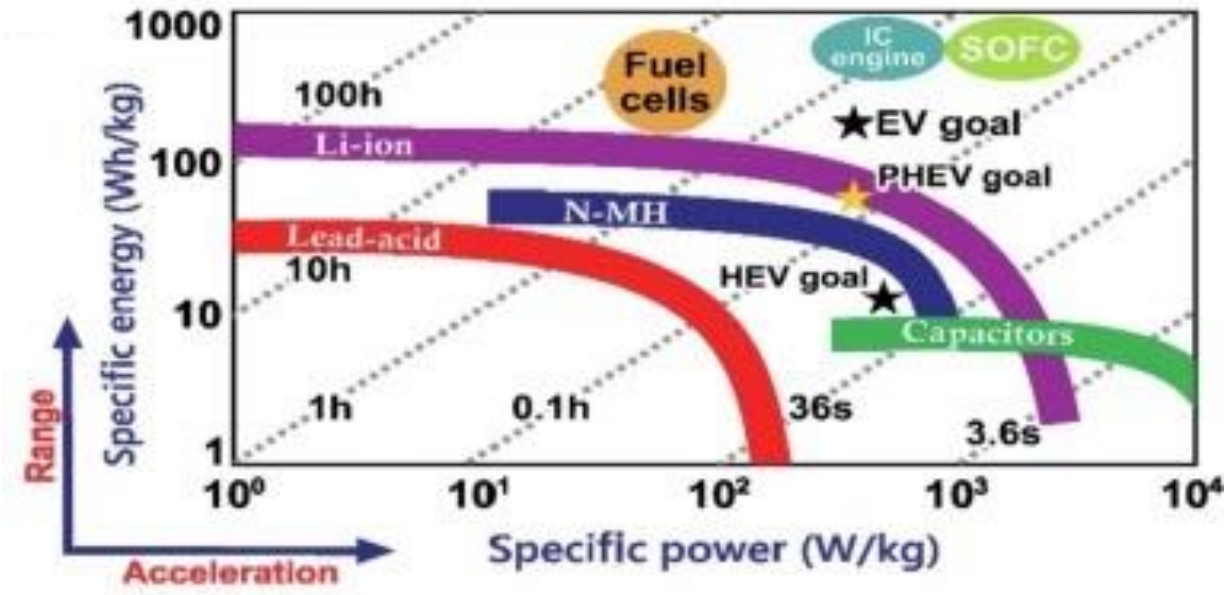


Figure 1.1: Ragone plot comparing the specific energy and specific power of common energy conversion and storage devices.[9]

1.2 Fuel Cells

Fuel cells are electrochemical devices that convert chemical energy into electrical energy.[10] Batteries and fuel cells are similar in that they convert chemical energy into electricity but these devices have fundamental differences.[11] A battery is used to store energy, and requires recharging or disposal once the stored energy is consumed.[11,12] In contrast, a fuel cell can function indefinitely, provided that the fuel cell is continuously supplied with fuel and atmospheric oxygen.[13]

All fuel cells have the same basic design that comprises two electrodes separated by a solid or liquid electrolyte. The electrolyte facilitates the transport of charged particles between electrodes.[14] Fuel cells can operate using a wide range of fuel sources such as natural gas and hydrocarbons provided that they contain hydrogen.[10] Fuel cell operation is governed by a redox reaction so no combustion occurs during fuel cell operation.

The fuel cell design varies across the different types of fuel cells. Fuel cells are classified structurally, based on the type of electrolyte material used.[4] There are five main types of fuel cells and these are summarized in Table 1.1. The main characteristics of fuel cells are compared in Table 1.1, including the significant process of fuel reformation. Fuel reforming is the conversion of hydrocarbons to simpler fuels such as hydrogen and carbon monoxide. Hydrocarbons have become a desired feedstock for fuel cells as pure hydrogen poses challenges like safety, storage and distribution.[4] This process can be performed externally, using a separate fuel processor or internally at the anode of the fuel cell.[7] Internal reformation offers

several advantages such as lowered operational costs, less maintenance and decreased system complexity.[5,7]

Fuel cells can be manufactured in various sizes, from small-scale devices producing a few watts of electricity to large-scale systems that can produce electricity up to 300 megawatts (MW).[8] Examples of devices that produce significant electricity are fuel cell electric and railway vehicles. The application of a fuel cell can be categorized as stationary, portable and transport.[13] Examples of different fuel cell applications are presented in Table 1.1.

Presently, the most widely used fuel cell is the hydrogen fuel cell.[16]The hydrogen fuel cell offers immense versatility and is used in various automotive and backup power applications.[15] The hydrogen fuel cell can be classified as any fuel cell in Table 1.1, as long as hydrogen is used as the source of fuel. Several major automobile manufacturers have developed hydrogen fuel cell electric vehicles (HFCEVs), such as Toyota, Honda, Hyundai and BMW (Figure 1.2).[18] Stationary fuel cells have been integrated into uninterruptible power supply (UPS) systems where continuous power supply is very important (Figure 1.3). Since 2020, Microsoft has employed hydrogen fuel cells as backup generators for data center servers (Figure 1.4)[19] Various warehouses have also begun using hydrogen fuel cells to power forklifts and other heavy machinery which reduces carbon emissions and improves air quality.[16] Fuel cell technology offers many benefits to various critical industries, such as locomotive transportation (Figure 1.5), and as a result fuel cell technology has experienced extensive development in recent years.

Table 1.1: Comparison of the structural characteristics and properties of the five main types of fuel cells. [13]

	Fuel Cells				
	PEMFC	AFC	PAFC	MCFC	SOFC
Fuel cell type (FC = fuel cell)	Proton Exchange Membrane FC	Alkaline FC	Phosphoric Acid FC	Molten Carbonate FC	Solid Oxide FC
Electrolyte material	Water-based, acidic membrane	Alkaline solution	Matrix	Porous ceramic matrix	Solid ceramic
Common Electrolyte	Perfluoro sulfonic acid	Potassium hydroxide	Phosphoric acid	Lithium, or potassium carbonates	Yttria stabilized zirconia
Fuel	Pure hydrogen	Pure hydrogen	Pure hydrogen	Methane, natural gas,	Hydro-carbons
Fuel reformer	Yes	Yes	Yes	No	No
Catalyst	Platinum	Nickel	Platinum	Various Non-precious metals	None
By-products	Water, heat	Water, heat	Water, heat	Water, heat, carbon dioxide	Water, heat, carbon dioxide
Operating Temperature	50 - 100 °C	90 – 100 °C	150 - 200 °C	600 - 700 °C	700 – 1000 °C
Conversion Efficiencies (CHP)[1]	60 %	60%	80 %	80%	80%
Output capacity	< 1 – 100 kW	10 – 100 kW	100 - 400 kW	300 kW – 3 MW	1 kW – 2 MW
Application	Portable Stationary Transport	Stationary	Stationary	Stationary	Portable Stationary
Examples	Vehicles	Military Equipment (e.g. radar	Large vehicles	Power plants	Distributed generation

[1] CHP systems refer to combined heat and power systems

		systems)			



Figure 1.2: Toyota Mirai electric vehicle which is powered by a hydrogen fuel cell.[18]



Figure 1.3: Bloom Energy Server powered by SOFCs.[18]



Figure 1.4: The hydrogen fuel cells used by Microsoft as backup generators for data center servers.[19]


Figure 1.5: The Coradia iLint train in Germany is the first passenger train powered by a hydrogen fuel cell.[16]

1.3 Solid Oxide Fuel Cells

SOFCs are electrochemical devices that convert chemical energy from fuel into electrical energy through electrochemical reactions.[10] The redox reaction that occurs in SOFCs is illustrated in Figure 1.6. This reaction starts at the cathode, where a source of oxygen gas such as atmospheric air is supplied. This oxygen is reduced to form oxide ions (Equation 1.1) that travel through the electrolyte to the anode.[10] Once arrived at the anode, the oxide ions react with the fuel gas (Equation 1.2). This oxidation process produces water, as well as carbon dioxide if hydrocarbons are the fuel source (Equation 1.3). Oxidation of the fuel releases electrons that flow through

the external circuit, which produces electricity.[17] The combined reduction and oxidation processes form the overall reaction occurring in SOFCs, shown in Equation 1.4.

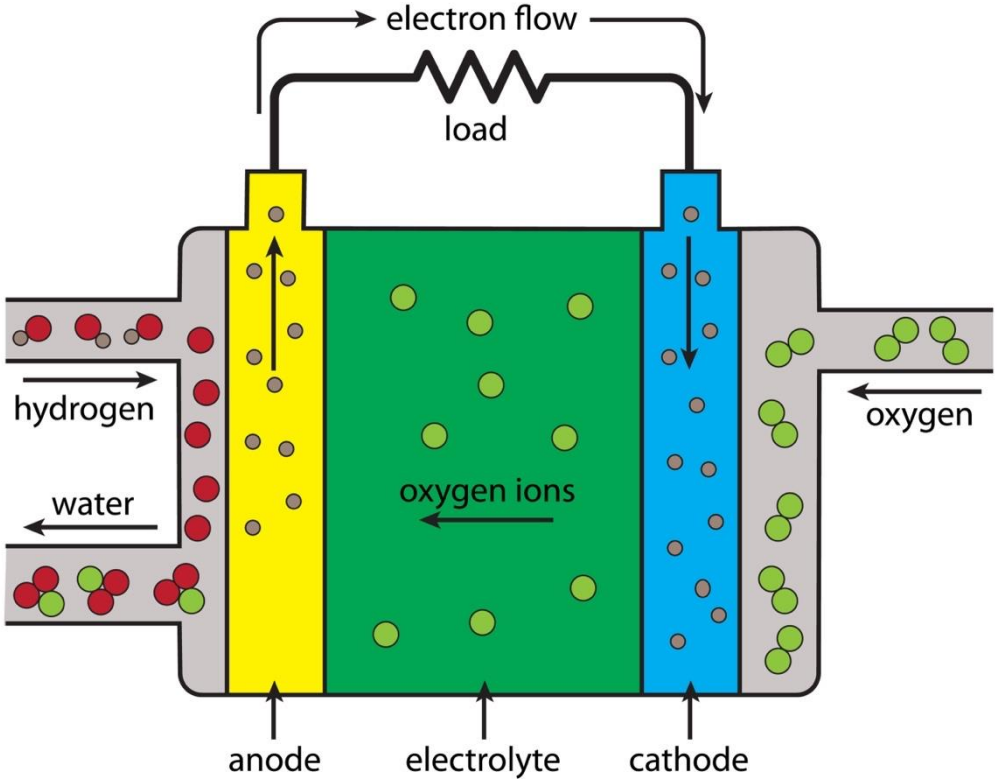


Figure 1.6: Schematic diagram of a Solid Oxide Fuel Cell (SOFC) illustrating the typical working principle.[27]

Cathode reaction (Reduction):

Equation 1.1: $O_2 + 4e^- \rightarrow 2O^{2-}$

Anode reaction (Oxidation):

Equation 1.2: $H_2 + O^{2-} \rightarrow H_2O + 2e^-$

Equation 1.3: $CO + O^{2-} \rightarrow CO_2 + 2e^-$

Overall reaction:

Equation 1.4: $O_2 + H_2 + CO \rightarrow H_2O + CO_2$

The properties of a functioning SOFC have been summarized in Table 1.2[23] and serve as guidelines when investigating potential improvements to the current SOFC model. SOFC electrodes must be porous to facilitate the diffusion of fuel and oxidizer gases as well as ion mobility (Figure 1.7).[22] The motion of ions also require electrodes that are ionically conductive.[23] SOFC electrodes must be electronically conductive too so that electrons used in redox reactions can travel through the

external circuit. These electrodes can thus be referred to as mixed conductors. As each electrode facilitates a redox reaction, the electrodes should be able to catalyse their respective redox reaction if necessary, and the anode must also have a fuel processing ability in the case that it is required.[24]

Table 1.2: The structural and chemical characteristics of cell components in SOFCs.[23]

Properties of a SOFC	
Electrode	**Electrolyte**
Porous	Impermeable
Ionically conductive	Ionically conductive
Electronically conductive	Electronic insulation
Catalyzing ability	
Stable in air at high temperatures (700 – 1000 °C)	Stable in air at high temperatures (700 – 1000 °C)
Inert to other cell components	Inert to other cell components
Comparable coefficients of thermal expansion	Comparable coefficients of thermal expansion

Unlike the electrodes, SOFC electrolytes need to be impermeable to prevent gas diffusion (Figure 1.7). Electrolytes must allow the motion of oxide ions from the cathode to the anode, and so need to be ionically conductive.[23] Another difference to electrodes is that electrolytes require electronic insulation. Electrons travelling through the electrolyte instead of the external circuit will result in a short circuit of the cell, which prevents any useful work from being done.[23]

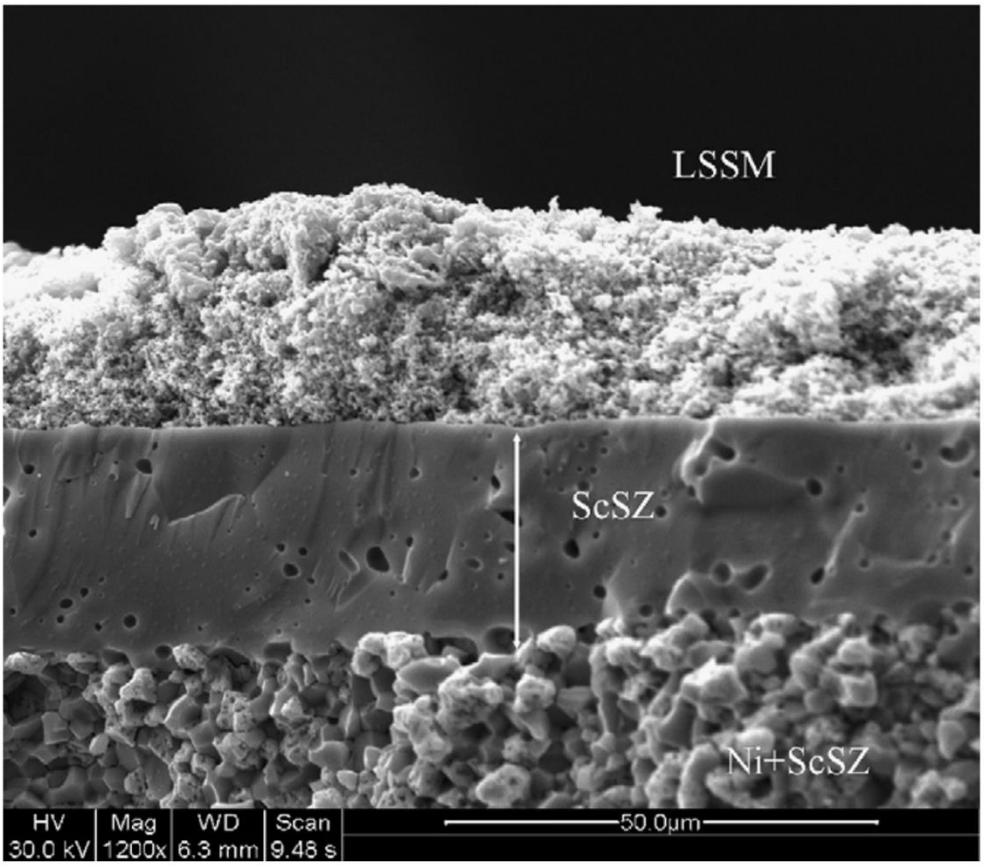


Figure 1.7: SEM image showing the cross section of a Scandium stabilized zirconia (ScSZ) and Ni supported film, ScSZ electrolyte, and Lanthanum strontium scandium manganate (LSSM) cathode of a SOFC.[33]

The electrodes and electrolyte of a working SOFC share some characteristics. For example, all cell components are required to be stable and not decompose in air at elevated temperatures, as operation can occur in these conditions. For this same reason, the anode must also be stable in fuel at these conditions too.[26] These cell components must be inert toward each other and not react under any conditions, so that the fuel cell's structural integrity is maintained.[26] Additionally, the electrodes and electrolyte should have similar coefficients of thermal expansion, as the constant heating and cooling causes expanding and contracting of cell components.[26] If this expansion and contraction does not occur at similar rates, delamination between adjacent components occur and results in device failure.[12] (Figure 1.8). While it is highly unlikely that the cell components will have the same coefficient of thermal expansion, these values should be comparable.

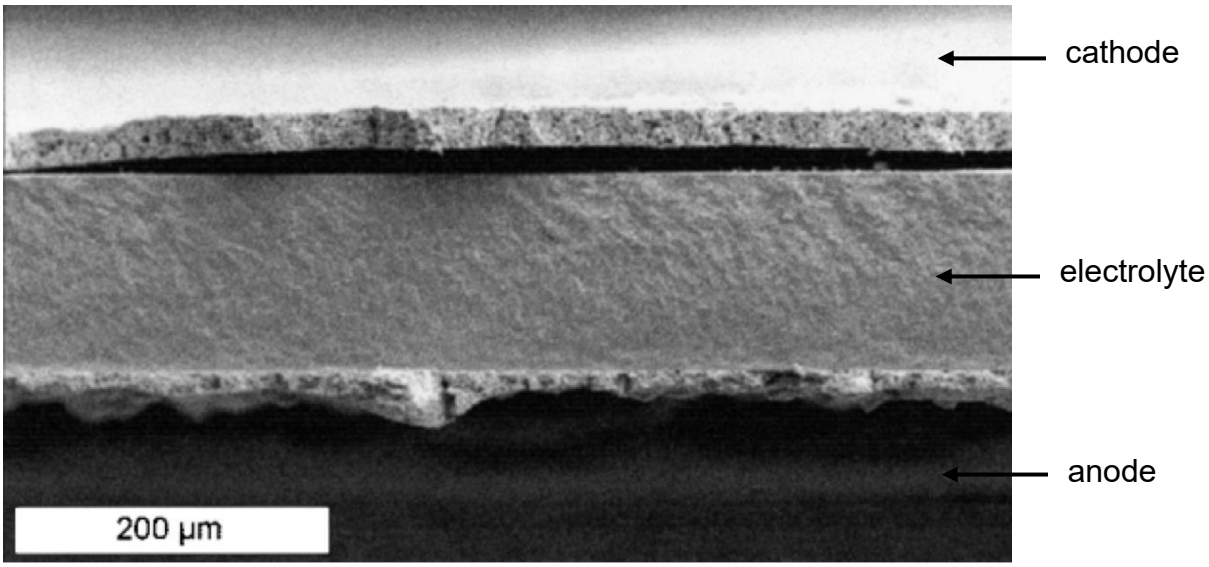


Figure 1.8: SEM image showing the cross section of a solid oxide fuel cell where layer delamination has occurred due to thermal expansion mismatch.[35]

The operation of SOFCs are limited by several drawbacks. These disadvantages, mostly attributed to the high operating temperatures, include significant start-up times, costly high-temperature materials and chemical and mechanical degradation.[13,24] However, SOFCs also have favourable properties that has gained attention by researchers. These fuel cells emit low levels of undesirable gases, such as SOx or NOx, which is a result of the fuel used.[15] The high operating temperatures of SOFCs results in a large amount of exhaust heat produced as a by-product.[24] This heat can be used for cogeneration or combined heat and power (CHP) applications, adding to the overall efficiency of the fuel cell.[28] Another advantage of high-temperature operation is improved reaction kinetics, eliminating the need for a metal catalyst.[24]

1.4 Solid oxide ion electrolytes

Common solid oxide ion electrolyte materials are metal oxides that have a defect structure. This defect results in oxygen vacancies through a charge balance of the material, which facilitates the motion of oxygen ions throughout the electrolyte.[14] For example, Bi_2O_3 with the $Fm\bar{3}m$ structure has oxygen vacancies as shown in Figure 1.9. To explain the oxygen vacancies in this structure, the Bi_4O_6 formula will be used. The oxide ions occupy the tetrahedral sites in between the Bi^{3+} ions. Since there are 8 tetrahedral sites in each unit cell and only 6 oxide ions in Bi_4O_6, 75% of the tetrahedral sites are occupied. There are four types of electrolytes that have gained significant attention for SOFC application; stabilized zirconia, doped ceria, doped lanthanum gallium oxide and doped bismuth oxide [12]. The substitution of atoms in the solid state is referred to as doping when small amounts of the substituent are added to the system.[14] On the other hand, stabilizing a material by atomic substitution involves larger amounts of the substituent in the system. [14] While noting

the accurate meaning of these concepts, the doped and stabilized terms are used interchangeably in literature sources and will be used in the same manner in this work.

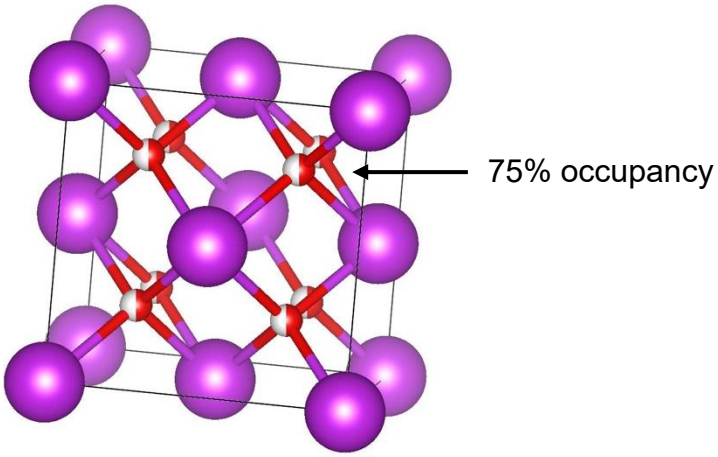


Figure 1.9: The defect fluorite structure of Bi_2O_3 crystallized in the Fm$\bar{3}$m structure.

The most commonly used SOFC electrolyte is yttria stabilized zirconia (YSZ) ($Y_xZr_{1-x}O_2$) which contains 3 – 10 mol% Y_2O_3 substituted into the ZrO_2 structure.[30] YSZ, has high mechanical strength (on the MPa scale) and presently the highest ionic conductivity reported at 1000 °C. Therefore, YSZ has emerged as the industry standard SOFC electrolyte material.[11] As shown in Figure 1.10, the conductivity of YSZ decreases significantly with decreasing temperatures, compared to doped ceria and doped lanthanum gallate. The minimum ionic conductivity for a functional SOFC electrolyte is 0.3 S cm^{-1}, which is the conductivity of YSZ at 500 °C within the intermediate temperature range (Figure 1.10). In efforts to improve the conductivity of a fluorite-type zirconia-based electrolyte, alternative materials were investigated that can be added as a substituent.[31] Scandium doped zirconia (ScSZ) has shown higher conductivity than YSZ at lower temperatures, and has comparable thermal and mechanical properties to YSZ.[25] The improved conductivity of ScSZ is clear when considering that the ScSZ conductivity at 780 °C is similar to that of YSZ at 1000 °C.[25] However, the high cost of scandium oxide and the aging phase transformation of ScSZ limits it's practical use in SOFCs.

Doped CeO_2 with a fluorite-type structure is a strong candidate as an electrolyte material for operation at lower temperatures of approximately 600 °C.[32] The ionic conductivity of Gadolinia doped ceria (10 mol% Gd_2O_3) at 600 °C is ~0.025 S cm^{-1} which is similar to that of YSZ at 800 °C (Figure 1.10). Samarium oxide (Sm_2O_3) can also be used to dope ceria, which produces comparable ionic conductivities to the gadolinia doped system.[33] The main challenge with doped ceria electrolytes is the reduction of Ce^{4+} to Ce^{3+} which occurs above 650 °C, and is a result of the formation of oxygen vacancies.[34] This reduction leads to undesirable lattice expansion and

electronic conduction. Therefore, the successful application of doped CeO_2 as a SOFC electrolyte can only occur at temperatures below 600 °C.

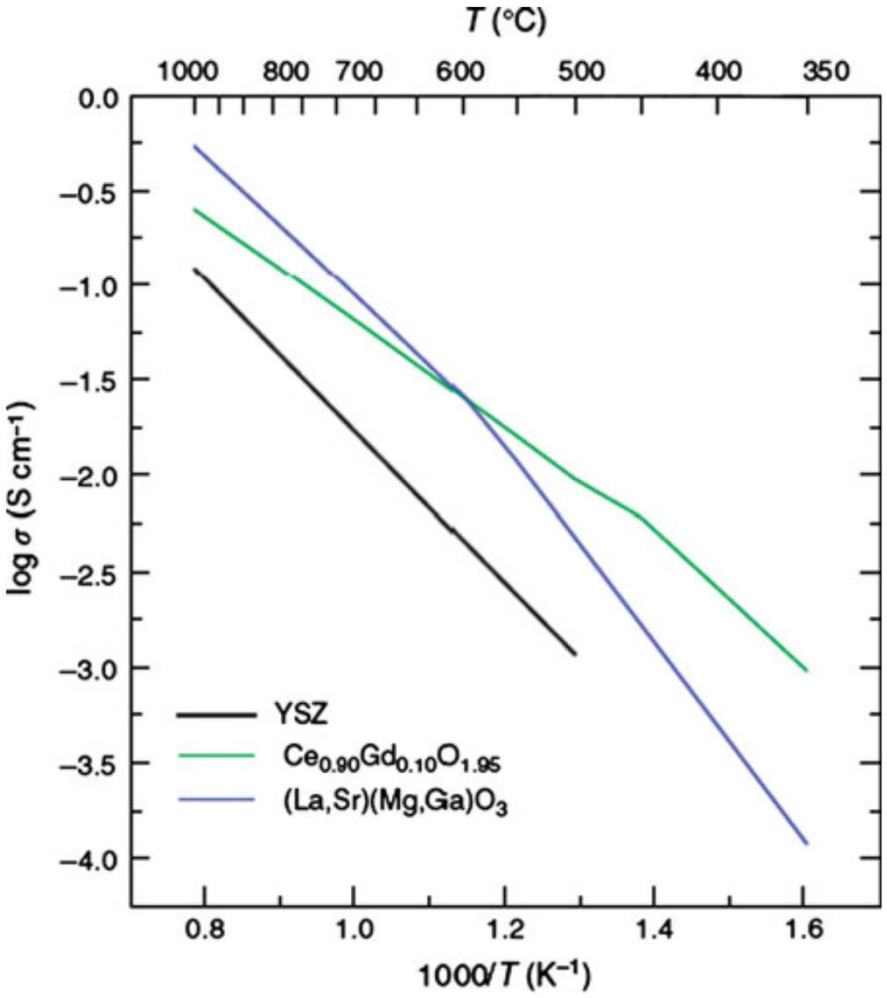


Figure 1.10: Arrhenius plots comparing the conductivities of common electrolytes used in SOFCs over 350-1000 °C. YSZ = yttria stabilized zirconia, $Ce_{0.9}Gd_{0.1}O_{1.95}$ = 10 mol% doped ceria, (La,Sr)(Mg,Ga)O_3 = LSGM = Strontium-Magnesium doped lanthanium gallium oxide.[5]

Doped lanthanum gallium oxide is an attractive electrolyte material because of its reasonable ionic conductivity (0.01 to 0.08 S cm^{-1}) at intermediate temperatures.[12] The most common material of this system is strontium and magnesium double doped lanthanum gallium oxide (LSGM or (La,Sr)(Mg,Ga)O_3) that crystallizes in a perovskite structure (Figure 1.10).[35] LSGM is chemically compatible with a range of cathodes, which contributes to its notable performance. However, the formation of single phase LSGM materials is challenging, as is the maintenance of chemical and mechanical stability.[35]

Another fluorite-related structure that is a promising SOFC electrolyte is doped bismuth oxide (Bi_2O_3). Below 700 °C, the δ-phase of Bi_2O_3 has conductivity values that are significantly higher than that of stabilized zirconia (Figure 1.11).[12] However,

the δ-phase is only stable within a narrow temperature range of 730 to 825 °C.[24] As such, dopants are added to the system to stabilize the highly conductive δ-phase at lower temperatures. Common dopants include yttria, dysprosium oxide and erbium oxide.[36] Like any electrolyte material, bismuth oxide also has several disadvantages. Above 500 °C and at low oxygen partial pressures, Bi_2O_3 has an electronic contribution to conductivity.[37] The low chemical stability of Bi_2O_3 often results in decomposition.[38] There have been numerous attempts to minimize the electronic conduction and decomposition of these materials by substituting Bi_2O_3 with a variety of dopants.[27,39,40]

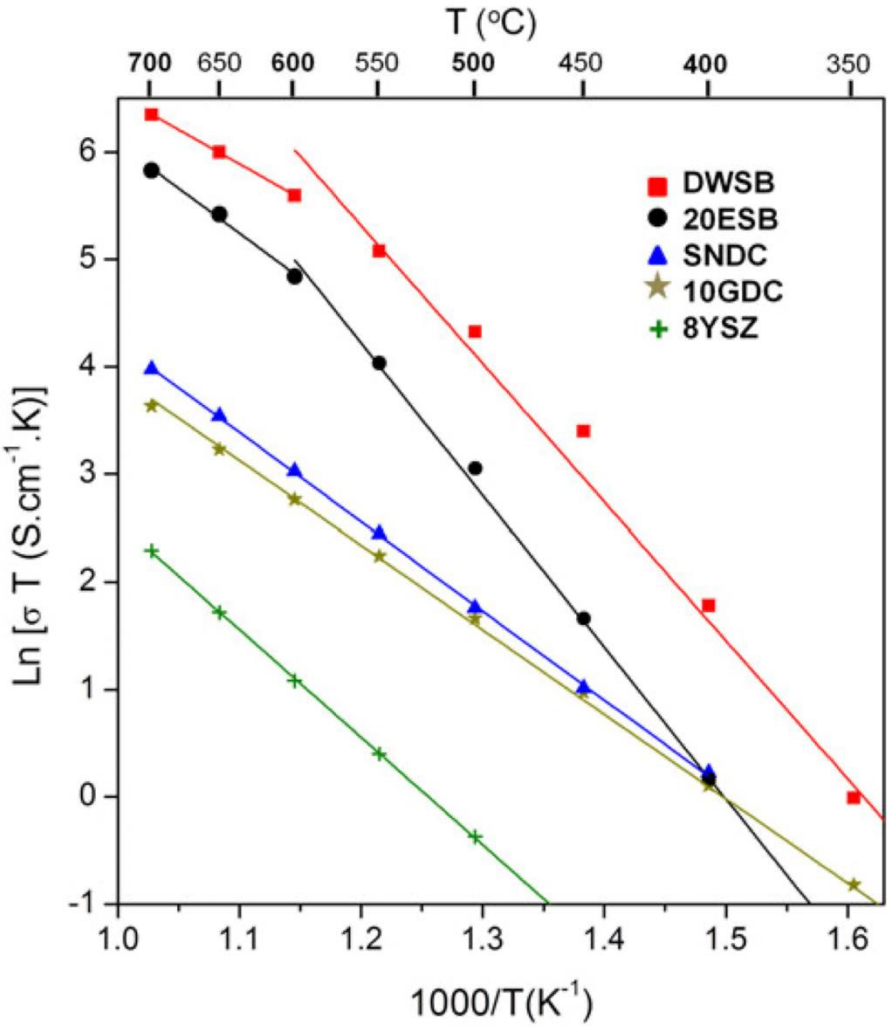


Figure 1.11: Arrhenius plots comparing the conductivities of bismuth oxide-based electrolytes with electrolytes commonly used in SOFCs; DWSB = Dysprosium-tungsten stabilized bismuth, 20ESB = 20 mol% erbium stabilized bismuth, SNDC= Samarium-Neodymium doped ceria, 10GDC = 10 mol% gadolinium doped ceria, 8YSZ = 8 mol% yttria stabilized zirconia.[8]

1.5 Pure Bi_2O_3

The pure Bi_2O_3 system comprises of six polymorphs; the α, β, γ, ε, ω and δ-phases.[13] The α-phase is the thermodynamically stable phase of the system at standard

temperature and pressure (STP) conditions.[41] The α-phase is monoclinic and crystallises in the $P2_{1/c}$ space group with cell dimensions described in Table 1.3. The δ-phase of Bi_2O_3 forms from the α-phase at approximately 730 °C , and is often referred to as the high-temperature phase.[38] The δ-phase is stable up to the melting point of Bi_2O_3, which is roughly 825 °C (Figure 1.12). δ-Bi_2O_3 is a face-centered cubic (fcc) phase that crystallises in the $Fm\bar{3}m$ space group (Table 1.3).[42] The δ-phase structure has been shown to share great similarity with the fluorite-structure, but has defects in the oxygen sublattice.[38] This defect nature of the oxygen sites contributes significantly towards the high ionic conductivity observed in δ-Bi_2O_3 materials.

The high temperature δ-phase can transform into the metastable β and γ-phases upon cooling before returning to the thermodynamically stable α-phase (Figure 1.12).[43] The transition to the β-phase occurs at around 650 °C.[39] The β-phase is tetragonal and crystallises in the $P\bar{4}2_1c$ space group, with cell parameters listed in Table 1.3. The γ-phase forms at 639 °C during the cooling of δ-Bi_2O_3 and exhibits a body-centered cubic (bcc) structure with space group $I23$.[38]

The ε and ω-phases have recently been reported following very specific synthesis conditions.[13] The ε-polymorph, with space group $Pbnb$, was prepared at 240 °C following a hydrothermal treatment of single crystals. The ε-phase was determined to exhibit a tetragonal unit cell. The continual heating of the $Pbnb$-phase resulted in a transformation into the monoclinic α-structure at 400 °C (Figure 1.12). The ω-phase exhibits a triclinic cell and crystallises in space group $P\bar{1}$. At 800 °C, the ω-phase forms from the α-structure on a BeO substrate.[13] The ω-structure is stable from 800 to 900 °C, where it then transforms into the δ-phase (Figure 1.12). The melting point of this polymorph has yet to be reported.

Table 1.3*:* Crystal structure details of the pure Bi_2O_3 polymorphs.[41]

	$\boldsymbol{\alpha}$	$\boldsymbol{\beta}$	$\boldsymbol{\gamma}$	$\boldsymbol{\delta}$	$\boldsymbol{\varepsilon}$	$\boldsymbol{\omega}$
Structure	Monoclinic	Tetragon-al	bcc	fcc	Orthorho-mbic	Triclinic
Space group	$P2_{1/c}$	$P\bar{4}2_1c$	$I23$	$Fm\bar{3}m$	$Pbnb$	$P\bar{1}$
Tempera-ture range	< 730	330 – 650	500 – 639	730 - 825	240 - 400	800 - 900
a (Å)	5.84	7.74	10.3	5.65	4.96	7.27
b (Å)	8.16	-	-	-	5.59	8.64
c (Å)	7.50	5.73	-	-	12.73	11.97
α (°)	-	-	-	-	-	87.7
β (°)	112.97(1)	-	-	-	-	92.2
γ (°)[2]	-	-	-	-	-	86.7

[2] The metastable γ-structure can persist to room temperature, which is the temperature at which the cell dimensions for this phase are reported in Table *1.3*.

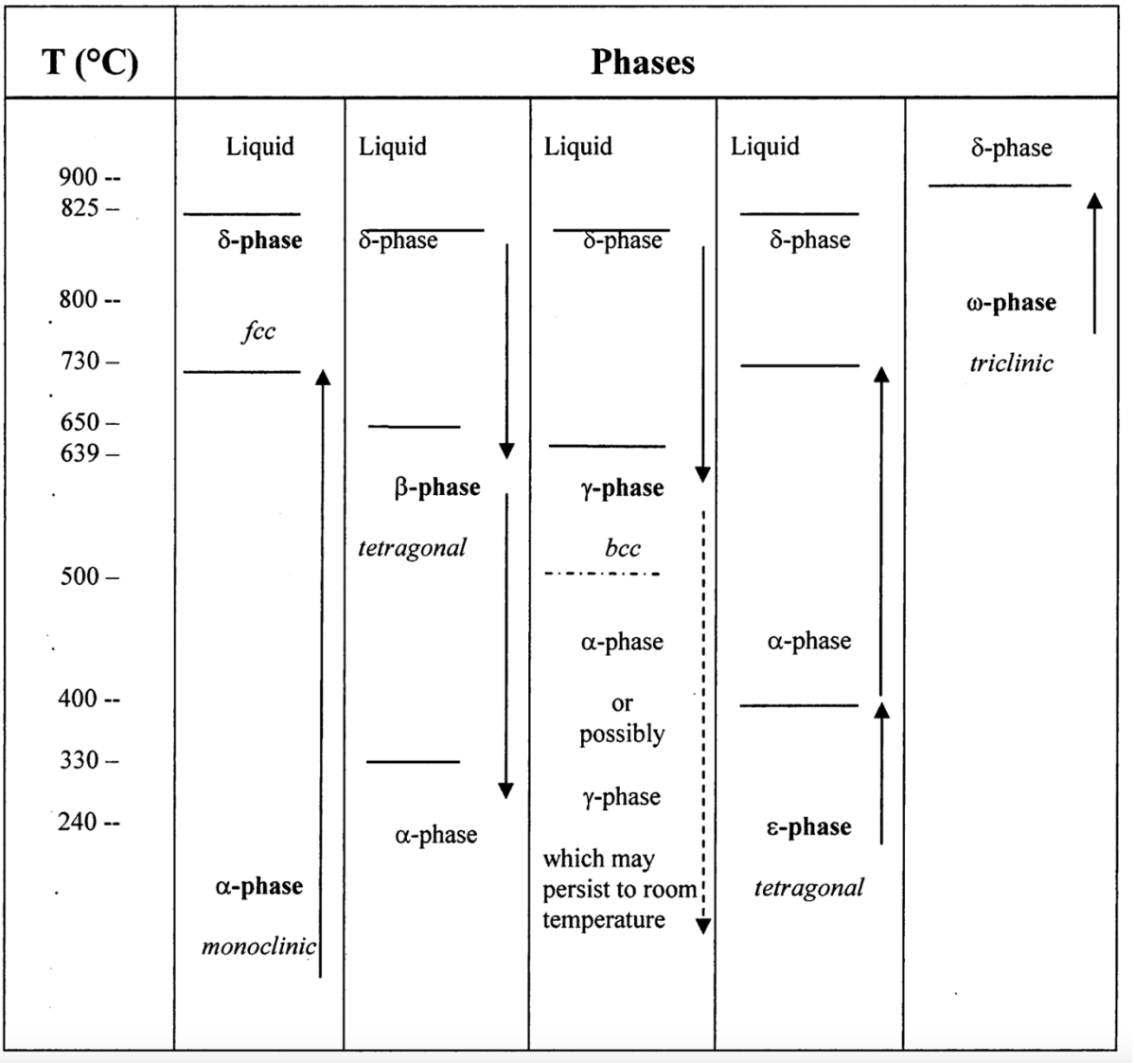


Figure 1.12: Various phase change behavior of pure Bi_2O_3 during heating and cooling regimes.[45]

1.5.1 The electrical properties of Bi_2O_3

The α-Bi_2O_3 was found to exhibit p-type conductivity at room temperature.[12] As holes are the mobile charge carriers, α-Bi_2O_3 has been characterized as being predominantly electronically conductive in the temperature range of 400-730 °C.[44] After 730 °C, a significant increase in the contribution of oxygen vacancies to conductivity was observed.[42] This data indicates that oxide ions are now the main mobile charge carriers. Since this change coincides with the α-δ phase transition, the δ-phase can be described as having n-type conductivity. The conductivity of the metastable phases have been determined to be mainly ionic, as oxide ions are the main charge carrier.[38]

Harwig and Gerards methodically measured the conductivities of the various Bi_2O_3 polymorphs (Figure 1.13).[41] The α-δ transition was marked by a conductivity

increase greater than 3 orders of magnitude. The transition of the δ-phase into the intermediate phases upon cooling resulted in significant decreases in conductivity (Figure 1.13). The significant ionic conductivity of the δ-structure results from the combined effect of several structural properties. These can be summarized as:
(1) The partially occupied (75% filled) oxygen sublattice
(2) The ability of the Bi^{3+}ion to accommodate highly disordered structures
(3) The presence of the $6s^2$ lone pair electrons in the Bi^{3+}ions which leads to significant cation polarizability, and in turn high anionic mobility.[21]

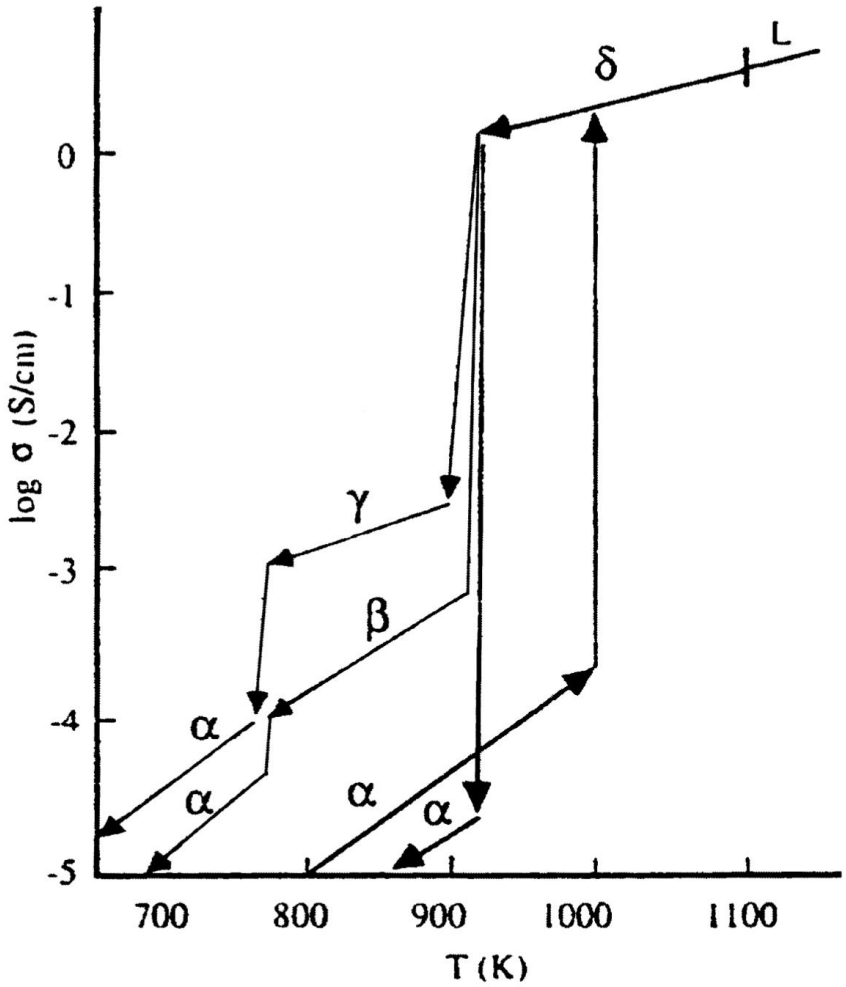


Figure 1.13: Arrhenius plot comparing the conductivities of the pure Bi_2O_3 polymorphs from 650 °C to 1100 °C.[21]

1.6 Doped Bi_2O_3

A significant shortcoming of the high-conductivity pure δ-phase is its limited stability range of 730 to 825 °C. Additionally, the δ to α transition is accompanied by a volume change that results in the cracking and structural decay of the material.[36] Pure Bi_2O_3 also tends to reduce into metallic bismuth in reducing atmospheres.[14] As such, the high-temperature cubic (fcc) phase must be stabilized to room temperature to overcome these drawbacks. Many studies have shown that the δ-phase of Bi_2O_3

can be stabilized at lower temperatures by the substitution of bismuth with metal dopants. This substitution, commonly referred to as doping, often results in reduced ionic conductivity and phase transformations.[25]

The phase composition of doped Bi_2O_3 has been reported to largely depend on three main factors. These include dopant ionic radii, dopant mole fraction and thermal treatment of the material.[45] Bismuth oxide materials have been doped with a range of different metals such as alkaline-earth metals, transition metals and rare-earth metals.[46–48] Previous work has shown that in substituted Bi_2O_3 systems, the δ-phase can remain stabilised at lower temperatures (approximately 400 °C) for significant periods when two or more metals are added to the system.[22] This simultaneous introduction of two or more dopant elements in the crystal lattice of the material is referred to as co-doping. Fung and Virkar reported success in δ-phase stabilization with their co-doping approaches using calcia (CaO), strontia (SrO), zirconia (ZrO_2) or thoria (ThO), in addition to yttria (Y_2O_3).[40] The $Y_2O_{3_x}Bi_2O_{3_{(1-x)}}$ system is the most comprehensively studied of stabilized Bi_2O_3 materials.

1.6.1 The Y_2O_3 - Bi_2O_3 system

The Y_2O_3 - Bi_2O_3 phase diagram has been explored by many investigators. Several researchers have shown that the $Y_2O_{3_{(0.25)}}Bi_2O_{3_{(0.75)}}$ material is suitable for practical use as a bismuth-based electrolyte in a SOFC.[49] This composition has the lowest yttria amount whereby no phase transformation occurs, shown by the gradual increase in conductivity from 500 to 700 °C.[55] Datta and Meehan[50] proposed that the δ-phase could be stabilized to room temperature with the addition of 21.5 to 23.5 mol% Y_2O_3.

However, further work by Watanabe and Kikuchi, and again Watanabe, showed the formation of a low-temperature phase within this composition range.[49,51] This low-temperature phase has hexagonal symmetry and transforms reversibly to the δ-phase at 720 °C.

The thermochemical stability of yttria-stabilized bismuth oxide was investigated in materials containing 22 – 32.5 mol% yttria.[31] Previously, investigators showed that materials containing less than 31.8 mol% Y_2O_3 are cubic only above ~840 °C.[55] Below this temperature, the cubic phase is metastable and undergoes a slow transformation to the hexagonal phase when annealed at 650 °C for more than 160 hours.[50]

Takahashi et al[52] examined the conductivities of sintered Y_2O_3 - Bi_2O_3 solid solutions, containing 0-60 mol% Y_2O_3 in air. Significant observations can be made from the Arrhenius plots of these solid solutions (Figure 1.14). As expected, the pure Bi_2O_3 material exhibits low conductivity below 730 °C, until the α to δ transition occurs. The conductivity of solid solutions containing less than 25 mol% Y_2O_3 show

significant hysteresis between the heating and cooling cycles. Figure 1.14 also shows how the magnitude of the conductivity jumps decrease with increasing yttria content, mostly from curves 3 to 8. Watanabe and Kikuchi[49] investigated the conductivity of the low-temperature hexagonal phase observed for 22.5 mol% Y_2O_3 stabilized Bi_2O_3. The d.c. conductivity results revealed that the stable hexagonal phase exhibited conductivity that was one order of magnitude less than that of the metastable cubic phase.

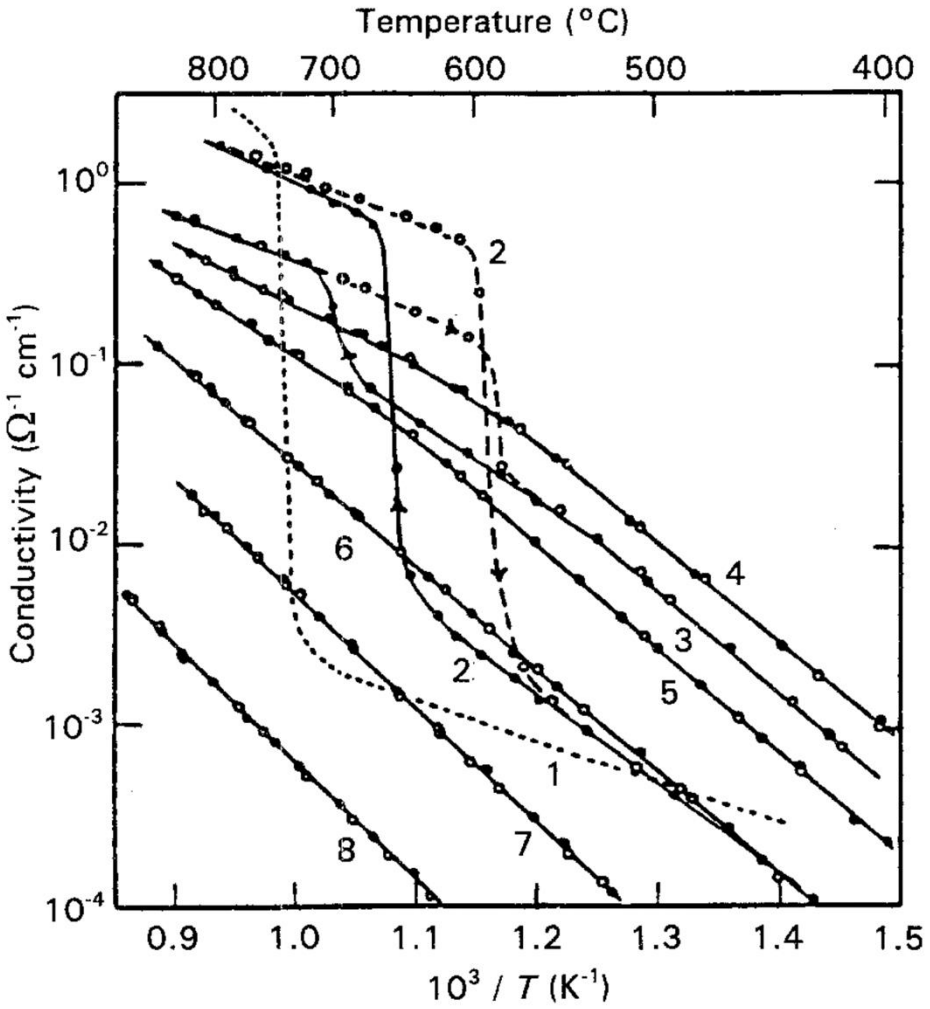


Figure 1.14: Arrhenius plots showing the conductivity of $(Bi_2O_3)_{1-x}(Y_2O_3)_x$ materials measured in air. 1: x = 0.0 , 2: x = 0.05 , 3: x = 0.20 , 4: x = 0.25 , 5: x = 0.33 , 6: x = 0.425 , 7: x= 0.50, 8: x = 0.60.[55]

The low temperature phase with hexagonal symmetry is commonly known as the rhombohedral phase. The aging of the highly conducting cubic phase into the less conducting rhombohedral phase is a common trait of Bi_2O_3 systems doped with less than 30 mol% of rare earth metals. Stabilized cubic phases are known to be metastable below 700 °C, which is a significant shortcoming of these materials.[43] There have been several approaches to improve the stability of stabilized Bi_2O_3 materials at lower temperatures, such as using multiple metal oxides as co-dopants.

The stabilization of the high-temperature cubic phase has been extensively investigated and still requires further research to become a suitable electrolyte. The work presented in this dissertation focusses on understanding the low-temperature rhombohedral phase instead, with the general aim of enhancing its suitability as a SOFC electrolyte.

1.7 The rhombohedral phase of doped Bi_2O_3

1.7.1 Structure

A relatively high conductivity phase within the intermediate temperature range (450 – 700 °C) was first revealed in the Bi_2O_3 – MO (M = Ca, Sr) systems.[48] The significant conductivity at a much lower temperature than that for stabilized zirconia attracted huge interest to this phase. As such, investigations were completed on this structure, commonly known as the rhombohedral phase of stabilized Bi_2O_3.

The rhombohedral phase was identified in the Bi_2O_3 – SrO and Bi_2O_3 – CaO systems as a solid solution that exists as two polymorphic forms.[54] The polymorphs represent the high-temperature and low-temperature forms named β_1 and β_2, respectively. Several researchers have also shown that a type of rhombohedral phase exists when substituting Bi_2O_3 with a range of lanthanide oxides (Ln_2O_3 where Ln = lanthanum to dysprosium).[46] Many accounts of work on the lanthanide series have focused on a specific composition; $\mathrm{Bi}_{1-x}\mathrm{Ln}_x\mathrm{O}_{1.5}$. The structure of this material has been reported as having a hexagonal unit cell with lattice parameters a and c being approximately 4 Å and 28 Å, respectively.[46,48,55]

The reported β_1 and β_2 polymorphs share great similarity, as shown by their comparable powder x-ray diffraction patterns. Therefore, it was suggested that the clear identification of polymorphism required a continuous recording technique, such as using a Guinier Lenné camera. This method was adopted when examining alkaline earth based systems to confirm the polymorphic nature of the rhombohedral phase, and later with rare earth based materials too [46,54], since both these systems exhibited two distinguishable polymorphic forms. The slight difference between the two polymorphs has been attributed to a difference in cationic ordering within the structures. The β_2 form is the thermodynamically stable rhombohedral phase (present at room temperature) and has thus been the most examined form in Bi_2O_3 rhombohedral phase investigations.

The structural determination of the rhombohedral phase was first completed in 1989 by Mercurio et al.[56] This work focused on the β_2 form of the $\mathrm{Bi}_{0.75}\mathrm{Sr}_{0.25}\mathrm{O}_{1.375}$ material. The structure determination was conducted using single crystal neutron diffraction and subsequent refinements. The mixed oxide material was melted so that a single crystal could be obtained for structural analysis. Further structural studies on the material were completed using powder x-ray diffraction together with Rietveld powder structure refinements and TEM investigations.[46,47,55,57] A structure of the

rhombohedral phase could be described by considering the several investigations on the doped Bi_2O_3 rhombohedral system (Figure 1.15).

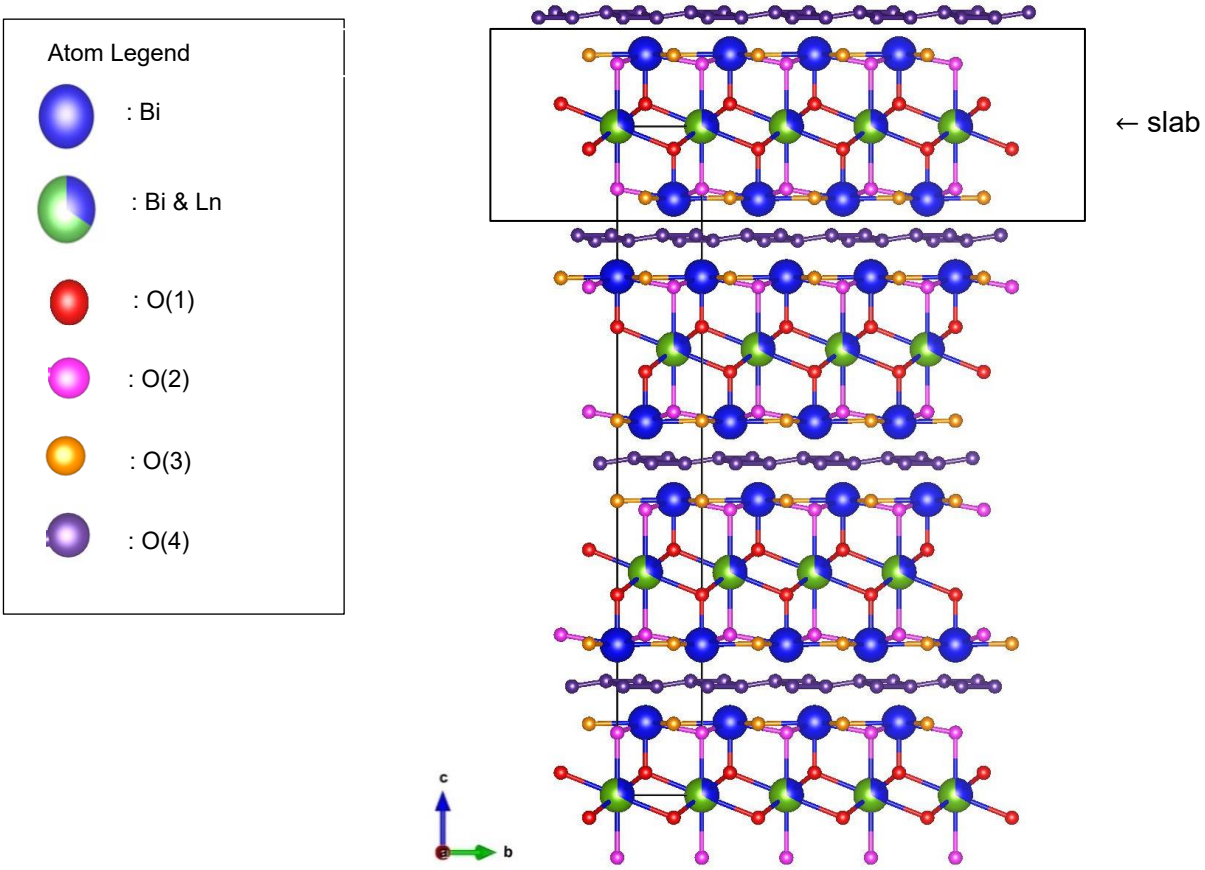


Figure 1.15: The β_2 rhombohedral structure of lanthanide stabilized bismuth oxide, determined using x-ray diffraction.[45]

The β_1 and β_2 forms crystallize in layered structures comprised of cationic slabs that are parallel to the c-axis in the β_1 and β_2 hexagonal cells (Figure 1.15).[58] A cationic slab contains two Bi^{3+} layers separated by a mixed Bi^{3+}/Ln^{3+} layer.[55,59,60] The mixed and pure Bi^{3+} nature of the layers were determined using interatomic distances that were obtained from atomic positions in the unit cell. [55,59,60] These correspond to the cationic layers of the cubic δ phase along the (111) plane, as shown in Figure 1.16. These related structures show a similar slab organization, as a result of the repeated shearing of three layers of the cubic fluorite structure.[56]

In the β_2 rhombohedral form, two cationic sites have been observed. The external Bi^{3+} layer has 6c metal sites, while the middle Bi^{3+}/Ln^{3+} layer contains 3a metal sites (Table 1.4). [46,55,57] There have also been several kinds of oxide ion sites identified in the rhombohedral structure. Fully occupied oxide ion sites have been located between the cationic slabs and contribute to the cohesion of these slabs

(Figure 1.15). These oxide ion sites are commonly referred to as O(1) in literature sources and occupy the 6c site. Partially occupied oxide ion sites are located near the interslab space in 6c sites, and are referred to as O(2) ions in the structure.[60]

While the general features of the rhombohedral structure have been established, there are additional oxygen sites that are partially occupied in the unit cell. These sites can be O(3) ions according to x-ray diffraction data, however neutron diffraction reveals O(3) and O(4) ions present in the rhombohedral structure.[46,55] The O(3) ions are located along the surface of the cationic slabs, and the O(4) ions have been identified near the middle of the interslab space (Figure 1.15). In the β_2 phase the occupancy decreases from the O(2) to O(4) sites, with approximate occupancies of 75%, 30% and 7% for O(2), O(3) and O(4) sites, respectively (Table 1.4). The occupancy of the O(3) and O(4) atoms allow one to distinguish between the β_1 and β_2 rhombohedral forms. The $\beta_1 \rightarrow \beta_2$ transition during cooling is evidenced by a decrease of oxygen ions in the interslab space and a corresponding oxygen ion increase within the slab.[55] This essentially means that the O(4) ions decrease while the O(3) ions increase. While the transition is signaled by a change in anion occupancy, there have been no reported changes in the cation lattice from the β_1 to β_2 forms.

Table 1.4: The atomic sites and occupancies of rhombohedral Bi_2O_3 - Lni_2O_3 systems.

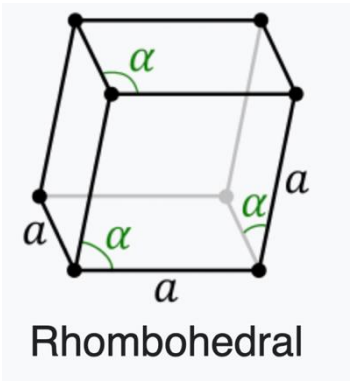
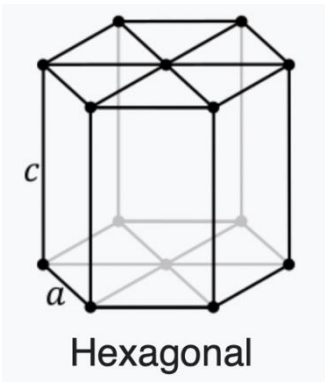
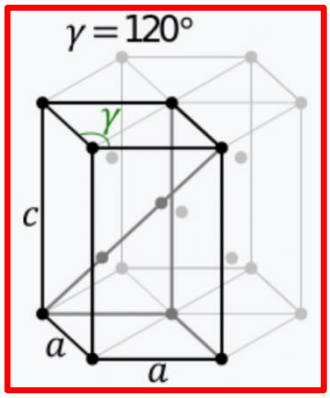
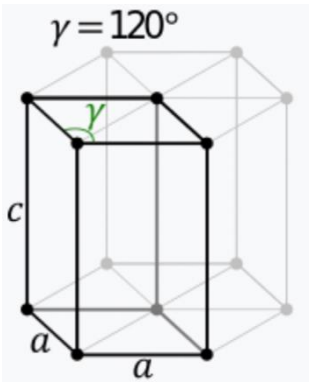
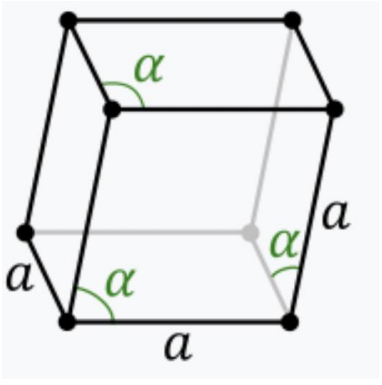
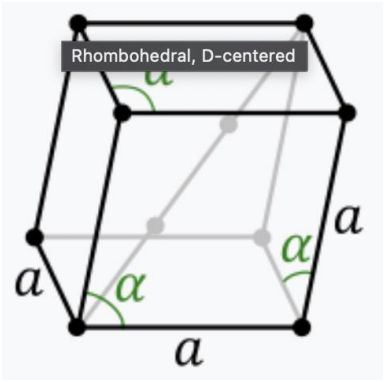
Atoms	**Site**	**Occupancy***
Bi	6c	1
Bi/Ln	3a	0.3/0.7
$O_{(1)}$	6c	1
$O_{(2)}$	6c	0.7
$O_{(3)}$	6c	0.3
$O_{(4)}$	18h	0.07

1.7.2 Crystallographic Structure

The crystallographic properties of the rhombohedral phase is characterized by the $R\bar{3}m$ space group, having a 3-fold rotary inversion axis found at the intersection of three mirror planes.[61] The rhombohedral structure system forms part of the hexagonal crystal family which comprises of two crystal systems; trigonal and hexagonal (Table 1.5). The trigonal and hexagonal systems are unique in that they can have either a rhombohedral or hexagonal lattice.[62] Consequently, the crystal structure is usually referred to as its lattice type, which is determined by the characteristic symmetry elements present. Therefore, the rhombohedral phase of interest in this project is more formally known as the rhombohedral lattice with a hexagonal unit cell.

Stabilized bismuthate has a hexagonal unit cell with two equal axes (a = b) and a height (c) perpendicular to the other axes, as shown in the table below. The hexagonal unit cell in the rhombohedral lattice has a 3-fold axis of symmetry. The hexagonal unit cells are arranged in layers, and the stacking of the hexagonal layers along the c-axis produces the rhombohedral structure of interest.[46,55,57]

Table 1.5: The hexagonal crystal family and its crystal systems, bravais lattices and unit cells. Images adapted from.[63]

Crystal Family	Hexagonal	
Crystal System	Trigonal	Hexagonal
Bravais lattice		
Hexagonal unit cell		
Rhombohedral unit cell		

1.7.3 Phase formation

The β_2 $Bi_{1-x}Ln_xO_{1.5}$ phase (Ln = La – Er, Y) has been isolated at room temperature using certain synthetic routes. The β_2 phase can either be isolated when synthesizing in its stability domain (≤ 650 °C) or by solid state synthesis at high temperatures followed by annealing at appropriate lower temperatures.[55,60,64] On the other hand, the β_1 form can be obtained by quenching the high temperature product that forms between 650 and 850 °C. When the quenched β_1 form undergoes low temperature annealing (≤ 200 °C), a transformation to the monoclinic ε phase can occur.[60] The monoclinic ε phase is closely related to the β_1 and β_2 forms, as illustrated by Figure 1.16 .It has been shown by previous researchers that the ε phase can undergo a phase transition to the β_2 form during heating, from 445 to 545 °C.[46,48,57] Thereafter, the β_2 form can transform to β_1 at approximately 650 °C. It has been confirmed that $Bi_{1-x}Ln_xO_{1.5}$ materials, whether in the ε, β_2 or β_1 form, transforms to the δ phase at higher temperatures (from ~800 °C). The β_1 and β_2 hexagonal unit cells as well as the ε monoclinic unit cell are structurally related to the δ cubic unit cell, also shown in Figure 1.16 and Table 1.6.

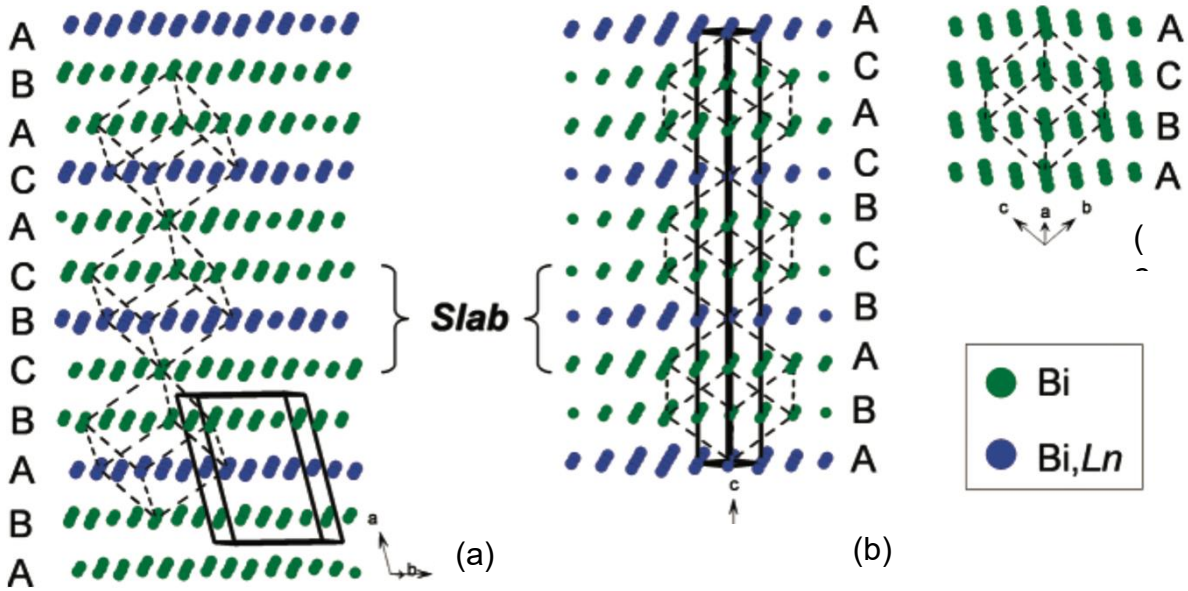


Figure 1.16: The structural relationship between (a) the ε-monoclinic, (b) β_1 or β_2-hexagonal and (c) δ-cubic cells.[44]

Table 1.6: Unit cell parameters and synthetic conditions for the ε, β_1/ β_2 and δ phases.[45]

	$\boldsymbol{\varepsilon}$	$\boldsymbol{\beta_1/\beta_2}$	$\boldsymbol{\delta}$
Unit Cell	Monoclinic	Hexagonal	Cubic (fcc)
a (Å)	9.492(2)	4.0253(1)	11.0488(1)
b (Å)	7.951(2)	----	----
c (Å)	7.028(2)	27.6004(9)	----
$\boldsymbol{\alpha}$ (°)	----	----	----
$\boldsymbol{\beta}$ (°)	104.74(1)	----	----
$\boldsymbol{\gamma}$ (°)	----	----	----
Synthesis Conditions	Quenching of the high-temperature β_1 form followed by final annealing (250 – 400 °C)	β_2: synthesis in stability domain (<650 °C) or slow cooling of high temperature synthesis	Reaction at 800 °C
		β_1: synthesis in its stability domain (650 to 850 °C) and preserved by sample quenching	

As β_2 is the thermodynamically stable form of rhombohedral doped Bi_2O_3 materials, it often coexists with the thermodynamically stable α phase of pure Bi_2O_3 when bismuth is the predominant metal in $Bi_{1-x}Ln_xO_{1.5}$.[58,60,65] In this case, Ln can range from lanthanum across the period to erbium, as well as yttrium. A relationship between the β_2 stability domain and lanthanide size has been shown, where a larger lanthanide generally results in a wider β_2 compositional domain.[50,58,66] This general trend is shown with selected lanthanide metals (and yttrium) in Table 1.7.

Table 1.7: Relationship between lanthanide (and yttrium) ionic radii and rhombohedral β_2 composition domain.[45]

Metals	**Ionic Radii (Å)**	**$\boldsymbol{\beta_2}$ Composition domain in $\mathbf{Bi_{1-x}Ln_xO_{1.5}}$**
La	1.16	15 – 35 %
Y	1.019	21.5 – 23.5 %
Ho	1.015	20.5 % - 24.5 %
Er	1.004	~ 22.2 %

The ε phase of $Bi_{1-x}Ln_xO_{1.5}$ can also be thermodynamically stable at room temperature for certain compositions.[60] The compositional domains of the β_2 and ε phases versus lanthanide ionic radii are shown in Figure 1.17. The diagram reveals

the potential existence of related mixed oxide superstructures, namely $Bi_4Ln_2O_9$ (or $Bi_{1.33}Ln_{0.67}O_3$) for large rare earth metals and $Bi_7Ln_2O_{13.5}$ (or $Bi_{1.56}Ln_{0.44}O_3$) for smaller lanthanides.[60] The β_2 cell parameters of the $Bi_4Ln_2O_9$ and $Bi_7Ln_2O_{13.5}$ materials show a linear dependence with average cationic radius, just like the widely studied $Bi_{0.775}Ln_{0.225}O_{1.5}$ system.[58] This figure shows the relative lanthanide amounts required to stabilize the β_2 and ε forms in relation to lanthanide ionic size. It is clear from this figure that the β_2 phase has a wider compositional domain while the ε phase tends to form when larger lanthanides are substituted in higher amounts in the Bi_2O_3 system.

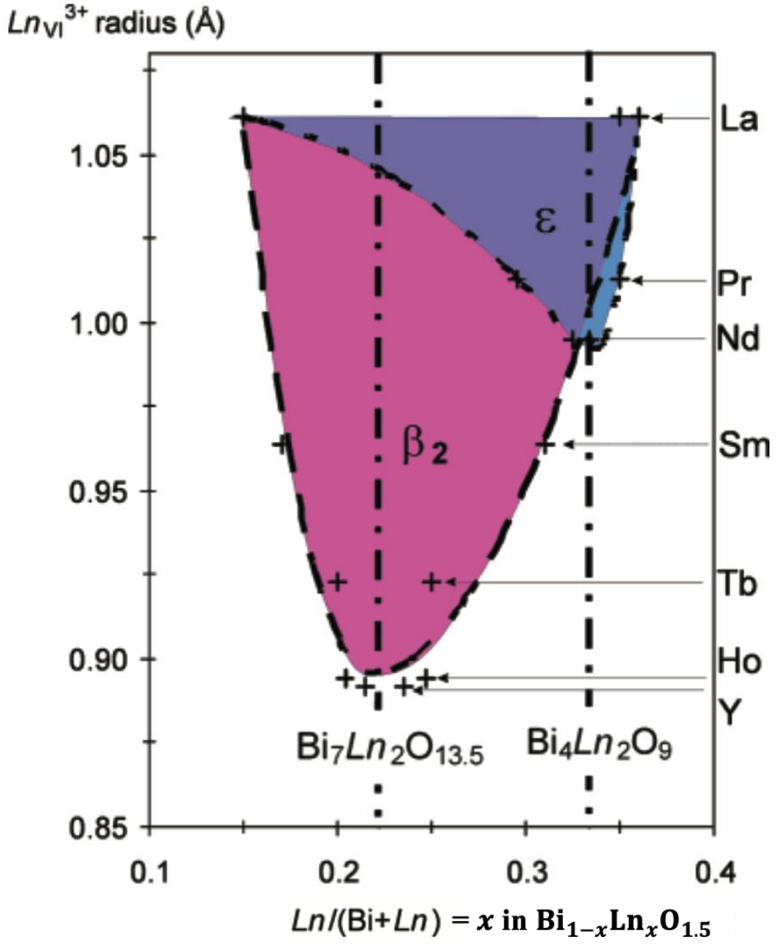


Figure 1.17: Relationship between the ε- and β_2-$Bi_{1-x}Ln_xO_{1.5}$ composition domains versus Ln^{3+} radius.[44]

The compositional domain of the β_2 rhombohedral phase can be further understood by describing its relation to that of the cubic (fcc) phase. As shown in Figure 1.18, the rhombohedral phase usually forms in lower dopant region of systems, where the cationic radii of added oxides are comparatively large.[47] On the other hand, the fcc structure is promoted by a greater dopant content of metal oxides with relatively smaller size (Figure 1.18).[67] Medium sized metal oxides can have a mixture of phases, the ratio depending on the composition of the dopant and bismuth oxide.[49]

Lastly, the thermal conditions during synthesis can also determine the phase that forms. The rhombohedral phase forms at lower temperatures (≤ 650 °C) while the cubic phase forms at higher temperatures (800 °C – 1000 °C).[41]

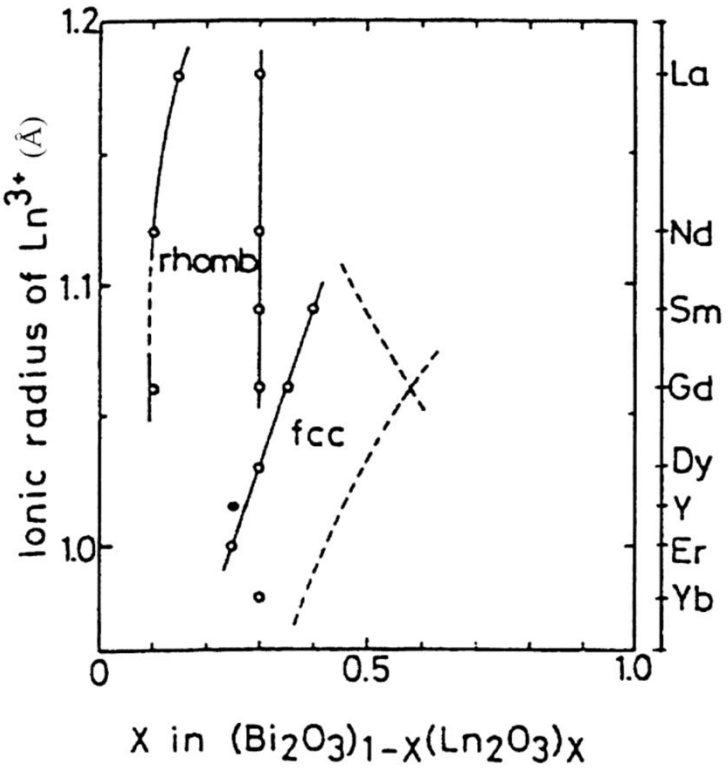


Figure 1.18: Formation ranges of the rhombohedral and fcc phases related to ionic radius (of Ln^{3+}) versus $Bi_{1-x}Ln_xO_{1.5}$ composition plot.[47]

1.7.4 Properties

The $\varepsilon \rightarrow \beta_2 \rightarrow \beta_1$ phase transitions in lanthanide substituted Bi_2O_3 occurs with an increase in cationic slab thickness along the c-axis of the cell.[55] This expansion has been attributed to the evolution of the oxygen sublattice occupancy.[68] The phase transitions are also accompanied by a conductivity jump on the Arrhenius plot. The $\varepsilon \rightarrow \beta_2$ transition is signaled by a conductivity increase of a decade, and the $\beta_2 \rightarrow \beta_1$ transition only has a third of decade conductivity jump.[69] The relative magnitudes of the conductivity jumps are independent of the lanthanide substituent and composition, unlike the alkaline earth substituted materials that show a correlation between conductivity increase and sample composition.[54,69]

Conflant *et al.*[54] determined the structural evolution versus temperature dependence of O^{2-} transport numbers using oxygen cell electromotive force measurements. The results revealed a pure anionic (oxide) conductivity for β_1 and mixed anionic/electronic conduction for the β_2 form. This faradaic output behaviour was further studied using the $Bi_{0.7}Ln_{0.3}O_{1.5}$ material and an amperometric membrane, which revealed similar behaviours as shown in Figure 1.19 corresponds to the

theoretical value of anion (oxide) conductivity and thus has an output of 100%, while β_2 decreases in ionic Faradaic output from 90 to 30% within the temperature range of 650 to 500 °C. The β_2 behaviour indicates the mixed oxide - electron conduction, and is followed by no response when converted to the ε phase below 470 °C. The ε behavior is expected as this form is not oxide conducting.

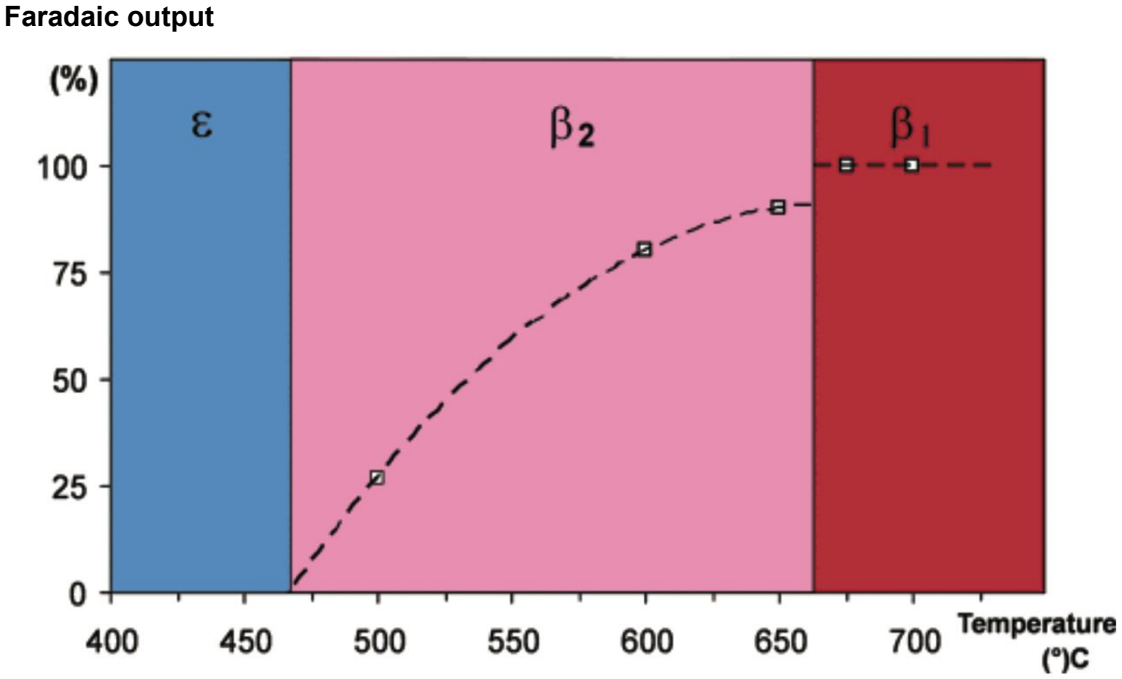


Figure 1.19: Faradaic outputs of the ε, β_2 and β_1 phases of $Bi_{0.7}La_{0.3}O_{1.5}$.[45]

The conductivity properties of the $Bi_{0.775}Ln_{0.225}O_{1.5}$ series have been investigated by many researchers in efforts to understand the mechanism behind significant conductivity in β_2-lanthanide substituted rhombohedral Bi_2O_3. Several studies have revealed that the highest conductivity of β_2-lanthanum substituted Bi_2O_3 at moderate temperatures is obtained by materials that have the largest cationic slab.[46,47,57,64] It appears that the greater cationic slab thickness results in lower electrostatic interactions between the slabs and oxygen atoms in the interslab space[46], or that the oxygen atoms don't protrude into the interslab space as significantly with a larger cationic slab. These are plausible explanations for the proportional substituent size and conductivity relationship of the rhombohedral material, shown in Figure 1.20.

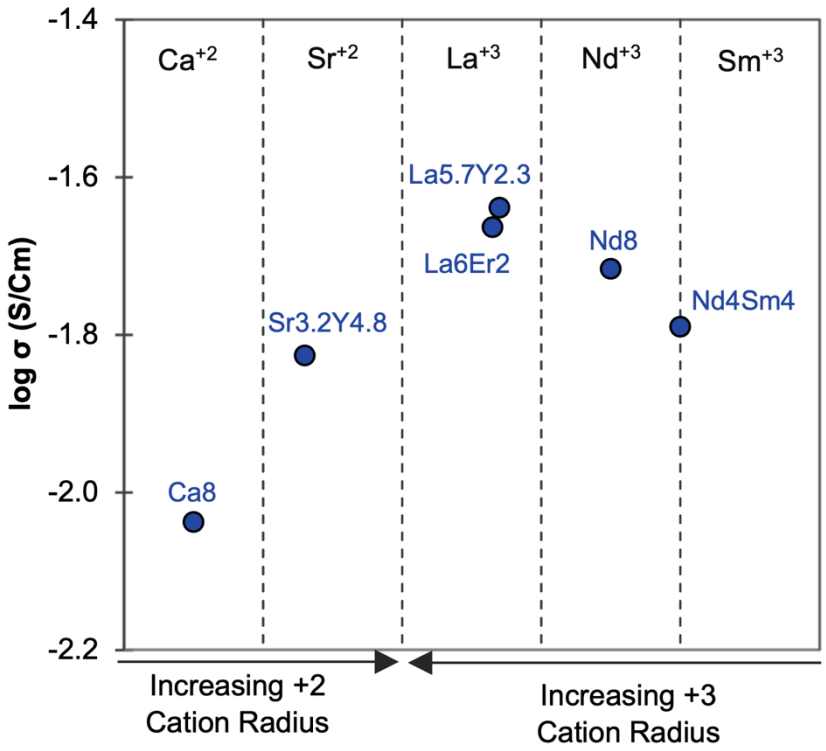


Figure 1.20: Conductivities of various rhombohedral stabilized Bi_2O_3 systems that are 8% cation doped. (e.g. Ca8 represents 8% Ca doped Bi_2O_3) The conductivities were measured at 500 °C.[70]

While considering the previous work of researchers, it has been established that the low-temperature rhombohedral phase holds great promise as an oxide ion conductor phase in SOFCs. However, there appears to be relatively few studies and even conflicting research focused on the rhombohedral structure of doped bismuth oxide. With that being said, the research that is available does provide a guide for further studies on the potential electrolyte phase. For example, do the proposed trends between structural parameters and phase formation overlook other elemental properties characteristic to a dopant? One may also critically discuss the previous structure determinations of the rhombohedral phase and investigate its reproducibility. There are several questions concerning the low-temperature phase, which presents the focus of this project.

1.8 Aims and Objectives

The overall aim of this project is to investigate the formation and conductive properties of the rhombohedral phase of doped Bi_2O_3. This will be done in efforts of gaining a deeper understanding of the phase as a potential SOFC electrolyte material.

Objective 1

Synthesize lanthanide substituted Bi_2O_3 materials that predominantly form the rhombohedral phase using the citrate sol-gel method, and thereafter characterize

materials with complementary techniques. The average crystalline structure of synthesized materials will be characterized using laboratory and synchrotron powder x-ray diffraction (PXRD). The local structure will be examined using Raman spectroscopy and the total scattering of the material by analysing the pair distribution functions (PDF). Characterization of the conductive properties of the stabilized Bi_2O_3 samples will be conducted using Electrochemical impedance spectroscopy (EIS).

Objective 2

Examine the effects of substituent size by varying the lanthanide oxide added to the Bi_2O_3 system. The substituents selected for this study are lanthanum, samarium and gadolinium. Lanthanum is selected as it is the largest lanthanide (1.16 Å) and has been reported to have the best rhombohedral phase stability of the lanthanides. Samarium was chosen as an intermediate sized substituent (1.079 Å) that can also form the rhombohedral phase according to some researchers. Gadolinium is the smallest substituent (1.053 Å) added to Bi_2O_3 which tends to favor formation of the cubic (fcc) phase based on the ion's size. However, there have been reports that gadolinium can also form the rhombohedral phase when added in small quantities.

Objective 3

Determine the influence of substituent concentration on phase formation and ionic conductivity. Each substituent was added to Bi_2O_3 in concentrations ranging from 15 mol% to 25 mol%. According to literature sources, the desired rhombohedral phase tends to form within this composition domain in lanthanide substituted Bi_2O_3 systems. It has been proposed that the conductivity and substituent amount are inversely related, which can be investigated within the composition domain selected.

Objective 4

Determine the optimized synthetic conditions to form and stabilize the rhombohedral phase during synthesis. Using the sol-gel method, the prepared dried gel is first calcined and then annealed, where the later step is crucial in obtaining phase-pure products of desired crystallinity. Therefore, the annealing step is the focus of improving the synthetic procedure and temperatures of either 610 °C or 750 °C are to be used. These temperatures were selected by considering the cubic to rhombohedral transition that is proposed to occur at approximately 650 °C. Samples were also annealed for different durations, namely 5, 10 and 15 hours, in efforts to develop the most suitable thermal treatment.

1.9 References

1. South Africa Coal Reserves and Consumption Statistics - Worldometer. https://www.worldometers.info/coal/south-africa-coal/ (2016).
2. South Africa Energy Information | Enerdata. https://www.enerdata.net/estore/energy-market/south-africa/ (2023).
3. Pilling, D. & Campbell, C. The cost of getting South Africa to stop using coal. https://www.ft.com/content/3c64950c-2154-4757-bf25-d93c7850be8f (2022).
4. Ni, M., Leung, M. & Leung, D. Technological development of hydrogen production by solid oxide electrolyzer cell (SOEC). *International Journal of Hydrogen Energy* **33**, 2337–2354 (2008).
5. Irvine, J & Connor, P. Solid Oxide Fuels Cells: Facts and Figures: Past Present and Future Perspectives for SOFC Technologies. (Springer London, 2013).
6. Huang, K. & Goodenough, J. B. Solid Oxide Fuel Cell Technology: Principles, Performance and Operations. (Elsevier, 2009).
7. Brandon, N. Solid Oxide Fuel Cell Lifetime and Reliability: Critical Challenges in Fuel Cells. (Academic Press, 2017).
8. Lee, K. T., Yoon, H. S. & Wachsman, E. D. The evolution of low temperature solid oxide fuel cells. *Journal of Materials Reearch* **27**, 2063–2078 (2012).
9. Wachsman, E.D & Lee, K.T. Lowering the Temperature of Solid Oxide Fuel Cells. *Science,* **334**, 935 - 939 (2011).
10. Singhal, S. C. *Solid Oxide Fuel Cells, History.* in *Encyclopedia of Applied Electrochemistry* (Springer, 2014).
11. Mahato, N., Banerjee, A., Gupta, A., Omar, S. & Balani, K. Progress in material selection for solid oxide fuel cell technology: A review. *Progress in Materials Science* **72**, 141–337 (2015).
12. Badwal, S. P. S. & Ciacchi, F. T. Oxygen-ion conducting electrolyte materials for solid oxide fuel cells. *Ionics* **6**, 1–21 (2000).
13. Singhal, S.C & Kendall, K. *High-temperature Solid Oxide Fuel Cells: Fundamentals, Design and Applications* (Elsevier, 1985).
14. Weissbart, J. & Ruka, R. A Solid Electrolyte Fuel Cell. *Journal of Electrocheical. Society.* **109**, 723 (1962).
15. Wilberforce, T., Alaswad, A., Palumbo, A., Dassisti, M. & Olabi, A. G. Advances in stationary and portable fuel cell applications. *International Journal of Hydrogen Energy* **41**, 16509–16522 (2016).
16. Alaswad, A., Palumbo, A., Dassisti, M. & Olabi, A.G. *Fuel Cell Technologies, Applications, and State of the Art: A Reference Guide.* (Elsevier, 2015).
17. Mekhilef, S., Saidur, R. & Safari, A. Comparative study of different fuel cell technologies. *Renewable and Sustainable Energy Reviews* **16**, 981–989 (2012).
18. Inc, W. I. 10 Hydrogen Fuel Cell Applications | Uses of Hydrogen. https://wha-international.com/10-hydrogen-fuel-cell-applications-you-might-not-know/ (2023).
19. Microsoft Kept Servers Running on Nothing but Hydrogen for 2 Days. https://www.popularmechanics.com/science/a33499249/microsoft-hydrogen-generator-test/ (2020).

20. Clean, Reliable and Affordable: The Bloom Energy Server. https://www.bloomenergy.com/technology/.
21. Sammes, N. M., Tompsett, G. A., Näfe, H. & Aldinger, F. Bismuth based oxide electrolytes - structure and ionic Conductivity. *Journal of the European Ceramic Society* **19**, 1801 - 1826 (1999).
22. Jiang, N. & Wachsman, E. D. Structural Stability and Conductivity of Phase-Stabilized Cubic Bismuth Oxides. *Journal of the American Ceramic Society* **82**, 3057–3064 (2004).
23. Mercurio, D., Farissi, M. E. & Frit, B. Fast Ionic Conduction in New Oxide Materials of the Bi_2O_3-Ln_2O_3-TeO_2 Systems (Ln = La, Sm, Gd, Er). *Solid State Ionics* **39**, 294 - 304 (1990).
24. Steele, B. C. H. & Heinzel, A. Materials for fuel-cell technologies. *Nature* **414**, 345–352 (2001).
25. Minh, N.Q. & Takahashi. T. *Science and Technology of Ceramic Fuel Cells* (Elsevier, 1995).
26. Ralph, J. M., Schoeler, A. C. & Krumpelt, M. Materials for lower temperature solid oxide fuel cells. *Journal of Materials Science* **36**, 1161–1172 (2001).
27. Why Solid Oxide Fuel Cells as a Remote Power Source. https://spsources.com/why-solid-oxide-fuel-cells/ (2022).
28. Takahashi, T., Esaka, T. & Iwahara, H. Conduction in Bi_2O_3 -based oxide ion conductors under low oxygen pressure. I. Current blackening of the Bi_2O_3-Y_2O_3 electrolyte. *Journal of Applied Electrochemistry* **7**, 299 - 302 (1977).
29. Huang, K., Feng, M. & Goodenough, J.B. Bi_2O_3-Y_2O_3-CeO_2 solid solution oxide-ion electrolyte. *Solid State Ionics* **89**, 17–24 (1996).
30. Sarat, S., Sammes, N. & Smirnova, A. Bismuth oxide doped scandia-stabilized zirconia electrolyte for the intermediate temperature solid oxide fuel cells. *Journal of Power Sources* **160**, 892–896 (2006).
31. Singhal, S. C. Advances in solid oxide fuel cell technology. *Solid State Ionics* **135**, 305–313 (2000).
32. Sahibzada, M., Steele, B. C. H., Barth, D., Rudkin, R. A. & Metcalfe, I. S. Operation of solid oxide fuel cells at reduced temperatures. *Fuel* **78**, 639–643 (1999).
33. Gu, H.*, Zheng, Y., Ran. R., Shao, Z., Jin.W., Xu.,N. & Ahn, J.* Synthesis and assessment of $La_{0.8}Sr_{0.2}Sc_yMn_{1-y}O_{3-\delta}$ as cathodes for solid-oxide fuel cells on scandium-stabilized zirconia electrolyte. *Journal of Power Sources* **183**, 471–478 (2008).
34. Wu, Y., Chang, Y. & Wang, S. Electrical Properties and Microstructural Analysis of Aliovalent-Ion (Y^{3+},Nb^{5+})–Doped Bismuth-Based Solid-Oxide Electrolyte. *Ferroelectrics* **455**, 123–128 (2013).
35. Ivers-Tiffée, E., Weber, A. & Herbstritt, D. Materials and technologies for SOFC-components. *Journal of the European Ceramic Society* **21**, 1805–1811 (2001).

36. Wang, S., Hsu, Y., Tsai, W. & Lu, H. The phase stability and electrical conductivity of Bi_2O_3 ceramics stabilized by Co-dopants. *Journal of Power Sources* **218**, 106–112 (2012).
37. Badwal, S. P. S. Electrical conductivity of single crystal and polycrystalline yttria-stabilized zirconia. *Journal of Materials Science* **19**, 1767–1776 (1984).
38. Steele, B. C. H. Appraisal of $Ce_{1-y}Gd_yO_{2-y/2}$ electrolytes for IT-SOFC operation at 500°C. *Solid State Ionics* **129**, 95–110 (2000).
39. Schlichting, K. W., Padture, N. P. & Klemens, P. G. Thermal conductivity of dense and porous yttria-stabilized zirconia. *Journal of Materials Science* **36**, 3003 - 3010 (2001).
40. Li, Y., Hutchinson, T.P., Kuang, X., Slater, P.R., Johnson, M.R. & Evans, I.R. Ionic Conductivity, Structure and Oxide Ion Migration Pathway in Fluorite-Based $Bi_8La_{10}O_{27}$. *Chemistry of Materials* **21**, 4661–4668 (2009).
41. Levin, E. M. & Roth, R. S. Polymorphism of bismuth sesquioxide. II. Effect of oxide additions on the polymorphism of Bi_2O_3. *Journal of Research of the National Bureau of Standards, Section A: Physics and Chemistry.* **68A**, 197 (1964).
42. Fung, K. Z. & Virkar, A. V. Phase Stability, Phase Transformation Kinetics, and Conductivity of Y_2O_3 - Bi_2O_3 Solid Electrolytes Containing Aliovalent Dopants. *Journal of the American Ceramic Society* **74**, 1970–1980 (1991).
43. Harwig, H. A. On the Structure of Bismuth sesquioxide: The α, β, γ and δ-phase *Zeitschrift für anorganische und allgemeine Chemie* **444**, 151–166 (1978).
44. Sillén, L. G. & Aurivillius, B. Oxide Phases with a Defect Oxygen Lattice. *Zeitschrift für Kristallographie - Crystalline Materials* **101**, 483–495 (1939).
45. Drache, M., Roussel, P. & Wignacourt, J.-P. Structures and Oxide Mobility in Bi−Ln−O Materials: Heritage of Bi_2O_3. *Chemical Reviews* **107**, 80–96 (2007).
46. Drache, M., Obbade, S., Wignacourt, J. P. & Conflant, P. Structural and Conductivity Properties of $Bi_{0.775}Ln_{0.225}O_{1.5}$ Oxide Conductors (Ln=La, Pr, Nd, Sm, Eu, Gd, Tb, Dy) with Rhombohedral Bi–Sr–O Type. *Journal of Solid State Chemistry* **142**, 349–359 (1999).
47. Iwahara, H., Esaka, T. & Sato, T. Formation of High Oxide Ion Conductive Phases in the Sintered Oxides of the System Bi_2O_3 Ln_2O_3 (Ln = La -Yb). *Journal of Solid State Chemistry* **39**, 173 - 180 (1981).
48. Takahashi, T., Iwahara, H. & Nagai, Y. High oxide ion conduction in sintered Bi_2O_3 containing SrO, Ca O or La_2O_3. *Journal of Applied Electrochemistry* **2**, 97 - 104 (1972).
49. Takahashi, T., Esaka, T. & Iwahara, H. High oxide ion conduction in the sintered oxides of the system Bi_2O_3-Gd_2O_3. *Journal of Applied Electrochemistry* **5**, 197 - 202 (1975).
50. Watanabe, A. & Kikuchi, T. Cubic - Hexagonal Transformation of yttria-stabilized bismuth sesquioxide, $Bi_{2-2x}Y_{2x}O_3$ (x= 0.215 - 0.235). *Solid State Ionics* **21**, 287 - 291 (1986).

51. Datta, R. K. & Meehan, J. P. The System Bi_2O_3 - R_2O_3 (R=Y, Gd). *Zeitschrift für anorganische und allgemeine Chemie* **383**, 328–337 (1971).
52. Watanabe, A. The dependence of polymorphism on the ionic radius of Ln^{3+} (Ln = La-Er, Y) in the oxide ion conductors $Bi_{0.775}Ln_{0.225}O_{1.5}$.
53. Takahashi, T., Iwahara, H. & Arao, T. High oxide ion conduction in sintered oxides of the system Bi_2O_3 - Y_2O_3. *Journal of Applied Electrochemistry* **5**, 187–195 (1975).
54. Conflant, P., Boivin, J.-C. & Thomas, D. Le diagramme des phases solides du systeme Bi_2O_3CaO. *Journal of Solid State Chemistry* **18**, 133–140 (1976).
55. Obbade, S. Powder Neutron Diffraction and TEM Investigations of $Bi_{0.775}Ln_{0.225}O_{1.5}$ Oxide Conductors (Ln=La, Pr, Nd, Sm, Tb, Dy) with Rhombohedral Bi–Sr–O type: Structural Relationships with Monoclinic ε-$Bi_{4.86}La_{1.14}O_9$ Form. *Journal of Solid State Chemistry* **168**, 91–99 (2002).
56. Mercurio, D. *et al.* Etude structurale par diffraction X sur monocristal et diffraction neutronique sur poudre de l'oxyde mixte $Bi_{0.7}Ln_{0.3}O_{1.5}$. *Journal of Solid State Chemistry* **80**, 133–143 (1989).
57. Mercurio, D. *et al.* Thermal Evolution of the Crystal Structure of the Rhombohedral $Bi_{0.75}Sr_{0.25}O_{1.375}$ Phase: A Single Crystal Neutron Diffraction Study. *Journal of Solid State Chemistry* **112**, 1–8 (1994).
58. Drache, M., Huve, M., Roussel, P. & Conflant, P. Polymorphism of $Bi_{1-x}Ln_xO_{1.5}$ phases. *Materials Research Bulletin* **38**, 113–124 (2003).
59. Drache, M., Schrotter, J.C. & Conflant, P. Evidence for Oxygen Nonstoichiometry in a Stabilized Bi-Ca-Pb-O Fluorite-type Phase. *Journal of Material Chemistry.* **3**, (1993).
60. Obbade, S., Drache, M., Conflant, P. & Suard, E. Ab Initio Determination of $Bi_{4.86}La_{1.14}O_9$ Monoclinic Structure from Powder Neutron Diffraction Data. Characterization of the Related Solid Solution. *Journal of Solid State Chemistry* **162**, 10–19 (2001).
61. Stout, G. H. & Jensen, L. H. *X-Ray Structure Determination: A Practical Guide*. (John Wiley & Sons, 1989).
62. Dent Glasser, L., Lachowski, E. & Cameron, G.G. Studies on sodium silicate solutions by the method of trimethylsilylation. *Journal of Applied Chemistry and Biotechnology* **27***,* 39 - 47 (1977).
63. Koch, E. *Application to the crystal systems. in International Tables for Crystallography Volume C: Mathematical, physical and chemical tables* (Springer Netherlands , 2004).
64. Drache, M., Wignacourt, J. P. & Conflant, P. Bi–La-Based Oxide Conductors with Rhombohedral Bi–Sr–O Type: Structural and Conductivity Properties Optimization by Polycationic Substitutions for La. *Journal of Solid State Chemistry* **149**, 341–348 (2000).
65. Sammes, N. M. & Gainsford, G. J. Phase stability and oxygen ion conduction in Bi_2O_3 - Pr_6O_{11}. *Solid State Ionics* **62**, 179–184 (1993).

66. Watanabe, A. Phase relations of hexagonal and cubic phases in holmia-doped bismuth sesquioxide, $Bi_{2-2x}Ho_{2x}O_3$ (x =0.205–0.245). *Solid State Ionics* **34**, 35–39 (1989).
67. Takahashi, T. & Iwahara, H. Oxide ion conductors based on bismuth sesquioxide. *Materials Research Bulletin* **13**, 1447–1453 (1978).
68. Withers, R. L. & Rossell, H. A TEM Study of Rhombohedral β Type Solid Solutions in the Bi_2O_3-SrO and Bi_2O_3-CaO Systems. *Journal of Solid State Chemistry* **118**, 66–73 (1995).
69. Conflant, P., Boivin, J.-C. & Thomas, D. Etude structurale du conducteur anionique $Bi_{0.765}Sr_{0.235}O_{1.383}$. *Journal of Solid State Chemistry* **35**, 192–199 (1980).
70. Jolley, A. G., Jayathilake, R. & Wachsman, E. D. Optimizing rhombohedral Bi_2O_3 conductivity for low temperature SOFC electrolytes. *Ionics* **25**, 3531–3536 (2019).

Chapter 2 - Experimental Methodology

In this work. materials were prepared using the citrate sol-gel method to form a fine powder. Thereafter, samples were characterised using laboratory and synchrotron powder X-ray diffraction to study the average structure and Raman scattering to investigate the material's local structure behaviour. Electrochemical Impedance Spectroscopy was also used as a characterisation technique to examine the conductive properties of samples as electrolyte materials.

2.1 Sol-gel synthesis

Inorganic materials, such as metal oxides and carbides, can be prepared by combining powder reactants and heating them to high temperatures (approximately 1000 °C).[1] This method is known as solid-state synthesis, which has attainable reaction conditions and leads to formation of large particle sizes.[2,3] However, drawbacks of the method such as unreacted starting material and decomposition introduces additional processing like ball milling to the synthetic method.[2,4] Also, controlling particle morphology while using solid-state techniques is often challenging.[5]

Alternative methods to solid-state chemistry have been developed such as solution techniques that include coprecipitation, hydrothermal processing, solvothermal methods and sol-gel chemistry.[1] Sol-gel chemistry refers to the synthesis of solid materials from solution-state precursors.[6] The sol-gel method has several advantages, including the ability to transform a chemically homogeneous precursor to a solid-state material.[1,7,8] The random order of the solution state is leveraged to ensure atomic level mixing of reagents, and subsequently produce complex inorganic materials at lower processing temperatures and shorter synthesis times.[2]

In a standard sol-gel synthesis, aqueous metal salts and a chelating agent are combined to form a solution, that transforms to a colloidal suspension known as a sol with heat (Figure 2.1).[1,3] Further heating of the sol thickens the solution and produces a network structure described as the gel.[2] Thereafter, the gel is simply converted to a metal oxide by pyrolysis in air, at a temperature dependant on the specific system.[3,9] Citric acid is a preferred chelating agent when preparing metal oxide powders, as it is a weak triprotic acid with three carboxylic acid moieties that easily dissociates.[5,10] This results in metal-citrate bonds forming within the solution. While metal-citrate gels are heated, excess citric acid and solvent are driven off, as well as gaseous species such as carbonates.[11]

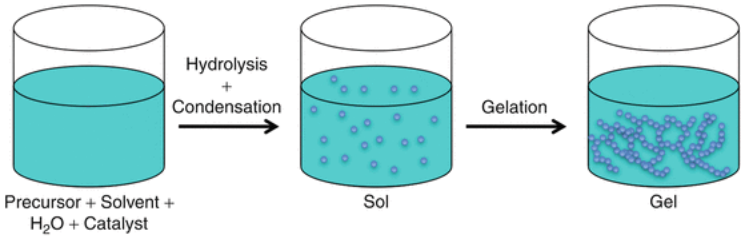


Figure 2.1: Schematic diagram showing the solution transformation during the Sol-gel method.[2]

2.2 X-ray Diffraction

X-rays are a form of high energy radiation or electromagnetic waves that lie in the high frequency end of the electromagnetic spectrum (Figure *2.2*).[12] X-rays have higher energy than ultraviolet radiation, but less than gamma rays with photon energies between 100 eV and 1000 keV and wavelengths from 10 nanometers to 10 picometers.[13] In 1985, Wilhem C Röntgen presented the discovery X-rays, that were labelled with the letter "X" to represent their unknown nature.[13,14] The discovery of x-rays occurred while Röntgen was investigating high tension electrical discharges in evacuated glass tubes.

It was determined that X-rays are most effectively produced by accelerating electrons and colliding them with a suitable material.[14] A strong electric potential can be created inside a vacuum tube between two electrodes, where electrons migrate from the cathode to the anode.

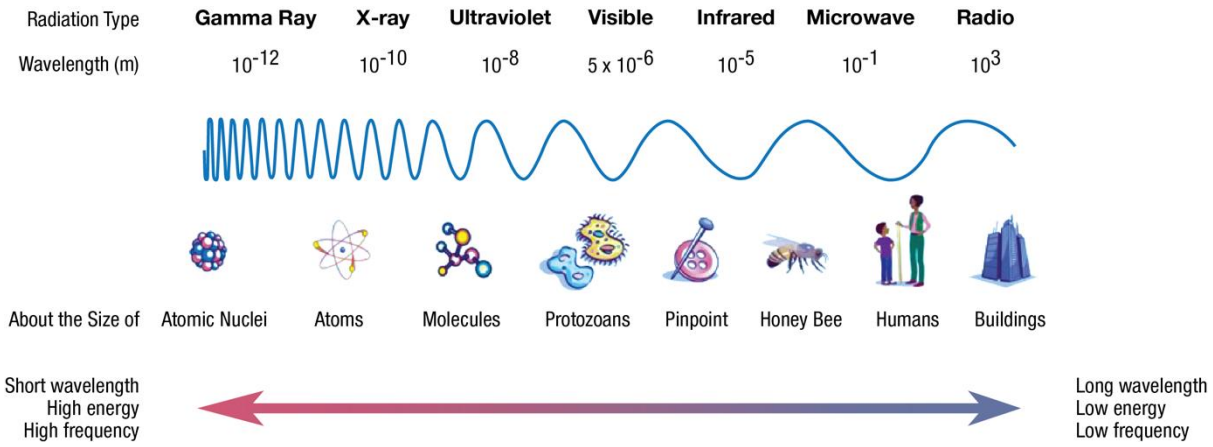


Figure 2.2: Graphical representation of the electromagnetic spectrum.[14]

2.2.1. Laboratory X-ray tubes

In standard laboratory equipment, x-rays are generated within a sealed-tube source (Figure 2.3). Within this source, electrons are accelerated and released from a hot cathode and then bombard a metal anode inside a vacuum tube.[12] As a result, the electrons prompt a series of electronic transitions within the atoms of the metal through the discharge of an electron from one of the metal atom's inner electron shells. Different metal targets have different characteristic electronic transitions and therefore produce X-rays of different wavelengths. These transitions cause the atoms to emit radiation as they return to their ground state [13,16]. Copper radiation is common in laboratory instruments, alternative x-ray sources include cobalt, chromium, molybdenum or silver (Table 2.1).

Table 2.1: Characteristics of anode materials in x-ray diffractometers [17]

Anode	**Wavelength**			**Beta Filter**	**Range in d(Å) $K\alpha_1$**	
	$K\alpha_1$	$K\alpha_2$	K_β		5° 2θ	150° 2θ
Cu	1.54059	1.54443	1.39223	Ni	17.66	0.7975
Cr	2.28973	2.29365	2.08489	V	26.25	1.1853
Fe	1.93604	1.93997	1.75660	Mn	22.19	1.0022
Co	1.78900	1.79283	1.62083	Fe	20.51	0.9261
Mo	0.70932	0.71361	0.63288	Zr	8.13	0.3672

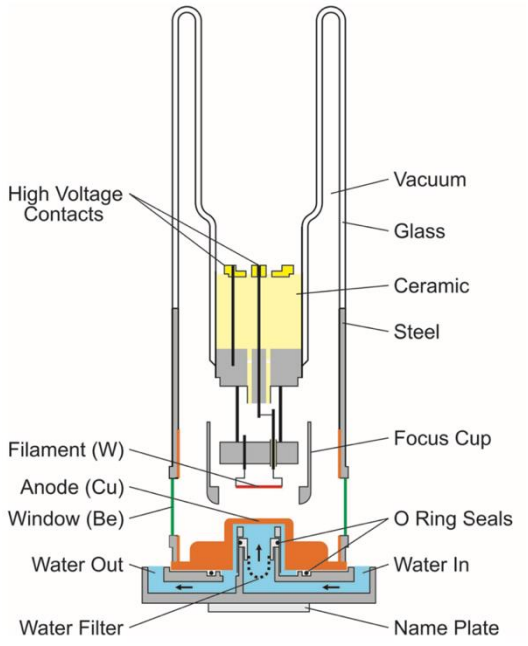


Figure 2.3: Schematic diagaram of a sealed laboratory X-ray tube with key components indicated.[12]

When the accelerated electrons have an energy greater than a specific threshold value that is dependent on the metal anode, an emission spectrum of x-rays is observed at discrete frequencies, sometimes referred to as spectral lines.[18] This emission spectrum is referred to as the characteristic radiation and consists of distinct peaks (Figure 2.4). The energy (and subsequent wavelength) of these peaks are determined by the metal target and subsequent electron transitions.[13,18] Two characteristic spectral lines are observed in the copper spectrum known as Kα and K_β, however the Kα line can appear as a doublet at higher resolution (Figure 2.4).[13] Kα is a 2p to 1s transition and has a longer wavelength while K_β is a 3p to 1s transition, and has a shorter wavelength. As the splitting of the 2p orbitals in copper is at a low value of 0.020 keV, the wavelengths of $K\alpha_1$ and $K\alpha_2$ are very similar at 1.54056 Å and 1.54439 Å .[13,18] The Kα spectral line is normally more intense than the K_β line, and is thus preferred in diffraction experiments. The K_β is removed with a filter, which is usually a metal having one proton less than the anode material (Figure 2.4).

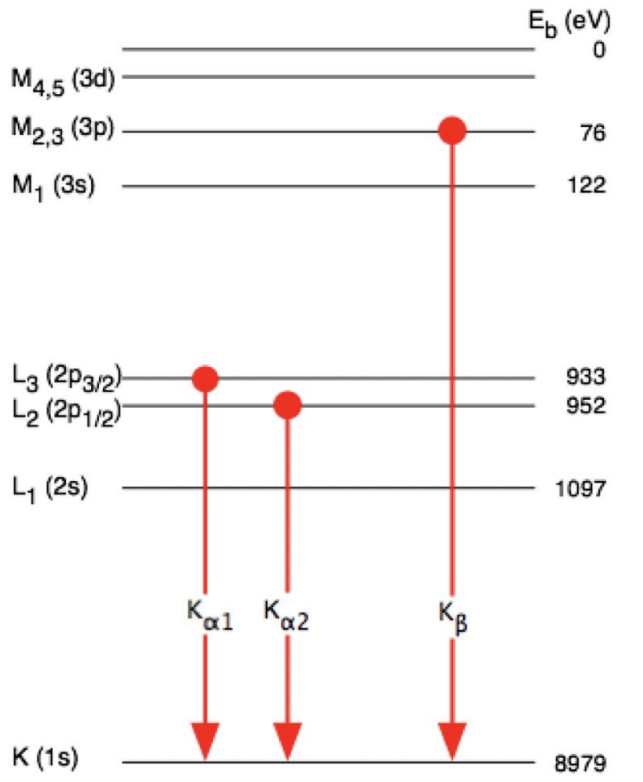


Figure 2.4: Atomic levels involved in K_β and K_α emissions. [13]

A standard x-ray emission spectrum from a copper anode is illustrated in Figure *2.5*. When electrons collide with atoms, they lose energy through multiple events.[12] This results in a continuous spectrum of x-rays known as Bremsstrahlung radiation.[12,19]

The shortest wavelength is determined by the maximum energy lost, and can be calculated using Equation 2.1.

$$\text{Equation 2.1: } E = eV = \frac{hc}{\lambda}$$

(where e =charge on electron, V = accelerating voltage)

This equation can be simplified to Equation *2.2*:

$$\text{Equation 2.2: } \lambda = \frac{12.398}{V}$$

(where V is in kV and λ is in Å)
Therefore, as shown by the equation above, as the accelerating voltage of the x-ray generator increases, the minimum wavelength that can be reached becomes shorter. Longer wavelengths can be obtained through multi-collision processes.[13]

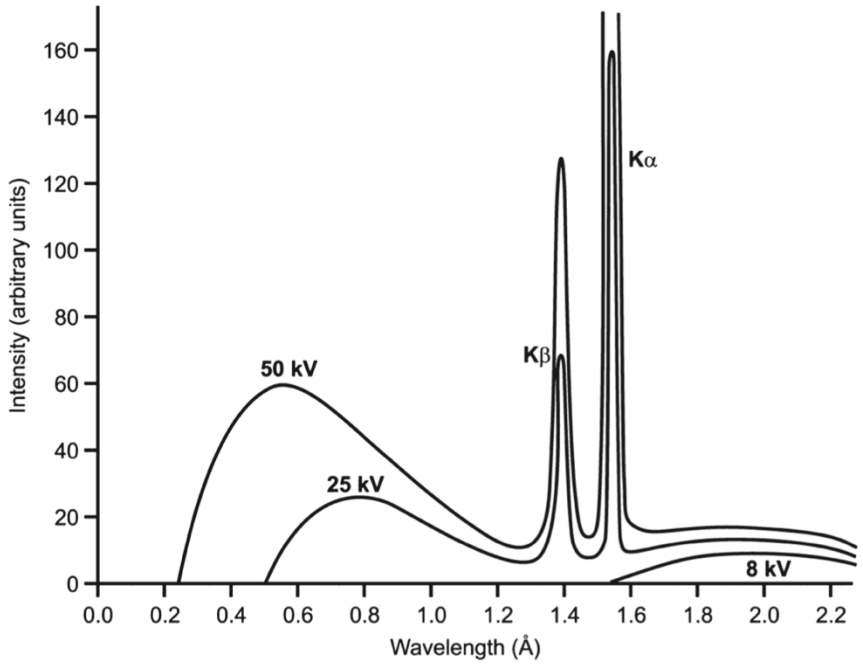


Figure 2.5: Typical x-ray emission spectra of a copper anode produced with with varying accelerating voltages.[12]

Laboratory-based X-ray tubes do have some disadvantages. These include the relatively low intensity and poorly collimated tubes. Collimators are devices that can narrow or shape an x-ray beam, and may occur as slits, tubes or a set of parallel plates in a powder diffractometer [19,20]. Also, laboratory-based tubes are not tunable, which refers to the very narrow range of X-ray wavelengths available and a different tube would be required to access wavelengths outside this narrow range.[14]

2.2.2. Synchrotron radiation

A synchrotron is a particle accelerator that generates electromagnetic radiation across a wide spectrum, from far infrared to x-rays.[14] Synchrotrons use an evacuated storage ring to mobilize high-energy electrons at highly relativistic velocities, which are close to the speed of light (2.99×10^8 m/s).[19] These accelerated electrons emit synchrotron radiation tangential to their orbital path, by bending magnets and insertion devices within the storage ring.

A storage ring is comprised of magnetic fields that accelerate and direct the flow of electrons (Figure 2.6).[13,21] Storage rings are composed of multiple segments, including a straight section followed by a curved section.[13] The curved section guides the electrons into the following straight section by a bending magnet, and it is in these curved sections where synchrotron radiation is emitted.[22] The straight sections consist of arrays of magnets, known as insertion devices, which create alternating magnetic fields that cause oscillation of the electron paths.[13,22] Each oscillation results in the emission of synchrotron radiation.[20] When Synchrotron radiation is emitted, the electrons lose energy, so to compensate for their energy losses radio-frequency generators or cavities are used to synchronously feed energy to the electron, hence the name Synchrotron.[23]

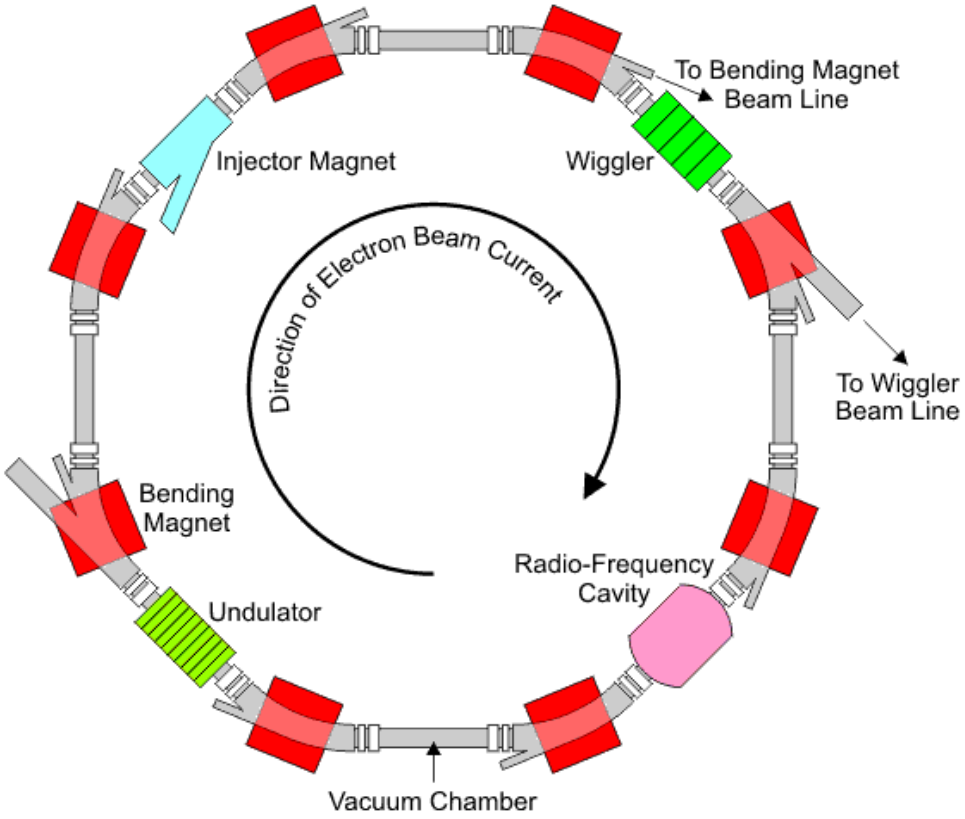


Figure 2.6: Schematic illustration of a synchrotron storage ring.[13]

For powder diffraction, the relevant synchrotron x-ray sources are the bending magnets and the insertion devices, known as wigglers and undulators.[12,13] These sources have their magnetic field oriented vertically, which causes the electron to be deflected horizontally.[14,21] The radiation emitted by a single electron forms a narrow cone with a specific angular width, leading to the highly collimated x-ray beam in the vertical direction.[19,20] In the case of bending magnets, the radiation is emitted tangentially across the entire curved section, resulting in the emission of a wide tangential fan of x-rays (Figure *2.7*).[13] On the other hand, insertion devices have a sinusoidally varying magnetic field, which causes the electrons to produce bursts of synchrotron radiation with a tangential direction.[13,16] When considering wigglers, these bursts of radiation add together incoherently, increasing the flux in proportion to the number of magnetic periods (Figure *2.7*).[20] In the case of undulators, the deflection of the electrons is relatively small and similar to the natural opening angle of the emitted radiation (Figure *2.7*).[13,20] The radiation from different oscillations interferes, causing the beam to be collimated in the horizontal plane.[21,24] Therefore, instead of spreading out in a horizontal fan like bending magnets or wigglers, the radiation is concentrated into a central cone on the axis, surrounded by additional weaker rings.[24] The flux density from this central cone is therefore very high on a small sample.[13] Synchrotron radiation is a continuous spectrum and in order to isolate radiation or X-rays of a specific wavelength, a monochromator is used.

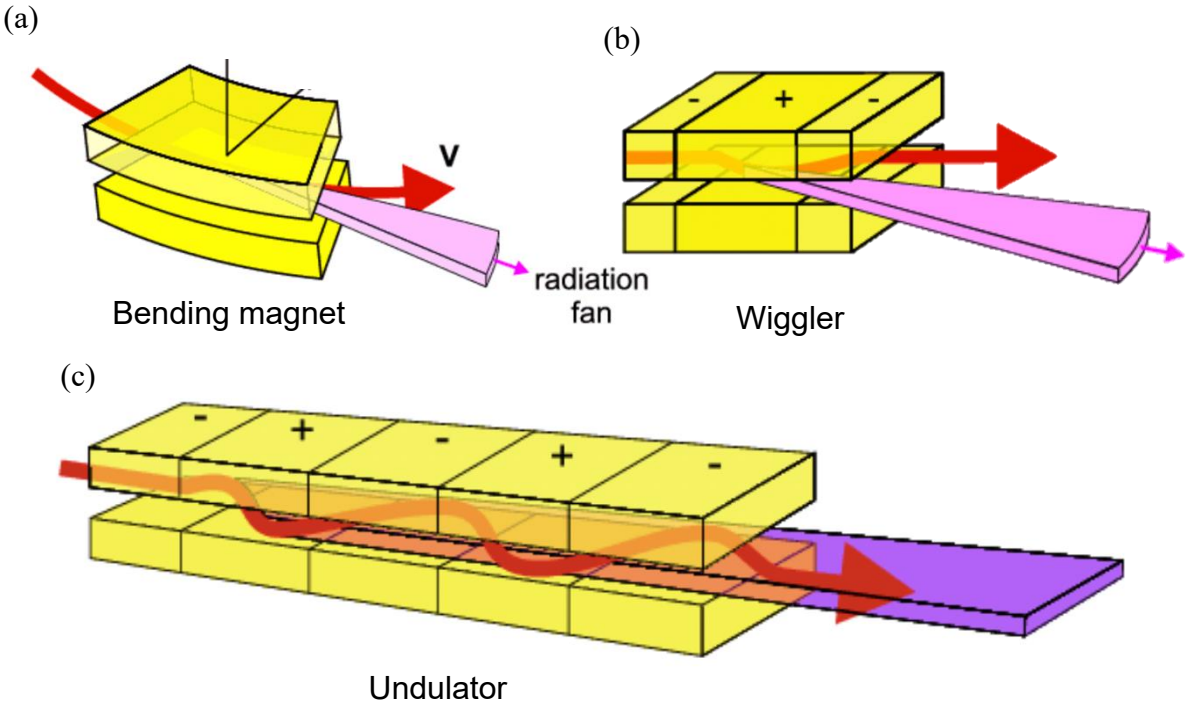


Figure 2.7: (a) Tangential fan of radiation emitted from a bending magnet (b) Fan of radiation emitted by a wiggler (c) Collimated beam emitted by an undulator.[14]

Normally, the electron energy in the storage ring is proportionally related to the energy of the emitted x-rays.[13,18] In the case of bending magnets and wigglers, the energy of the emitted x-rays are directly influenced by the curvature of the ring, which can also be referred to as a larger magnetic field.[25] While undulators have discrete peaks observed at integer multiples of a certain energy, bending magnets and wigglers have continuous spectra.[18,25] The energy of the undulators depend on the strength of the magnetic field.[18]

The application of synchrotron x-ray radiation offers several advantages compared to laboratory sources when conducting high-quality powder diffraction measurements. Synchrotron radiation is designed to be extremely intense as it is highly collimated vertically, which produces significantly improved 2θ resolution.[13,14] The wavelength can be selected in accordance with the requirements of a specific measurement. Synchrotrons also produce tunable electromagnetic radiation, unlike laboratory-based tubes.

2.2.3. Single atom X-ray scattering

Scattering of radiation is described as the process where radiation is deflected from its original path by interacting with matter. Scattering of radiation such as x-rays or neutrons by a material is caused by its interaction with atoms that compose the substance. The scattering process of x-rays in particular is caused by the interaction between a photon and the electrons surrounding the atomic nuclei (*Figure* 2.8).[13]

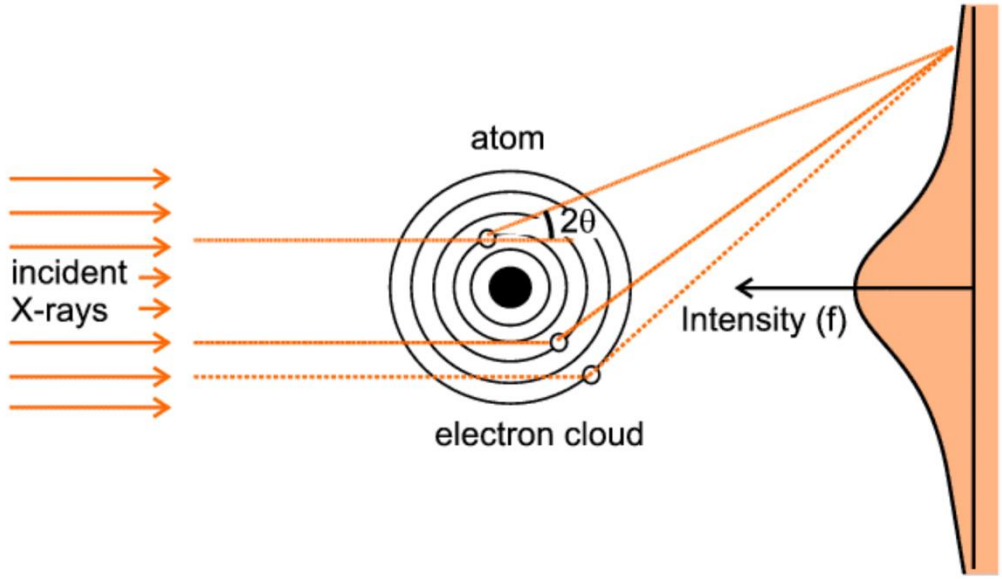


Figure 2.8: A schematic illustration of X-ray scattering by electrons of an atom.[13]

When an isolated atom scatters incident X-rays, the X-rays are scattered in all directions with decreasing intensity as the scattering angle increases. This is shown by the scattering factor curves in Figure 2.9. At $\theta = 0$, the scattering factor f is equal to the number of electrons in the atom or ion.When there is more than one atom, the incoming X-rays are scattered in all directions by each atom. The scattered waves can interfere, either constrictively or destructively. The electron distribution around an isolated atom nucleus can be considered, according to quantum mechanical behavior, as an electron density that reaches its maximum at the nuclear position and gradually decreases as distance from the nucleus increases.[13,19,20] Each unit of volume surrounding this nuclear position has the ability to scatter x-rays.[20] The coherently scattered x-rays will interact with those scattered from other nearby volumes, depending on the angle of scattering.[20,22] The interference results in a phase shift between the scattered waves originating from different unit volumes.

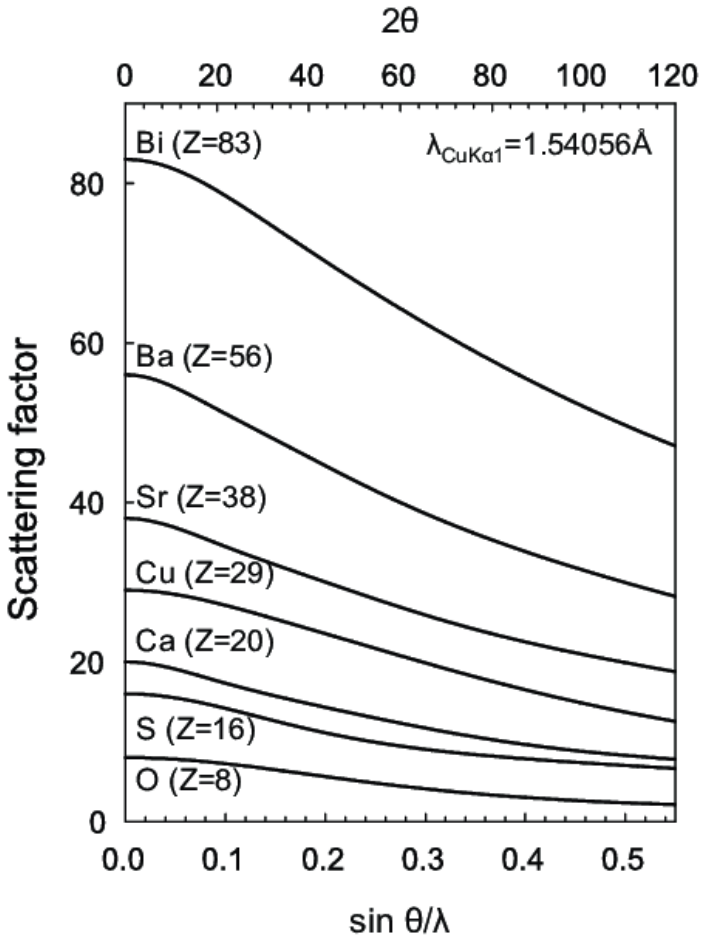


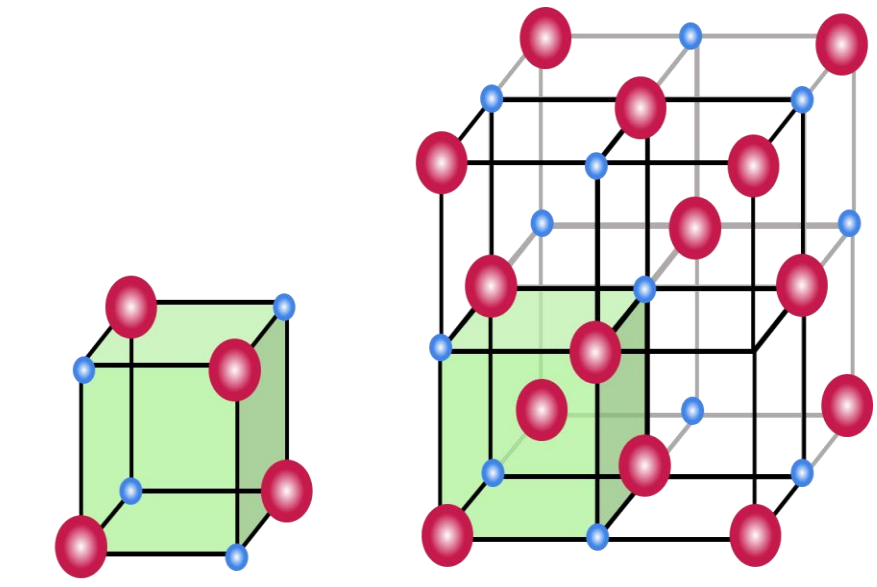
Figure 2.9: X-ray Scattering factor for selection atoms as a function of 2θ and $\sin\theta/\lambda$.[19]

The scattering of electrons around an atom is known as the atomic scattering factor or form factor.[13,22,24] An isolated atom can be assumed to consist of a spherically

symmetric distribution of electrons.[25] As the electron density is highest at the atomic nucleus and gradually decreases to zero at larger distances, the atomic scattering factor has a peak at forward scattering angles and smoothly decreases at large back scattering angles (Figure 2.9). The decrease in the atom scattering factor as the scattering angle increases is primarily responsible for the overall appearance of a x-ray powder pattern.[18] The peaks with the highest intensity are observed at small scattering angles, and intensities decrease with increasing scattering angle. If the atoms are in an ordered array, such as in a crystal, then constructive interference will only occur at the Bragg angles.

2.2.4. Bragg's Law and Ewald's sphere

X-ray diffraction occurs when a beam of monochromatic electromagnetic radiation is scattered by the electrons of atoms present in a crystalline material. Diffraction occurs when the atoms within a crystallite interacts with electromagnetic radiation of a comparable wavelength to the interatomic distances.[12,13,20] This radiation could be X-rays, that have wavelengths of approximately 1 Å. An ideal crystal consists of an infinite arrangement of atoms that repeats periodically in three dimensions, while a crystallite can be described as a solid-state domain that shares the same structure as a single crystal.[20] The three-dimensional arrangement of atoms is known as the crystal lattice, and it is characterized by the unit cell which is the basic repeating unit (Figure 2.10).[13,26] The unit cell has dimensions a, b and c, and angles α, β and γ. The diffraction experiment can be described as exposing a single crystal to a monochromatic radiation beam which produces discrete diffracted beams that appear as spots in the single crystal XRD pattern (Figure 2.11a). The results produced include the intensity of the diffracted beam and the angle between the incident beam and the diffracted beam, known as the diffraction angle.[12]



(a) (b)

Figure 2.10: Diagram illustrating (a) a unit cell and (b) a crystal lattice.[12]

As crystals are 3D objects, single crystal diffraction produces 3D diffraction patterns containing each peak recorded individually.[12] A powder consists of many crystallites oriented in randomly different directions. The X-rays scattered by these small randomly oriented crystals in the polycrystalline are rotated around the X-ray beam, producing rings for a random sample (Figure 2.11b).[12] To obtain a powder diffraction pattern, a portion of the rings are integrated. The conversion of individual peaks to rings reduces the diffraction information from 3D to 1D, meaning that single crystal diffraction offers more information about a material than powder diffraction. However, not all materials exist as single crystals, and rely on powder diffraction for characterization. A diffraction pattern of a polycrystalline material contains sharp well-defined peaks, often referred to as Bragg peaks [12–14].

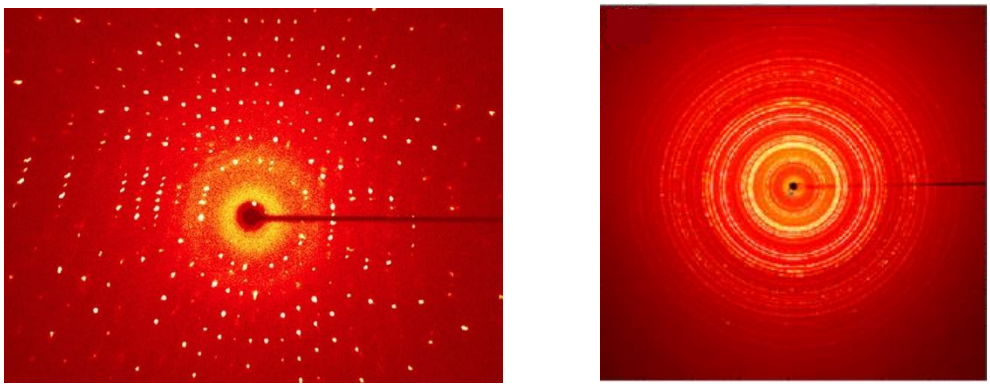


Figure 2.11: (a) Single crystal diffraction and (b) powder diffraction.[12]

In powder diffraction measurements, it is generally assumed that the sample is isotropic, meaning that there is a crystallite or powder particle in the beam with every possible orientation, that has equal probability of being sampled.[14,19] Therefore, a powder produces scattering in specific discrete directions and intensities that are determined by the cell dimensions and cell components respectively.[12] The scattered or diffracted beams of single crystal samples would appear as distinct spots on an x-ray film or a two-dimensional detector. When considering a microcrystalline powder, there will be many crystallites in different orientations. The ideal powder would consist of individual crystallites of approximately 1 μm or less in size, in all possible orientations with equal probability.[12,27] The different orientations of the crystallites would result in a single diffraction spot becoming spread out on the surface of the sphere.[13,19,20] As a result, the orientation of the vector is lost and the three-dimensional vector space is reduced to one dimension that is represented by the vector's magnitude.[12,13]

The Bragg equation, developed by W.L. Bragg in 1912, is the most well-known method for interpreting the peak positions in a diffraction pattern.[13,16,20] The Bragg

equation is used to explain the concept of x-ray diffraction as a reflection of x-rays by sets of parallel lattice planes, which are classified by the Miller indices (hkl) (Figure 2.12).[13] All the planes in a set of a crystal lattice are the same, and are spaced apart by a distance d.

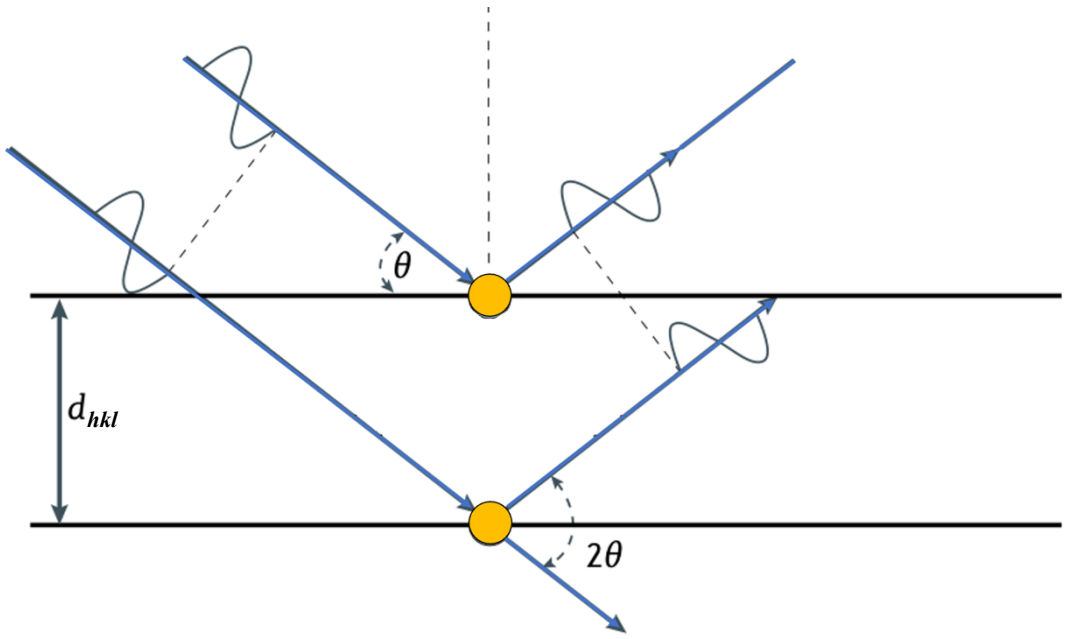


Figure 2.12: Schematic diagram illustraring the Bragg equation.[19]

With reference to the Bragg equation in Equation *2.3*

Equation 2.3: $n\lambda = 2d\sin\theta$

n is the order of diffraction, λ is the wavelength of the radiation source, d refers to the spacing between specific crystal planes and 2θ is defined as the diffraction angle (Figure 2.12). The presence of Bragg peaks at discrete 2θ values satisfies the Bragg equation for each set of crystallographic planes within the crystal lattice.[16] Each Bragg spot is identified by three integers, (hkl), which represents the Miller indices associated with the corresponding crystallographic planes.[16,20]

Conventional electromagnetic waves are considered as sine waves that possess a periodic repetition every 2π radians.[12,13,16] The spatial length of each period is referred to as λ. When X-rays are scattered by atoms, the various path lengths available in different planes results in a phase shift (Figure 2.13).[12] A phase shift occurs when two identical waves are not coincident with respect to each other.[19] This can either be quantified by a linear shift or a phase shift, using a length or angular scale, respectively.

When two waves coexist, the overall amplitude is determined by the sum of individual amplitudes and the phase shift (Figure 2.13). The phase shift results in constructive interference when the wave separation is zero, or a multiple of the wavelength λ ($n\lambda$). If this is not satisfied, destructive interference occurs.

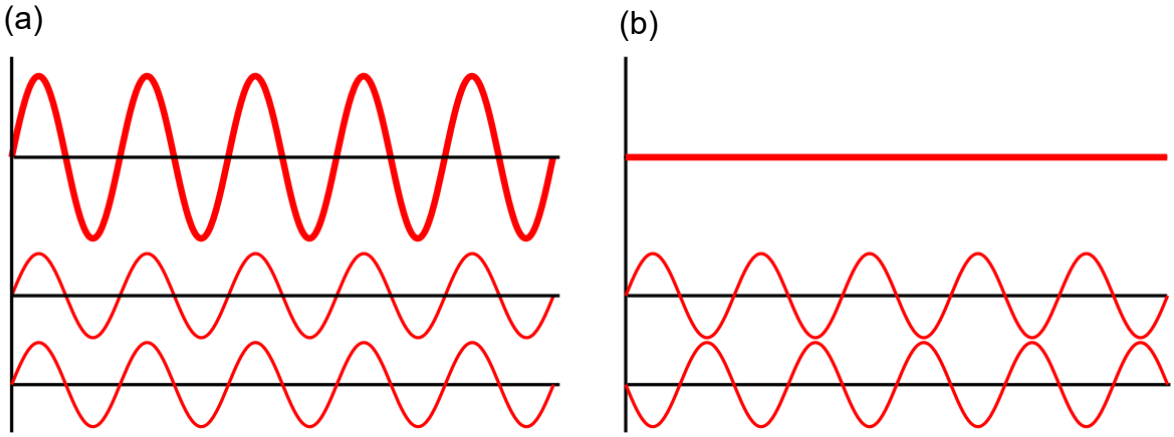


Figure 2.13: The intereference of two sinusoidal waves in the lower diagarams that results in (a) constructive wave interference and (b) complete destructive wave interference.[2]

The reciprocal lattice provides a framework for understanding the relationship between real-space structure of a crystal and its diffraction pattern.[12] The real lattice is a periodic function in physical space and the reciprocal lattice exists in the mathematical space of spatial frequencies, known as reciprocal space. The reciprocal lattice emerges from the Fourier transform of the real lattice. [13] There is a correlation between the points within the reciprocal lattice and the vectors that define the crystallographic planes. Each crystallographic plane (hkl) corresponds to one point within the reciprocal lattice.[12,14] Diffraction occurs when the magnitude of the scattering vector is a whole-number multiple of reciprocal lattice spacings ($1/d$).[12]

Bragg's Law and the Ewald Sphere are two different ways of understanding the conditions for diffraction in crystals. The Ewald's sphere is a geometric construction that provides a visual interpretation of the diffraction conditions (Figure 2.14).[13] A crystal can be described as a real lattice of atoms, but can also be described by a reciprocal lattice of points. The Ewald Sphere is constructed by selecting an origin in reciprocal space and drawing a vector from the origin in the direction of the incident wave. The length of the vector is $1/\lambda$, where λ is the wavelength of the incident wave (Figure 2.14). The Ewald Sphere is constructed at the tip of the incident wavevector, with a radius of $1/\lambda$. The energy of the waves (electron, neutron or x-ray) depends upon the magnitude of the wavevector, so if there is no change in energy (elastic scattering) these have the same magnitude, that is they must all lie on the Ewald sphere.[16] A diffraction peak occurs when a reciprocal lattice point intersects the surface of the Ewalds sphere. This geometric condition is equivalent to satisfying Bragg's Law. The Bragg equation can be used to show that diffraction occurs when

the scattering vector is equal to the reciprocal lattice vector.[13] The scattering vector is dependent on the experiment's geometry, while the reciprocal lattice is determined by the crystalline sample, in particular its orientation and lattice parameters.[13,20] Ewald's
construction combines these two concepts in an approach that simply determines when the Bragg equation is satisfied (Figure 2.14).[12]

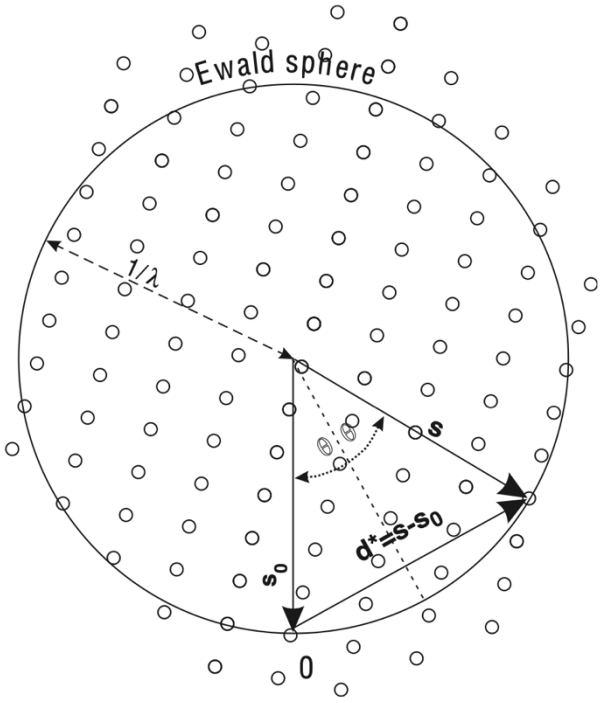


Figure 2.14: Geometrical construction of the Ewald circle. The "0" marks the origin of recirpocal space. The vectors are defined in the text.[13]

The intersection of the smeared reciprocal lattice with the Ewald sphere in the form of circles leads to the formation of diffracted x-rays with a reflection of hkl.[12,14,16] These x-rays form coaxial cones known as the Debye-Scherrer cones (Figure 2.15).[12] While the smearing of reciprocal space simplifies the measurement, it also results in a loss of valuable information. As the orientation of the vector becomes indiscernible, the three-dimensional reciprocal space is projected onto the 2θ axis.[16]

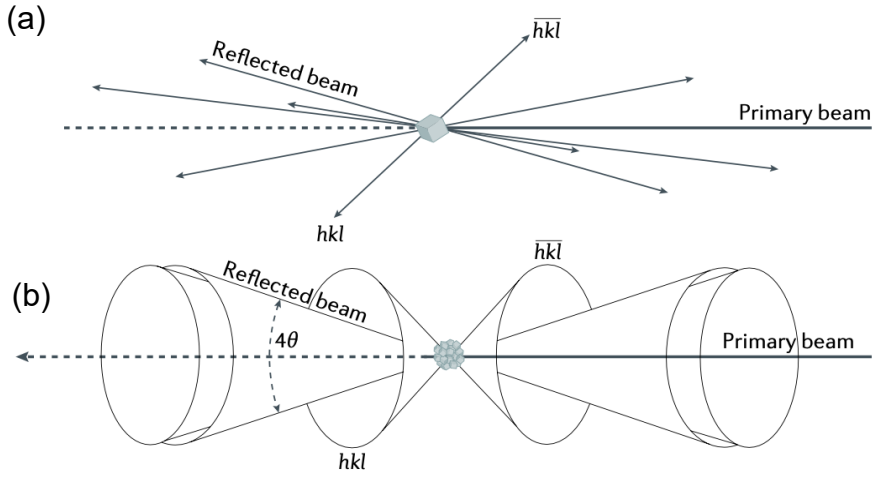


Figure 2.15: Comaprison between the scattered beams originating from a single crystal (a) and a powder (b). For the latter, Debye-Scherrer cones are drawn.[16]

2.2.5. Detectors

The detector system has a huge role in any powder diffraction experiment. X-ray detectors can be distinguished as point, linear or area detectors depending on whether the diffraction pattern is measured in zero, one or two spatial dimensions.[13,14] Point detectors require scanning in order to measure the diffraction pattern, while linear or area detectors can remain fixed.[13] Linear and area detectors provide relatively fast data acquisition, but are generally more susceptible to detecting unwanted scatter from the air or sample environment due to their open system structure.[20,27] Both linear and area detectors are classified as position-sensitive detectors (PSD).[20] Point detectors are not commonly used anymore.

A typical laboratory instrument can have either a single point counter or a one-dimensional linear position sensitive detector (LPSD).[13] The LPSD is multichannel, and so the intensities of diffracted x-rays are recorded at different angles at the same time. Traditional lab-based measurements use a one-dimensional detector, that integrates measurements along a line across the diffraction rings. On the other hand, a 2D detector allows for integration over the whole ring, or the measured part of it which results in improved counting statistics.[15] 2D detectors also collect data more quickly than LSPDs and are favourable when studying granular or textured materials. The reason for this it that 2D detectors are able to integrate the effects of grain size and directly characterize the texture.[12]

2.2.6. Bragg-Brentano and Debye-Scherrer

The main laboratory diffractometers are the Bragg-Brentano (reflection) and the Debye-Scherrer (transmission) geometries (Figure 2.16).[12,14] Bragg-Brentano geometry is more common in laboratory-based diffractometers, while Debye-Scherrer geometry is generally used at synchrotrons. Both configurations include the x-ray source positioned on the incidence side of the instrument, and the x-ray detector mounted on the opposite side of the sample to measure diffracted x-rays.[12] A goniometer is an instrument that provides accurate and precise measurements of angles, and is added to the diffractometer set-up for precise control over the incident and diffracted angles in relation to the sample.[19] The sample is placed in the center of the instrument. Bragg-Brentano systems contain physical slits that create a diverging x-ray beam to illuminate a flat sample (Figure 2.16).[13,16] These samples are prepared by packing a powder into a cavity in a sample holder, which is then diffracted towards the detector. There are several Debye-Scherrer geometries that can be used, involving a collimated high energy X-ray beam being focused on a very small spot (significantly smaller than a capillary). A thin capillary is then placed in the path of the X-ray beam and the beam penetrates through the capillary completely,

while being diffracted by the material within the capillary. The high energy X-rays and small beam sizes at synchrotrons make Debye-Scherrer geometries more accessible.

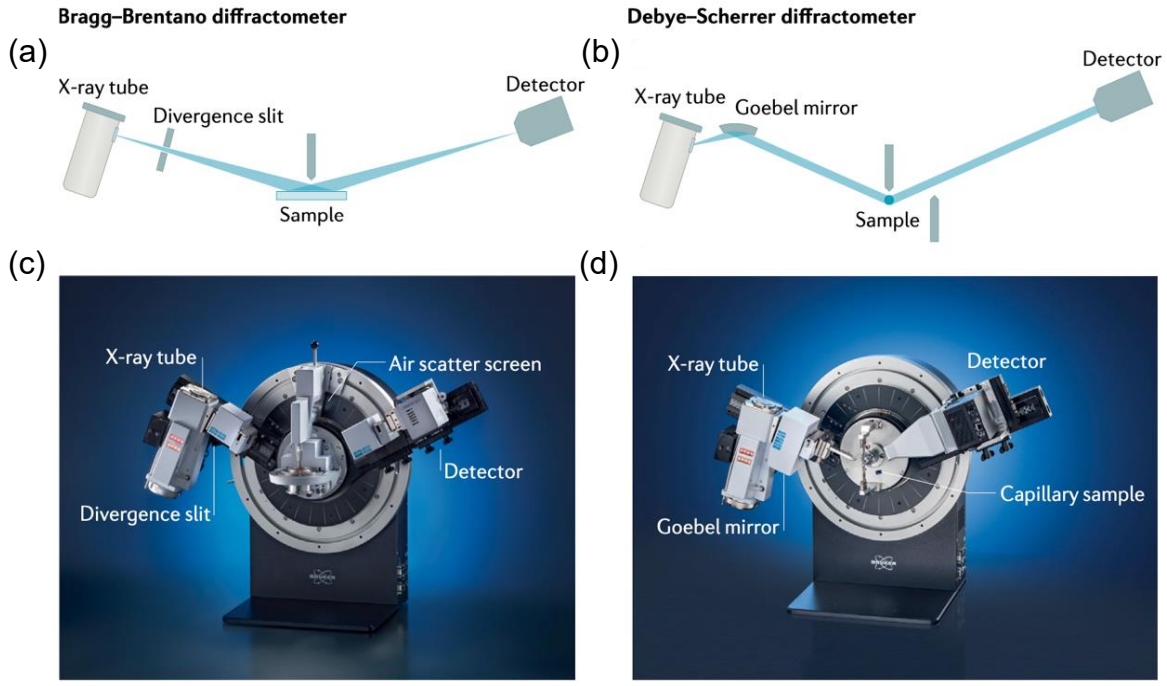


Figure 2.16: Schematic of (a) Bragg-Brentano and (b) Debye-Scherrer diffractometers. Photographs of a (c) Bragg-Brentano diffractometer and (d) Debye-Scherrer diffractometer, courtesy of Bruker.[12]

2.2.7. Rietveld refinement

Detectors only measure the intensity of the scattered wave and do not provide its phase information. This results in a great loss of information regarding the phases of structure factors.[14,19] This is further complicated in powder diffraction (compared to single crystal) as individual reflections overlap to form a single peak in a powder pattern.[20] Furthermore, the increasing peak density with increasing scattering angles makes it difficult to measure the amplitudes of structure factors. This is known as the powder problem.

An approach to overcoming the powder problem is the intensity extraction method.[16,27] This method aims to increase the peak separation in a powder diffraction pattern by either improving the diffractometer resolution or by using a multiple pattern approach.[13,14] If consistent intensities can be extracted using any of these methods, solving the structure can continue in a similar manner to single crystal data. Another method to overcome the powder problem is the profile fitting method. This involves modeling the entire powder pattern and refining the model so that the model with the most accurate representation of the diffraction data can be identified.[12,16]

The Rietveld Refinement method is a least squares fitting method that is guided by the crystal structure and diffraction experiments.[28] Hugo Rietveld recognized that a neutron powder diffraction can be interpreted as a smooth curve with Gaussian peaks over a smooth background.[28] Rietveld created a mathematical expression to represent the observed intensity at each step of the scan, and thus extract significant information from the pattern. This equation is shown in Equation 2.4, where the calculated intensity (Y_c) is the sum of the background intensity (Y_b) and each of the Bragg reflections (Y_h , h represents *hkl*).

Equation 2.4: $Y_c = Y_b + \sum Y_h$

This expression includes contributions from both the background and Bragg reflections that are close to the powder pattern step. Therefore, to analyze diffraction data, a method is required that includes parameters describing the Bragg peaks and the background of a powder pattern.[20,28,29] Rietveld developed a widely used method that is considered as a whole-pattern approach.[12,28] This approach involves a structural model that is used to calculate a powder pattern, and the calculated intensity at each step in 2θ is compared to the corresponding observed intensity.[28] Certain parameters are then adjusted to minimize the difference between calculated and observed intensities, in a process called least squares minimization.[29] The quantity minimized is shown in Equation 2.5 where w_i represents the weight, $y_{obs,i}$ is the observed intensity and $y_{calc,i}$ is the calculated intensity.

Equation 2.5: $\sum_{i=1}^{N} w_i (y_{obs,i} - y_{calc,i})^2$

This method has been named after its founder, and is known as a Rietveld refinement. This is an iterative process with the goal of improving the model at each iteration.[28] The improved model is then used to start the next refinement. A Rietveld refinement involves the modeling of the complete powder pattern.[19,20] This large task can be simplified by separating the content obtained from a powder pattern according to their origin.

The peak positions are geometrically determined by the crystallographic lattice and space group symmetry of the sample.[20] Instrumental factors also influence the peak positions such as the specimen displacement, that arises when the sample is not flat [12,20]. Sample height errors manifest as peak shifts along the 2θ scale.[19]

Peak intensities are determined by the averaged crystal structure described by its atomic positions, occupancies and displacement parameters.[20,28,29] The intensities are also influenced by several instrumental contributions such as absorption of radiation used, surface roughness and preferred orientation.[20] The absorption of x-ray beams results in a reduction of the diffracted intensity.[13,19] Surface roughness, which is created by varying packing density as a function of depth, reduces the peak

intensities at low Bragg angles.[12,13] Preferred orientation occurs when crystallites tend to align themselves in a non-random orientation, and this causes a strong increase in diffracted intensities.[16,20] These are just a few instrumental contributions to the peak intensity. The peak profile of a Bragg reflection can be considered as a mathematical convolution of the instrument and sample microstructure.[20,21] The instrument contribution, also known as the instrumental resolution function, includes the emission profile and various horizontal and vertical aberrations of the diffractometer.[14,20] The emission profile describes the x-ray radiation source used. Laboratory x-rays can typically be characterized by a series of Voigt profiles that range from one to five profiles.[16,19] These profiles demonstrate the wavelength distribution that is related to the level of monochromatisation.

The sample's microstructure contribution includes factors such as microstrain and domain size, commonly known as sample broadening.[12,20] Microstrain broadening is a result of local variations in the d-spacings within crystallites of a diffracting specimen.[20] Strain is the difference compared to a reference d-spacing, such as an average value. When the diffraction from different regions in the specimen with varying strain are combined, the coherent or incoherent superposition is called microstrain.[12,29] Size broadening occurs due to the finite size of crystallites, specifically the coherently diffracting domains, that contribute to the diffraction pattern.[16,20] Crystallites are normally not identical, but vary especially in size and shape. As the average size is an important parameter, this variation is often described in terms of a distribution of crystallite sizes.[24]

It has been demonstrated how each part of the powder pattern is influenced by both the sample and the instrument. For a successful Rietveld refinement, is it essential that initial values for all parameters fall within a relatively narrow range of convergence.[13] Different aspects of the pattern should be examined separately so that the starting values are compatible with the sample and instrumental details.

The performance of this process can be monitored using various figures of merit. The most direct measure of inconsistency is the weighted profile R-factor (R_{wp}), which is obtained by taking the square root of the minimized quantity and scaling it with the weighted intensities.[20,29] The mathematical expression of R_{wp}^2 is shown in Equation 2.6.

Equation *2.6:* $$R_{wp}^2 = \frac{\sum_i w_i (y_{C,i} - y_{O,i})^2}{\sum_i w_i (y_{O,i})^2}$$

When an ideal model is considered for a Rietveld refinement, the average value of $(y_{C,i} - y_{O,i})^2$ will equal $\sigma^2[y_{O,i}]$, where $\sigma^2[y_{O,i}]$ represents an uncertainty estimate for $y_{O,i}$ [19]. An ideal model will also be shown by the $w_i(y_{C,i} - y_{O,i})^2$ being equal to one.

Another discrepancy factor is the "best possible" R_{wp} quantity, which is known as the expected R factor (R_{exp}).[16,28] If N represents the number of data points, the R^2_{exp} factor can be determined by Equation 2.7.

$$\text{Equation 2.7 : } R^2_{exp} = \frac{N}{\sum_i w_i (y_{O,i})^2}$$

A related statistical concept is known as "χ^2". This concept can be understood by again considering that when the model is ideal and the standard unit values are accurate, the expected value for $(y_{C,i} - y_{O,i})^2 / \sigma^2[y_{O,i}]$ is one.[15,16] The average of these terms can then be defined as the χ^2 term, expressed in Equation 2.8.

$$\text{Equation 2.8: } \chi^2 = \left(\frac{1}{N}\right) \frac{\sum_i w_i (y_{C,i} - y_{O,i})^2}{\sigma^2[y_{O,i}]}$$

The χ^2 value can also be determined using the R_{exp} and R_{wp} factors.[29] The term "goodness of fit" (G) is also often used (Equation 2.9), and $G^2 = \chi^2$.

$$\text{Equation 2.9: } \chi^2 = \left(\frac{R_{wp}}{R_{exp}}\right)^2$$

While refining a structural model to the observed pattern, the χ^2 value starts as large when the model is a poor fit and decreases as the agreement between model and data improves.[19,29] In mathematical terms, a least-squares refinement should never result in an increase in the χ^2 value. However, there are instances where small increases occur when parameters are correlated.[20] The χ^2 value should never go below one, in other words the smallest value R_{wp} can be is R_{exp}. If this does occur during a refinement, it may either mean that the standard uncertainties for the data are overestimated or so many parameters have been introduced that the model is adjusting to fit noise.[12,20] When the χ^2 value is close to one, it does not necessarily mean that the model is accurate. The least squares minimization process may tend to values that are not scientifically correct. It is thus important that the refined values are inspected and are reasonable within the context of the sample measured and instrument used.

2.2.8. Pair Distribution Function

X-ray and Neutron diffraction methods are commonly used to investigate the structure of materials. These techniques have been most effective when studying materials with long-range order, such as crystals.[30] However, these diffraction methods do not incorporate the short-range order of materials, and valuable information on the structure at a local scale is lost. Bragg scattering is prominent in diffraction patterns as distinct Bragg peaks and is used to determine the average structure of materials.[19] On the other hand diffuse scattering, which contains short-range structural information, is either too weak to detect or removed from the

diffraction pattern during background subtraction.[30] Total scattering includes both Bragg scattering and diffuse scattering, and its analysis can provide information on the short- and long-range order of relevant materials.[32] The Fourier transformation of a material's total scattering produces its pair distribution function (PDF).

The diffracted intensity is measured as a function of the momentum transfer of the scattering particle (Q).[33] Q is determined as the difference between the incident and scattered wavevectors, $\mathrm{k_{init}}$ and $\mathrm{k_{final}}$ respectively (Equation 2.10). Consequently, Q is also known as the diffraction vector. As the intensity is a function of wavevector, the data primarily exists in the reciprocal space.[34] However, a Fourier transform converts the data into real space which provides a representation of the real structure.[31] The function can be studied in either the reciprocal or real space, but it is more common to determine the crystal structure in its real space equivalent.

Equation 2.10: $Q = \frac{4\pi\sin\theta}{\lambda}$

The Debye scattering equation, that calculates the scattered intensity from a material, is the origin of the PDF method.[35] While crystallography is based on the periodic repetition in a crystal structure, atoms still vibrate about their structural positions and thus produce disorder in the material.[36] The Debye-Waller approximation was introduced into crystallographic analysis to incorporate the influence of lattice vibrations. The Debye-Waller factor decreases Bragg peak intensity as Q increases, to a point where the Bragg peaks disappear at certain Q values.[37] The "lost" intensity appears in between the Bragg peaks as diffuse scattering, which are widely spread over Q space unlike Bragg peaks that are limited to specific reciprocal lattice points in Q space.[38] As diffuse scattering is significantly weaker than Bragg peaks, it is understandable why is it usually removed with the background during analysis. PDF analysis carries significance by considering the total scattering (Bragg and diffuse scattering) of materials.[39]

The total scattering structure function S(Q) is the normalized, measured scattering intensity from a sample in reciprocal space.[30] The Fourier transform of the scattering intensity S(Q) produces the atomic pair distribution function g(r) in real space.[19] The g(r) function is a probability distribution of finding two atoms separated by an interatomic distance, r.[14] The closest distance that two atoms can approach one another is denoted as $\mathrm{r_{nm}}$, and relates to the first peak in a PDF.[32] While there are no peaks before the $\mathrm{r_{nm}}$ peak, small ripples may appear at shorter distances from noise contributions to the system. Every peak in a PDF corresponds to an atom-atom relationship in the material.[40] That is why a structure model that contains atomic positions in space can be converted to a PDF and compared with experimental functions.

A closely related function is the pair density function, p(r).[30] The p(r) function is defined as the product between the average number density and the pair distribution function g(r), as shown in Equation 2.11.[41] The g(r) and p(r) functions focus on the low-r short-range order. This is a consequence of the amplitudes and experimental uncertainties falling off like 1/r.[14]

Equation 2.11: $p(r) = \rho_0\, g(r)$

The reduced pair distribution function G(r) is the most widely used correlation function in PDF analysis.[33] G(r) can be mathematically defined with Equation 2.12. The G(r) function offers advantages that are owed to this function's preferred use. Firstly, the G(r) function is directly obtained from the Fourier transform of the scattering intensity S(Q).[42] Therefore, it is most related to the data and unlike the g(r) and p(r) functions, an average number density ρ_0 does not have to be assumed. The density information is already present in the slope of the G(r) function at low-r values.[43]

Equation 2.12: $G(r) = 4\pi\rho_0$

Another advantage of the G(r) function is that the experimental uncertainties are constant with r.[44] This assists when examining the difference between a model curve and a measured one, as the difference curve will only reflect structural information. Fluctuations due to uncertainties are constant and can thus be ignored, unlike in g(r) and p(r) functions. Since the fluctuations are expected to fall off as 1/r in these functions, structural information can not be easily obtained from their difference curves.[43] Complications may also arise in the g(r) and p(r) functions when fitting models to the measured data. The refinement will give greater weighting to the low-r data unless a statistically residuals function is used.[42] On the other hand, the G(r) function fits the model equally as the statistical uncertainties are constant across the measured data.

A feature of the G(r) function that should be noted are termination ripples that appear with a wavelength of approximately $2\pi/Q_{max}$.[45] Since the scattering intensity S(Q) is only measured over a finite Q range in a real experiment, these termination ripples occur in the function.[30]

When a system contains more than one kind of atom, the interaction between specific atoms may be of interest. The functions discussed above are general and relate to the whole system, but the distribution of specific atom pairs can be studied using the partial pair distribution function.[39] The partial PDF, $g_{\alpha\beta}(r)$ corresponding to atoms α and β, shows the distribution of atom pairs in the material from the atoms of interest.[30] The total PDF can be mathematically defined as the sum of the partial

functions, as shown in Equation 2.13.[41] The partial reduced PDF can be obtained as a Fourier transform of the partial structure function.[30]

Equation 2.13: $g(r) = \sum_{\alpha} \sum_{\beta} g'_{\alpha\beta}(r)$

A typical PDF pattern G(r) for a material contains structural information that can be directly obtained from inspection (Figure 2.17).[46] The peak position indicates the interatomic distance between atoms.[38] The first peak at r_{nm}, denoting the shortest atom-atom distance, is normally a sharp peak. The following peaks are generally less defined and broader. However, all PDF peaks are sharp in crystals as a result of the long-range order. Peak width is related to disorder inside the material regarding either structural disorder, atomic disorder or a combination of both.[34] Atomic disorder can occur as thermal and zero-point motion of atoms, and any fixed displacement of atoms from ideal lattice sites produce a distribution of atom-atom distances.[43] The peak width and shape thus provide information regarding the real atomic probability distribution. Peak area is related to the abundance of relevant pairs weighted by their scattering power.[39] The integrated peak intensity gives the coordination number of the origin atom.[32] When more than one atom is present in a sample, a weighting factor needs to be added to extract the intensities from different chemical species.[30] The largest distance where peaks are visible shows the size of coherent domain.[38]

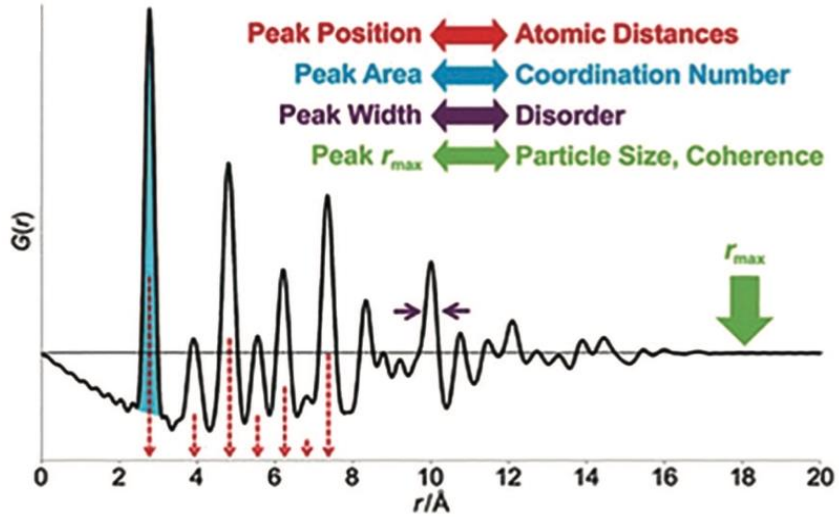


Figure 2.17: A PDF pattern G(r) illustrating the structural information contained in the function.[46]

The most significant criteria for an effective total scattering measurement is scattering data covering a large range of Q.[31] Since Q is inversely proportional to wavelength, a short wavelength is required. A high flux of radiation source is also necessary as the atomic form factor and structural disorder can lead to dampening (significant intensity) in the high Q region.[34] The conditions for a successful total scattering measurement means that PDF experiments needs to be completed at x-

ray synchrotron or high flux neutron facilities. To achieve a wide Q range, a large 2D detector needs to be placed behind the sample in close proximity.[14] The set-up for x-ray PDF experiments is shown in Figure 2.18 below. The signal from the 2D image will be integrated into a 1D total scattering function S(Q).[38] Once the total scattering experiments are completed, a background containing the air and sample container scattering is removed, and the diffuse scattering is preserved along with the Bragg and inelastic scattering.[45] The inelastic scattering is automatically removed with a PDF processing software.[42]

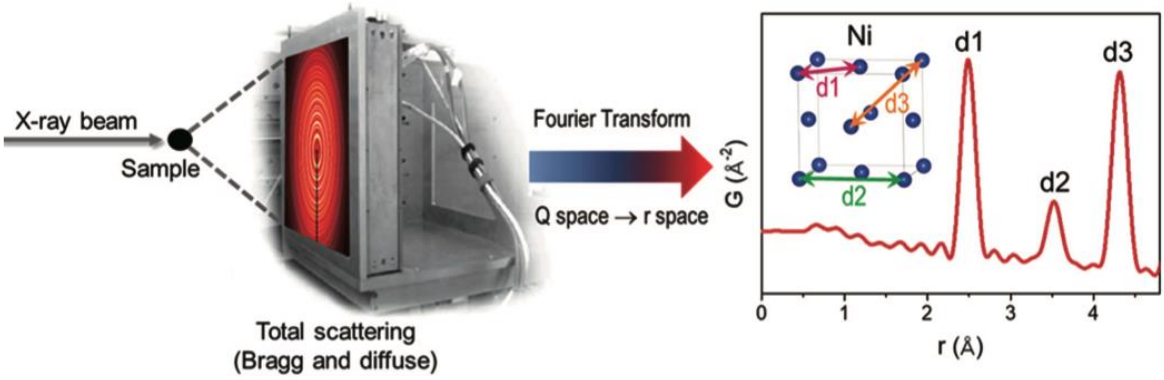


Figure 2.18: A schematic diagarm illustrating the experimental set-up for PDF measurements at a synchrotron.[35]

2.3 Raman Spectroscopy

Spectroscopy is the study of the absorption and emission of radiation with matter.[47] Raman spectroscopy occurs when monochromatic radiation is directed at a sample and results in reflection, absorption or scattering of incident radiation.[47–49] When photons are scattered, their subsequent frequency differs from that of the incident photon.[49] This is a result of the varying vibrational and rotational properties of a sample. This scattered light can be categorized into either Rayleigh or Raman scattering.[47,50]

Rayleigh and Raman scattering can be distinguished by their different scattering strengths; the former is strong while the latter is very weak.[48] On the other hand, scattered light is more commonly set apart according to its frequency difference to the incident beam. Rayleigh scattering has the same frequency of the incident beam, while Raman scattering is characterized by a frequency change between incident and scattered photons.[49,50] The Raman shift is thus defined as the energy difference between the incident and scattered photon. Raman scattering can be further classified as either Stokes or anti-Stokes scattering As illustrated in Figure 2.19, Stokes scattering refers to the energy of the scattered photon that is less than that of

the incident photon, while anti-Stokes scattering describes the scattered beam that has more energy compared to its incident beam.[47–49] The reduced energy of the scattered photon is a result of energy transfer from the photon to the molecule, and the opposite is true when the scattered beam has more energy than its interaction with a sample. Raman spectroscopy measures the vibrational frequency shift from the incident beam frequency.[47] Raman spectra are measured in the UV-visible region, where both the excitation and Raman are visible.

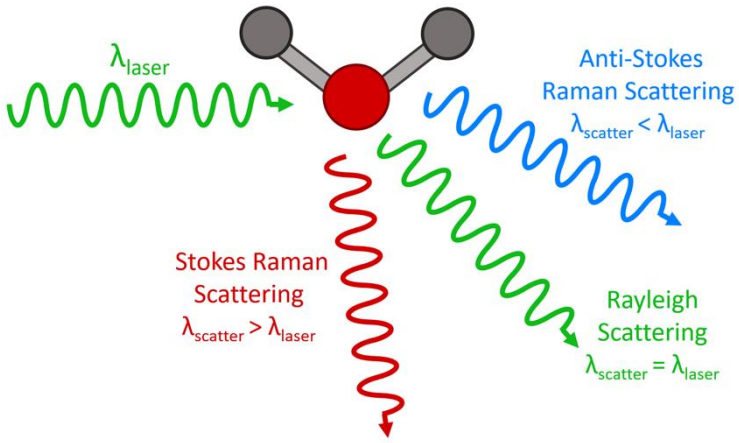


Figure 2.19: Schematic diagram illustrating the Raman Principle where irradiated photons results in Rayliegh and Raman scattering. [47]

2.3.1 Factors determining vibrational frequencies

The vibrational frequency ($\tilde{\nu}$) of a diatomic molecule is determined using Equation 2.14 below.

$$\text{Equation 2.14: } \tilde{\nu} = \frac{1}{2\pi c}\sqrt{\frac{K}{\mu}}$$

The symbols K and μ represent the force constant and reduced mass respectively. Equation 2.14 shows that the vibrational frequency is proportional to $\sqrt{K}$ (force constant effect) and is inversely proportional to $\sqrt{\mu}$ (mass effect).[48]

2.3.2 Selection Rules for Infrared and Raman Spectra

Selection rules allow one to determine if a vibrational mode is active in the IR and Raman spectra.[48,51] The selection rules are different for these spectra, owing to their distinct origins. According to quantum mechanics, an IR-active vibration mode is characterized by a change in the dipole moment throughout the vibration. A Raman-active vibration mode is indicated by changes in the polarizability during the vibration.[48] Polarizability is a proportionality constant (α) in the relation between the electric dipole moment (P) and electric field strength (E) as shown in Equation 2.15.

Equation 2.15: $P = \alpha E$

For Raman-active vibrations, the polarizability (α) can not remain constant with the vibration and therefore the rate of change of polarizability must not be zero.[47,48] The nature of the polarizability can be explained by considering a molecule placed in an electric field (laser beam). This molecule undergoes distortion as the positively charged nuclei are attracted towards the negative pole, while the electrons are drawn towards the positive pole.[48,50] This charge separation creates an induced dipole moment (P), shown in Equation 2.15.

In actual molecules, such a simple relationship does not hold since both P and E are vectors consisting of three components in the x, y and z directions.[48] The active modes are thus characterized by their symmetry in matrices that reflect the three-dimensional nature of the P and E vectors.

Classifying active modes can also be achieved by considering the symmetry of the molecule.[48,52,53] This can be shown using the CO_2 molecule and its vibrations (Figure 2.20). Diagram A illustrates a vibration that is symmetric in relation to the center of symmetry ($\nu 1$). This symmetrical vibration is Raman-active but not IR-active, unlike the vibrations in diagrams B and C. The antisymmetric vibrations, denoted $\nu 2$ and $\nu 3$ in Figure 2.20, are IR-active but not Raman-active.[48] This condition is referred to as the mutual exclusion principle and is applicable to any molecule with a center of symmetry, even if there is no atom at the center of symmetry. While the IR and Raman activities may be determined by inspection for a simple molecule such as CO_2, this is not the case for more complex molecules. Group theoretical calculations provides a methodical approach to classifying IR and Raman active modes of normal vibrations for all types of molecules.[48]

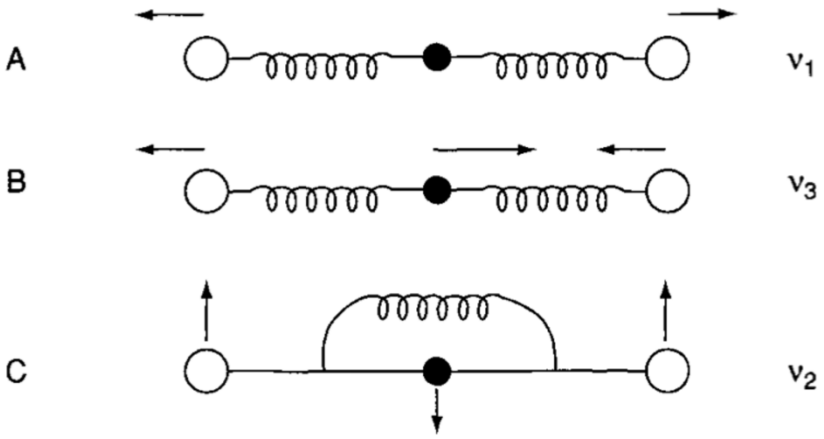


Figure 2.20: A mechanical model illustrating the stretching vibrations in a CO_2 molecule.[48]

Group theory involves the study of symmetry, and the combination of symmetry elements present in a structure.[54–56] Symmetry elements are operations performed on a molecule that produce a superimposable structure to the original. Examples of symmetry elements include rotation axes, planes of symmetry and centers of symmetry. Every molecule has a set of symmetry elements that collectively form a point group, which is represented by a character table, as shown in Table 2.2. A character table is the complete set of irreducible representations of a symmetry group.[54] The final two columns of the character table provide information about IR and Raman activities of normal vibrations. In the linear rotation column, the symmetry species of translational and rotational motion along the x, y and z axes are listed as (Tx, Ty, Tz) and (Rx, Ry, Rz) respectively (Table 2.2). In the quadratic column, the symmetry species of the six components of polarizability are shown. A vibration is considered IR-active if it falls within a symmetry species that includes any translational components and is Raman-active if it belongs to a symmetry species that contain any polarizability components.[48,54,56] Degenerate species are indicated by components in parentheses.

Table 2.2: The character table of the D_{3d} point group.

D_{3d} **(3m)**	**E^3**	**$2C_3$**	**$3C_2$**	i	**$2S_6$**	**$3\sigma_d$**	**Linear, rotation**	**Quadratic**
A_{1g}	1	1	1	1	1	1		$x^2 + y^2, z^2$
A_{1g}	1	1	-1	1	1	-1	R_z	
E_g	2	-1	0	2	-1	0	(R_x, R_y)	$(x^2\text{-}\, y^2, xy)$ (zx, yz)
A_{1u}	1	1	1	-1	-1	-1		
A_{2u}	1	1	-1	-1	-1	1	z	
E_u	2	-1	0	-2	1	0	(x, y)	

2.3.3 Instrumentation

A standard Raman spectrometer is comprised of four major components. These include the excitation source, a sample illumination and collection system, a wavelength selector and lastly a detection and computer control (Figure 2.21).[48]

[3]Table 4.1 symbols: E = Identity, S = Improper rotation, C = Symmetry axis, i = center of inversion, σ = mirror plane

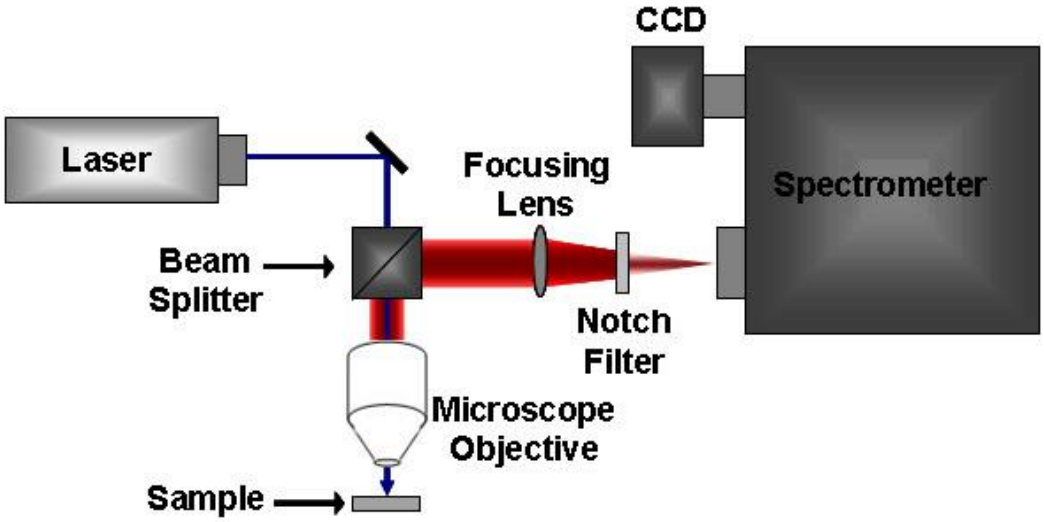


Figure 2.21: Diagram of a standard Raman spectrometer.[48]

Raman scattering requires a single wavelength of radiation with adequate power.[48,57,58] The most commonly used radiation sources in Raman spectroscopy are continuous-wave (CW) lasers such as positively charged noble gases.[48] These lasers are mostly Ar^+ and Kr^+ with wavelength ranges of 351.1 to 514.5 nm and 337.4 to 676.4 nm respectively. Lasers are the preferred excitation sources for Raman spectroscopy because of their advantageous properties. Firstly, laser beams are mostly monochromatic and extraneous lines are significantly weaker.[48,58] These undesired lines can easily be removed by using notch filters or pre-monochromators (Figure 2.21).

The basic components of a noble gas ion laser are illustrated in Figure 2.22. The argon or krypton gas is stored in the plasma tube and is ionized when a very high current discharge is passed through plasma tube.[48,57] The ionization fills the excited state involved in the lasing. The laser emission generates photons of equal energy, phase, and direction, and this process continues until an equilibrium between excitation and emission is reached.[57]

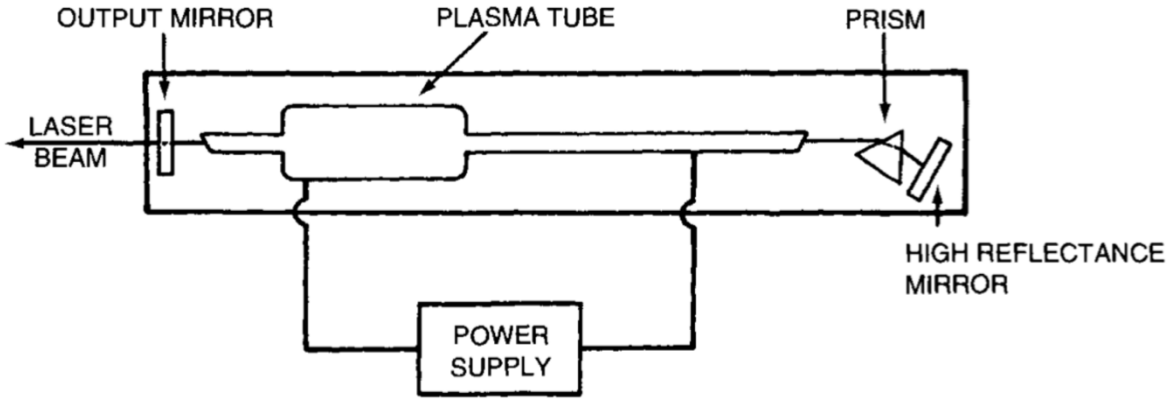


Figure 2.22: Diagram of the basic components of a noble gas ion laser.[57]

A wavelength selector only allows a specific range of radiation with a certain wavelength to pass through.[57,58] The simplest type is an interference filter, which relies on two flat surfaces to create a constructive interference and allow a certain number of wavelengths to be transmitted.[48] Interference filters are designed for individual wavelengths, and any other wavelength that corresponds to this wavelength divided by an integer.[48,58]

It's been established that Raman scattering is inherently weak, and so sensitive detection techniques are required. Spectrometers that are equipped with monochromators and single detectors collect and focus scattered light on a photomultiplier tube and this tube converts photons into an electric signal.[48,49] The electron pulses that give rise to the Raman signal are processed using the photon-counting method.[48] Photon-counting is the preferred method as it can electronically discriminate undesired signals from photon pulses and thus provide increased sensitivity.[48]

2.4 Electrochemical Impedance Spectroscopy

Electrochemical impedance spectroscopy (EIS) is a technique that involves the perturbation of an electrochemical system that is in equilibrium or in steady state, by applying a sinusoidal signal over a range of frequencies.[59–61] This signal can either be ac voltage or ac current and produces a corresponding sinusoidal response in the system, which is either current or voltage, respectively. This provides valuable information about the impedance of the system across the frequency range. The electrochemical system being studied must be linear and time-invariant, meaning that both the input and the output signals have the same frequency and the system's behaviour remains constant over time.[59,60] However, in real electrochemical cells, the current-voltage relationship is not linear (Figure 2.23). Therefore, to achieve a linear relationship between the applied signal and the response, the perturbation applied to the system needs to have a small amplitude.[59] This ensures that the measurements fall within an approximate linear range. The resulting response is then measured over a wide range of frequencies.

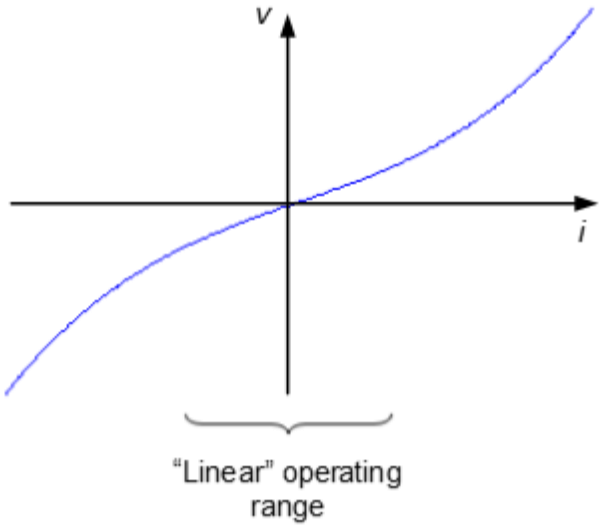


Figure 2.23: A plot representing a typical current-voltage relationship for an electrochemical cell.[60]

The total opposition to current flow in an electric circuit containing resistors, capacitors, and inductors is known as impedance.[59–61] Analysis of impedance can determine the underlying mechanisms of an electrochemical reaction. EIS stands out from other techniques in its ability to distinguish between electrical, electrochemical, and physical processes occurring in a real electrochemical system.[59] When a complex electrochemical system is broken down into separate processes with different time constraints, each process can be individually analysed.[59,61] Measuring the impedance at a range of frequencies enables this, as slow processes are probed

at low frequencies and fast processes are probed at high frequencies. The impedance of an electrochemical system can be represented by an equivalent electrical circuit, consisting of interconnected passive and distributed elements. The value of these elements can be determined and then used to interpret impedance data.

2.4.1 The impedance of an electric circuit

In efforts to determine the impedance of a circuit, a low amplitude alternating voltage may be applied to a system at a particular frequency, to produce a resulting current that is measured.[62] The impedance of the circuit at this frequency is defined as $Z(\omega)$ in Equation 2.16, which is also expressed as a complex number. The real part of $Z(\omega)$ is Z', which represents resistance on the x-axis, and Z'' is the imaginary part which indicates reactance on the y-axis.[59,62] The magnitude of impedance denoted as $|Z|$, and the phase represented as $\varphi = \omega t$, can also be derived from these measurements.[59,63] The impedance spectrum is generated by measuring the impedance over a range of excitation frequencies, and this is known as an Electrochemical Impedance Spectroscopy experiment.[59,61,63]

Equation 2.16: $Z(\omega) = |Z|e^{j\varphi} = |Z|(\cos\varphi + j\sin\varphi)$

Equation *2.17:* $Z(\omega) = Z' + jZ''$

Once an EIS data set has been collected over a range of excitation frequencies, it can be modelled using an equivalent electrical circuit. Before fitting data to an equivalent circuit, the validity of impedimetric data must be assessed. The Kramers-Kronig equations (Equation 2.18 and Equation 2.19) allow one to calculate the real component of the impedance from the imaginary part and vice versa.[59,63]

Equation 2.18: $Z'(\omega) = R_\infty + \frac{2}{\pi}\int_0^\infty \frac{x\,Z(x) - \omega Z(\omega)}{x^2 - \omega^2}\,dx$

Equation 2.19: $Z''(\omega) = \frac{2\omega}{\pi}\int_0^\infty \frac{x\,Z(x) - \omega Z(\omega)}{x^2 - \omega^2}\,dx$

These empirical relations enable the identification of errors in impedance measurements of the relevant electrochemical system.[64] A reliable data set is generally determined by the following properties:

1. Linearity: A system's linearity is demonstrated by the input and output signals having the same frequency.
2. Causality: This characteristic shows that the input signal and the system's response have an exclusive cause-and-effect relationship.
3. Stability: A stable system should be able to recover to its initial condition once the perturbation ends and remain stable until another external stimulus is applied.
4. Finiteness: Both the real and imaginary parts of the system must have finite values over the whole frequency range. This implies that the impedance must tend to a constant value when the frequency approaches zero or infinity.

2.4.2 Graphical representations of EIS data

The Nyquist and Bode plots are the most frequently used formats when plotting impedimetric data. A Nyquist plot has the imaginary component (- Z'') of the impedance plotted against the real impedance (Z') at each excitation frequency (Figure 2.24Figure 2.24: (a): A typical Nyquist plot. (b): Typical Bode plots separated into the modulus of impedance and phase plots.[59]a). The Nyquist plot allows one to model the data using a physically meaningful equivalent circuit, but it has some disadvantages. Since the large impedance values at low frequencies determine the scale of the axis, the plot at high frequencies may be less clear and zooming into that region will be necessary.[62] The most significant limitation of this plot is that it does not show the direct relationship between frequency and impedance.[59]

The Bode plot is also used when interpreting data, as its display of impedance data over a wide frequency range is clear (Figure 2.24). This is possible because the modulus of impedance and frequency are presented in a logarithmic scale.[59] The scale of the axes thus allows matching of the excitation frequency with the modulus of impedance and the phase values.

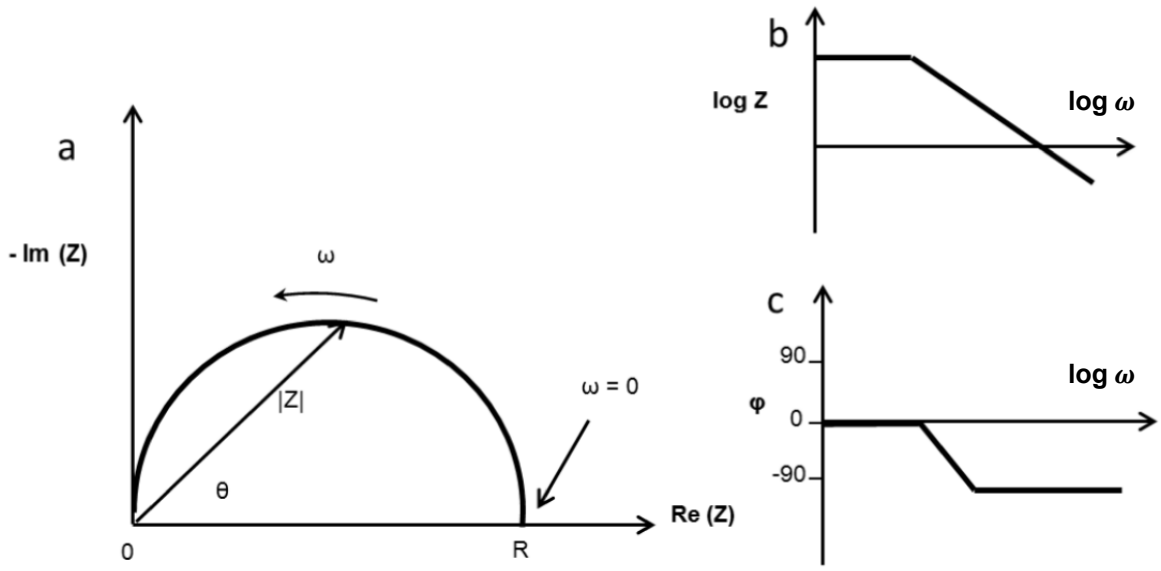


Figure 2.24: (a): A typical Nyquist plot. (b): Typical Bode plots separated into the modulus of impedance and phase plots.[59]

2.4.3 Electric circuit components

The opposition to current flow is known as either resistance or reactance.[62] In dc circuits, resistance occurs where current is only opposed by resistors (Figure 2.25) according to Ohm's Law. On the other hand, reactance is present in ac circuits where current flow is impeded by resistors as well as capacitors (X_C) and inductors (X_L).[59,63] All these elements are measured in Ohm, and the impedance of a resistor is denoted as Z_R, which only includes the real component.[59] Since resistors have voltage and current waveforms that are in-phase with each other, a resistor's

impedance is independent of frequency and has only a real component (Figure 2.26).

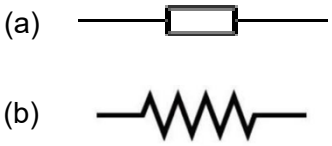


Figure 2.25: (a) and (b) resistor symbols as represented in electric circuits diagrams.

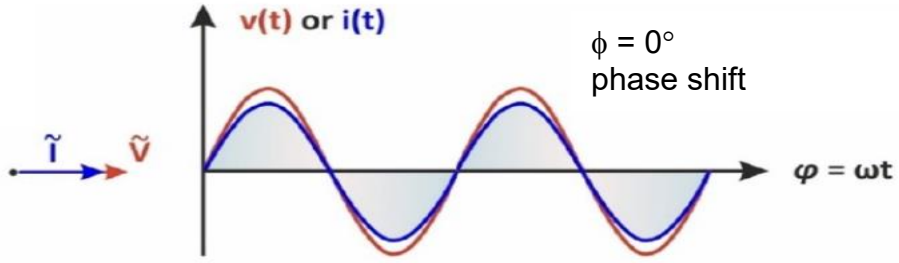


Figure 2.26: Phase diagram for v(t) and i(t) sinusoidal waveforms when an alternating voltage is applied to a resistor.[59]

The different characteristics of Z_R, X_c and X_L in ac circuits allow the possibility to distinguish between the responses of the individual passive elements. Unlike the resistor impedance which only has a real component and is independent of frequency, [59,64], capacitor reactance only contains an imaginary component and is inversely related to frequency. Inductor reactance also contains only an imaginary part, but it is proportional to the excitation frequency.

A capacitor is used to store electricity electrostatically in an electric field (Figure 2.27).[59] An ideal capacitor (C) has real impedance that is zero and imaginary impedance that is inversely proportional to the capacitance and frequency.[59,63] Capacitors have a 90° phase shift of the imaginary impedance as the voltage and current waveforms are “out-of-phase” with respect to each other (Figure 2.28).[62] However, in real electrochemical cells the phase shift between voltage and current due to a capacitive element is typically lower than 90°. So, to sufficiently model the impedimetric data, a constant phase element (CPE) is used instead of an ideal capacitor.[59,60]

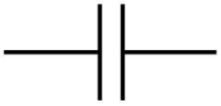


Figure 2.27: Capacitor symbol as represented in electric circuit diagrams.[59]

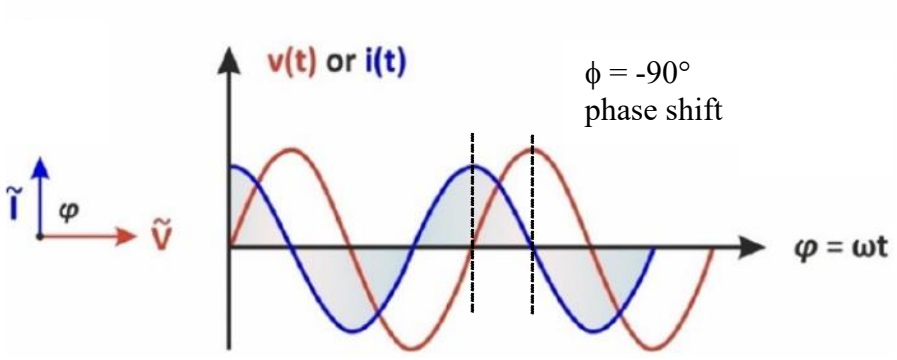


Figure 2.28: Phase diagram for v(t) and i(t) sinusoidal waveforms when an alternating voltage is applied to a capacitor.[59]

The constant phase element (CPE) is an imperfect capacitor that is mostly used in equivalent circuit modelling of impedimetric data (Figure 2.29).[60] The cause of CPE can be attributed to the surface roughness of solid electrodes when dealing with solutions and/or non-ideal materials when dealing with solid state cells. This leads to an uneven distribution of properties such as resistance and capacitance within the cell.[59] Alternatively, it has also been proposed that the CPE is a result of the combined effects of fast diffusion and slow kinetics in the adsorption of ions or impurities from a solution electrolyte onto the electrode surface.[59,64] The CPE impedance is also inversely related to the frequency like an ideal capacitor.

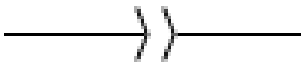


Figure 2.29: A constant phase element symbol as represented in electric circuits diagrams.[59]

When the circuit contains a resistor and a capacitor connected in parallel, the Nyquist plot is represented by a semicircle (Figure 2.30).[59] In this circuit, the capacitive reactance tends to zero at very high frequencies and so all the current passes through the capacitor. The circuit then acts as a short circuit and the impedance is zero.[62,63] The capacitive reactance tends to infinity at very low frequencies, and then all the current passes through the resistor.[59,63] There is a constant current flow when the frequency is low, as a constant current can flow through a resistor but not a capacitor. The current passes through both the capacitor and resistor when the system is at intermediate frequencies.

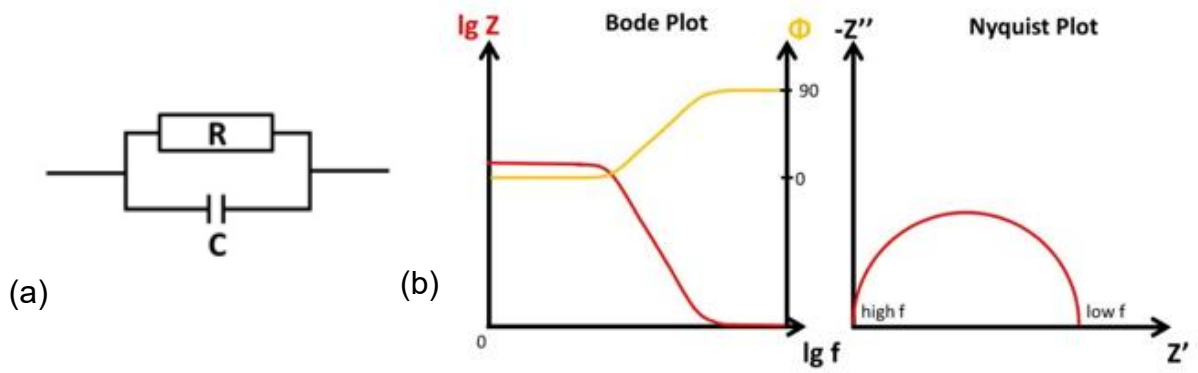


Figure 2.30: (a) The Randles equivalent circuit and (b) the corresponding Bode and Nyquist plots of the Randles circuit.[59]

The measurement of an electrochemical cell's impedance in the presence of a redox couple is referred to as faradaic EIS.[59,60] This is done by applying a small sinusoidal voltage perturbation in addition to a dc potential that matches the standard potential (E°) of the redox reaction.[59] The faradaic process can be represented as a general impedance (Z_F) that combines the effects of the redox reaction's kinetics and the diffusion of the redox species to the working electrode's surface.[59,61] This is mathematically represented by Equation 2.20.

Equation 2.20: $Z_F = R_{ct} + Z_W$

The kinetics of the faradaic process is related to the charge transfer resistance (R_{ct}) in a heterogeneous electrochemical process.[63] This relation assumes that the redox species are not absorbed on the electrode surface. Meanwhile, the mass transport of the redox species towards the electrode surface is represented by the Warburg impedance (Z_W).[59,62,63] The Warburg impedance assumes that this diffusion is linear and extends semi-infinitely.[59] The charge transfer resistance and Warburg impedance is modelled with one of the most used equivalent electrical circuits; the Randles circuit (Figure 2.31).[59,60]

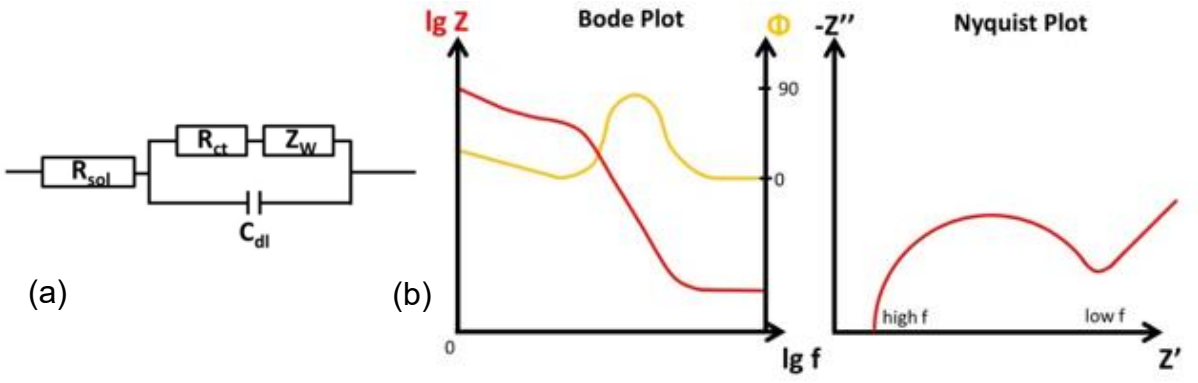


Figure 2.31: (a) The Randles equivalent electric circuit over a wide frequency range; (b) the Bode and Nyquist plots of the Randles equivalent circuit.[59]

The different components of the faradaic process can be identified in its corresponding Nyquist plot. The semicircle models the charge transfer process in such a way that the diameter is equal to the charge transfer resistance (Figure 2.32).[59,63] This is true in the case of ideally polarizable electrodes where the capacitance is reflected by an ideal capacitor,[59] obtained experimentally only in the case of perfectly flat electrodes.[60] The straight line represents the mass transfer process that is described by Warburg impedance.[59,62]

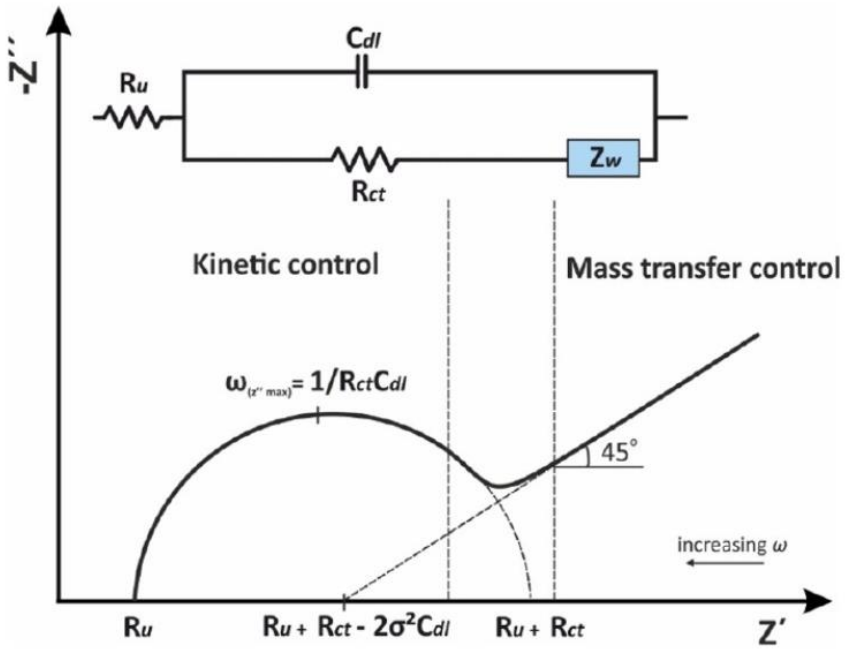


Figure 2.32: The labelled Nyquist plot in correlation with the Randles equivalent circuit over a wide frequency range.[62]

The Warburg impedance (Z_W) is an electrical element that represents the mass transport of redox species and is illustrated as a 45° line at the low frequency portion of the Nyquist plot (Figure 2.32).[59,63] This mass transport describes the time-

dependent diffusion of chemical species, instead of a steady state.[60,65] However, in several electrochemical systems, the impedimetric response cannot be explained using the Warburg impedance of the linear diffusion model that assumes unlimited length, but rather by a diffusion region with finite boundaries at steady state.[59]

The finite diffusion of species can be categorized into two types. Firstly, a permeable (or transmissive) boundary occurs when the finite-diffusion region allows the diffusing species to pass through (Figure 2.33). This forms a concentration gradient over time, resulting in current flow in the electrochemical cell.[59,63,65] On the other hand, an impermeable (or reflective) boundary results in the finite diffusion region becoming impermeable to the diffusing species after a certain time (Figure 2.33).[59,60,65] At this point, charge transfer is no longer possible, and the concentration gradient of the diffusing species decreases until it is zero.[65]

At low frequencies, the impedance profile of a permeable boundary resemble that of Warburg impedance until the species have diffused completely across the film.[59] As the frequencies decrease further a semicircle forms, indicating that the diffusing species have left the finite diffusion layer and a dc current flows within the film (Figure 2.33).[59,64] It is worth mentioning that the impedance spectrum curvature is observed at lower frequencies for thicker films. Solid oxide fuel cells are a common example of systems that have finite length.

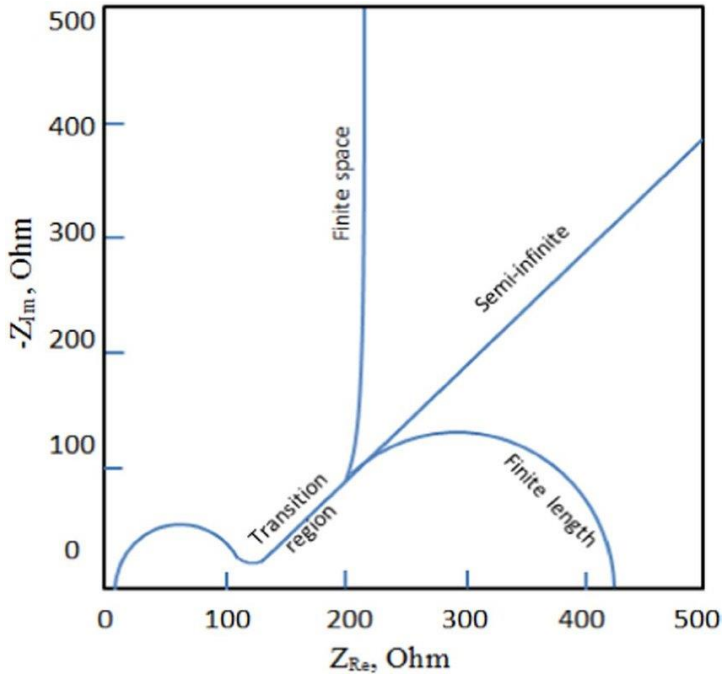


Figure 2.33: A representative Nyquist plot representing different mass transfer mechanisms at low frequencies. [60]

2.5 Experimental Procedure

2.5.1 Synthesis Method

The starting materials for this experiment were bismuth nitrate pentahydrate ($Bi(NO_3)_3.6H_2O$, 99.9% purity, Sigma Aldrich), lanthanum nitrate hexahydrate ($La(NO_3)_3.5H_2O$, 99.9% purity, Sigma Aldrich), samarium nitrate hexahydrate ($Sm(NO_3)_3.5H_2O$, 99.9% purity, Sigma Aldrich), gadolinium nitrate hexahydrate ($Gd(NO_3)_3.5H_2O$, 99.9% purity, Sigma Aldrich) and glacial acetic acid (98% pure, MK Chemical). The metal precursors were accurately weighed according to the reaction stoichiometry to produce 5 grams of the final product. The precursors were then dissolved in the acetic acid solvent (300 mL) and placed on continual heat and stirring until the metal salts dissolved. While heating and stirring was continued, excess citric acid monohydrate ($C_6H_8O_7.H_2O$, ACS reagent, Sigma Aldrich) was added to the solution as a chelating agent (5 times more than the reaction stoichiometry). At this point, a sol was formed that contained complexed metal ions and was heated for approximately 3 hours until a thick gel was produced. The gel underwent the first heat treatment, known as calcination, at 500 °C for 12 hours. The calcination step drove off unreacted citric acid, acetic acid solvent and carbonates as mentioned above. During this step, rearrangement of the solid structure and crystallization also occurred. Once calcination was completed, the sample was a soft yellow powder that was ground using a pestle and mortar until a fine, homogeneous powder formed. At this stage the second heating step, annealing is completed. The calcined powders were reheated at a higher temperature, which was either 750 °C or 610 °C depending on the desired final product. Annealing of the fine powders resulted in agglomeration and thus an increased crystallize size. The annealing step

also converted impurities to the desired phase, to form a phase-pure product. Once cooled, the yellow powder was ground again so that the final powdered sample was smooth homogeneous (Figure 2.34). The synthetic method is summarized in Figure 2.35.



Figure 2.34: Final powders after the annealing step: $Bi_{0.75}Sm_{0.25}O_{1.5}$ and $Bi_{0.85}O_{1.5}Sm_{0.15}O_{1.5}$ from left to right.

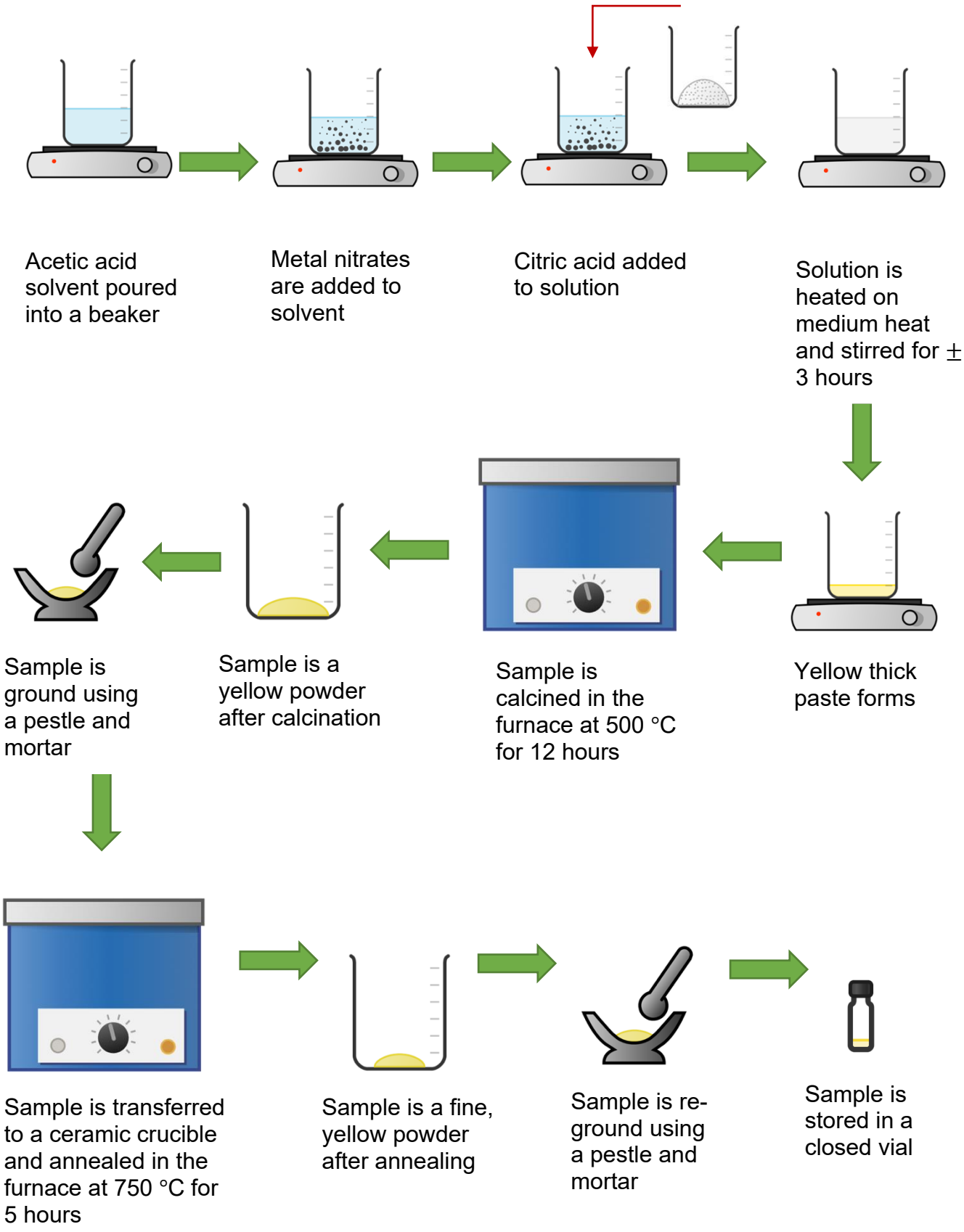


Figure 2.35: A schematic representation of the citrate sol-gel synthesis method.

2.5.2 Laboratory X-ray diffraction

Laboratory X-ray powder diffraction measurements were made using the Bruker D2-Phaser desktop diffractometer at ambient temperatures (Figure 2.36). The sealed tube contains the Co K_{a1}/ K_{a2} X-ray source with wavelengths of 1.78900/1.79283 Å and radiation power of 30 kV and 10 mA was used. The instrument is comprised of a 0.6 mm divergent slit, 2.5° primary and secondary beam Söller slits and a Lynxeye linear position sensitive detector, that enables an effective angular range of 5° 2θ. Powder diffraction patterns were collected from 20° to 120° 2θ, at a step size of 0.026° 2θ for durations that varied between 15 minutes, 30 minutes and an hour. All X-ray powder diffraction patterns were quantitatively analysed using the Rietveld method, as implemented in Bruker AXS TOPAS software (Version 7, 2020).

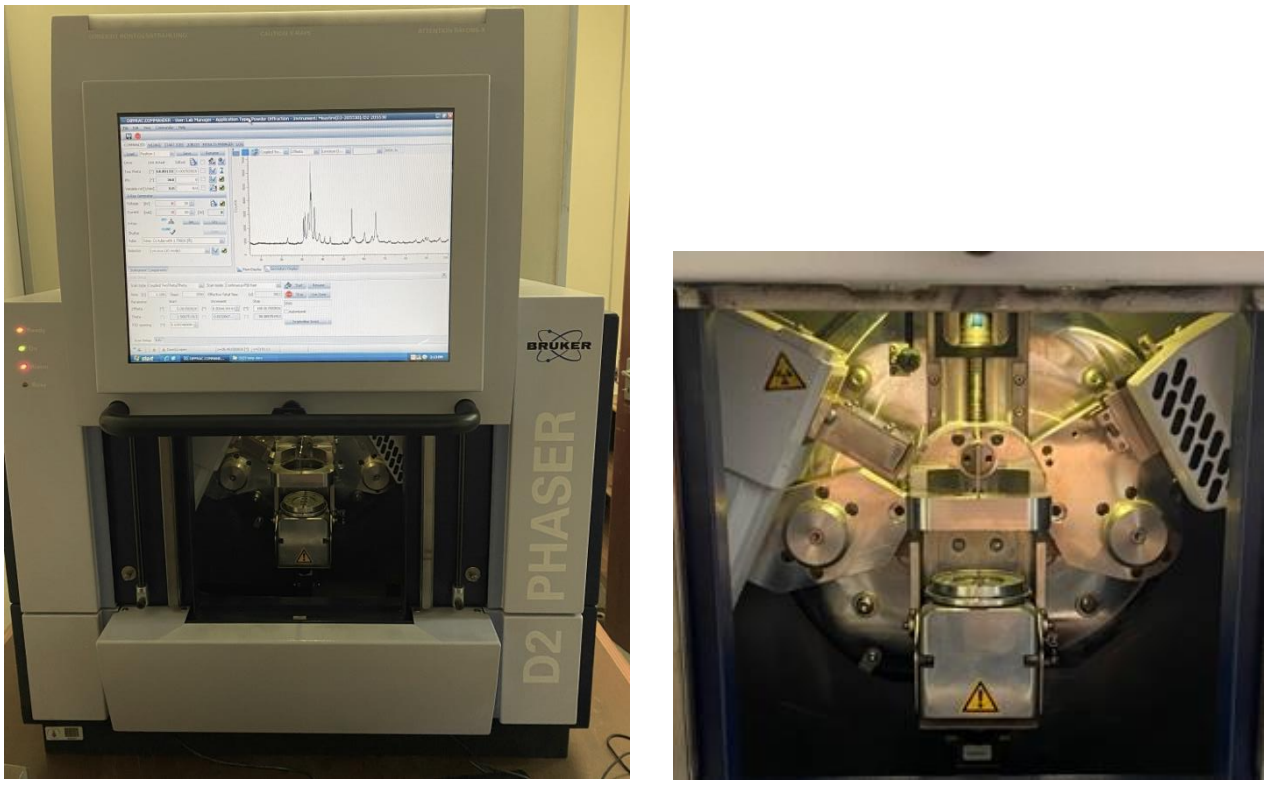


Figure 2.36: Bruker D2-Phaser desktop diffractometer at the School of Chemistry, University of the Witwatersrand.

2.5.3 Synchrotron X-ray diffraction and total scattering

High-resolution synchrotron X-ray diffraction and total scattering measurements were conducted at beamline ID31 of the European Synchrotron Radiation Facility (ESRF) (Figure 2.37).Cylindrical slots of approximately 1 mm contained the sample powders, and were secured with Kapton windows within a sample holder, having 16 slots per hold, that allowed high-throughput. Transmission measurements were made with an incident X-ray energy of 75.00 keV (λ = 0.1653 Å). The intensities were captured by

a Pilatus CdTe 2M detector with 1679 × 1475 pixels. The sample-to-detector distance was about 1.5 m for the high-resolution measurement and 0.3 m for the total scattering measurement. Empty slots with secured windows were also measured and the data subtracted from the sample measurements as part of the background. Geometry calibration was done using the NIST SRM 660b (LaB_6) and the pyFAI software, that also incorporated polarization corrections.

Initial PDF data were automatically processed using the PDFgetX3 software, with a Q_{max} value of 28 $Å^{-1}$. The data underwent reprocessing with a Lorch modification function to minimize termination effects and the influences from high frequency noise. The intensities of small-angle scattering were extrapolated from a Q_{min} value of 0.3375 $Å^{-1}$ to 0. Material compositions were estimated using atomic proportions provided to beamline scientists.



Figure 2.37: Beamline ID31 at ESRF.[13]

2.5.4 Raman Spectroscopy

Raman spectroscopy measurements were completed using the Horiba LabRAM HR (Evolution) Raman spectrometer (Figure 2.38). The system was comprised of an argon ion excitation laser with a wavelength of 514.532 nm and a Symphony CCD detector that was filled with liquid nitrogen and had a grating of 600 lines per mm. Calibration of the instrument was completed with a silicon standard.

In-situ variable temperature measurements were done using an Olympus optical microscope attachment with a 50× LWD objective lens and a Linkham TS1500 sample stage that was purged with argon gas. The sample was heated at a rate of

10 °C per minute from 23 °C to 750 °C, and measurements were taken every 50 °C. Two sets of 90 second collections were measured and then combined to produce the final Raman spectrum.

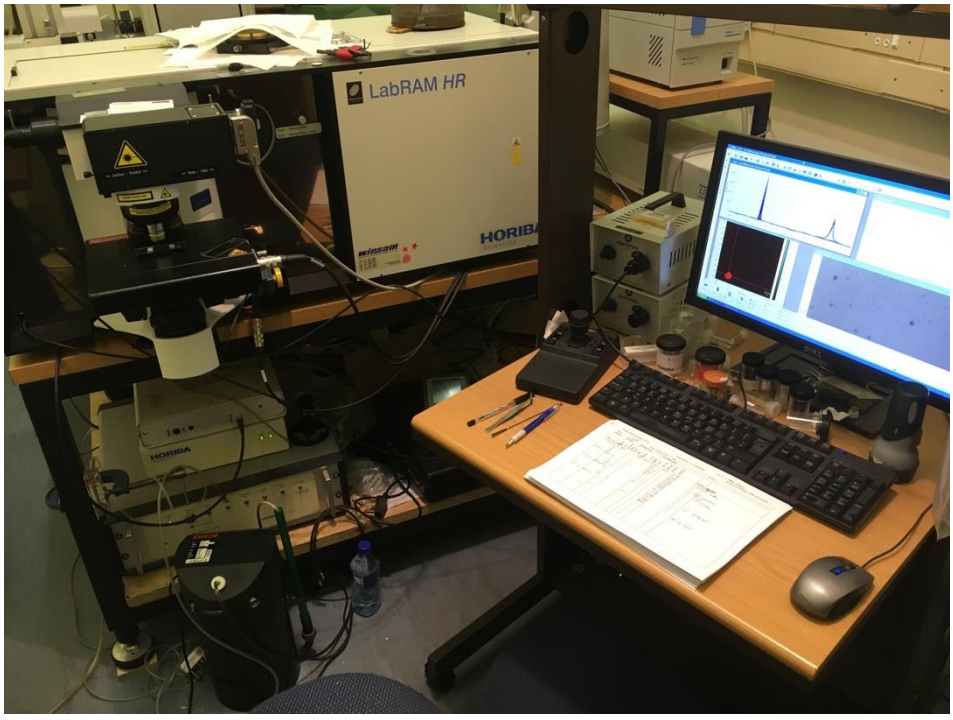


Figure 2.38: Horiba LabRAM HR (Evolution) Raman spectrometer at the Biology School, University of the Witwatersrand.

2.5.5 Electrochemical Impedance Spectroscopy

2.5.1 Pellet Preparation

Approximately 1 gram of the powdered sample was weighed and then pressed into a pellet using a 13 mm die and a hydraulic press set to 6 tons for 10 minutes. This produced a pellet around 2 mm thick. The pellets were then sintered in a tube furnace. The ends of the tube furnace were closed with fiberglass insulating material to prevent heat loss during operation. Prior to sintering, the accuracy of the tube furnace temperature was investigated. The actual temperature of the tube furnace was recorded by inserting a thermocouple into the middle of the tube furnace, where the sample boat would be placed. The comparison showed the actual temperature was 60 °C lower than the selected temperature. Using this information, the tube furnace temperature was set so that the desired temperature was reflected on the thermocouple.

Pellets were placed in the sample boat and then inserted into the tube, such that the boat was at the center of the tube (Figure 2.39). The pellets were sintered at the annealing temperature (750 °C or 610 °C) for 12 hours after heating at a ramp rate of 10 °C per minute. The pellets were analysed using Lab XRD to examine if any

crystallographic changes had taken place during sintering, to ensure the desired phase and structure had been maintained.

Pellets were sputter coated using a Quorum Q15OT ES coater. The instrument bleed gas was argon, the chamber pressure was 1 x 10^{-2} mBar and the current was set to 20 mA. The pellets were sputtered with a gold coating of 9.9 nm of gold on either side, while the pellet edges were covered with masking tape to prevent being sputter coated too.



Figure 2.39: 13 mm $Bi_{1-x}Ln_xO_{1.5}$ pellets in a boat before sintering at 750 °C for 12 hours.

2.5.2 Electrochemical Impedance Measurements

Impedance was measured with a Bio-Logic MTZ-35 impedance analyzer, running MT Lab software, and in conjunction using an HF-1100 furnace and an HT-1100 sample holder (Figure 2.40). The quartz tube was removed from the sample holder before it was placed in the furnace. Measurements were then preceded by an open and closed circuit cell compensation to account for the contributions of miscellaneous impedances recorded by the instrument. The instrument was set up to measure the impedance of materials from 200 °C to 750 °C (or 610 °C) in 50 °C increments. A heating and cooling rate of 10 °C per minute was used and a 30-minute soak period was set at temperatures of measurement to ensure stabilization at each measurement point.

The frequency range was 10 MHz to 0.1 Hz with an AC amplitude of 10 mV. The pellet was placed in between the platinum electrodes of the sample holder that are 12 mm in diameter. The sample holder was placed into the furnace and connected using a two-terminal connection. Temperature was monitored for both the furnace and sample holder using their integrated thermocouples. All impedance data were evaluated using the Bio-Logic EC Lab software (version 11.47).

The pellets were sintered in a tube furnace. Prior to sintering, the accuracy of the tube furnace temperature was investigated. The actual temperature of the tube furnace was recorded by inserting a calibrated external thermocouple into the middle of the tube furnace, where the sample boat would be placed. The set temperature and the actual temperature showed a 60 °C difference, where the actual temperature

was lower. Using this information, the tube furnace temperature was set so that the desired temperature as was reflected by the external thermocouple.

Pellets were placed in a Coors sample boat and then inserted into the tube such that the boat was at the centre of the tube. The furnace temperature was ramped at a rate of 10 °C per minute and the pellets were sintered at 750 °C for 12 hours. The pellets were analysed using the Bruker D2 XRD to examine the crystallographic changes (if any) that took place during pelletisation and sintering, to ensure the desired phase and structure had been maintained.

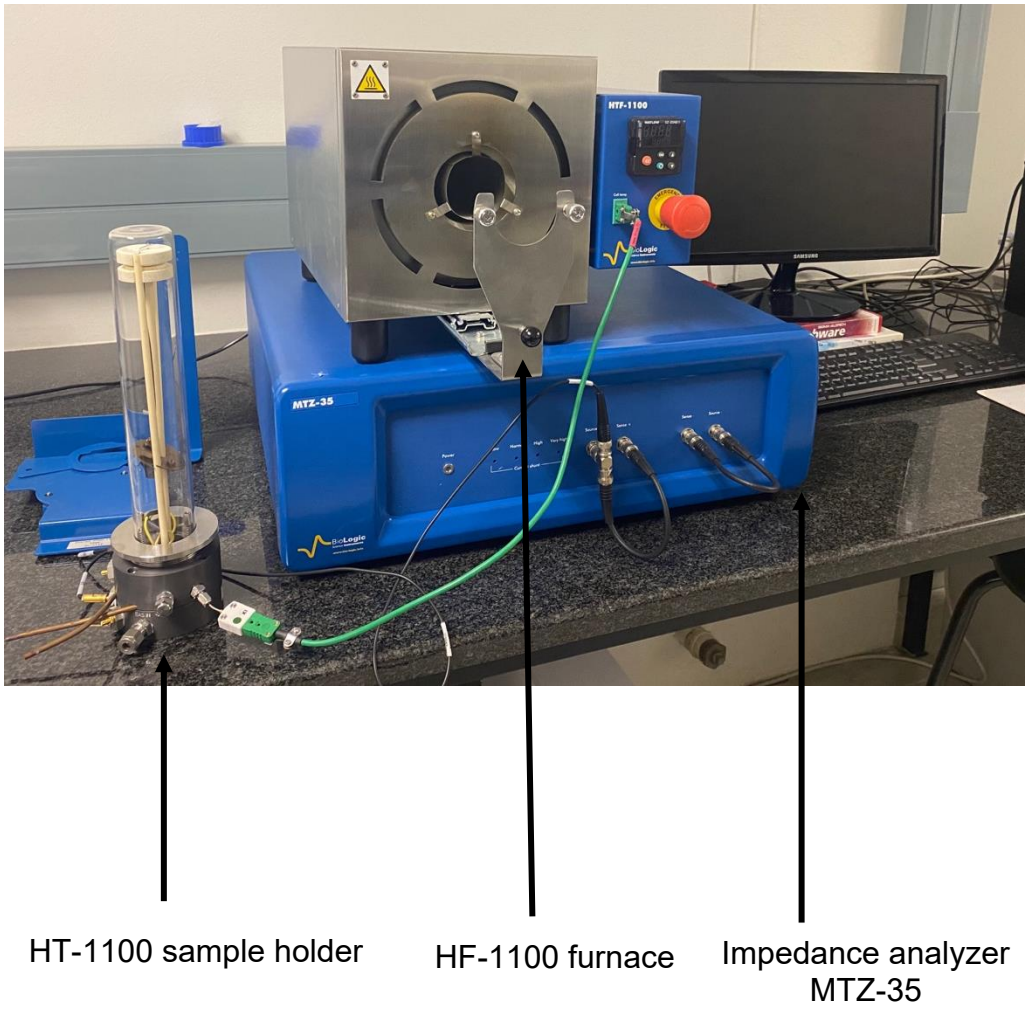


Figure 2.40: Bio-Logic MTZ-35 impedance analyzer coupled with a HF-1100 furnace and HT-1100 sample holder at the School of Chemistry, University of the Witwatersrand.

2.6 References

1. Danks, A. E., Hall, S. R. & Schnepp, Z. The evolution of 'sol–gel' chemistry as a technique for materials synthesis. Materials Horizons. **3**, 91–112 (2016).
2. Dislich, H. Sol-gel: Science, processes and products. Journal of Non-Crystalline Solids **80**, 115–121 (1986).
3. Afonina, L. I. & Naydenko, E. S. Synthesis of High-Pure Bismuth Citrate Using the Solid-Liquid Reactions. Chemistry for Sustainable Development. **17,** 235 - 241 (2009).
4. Zayat, M. & Levy, D. Blue $CoAl_2O_4$ Particles Prepared by the Sol−Gel and Citrate−Gel Methods. Chemistry of Materials. **12**, 2763–2769 (2000).
5. Li, Y., Xue, L., Fan, L. & Yan, Y. The effect of citric acid to metal nitrates molar ratio on sol–gel combustion synthesis of nanocrystalline $LaMnO_3$ powders. Journal of Alloys and Compounds **478**, 493–497 (2009).
6. Mali, A. & Ataie, A. Structural characterization of nano-crystalline $BaFe_{12}O_{19}$ powders synthesized by sol–gel combustion route. Scripta Materialia **53**, 1065–1070 (2005).
7. Hsu, K.-F., Tsay, S.-Y. & Hwang, B.-J. Synthesis and characterization of nano-sized $LiFePO_4$ cathode materials prepared by a citric acid-based sol–gel route. Journal of Materials Chemistry. **14**, 2690–2695 (2004).
8. Zhao, L., Fang, K., Jiang, D., Li, D. & Sun, Y. Sol–gel derived Ni–Mo bimetallic carbide catalysts and their performance for CO hydrogenation. Catalysis Today. **158**, 490–495 (2010).
9. Jumanath, E. C. & Pradyumnan, P. P. Growth and structural studies of hybrid single crystal of cadmium citrate hexahydrate. Journal of Molecular Structure. **1193**, 231–238 (2019).
10. Barbooti, M. & Al-Sammerrai, A. Decomposition of Citric Acid. Thermochimica Acta. **98**, 119 - 126 (1986).
11. Wen, W. & Wu, J.M. Nanomaterials via solution combustion synthesis: a step nearer to controllability. RSC Advances. **4**, 58090–58100 (2014).
12. Kaduk, J. A. et al. Powder diffraction. Nature Reviews Methods Primers **1**, 77 (2021).
13. Billinge, S. J. L. & Dinnebier, R. E. Powder Diffraction: Theory and Practice. (Royal society of chemistry, Cambridge, 2008).
14. Ren, Y. & Zuo, X. Synchrotron X-Ray and Neutron Diffraction, Total Scattering, and Small-Angle Scattering Techniques for Rechargeable Battery Research. Small Methods **2**, 1800064 (2018).
15. Snyder, R. L., Fiala, J. & Bunge, H. J. Defect and Microstructure Analysis by Diffraction. (International Union of Crystallography, 2000).
16. Balzar, D. Voigt-function model in diffraction line-broadening analysis. (International Union of Crystallography, 1999).
17. Buras, B., David, W. I. F., Gerward, L., Jorgensen, J. D. & Willis, B. T. M. Energy-dispersive techniques. in International Tables for Crystallography Volume C:

Mathematical, physical and chemical tables (ed. Prince, E.) 84–88 (Springer Netherlands, Dordrecht, 2004). doi:10.1107/97809553602060000580.
18. Deutsch, M. et al. X-Ray Spectrometry of Copper: New Results on an Old Subject. Journal of Research of NIST. **109**, 75–98 (2004).
19. Dinnebier, R. & Scardi, P. X-ray powder diffraction in education. Part I. Bragg peak profiles. Journal of Applied Crystallography. **54**, 1811–1831 (2021).
20. Dinnebier, R. E., Leineweber, A. & Evans, J. S. O. Rietveld Refinement: Practical Powder Diffraction Pattern Analysis Using TOPAS. (De Gruyter, Berlin Boston, 2019).
21. Chitturi, S. R. et al. Automated prediction of lattice parameters from X-ray powder diffraction patterns. Journal of Applied Crystallography **54**, 1799–1810 (2021).
22. Parrish, W. & Langford, J. I. Powder and related techniques: X-ray techniques. in International Tables for Crystallography Volume C: Mathematical, physical and chemical tables (ed. Prince, E.) 42–79 (Springer Netherlands, Dordrecht, 2004). doi:10.1107/97809553602060000578.
23. Properties of Synchrotron Radiation. http://pd.chem.ucl.ac.uk/pdnn/inst2/prop.htm.
24. Woolfson, M. M. An Introduction to X-Ray Crystallography. (Cambridge University Press, Cambridge ; New York, NY, USA, 1997).
25. Cheary, R. W. & Coelho, A. A fundamental parameters approach to X-ray line-profile fitting. Journal of Applied Crystallography **25**, 109–121 (1992).
26. Rao, C. N. R., Joshi, S. K. & Mashelkar, R. A. Solid State Chemistry: Selected Papers of C.N.R. Rao. (World Scientific, Singapore, 1995).
27. Hurst, V. J., Schroeder, P. A. & Styron, R. W. Accurate quantification of quartz and other phases by powder X-ray diffractometry. Analytica Chimica Acta **337**, 233–252 (1997).
28. Toby, B. H. R factors in Rietveld analysis: How good is good enough? Powder Diffraction Journal **21**, 67–70 (2006).
29. Evans, J. S. O. & Evans, I. R. Structure Analysis from Powder Diffraction Data: Rietveld Refinement in Excel. Journal of Chemical Education **98**, 495–505 (2021).
30. Egami, T. & Billinge, S. J. L. Underneath the Bragg Peaks: Structural Analysis of Complex Materials. (Pergamon, Kiddington, Oxford, UK ; Boston, 2003).
31. Scattering of X-rays by a Collection of Electrons as in an Atom. http://pd.chem.ucl.ac.uk/pdnn/diff1/scaten.htm.
32. Keen, D. A. & Dove, M. T. Local structures of amorphous and crystalline phases of silica, SiO_2, by neutron total scattering. Journal of Physics: Condensed Matter **11**, 9263–9273 (1999).
33. Egami, T. PDF Analysis Applied to Crystalline Materials. in Local Structure from Diffraction (eds. Billinge, S. J. L. & Thorpe, M. F.) 1–21 (Springer US, Boston, MA, 2002). doi:10.1007/0-306-47077-2_1.
34. Miyanaga, T. Local Structure and Dynamics of Functional Materials Studied by X-ray Absorption Fine Structure. Symmetry **13**, 1315 (2021).

35. Wang, X., Tan, S., Yang, X.-Q. & Hu, E. Pair distribution function analysis: Fundamentals and application to battery materials. Chinese Physics B **29**, 028802 (2020).
36. Chapter 2 Crystallographic analysis of complex materials. in Pergamon Materials Series (eds. Egami, T. & Billinge, S. J. L.) vol. 7 25–51 (Pergamon, 2003).
37. Li, L., Xie, Y., Maxey, E. & Harder, R. Methods for operando coherent X-ray diffraction of battery materials at the Advanced Photon Source. Journal of Synchrotron Radiation **26**, 220–229 (2019).
38. Wang, X., Tan, S., Yang, X.-Q. & Hu, E. Pair distribution function analysis: Fundamentals and application to battery materials. Chinese Physics B **29**, 028802 (2020).
39. Scavini, M., Coduri, M., Allieta, M., Brunelli, M. & Ferrero, C. Probing Complex Disorder in $Ce_{1-x}Gd_xO_{2-x/2}$ Using the Pair Distribution Function Analysis. Chemistry of Materials Journal **24**, 1338–1345 (2012).
40. From Semiconductors to Proteins: Beyond the Average Structure. https://www.researchgate.net/publication/321594321_From_Semiconductors_to_Proteins_Beyond_the_Average_Structure.
41. Billinge, S. J. L., DiFrancesco, R. G., Kwei, G. H., Neumeier, J. J. & Thompson, J. D. Direct Observation of Lattice Polaron Formation in the Local Structure of $La_{1-x}Ca_xMnO_3$ Physical Review Letters **77**, 715–718 (1996).
42. Structural Analysis of Molecular Materials Using the Pair Distribution Function | Chemical Reviews. https://pubs.acs.org/doi/10.1021/acs.chemrev.1c00237.
43. Billinge, S. J. L. The rise of the X-ray atomic pair distribution function method: a series of fortunate events. Philosophical Transactions of the Royal Society A: Mathematical, Physical and Engineering Sciences **377**, 20180413 (2019).
44. (IUCr) Pair distribution function analysis in materials science. Acta Crystallographica Section A: Foundations and Advances vol. 77 C263–C263 https://scripts.iucr.org/cgi-bin/paper?S0108767321094198 (2021).
45. Proffen, T. et al. Atomic pair distribution function analysis of materials containing crystalline and amorphous phases. Zeitschrift für Kristallographie - Crystalline Materials **220**, 1002–1008 (2005).
46. Local structure studies of materials using pair distribution function analysis - NASA/ADS. https://ui.adsabs.harvard.edu/abs/2013PhDT.....182P/abstract.
47. Kudelski, A. Analytical applications of Raman spectroscopy. Talanta **76**, 1–8 (2008).
48. Ferraro, J. R., Nakamoto, K. & Brown, C. W. Introductory Raman Spectroscopy. (Academic Press, Amsterdam ; Boston, 2003).
49. Cialla-May, D., Schmitt, M. & Popp, J. Theoretical principles of Raman spectroscopy. Physical Sciences Reviews **4**, (2019).
50. Schrader, B. Chemical Applications of Raman Spectroscopy. Angewandte Chemie International Edition in English **12**, 884–908 (1973).
51. Hardcastle, F. D. & Wachs, I. E. The molecular structure of bismuth oxide by Raman spectroscopy. Journal of Solid State Chemistry **97**, 319–331 (1992).

52. Rubbens, A., Drache, M., Roussel, P. & Wignacourt, J. P. Raman scattering characterization of bismuth based mixed oxides with Bi_2O_3 related structures. Materials Research Bulletin **42**, 1683–1690 (2007).
53. Davies, J. E. D. Solid state vibrational spectroscopy—The infrared and raman spectra of the bismuth(III) oxide halides. Journal of Inorganic and Nuclear Chemistry **35**, 1531–1534 (1973).
54. Carter, R. L. Molecular Symmetry and Group Theory. (John Wiley & Sons, 1997).
55. Kettle, S. F. A. Symmetry and Structure: Readable Group Theory for Chemists. (John Wiley & Sons, 2008).
56. Rodríguez-Lara, B. M., El-Ganainy, R. & Guerrero, J. Symmetry in optics and photonics: a group theory approach. Science Bulletin **63**, 244–251 (2018).
57. Coates, J. Vibrational Spectroscopy: Instrumentation for Infrared and Raman Spectroscopy. Applied Spectroscopy Reviews **33**, 267–425 (1998).
58. Dubessy, J., Caumon, M.-C., Rull, F. & Sharma, S. Instrumentation in Raman spectroscopy: elementary theory and practice. in Raman spectroscopy applied to Earth sciences and cultural heritage (eds. Dubessy, J., Caumon, M.-C. & Rull, F.) vol. 12 0 (European Mineralogical Union, 2012).
59. Lazanas, A. Ch. & Prodromidis, M. I. Electrochemical Impedance Spectroscopy─A Tutorial. ACS Measurement Science Au Journal **3**, 162–193 (2023).
60. Boukamp, B. A. A Linear Kronig-Kramers Transform Test for Immittance Data Validation. Journal of the Electrochemical Society **142**, 1885–1894 (1995).
61. Schönleber, M., Klotz, D. & Ivers-Tiffée, E. A Method for Improving the Robustness of linear Kramers-Kronig Validity Tests. Electrochimica Acta **131**, 20–27 (2014).
62. Schönleber, M. & Ivers-Tiffée, E. Approximability of impedance spectra by RC elements and implications for impedance analysis. Electrochemistry Communications **58**, 15–19 (2015).
63. Yrjänä, V. DearEIS - A GUI program for analyzing impedancespectra. Journal of Open Source Software **7**, 4808 (2022).
64. Tan, M. Y., Tan, K. B., Zainal, Z., Khaw, C. C. & Chen, S. K. Subsolidus formation and impedance spectroscopy studies of materials in the $Bi_2O_{3(1-x)}$ - $Y_2O_{3(x)}$ binary system. Ceramics International **38**, 3403–3409 (2012).
65. Abrahams, I., Krok, F., Malys, M. & Wrobel, W. Phase transition studies in BIMEVOX solid electrolytes using AC impedance spectroscopy. Solid State Ionics **176**, 2053–2058 (2005).

Chapter 3 - An X-ray diffraction study of the average and local structure of rhombohedral bismuth oxide

Powder X-ray diffraction serves as the primary technique for characterizing materials and phase formation in this dissertation. A large part of this research focuses on understanding the structural properties of various Bi_2O_3 materials which is achieved by investigating the influence of four key variables: substituent size, substituent concentration, annealing duration, and annealing temperature. These variables are examined from an average crystalline structure perspective at an atomic scale using X-ray diffraction. Furthermore, the phase formation and stability of selected samples were also studied to gain a deeper understanding of phase behaviour. To further investigate the total scattering behaviour of rhombohedral Bi_2O_3 materials, PDF analysis was conducted on selected samples.

Two in-depth reviews are presented concerning the structural characterization of $Bi_{0.775}Ln_{0.225}O_{1.5}$ materials, employing either x-ray diffraction or neutron diffraction techniques. The findings from these studies, extensively reviewed in the following section, have been widely adopted as reference structural models in prominent research [1–3].

3.1 Literature Review

Drache and coworkers [4] investigated the $Bi_{0.775}Ln_{0.225}O_{1.5}$ materials where Ln varied as La, Pr, Nd, Sm, Eu, Gd, Tb and Dy. The aim of this work was to explore the possible rhombohedral polymorphism behavior of the $R\bar{3}m$ phase with hexagonal structure. Previous work has reported that the room temperature rhombohedral phase (β_2) can transform to a closely related rhombohedral β_1 form at high temperatures [5,6]. Therefore, different bismuth lanthanide materials were examined with respect to their structural and conductivity properties to gain further insight into the relevant phase behaviour.

It has been proposed that bismuth lanthanide oxides transform from the β_2 low temperature form to different phases depending on the Ln^{3+} size [4]. Larger lanthanides (ionic radii between 1.17 and 1.079 Å), such as La, Pr, Nd and Sm transform to the β_1 form upon heating. Intermediate sized lanthanides (ionic radii from 1.066 to 1.053 Å), including Eu and Gd, transform to a phase mixture of the β_1 and $Fm\bar{3}m$ δ - cubic Bi_2O_3 forms. As heating continues, these lanthanides may transform further to a single cubic phase. The smaller lanthanides (ionic radii between 1.04 and 1.004 Å), such as Tb, Dy and Er, change directly to the δ - cubic structure. The relationship between the β_2 and β_1 polymorphic forms in the $R\bar{3}m$ phase has been attributed to cation and/or anion ordering in substituted bismuth

oxides by several researchers. The possible disordering at high temperatures is further explored in the work of Drache et al. [4] to explain the structural transition.

$Bi_{0.775}Ln_{0.225}O_{1.5}$ samples were prepared by the solid state reaction of Bi_2O_3 and Ln_2O_3. The synthesis method started with an initial prefiring of the oxides at 600 – 700 °C in air, followed by stoichiometric amounts being ground in an agate mortar. Thereafter the mixture underwent two thermal treatments at 650 °C for 15 hours each. Synthesis of the powder sample was complete once the exclusive presence of the hexagonal phase was measured by x-ray diffraction (Cu K_a radiation).

The starting model for refinements was the rhombohedral $R\bar{3}m$ Bi – Sr - O structure with a hexagonal unit cell (Z = 9). The lattice parameters of a and c are 4.024 Å and 27.60 Å respectively, and further structural data is summarized in Table 3.1.

Table 3.1: Structural information of the rhombohedral $R\bar{3}m$ Bi – Sr - O structural model

	Wyckoff Position	**Fractional Coordinates**	**Occupancy**
M1	3a	(0;0;0)	1
M2	6c	(0;0;0.22)	1
O1	6c	(0;0;0.33)	1
O2	6c	(0;0;0.09)	0.7 – 0.8
O3	6c	(0;0;0.44)	0.4 – 0.5

The Bi 6c site was refined with a full occupancy while the mixed Bi,Ln 3a site was occupied according to the stoichiometric ratio of the metals (Table 3.1). The oxide ions were spread across three kinds of 6c sites, referred to as $O_{(1)}$, $O_{(2)}$ and $O_{(3)}$. The lattice parameters were refined. The refinement of the cation positions involved refining the atomic coordinates (specifically the z coordinate of the Bi 6c site) and the thermal parameters. The anion refinements involved refining the atomic coordinates and their respective thermal parameters. The occupancy factors of sites with partial occupancy were also refined with constraints added according to the composition. The most relevant findings from refinements have been listed in Table 3.2 below.

Table 3.2: The refined parameters of $Bi_{0.775}Ln_{0.225}O_{1.5}$ materials reported by Drache and co-workers [4].

Ln	a (Å)	c (Å)	z Bi	z $O_{(1)}$	z $O_{(2)}$	z $O_{(3)}$	Occupancy $O_{(2)}$	Occupancy $O_{(3)}$
La	4.024	27.60	0.2243	0.300	0.092	0.441	0.82	0.43
Pr	3.998	27.51	0.2244	0.302	0.095	0.445	0.81	0.44
Nd	3.992	27.46	0.2247	0.303	0.097	0.445	0.77	0.48
Sm	3.978	27.39	0.2248	0.305	0.093	0.445	0.70	0.55
Eu	3.974	27.35	0.2253	0.300	0.090	0.450	0.81	0.44
Gd	3.972	27.34	0.2252	0.299	0.091	0.446	0.78	0.47
Tb	3.965	27.32	0.2252	0.303	0.088	0.447	0.78	0.47
Dy	3.955	27.30	0.2252	0.300	0.091	0.452	0.72	0.53

The “a” and “c” cell parameters were examined as a function of lanthanide (Ln^{3+}) radius, which revealed two different linear domains present (Figure 3.1). The first was observed for the larger lanthanides including La, Pr, Nd, Sm and Eu. The second linear range was present for the smaller lanthanides such as Gd, Tb and Dy. The presence of these two linear domains support the hypothesis of two kinds of bismuth-lanthanide ordering in the mixed layer.

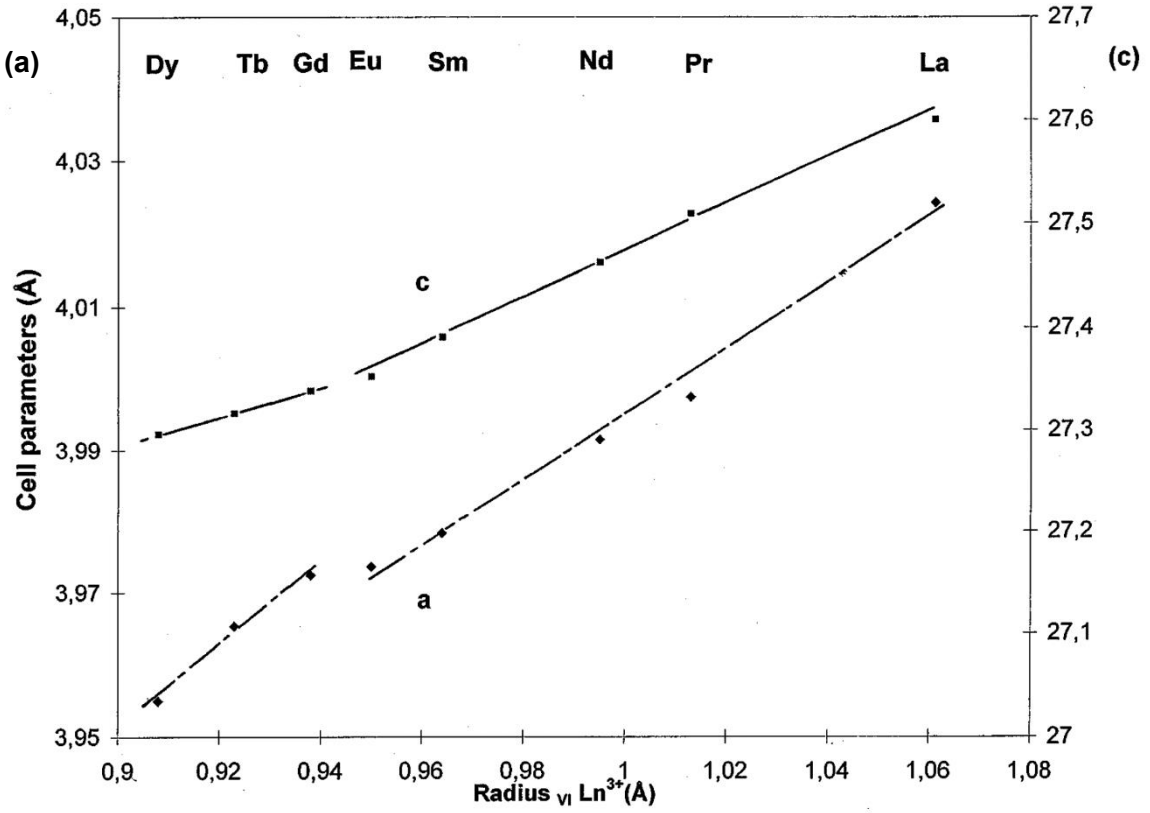


Figure 3.1: Correlation between $Bi_{0.775}Ln_{0.225}O_{1.5}$ lattice constants and Ln^{3+} radii at room temperature.[4]

The variable-temperature structure of $Bi_{0.775}Ln_{0.225}O_{1.5}$ materials showed that the lattice parameters of all samples exhibited pseudolinear behavior between 20 °C and 700 °C (Figure 3.2). Between 700 °C and 750 °C an abrupt increase of both cell parameters in the larger lanthanides (La, Pr, Nd, Sm and Eu) was characterized as the $\beta_2$to β_1 transition. This was supported by the refined diffraction data at elevated temperatures, which showed that the materials maintained the hexagonal structure of the rhombohedral phase but with significantly larger cell parameters and a linear expansion behavior (Figure 3.2).

The structural change of smaller lanthanides (Gd, Tb, Dy) at 700 °C represents the formation of the cubic δ - phase which is present from 700 °C to 900 °C. The δ - phase is preserved to room temperature upon quenching.

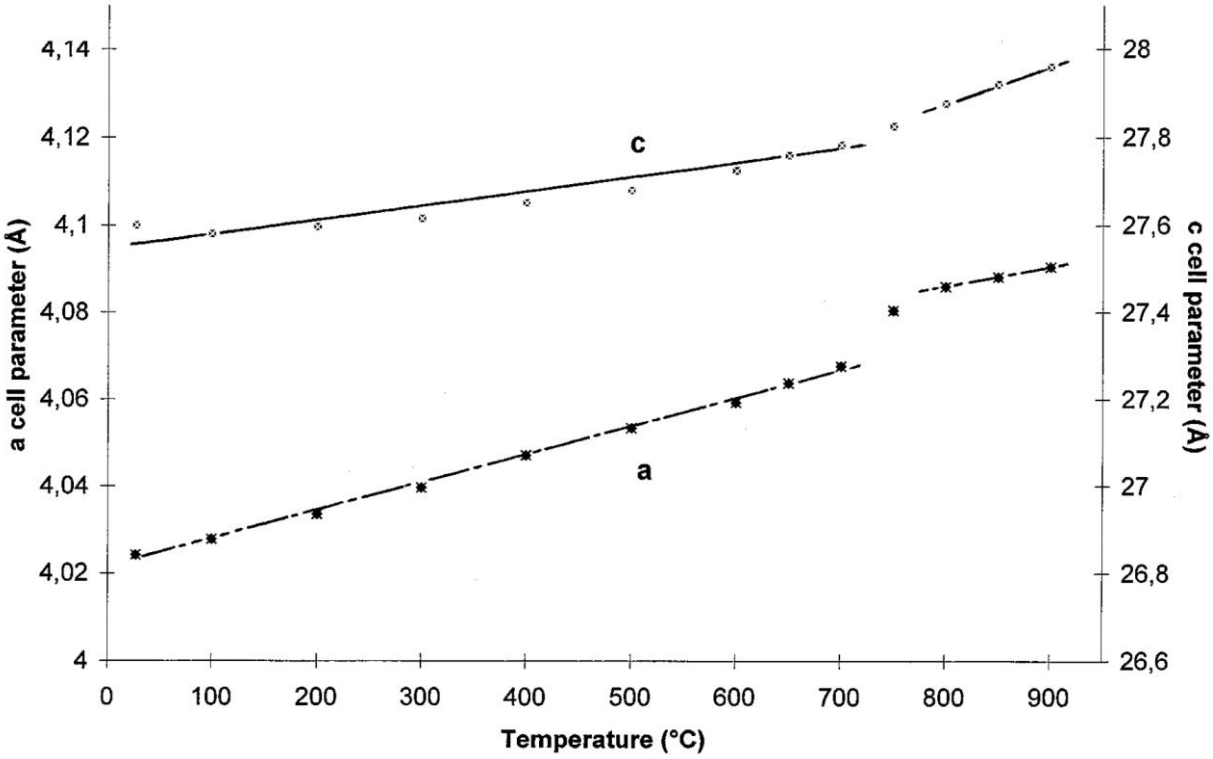


Figure 3.2: The variable temperature evolution of $Bi_{0.775}La_{0.225}O_{1.5}$ lattice parameters from 0 to 900 °C. [4]

The occupancy factors of the $O_{(2)}$ and $O_{(3)}$ ions show an interesting trend across the range of lanthanides. There is a decrease in the $O_{(2)}$ occupancy factor from La to Sm, followed by a sharp increase in the Eu $O_{(2)}$ occupancy factor. Thereafter, the $O_{(2)}$ occupancies decrease again Eu to Dy. This decreasing $O_{(2)}$ occupancy is mirrored by an increase in $O_{(3)}$ occupancy in the same two domains. Since the $O_{(2)}$ site is closer to the mixed Bi,Ln layer, the decrease in its occupancy can be

correlated to the decrease in the lanthanide ion size. The break in the linear relationship between lanthanide ion size and occupancies again support the proposed theory that different ordering exists in the bismuth-lanthanide layer for the β_2 toβ_1 phases. The final proposed rhombohedral structure after refinements is illustrated in Figure 3.3.

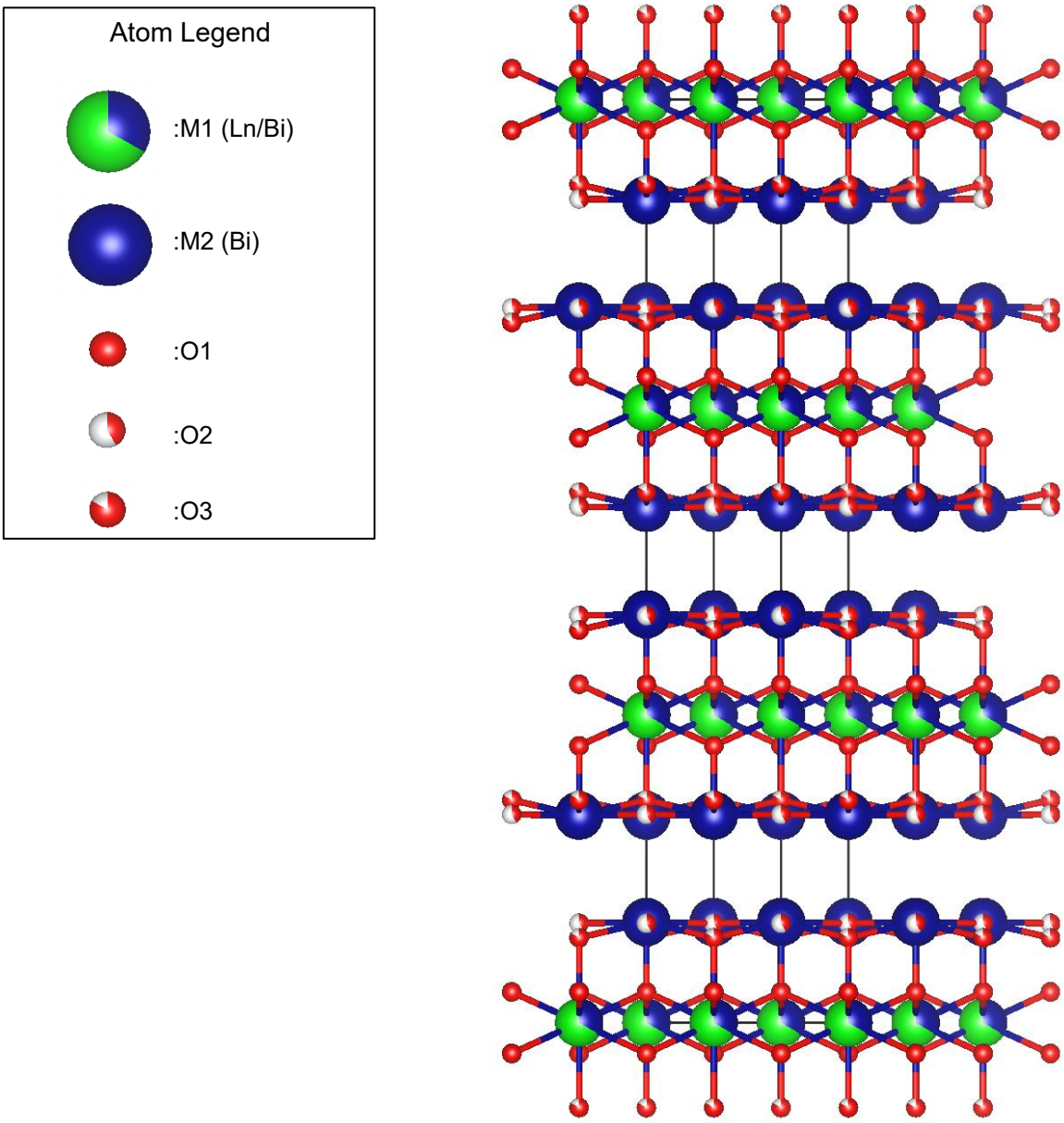


Figure 3.3: The R$\bar{3}$m rhombohedral crystal structure of $Bi_{0.775}Ln_{0.225}O_{1.5}$ materials presented in a ball and stick model, determined using powder x-ray diffraction by Drache et al. [4]

The crystal structure of bismuth lanthanide mixed oxides was investigated using powder neutron diffraction and TEM measurements by Obbade and coworkers.[7] $Bi_{0.775}Ln_{0.225}O_{1.5}$ materials where Ln = La, Pr, Nd, Sm, Tb and Dy were previously

studied in a crystal structural investigation using x-ray diffraction by Drache et al [4]. While this study provided further insight in the $R\bar{3}m$ structure, there was a major limitation concerning the analysis of oxygen sites. Due to the presence of heavy atoms in the material, such as bismuth and rare earth metals, x-ray diffraction fails in the localization of all oxygen sites. The accurate analysis of these oxygen sites are required to understand the oxide conduction mechanism in these materials.

The $Bi_{0.775}Ln_{0.225}O_{1.5}$ compounds were synthesized by the solid-state reaction of Bi_2O_3 and Ln_2O_3. Stoichiometric amounts of the oxides were heated with two 15-hour treatments at 815 °C, with grinding in between heating. Thereafter, the samples were annealed at 610 °C for 60 hours. An indication that the synthesis process was complete is the presence of the single hexagonal β_2 phase according to x-ray diffraction.

Lanthanides were selected according to scattering lengths that would not potentially hinder the neutron diffraction measurement. The coherent scattering lengths of the elements in the materials are listed in Table 3.3 below. The neutron powder patterns were refined using a range of methods such as Rietveld, FullProf and a revised Young and Wiles program. The peaks were best represented by a Gaussian function. The profile parameters and background were refined simultaneously, where the background was described by a fifth-order polynomial. The profile parameters such as the peak shapes, zero-point correction and scale factors were refined independently from the cell dimensions and crystal structure parameters. Thereafter, the refinement of the average crystal structure was performed in the centrosymmetric $R\bar{3}m$ space group. The selected starting model was from the powder x-ray crystal structure investigation of $Bi_{0.775}Ln_{0.225}O_{1.5}$ by Drache and coworkers [4]. The main results of the crystal structure refinement are described in Table 3.4. The $Bi_{0.775}Pr_{0.225}O_{1.5}$ compound was selected for the first refinement, as Bi and Pr have the largest difference between their coherent scattering lengths and thus produces the best resolution. The refinement of this crystal structure model combined with a subsequent Fourier difference analysis led to the proposal of an additional fourth oxygen site.

Table 3.3:Neutron coherent scattering lengths of selected elements [8].

Elements	**Atomic scattering lengths (fm)**
La	8.240
Pr	4.580
Nd	7.690
Tb	7.380
Bi	8.526
O	5.805

Table 3.4: Summarized information from the Rietveld refinements of $Bi_{0.775}Ln_{0.225}O_{1.5}$ materials. Displacement parameters and site occupancies are included for the representative Pr substituted material.

Atoms	Site	Atomic coordinates	B_{eq}*	Occupancy*
Bi	6c	$0,0,z$	1.59	1
Bi/Ln	3a	$0,0,0$	1.80	0.3/0.7
$O_{(1)}$	6c	$0,0,z$	2.27	1
$O_{(2)}$	6c	$0,0,z$	4.46	0.7
$O_{(3)}$	6c	$0,0,z$	4.40	0.3
$O_{(4)}$	18h	$x,2x,z$	5.37	0.07

* $Bi_{0.775}Pr_{0.225}O_{1.5}$ compound

Once refinements were all complete, a comparison between the calculated and observed patterns showed strong correlation as shown by the minimal difference curve (Figure 3.4). As expected, the average crystal structure of the $Bi_{0.775}Ln_{0.225}O_{1.5}$ system was described as a hexagonal cell in the $R\bar{3}m$ rhombohedral space group. The structure is comprised of hexagonal layers stacked along the c-axis with alternating slabs and inter-slabs (Figure 3.5). The slab appeared to be made up of three metal layers; the middle layer that is mixed with bismuth and a lanthanide, and two external bismuth only layers. The more precise determination of oxygen sites using neutron diffraction resulted in the localization of four oxygen sites. The proposed structure comprises $O_{(1)}$ and $O_{(2)}$ present in the slab near the external Bi only layers , and $O_{(3)}$ on the periphery of the cationic slab (Figure 3.5). The $O_{(4)}$ atoms occur in the inter-slab space. The atom displacement parameters showed that $O_{(2)}$, $O_{(3)}$ and $O_{(4)}$ atoms have relatively higher displacements than other atoms.

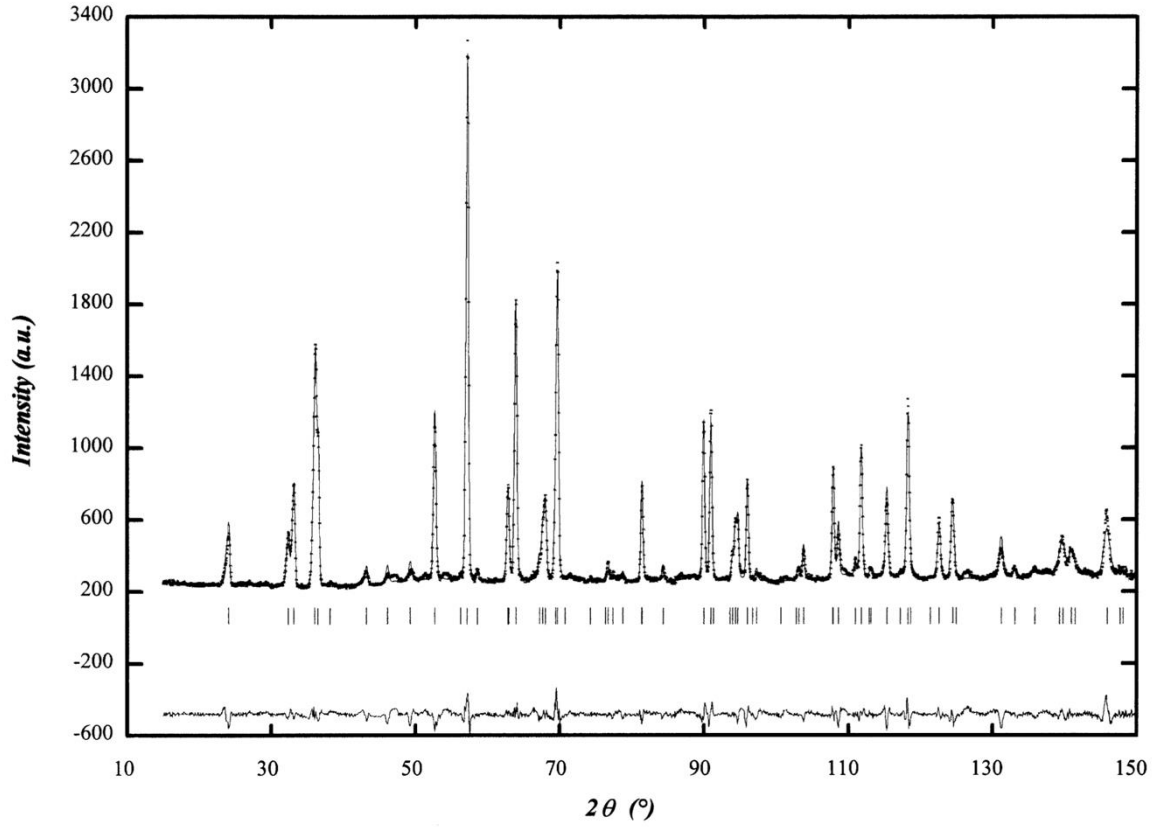


Figure 3.4: Rietveld refinement of the neutron diffraction pattern of $Bi_{0.775}Pr_{0.225}O_{1.5}$.[7]

The interatomic distances in the mixed bismuth-lanthanide layer generally increased as the lanthanide size (from terbium to lanthanum) increased, as shown by interatomic distances between metal and oxygen sites in Table 3.5. These results support the idea of a mixed bismuth-lanthanide layer in the middle of the cationic slabs. The lanthanum compound differs from the others in that it's $O_{(3)}$ atoms are located inside the metal slabs, unlike the other compounds where it is located along the periphery of the slabs.

Table 3.5:Interatomic distances between metal and oxygen in the mixed bismuth-lanthanide layer and the bismuth only layer for selected lanthanides.

	Ln			
	La (Å)	**Pr (Å)**	**Nd (Å)**	**Tb (Å)**
(Bi, Ln) – $O_{(1)}$	2.50	2.48	2.47	2.44
(Bi, Ln) – $O_{(2)}$	2.58	2.51	2.50	2.40
Bi – $O_{(1)}$	2.07	2.10	2.09	2.13
Bi – $O_{(2)}$	2.36	2.36	2.36	2.36
Bi – $O_{(3)}$	2.33	2.31	2.31	2.30
Bi – $O_{(4)}$	2.66	2.73	2.62	2.71

It was also found that the partial occupancies of the sites $O_{(2)}$, $O_{(3)}$ and $O_{(4)}$ remain constant across the range of lanthanides substituted in the mixed layer. The oxygen sites close to the bismuth environments are strongly occupied with $O_{(1)}$ and $O_{(2)}$ having occupancies of 100% and 75%, respectively. On the other hand, the oxygen sites that are on the periphery of these cationic slabs (Figure 3.5), have significantly lower occupancies of approximately 30% and 7% for $O_{(3)}$ and $O_{(4)}$, respectively. These observations suggest that the ionic conductivity within this structure is due to the motion of $O_{(3)}$ and $O_{(4)}$ between the cationic slabs.

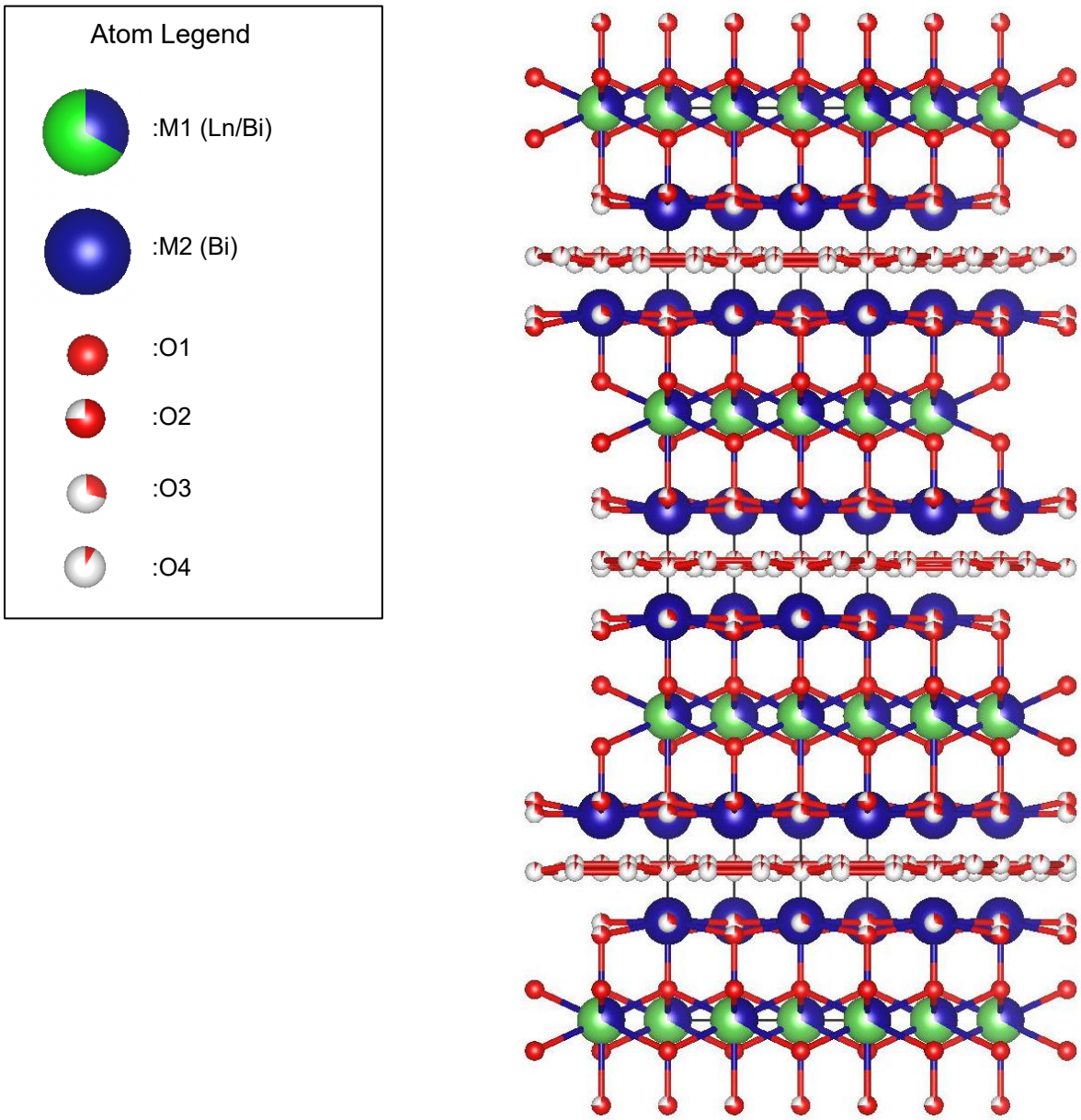


Figure 3.5: The proposed $R\bar{3}m$ rhombohedral crystal structure of $Bi_{0.775}Ln_{0.225}O_{1.5}$ materials presented in a ball and stick model determined using powder neutron diffraction by Obbade et al.[7]

Previous research has provided valuable context to guide experimental work. X-ray and neutron diffraction measurements revealed rhombohedral phase behaviour when substituting certain lanthanides in bismuth oxide at a substitution rate of 22.5%. The accuracy of the neutron diffraction technique provides confidence in the structure measured, which has thus been used as the model structure for x-ray diffraction and PDF refinements. This informed the selection of lanthanide substituents for further investigation. Based on previous studies, neutron diffraction proved more reliable due to its sensitivity to oxygen atoms and will therefore serve as the starting model for refinements.

The selection of substituents was guided by structural considerations. Literature suggests a correlation between rhombohedral phase stability and dopant size, with larger dopant ions favouring rhombohedral phase formation [2,9]. Lanthanum (La^{3+}), having an ionic radius of 1.17 Å compared to bismuth (Bi^{3+}) with an ionic radius of 1.16 Å, is expected to exhibit high rhombohedral phase stability. Lanthanum was thus chosen to provide a stable rhombohedral structure for detailed characterization, including room temperature powder X-ray diffraction and total scattering. Although gadolinium (Gd^{3+}), with an ionic radius of 1.053 Å is smaller than Bi^{3+} and typically stabilizes the fcc cubic phase, numerous studies suggest that it can also stabilize the rhombohedral phase in Bi_2O_3 systems within a specific dopant concentration range (10-30% Gd_2O_3) [9,10]. Some studies even propose that the rhombohedral phase can be the sole phase at 20% Gd_2O_3 doping [11]. The selection of Gd^{3+} allows for investigating this apparent exception to the general trend between rhombohedral phase stability and dopant size**.** Samarium (Sm^{3+}), with an intermediate ionic radius of 1.079 Å between La^{3+} and Gd^{3+}, is expected to exhibit significant rhombohedral phase stability. However, Sm^{3+} doped systems often show lower rhombohedral phase compositions than anticipated [3]. This unexpected behaviour warrants further investigation to gain a better understanding of its influence on the rhombohedral phase stability. The inclusion of Sm^{3+} will also provide valuable insights into the relationship between dopant size and rhombohedral phase stability by comparing the three dopants (La^{3+}, Gd^{3+}, and Sm^{3+}). Once examining the three dopants at a fixed composition to gain further understanding of their structural properties, suitable samples were selected to study the other key variables; substituent concentration, annealing duration and annealing temperature.

The materials characterized in this chapter were synthesized using the citrate sol-gel method [12] described in Chapter 2 (Experimental methodology). This method involves metal salts dissolved in glacial acetic acid and heated to form a thick gel. Unless otherwise stated, the sample then underwent a calcination step at 500 °C for 12 hours followed by an annealing step at 750 °C at 5 hours, with sample grinding in between heat treatments.

3.2 Results and Discussion

3.2.1 Laboratory powder X-ray Diffraction

3.2.1.4. Substituent Type

The effects of substituent type were investigated using powder XRD. Selected materials with composition $Bi_{0.75}Ln_{0.25}O_{1.5}$ were measured using laboratory XRD as well as at the synchrotron. In this composition, Ln was varied as lanthanum, samarium and gadolinium. The XRD patterns of the three materials are compared in Figure 3.6. From inspection, it is clear that the La substituted material is quite distinct from the Sm and Gd-substituted material. While the patterns largely display the same peaks, the 25 mol% La-substituted sample produced a downward shift in its pattern (to lower 2θ values). While this was expected due to lanthanum's large size, this shift is quite significant. A possible contributing factor to the downward shift may be effects of the zero-background holder. The peaks in the La substituted material are not as well resolved as the other two materials, which may indicate peak overlap of multiple phases. The La substituted material also has a noisier background signal, and so this material shows the need for high-resolution synchrotron data. The La-substituted materials seem to have minor additional peaks that are not present in the Sm and Gd-substituted material, such as peaks just before 70°. The data were thus analysed quantitatively.

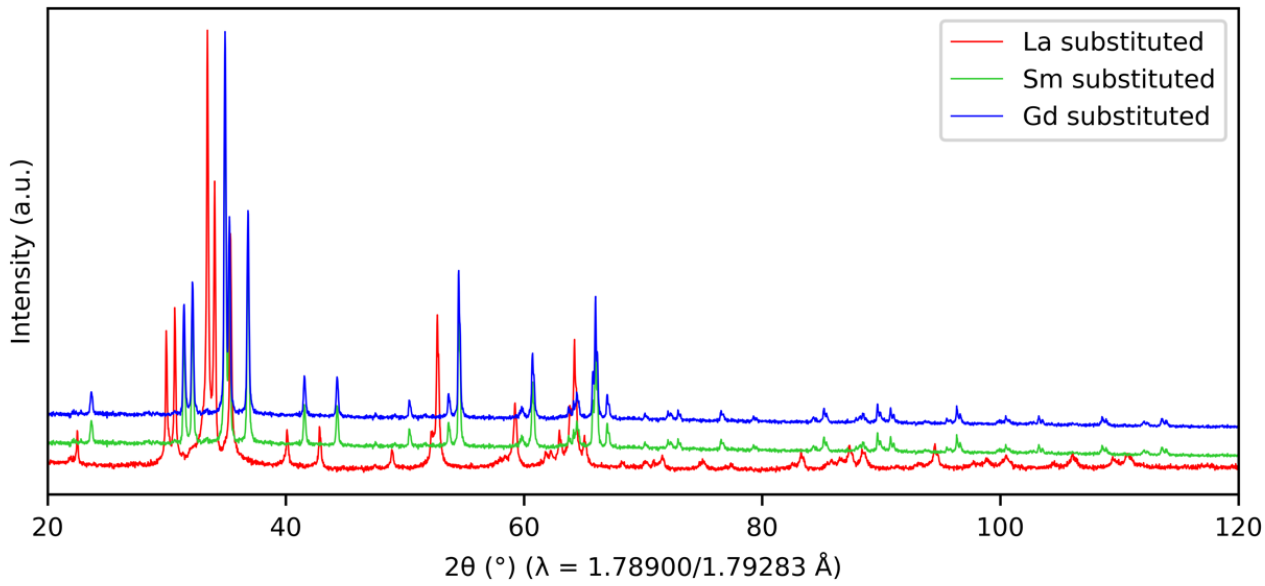


Figure 3.6: Superimposed laboratory XRD patterns for $Bi_{0.75}Ln_{0.25}O_{1.5}$ materials where Ln = La, Sm or Gd.

Rietveld refinement of the diffraction patterns was used as a tool for a detailed, quantitative analysis of the XRD results. First a calibration using a LaB_6 standard to characterize the instrument profile was done in TOPAS. A model structure ($R\bar{3}m$

phase obtained from the work of Obbade et al.[51]) was then fitted to the experimental pattern by refining certain parameters. The refined parameters included the lattice parameters, crystallite size and isotropic displacement parameters (IDPs). The metal IDPs were all constrained to refine to the same value (since the metals behave similarly with regards to their vibrations in their lattice), and the same was applied to the various oxygen sites. All other structural parameters remained fixed, such as atomic coordinates and site occupancies, where the lanthanide substituent occupancy was set according to the sample composition. In Rietveld refinement guidelines[82] it is stipulated that IDPs and occupancies cannot be refined simultaneously, and so the IDPs were selected for refinement. These guidelines also propose that that non-special positions may be refined, but attempted refining of these positions produced unreasonable values. The crystallite size was refined and, while it is common practice to refine both crystallite size and strain simultaneously, the refined strain values were not realistic and therefore not refined. The conservative approach taken to the Rietveld refinements were completed with the aim of producing reliable values that could be quantitatively examined.

Analysis of the three lanthanide-substituted bismuth oxide samples revealed distinct structural and phase behaviour. The 25 mol% La-substituted sample exhibited a rhombohedral phase with evidence of an underlying phase, indicated by unresolved peak bases in the XRD pattern (Figure 3.7). This sample also had a significantly larger unit cell volume compared to the other two samples. The Lanthanum sample, with the largest ionic radius (1.16 Å), had a unit cell volume of 447 Å³. On the other hand, gadolinium, the smallest substituent (ionic radii of 1.053 Å), had a unit cell volume of 428 Å³. These results showed a proportional trend between unit cell volume and substituent size, which was expected. In contrast to the La-sample, the 25 mol% Sm-substituted sample (ionic radii of 1.079 Å) demonstrated exceptional crystallinity with a crystallite size of 182 nm (Table 3.6), which was the highest among the three materials. This high crystallinity is evident in the sharp, well-resolved Bragg peaks that match the rhombohedral $R\bar{3}m$ phase (Figure 3.7b). Notably, the Sm-substituted sample showed a minimal intensity mismatch and no evidence of additional phases. The 25 mol% Gd-substituted sample shared many structural similarities with the Sm-substituted material (Figure 3.7c), correlating with the minor difference in their ionic radii. The Rietveld refinement of the laboratory XRD pattern for $Bi_{0.75}Gd_{0.25}O_{1.5}$ revealed the sample was mostly characterized by the rhombohedral phase (97%), but the material also contained minor traces of the $Fm\bar{3}m$ cubic phase (3%) (Figure 3.7c). The Sm size thus appears optimal for stabilizing the rhombohedral phase, as the La- and Gd-substituted samples did not display single-phase formation as observed in the Sm-substituted sample. The metal and oxygen isotropic displacement parameters (IDPs) were quite similar across all three samples, with the metal IDPs ranging between 3.86 and 4.31 $Å^2$and the oxygen IDPs falling between 5.28 and 5.60 $Å^2$.All three materials displayed a significant intensity difference,

where the observed pattern has greater intensity than the calculated pattern. This is mostly shown in the difference curve of the La-substituted sample (Figure 3.7c). Common parameters for intensity correction, such as surface roughness, absorption, multiplicity or an overspill effect, are used to compensate for lower intensities in the observed patterns, so these are thus not applicable in this case.

The only intensity correction factor that does account for increased intensities is preferred orientation which describes the tendency of crystallites to align themselves in a certain direction. However, there was no correlation between preferred orientation and equivalent lattice planes, and so preferred orientation was not considered for these samples. The layered nature of the rhombohedral structure may be a source of stacking faults in the samples. Stacking faults is a possible explanation for the heightened intensities, but this requires a thorough analysis uch as extensive calculated modelling for confirmation. Nevertheless, all materials with lanthanide substituents ranging in ionic radii from 0.01709 to 0.116 Å successfully stabilized the rhombohedral phase as the dominant phase.

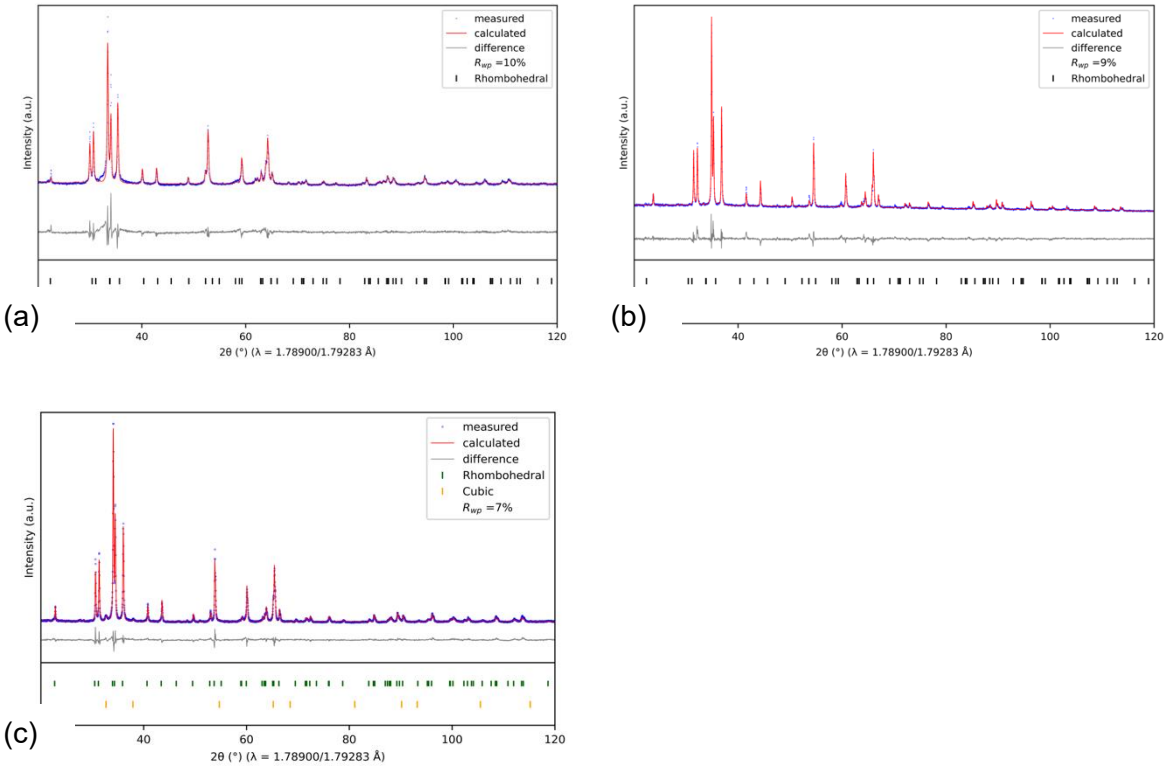


Figure 3.7: Rietveld Refinement of the laboratory XRD patterns of (a) $Bi_{0.75}La_{0.25}O_{1.5}$, (b) $Bi_{0.75}Sm_{0.25}O_{1.5}$ and (c) $Bi_{0.75}Gd_{0.25}O_{1.5}$.

Table 3.6 Parameters obtained from Rietveld refinements for the $Bi_{0.75}Ln_{0.25}O_{1.5}$ materials.

Sample	a lattice parameter (Å)	c lattice parameter (Å)	Unit cell volume ($Å^3$)	Metal IDPs ($Å^2$)	Oxygen IDPs ($Å^2$)	Crystallite size (nm)
$Bi_{0.75}La_{0.25}O_{1.5}$	4.03198(2)	27.539(4)	447	4.15	5.38	56.8(5)
$Bi_{0.75}Sm_{0.25}O_{1.5}$	3.9721(2)	27.3689(9)	432	3.86	5.60	116(2)
$Bi_{0.75}Gd_{0.25}O_{1.5}$	3.959(3)	27.285(3)	428	4.31	5.28	98.2(2)

3.2.1.2 Substituent Concentration

The results shown above by varying substituent type have indicated that the Sm-substituted material has the best rhombohedral phase formation and crystalline properties. The Sm-substituted Bi_2O_3 system was thus selected to study the effects of substituent concentration. The samarium concentration was ranged from 15 mol% to 25 mol% in bismuth oxide. The XRD patterns of the Sm-substituted system are shown alongside in Figure 3.8 for varying concentrations. From visual inspection it is clear that the 15 mol% Sm sample clearly consists of a phase mixture while the 20 mol% and 25 mol% Sm appear to mostly comprise of the rhombohedral phase. The pattern for the 15 mol% substituted material also shows a slight shift to higher 2θ values compared to the other two materials. A smaller unit cell would account for the shift in this direction, but this is not expected in the 15 mol% Sm sample. Sm^{3+} has an ionic radii of 1.079 Å and Bi^{3+}has a radii of 1.17 Å, so the sample with the lower samarium content should have a larger unit cell. The size of the shift suggests a probable influence of sample packing in the zero-background holder. All three materials were quantitatively analysed using Rietveld refinement to gain further insights.

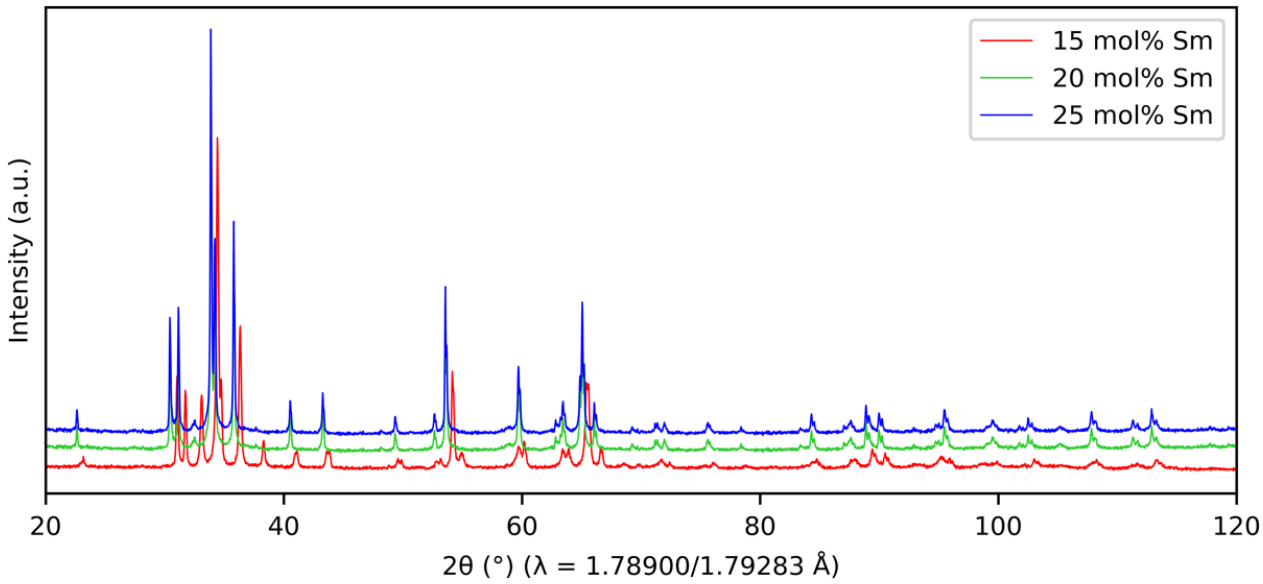


Figure 3.8: Superimposed laboratory XRD patterns of $Bi_{(1-x)}Sm_x O_{1.5}$ where x ranges from 15 to 25 mol%

Rietveld analysis of the 15 mol% Sm-substituted Bi_2O_3 sample (Figure 3.9a) revealed a phase mixture consisting of 77% rhombohedral and 23% $Fm\bar{3}m$ cubic phases as the average structure, indicating that this substitution level may be insufficient for stabilizing a single rhombohedral phase. In contrast, the 20 mol% Sm-substituted sample shows a predominantly rhombohedral phase (Figure 3.9b), with Rietveld refinement suggesting the presence of a minor cubic phase. This is supported by the observation of a broad peak base in the most intense peak of the XRD pattern, which suggests the possible presence of an underlying phase. A small peak is observed at approximately 33° just before the most intense peak. This peak grows when decreasing the Sm concentration into a cubic $Fm\bar{3}m$ peak, as seen in the $Bi_{0.85}Sm_{0.15}O_{1.5}$ material. While the refinement of the 20 mol% Sm-substituted sample could not definitively detect cubic traces at the current detection limit, the presence of a minor cubic phase in the sample seems likely. These results suggest that 20 mol% lanthanide substitution in Bi_2O_3 can lead to the formation of a predominantly rhombohedral phase, but achieving a phase-pure material might require a higher lanthanide content. The 25 mol% Sm-substituted sample formed the desired rhombohedral phase with no detectable impurity phases based on laboratory XRD measurements, as shown above (Figure 3.7b).

The refined parameters showed that the unit cell volume decreased in size with increasing Sm concentration (Table 3.7). The 15 mol% Sm-substituted sample exhibited a larger unit cell volume of 437 Å³ compared to the 20 mol% and 25 mol% samples, which have volumes of 432 Å³. Furthermore, the 15 mol% sample displayed broader and less resolved peaks in the diffraction pattern, indicative of lower crystallinity which was supported by a crystallite size of 68.9 nm compared to the other two materials. These refined values confirmed that 15 mol% Sm substitution is too low to form the pure rhombohedral phase with good crystallinity.

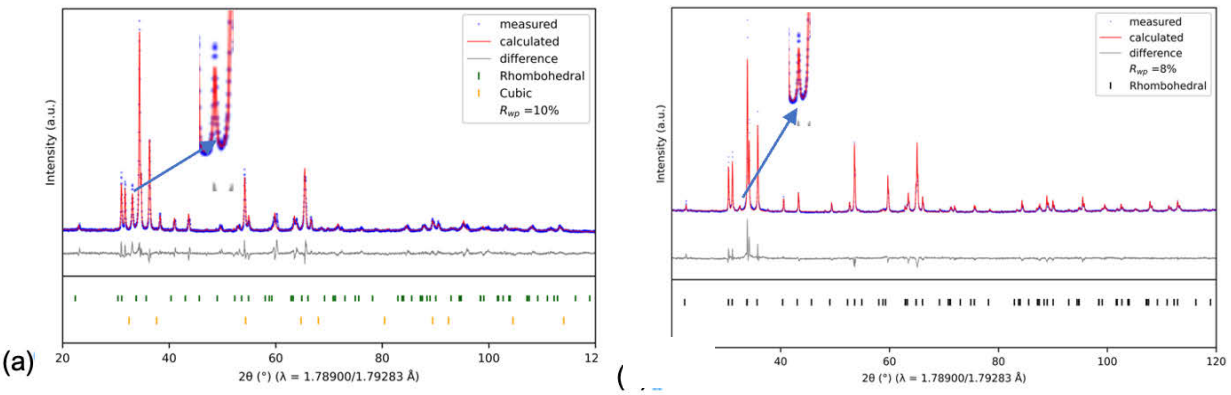


Figure 3.9: Rietveld Refinement of the laboratory XRD patterns of (a) $Bi_{0.85}Sm_{0.15}O_{1.5}$ and (b) $Bi_{0.85}Sm_{0.20}O_{1.5}$.

Table 3.7: Parameters obtained from Rietveld refinements for the $Bi_{1-x}Sm_xO_{1.5}$ materials.

Sample	a lattice parameter (Å)	c lattice parameter (Å)	Unit cell volume ($Å^3$)	Metal IDPs ($Å^2$)	Oxygen IDPs ($Å^2$)	Crystallite size (nm)
$Bi_{0.85}Sm_{0.15}O_{1.5}$	3.968(2)	27.66(2)	437	1.83	4.37	68.9(4)
$Bi_{0.80}Sm_{0.20}O_{1.5}$	3.9737(0)	27.425(8)	432	1.54	5.60	131.(3)
$Bi_{0.75}Sm_{0.25}O_{1.5}$	3.9721(2)	27.3689(9)	432	3.86	5.60	116.(2)

3.3.1.3 Annealing Duration

The 25 mol% Sm-substituted Bi_2O_3 material was selected for further investigation due to its tendency to form the rhombohedral phase and desired structural properties. The $Bi_{0.75}Sm_{0.25}O_{1.5}$ material was subjected to heating treatments of different durations to examine its effects on phase formation and crystallinity. The comparative XRD patterns for 5-, 10- and 15-hour annealing regimes at 750 °C on the $Bi_{0.75}Sm_{0.25}O_{1.5}$ material show all form a single rhombohedral phase (Figure 3.10). The 10- and 15-hour samples were highly crystalline, as indicated by their sharp Bragg peaks, while the 5-hour sample had lower intensities which is a probable result of sample packing in the zero-background holder. Besides this distinction, there appears to be no significant difference between the materials, which was confirmed by their refined lattice parameters that are almost identical (Table 3.8). It was proposed that longer annealing durations improve the crystallinity of the material, however this was not the case for the $Bi_{0.75}Sm_{0.25}O_{1.5}$ material. Rietveld refinement showed that the crystallite size decreased as annealing time was increased, which suggests that there are other factors to also consider when studying this parameter. The crystallite size decreased from 116 nm to 72.8 nm as annealing time increased from 5 hours to 15 hours. The atom displacement parameters did not show any trend with increasing annealing time and have small differences between samples. The Rietveld refinement of these materials are further examined to characterize the samples.

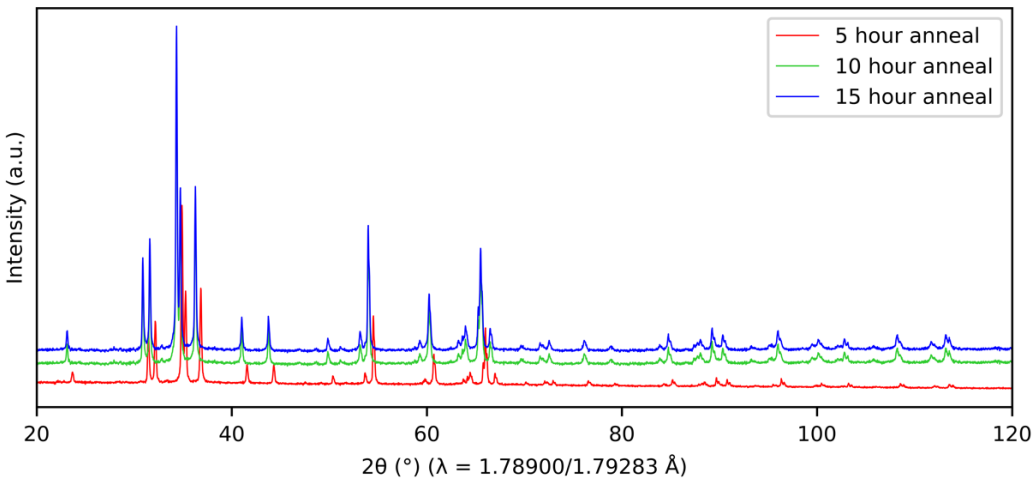


Figure 3.10: Superimposed laboratory XRD patterns of $Bi_{0.75}Sm_{0.25}O_{1.5}$ subjected to 5-, 10- and 15-hour annealing treatments.

Table 3.8: The refined lattice parameters of $Bi_{0.75}Sm_{0.25}O_{1.5}$ subjected to 5-, 10- and 15-hour annealing treatments.

Annealing time (h)	**a lattice parameter (Å)**	**c lattice parameter (Å)**	**Unit cell volume (Å³)**	**Metal IDPs (Å²)**	**Oxygen IDPs (Å²)**	**Crystallite size (nm)**
5	3.9721(2)	27.3689(9)	432	3.86	5.60	116.(2)
10	3.9737(7)	27.362(2)	432	3.64	4.38	110.(9)
15	3.976(9)	27.3669(1)	434	4.24	4.73	72.8(2)

Rietveld analysis of the 10-hour annealed sample (Figure 3.11a) revealed a strong fit to the rhombohedral R$\bar{3}$m phase with minimal intensity mismatch, supporting its rhombohedral phase formation properties. Interestingly, the 10-hour annealed sample showed high similarity to the 5-hour annealed samples, with comparable crystallite sizes of 110 nm and 166 nm and identical unit cell volumes of 432 Å³ (Table 3.8). This suggests that longer annealing times may not significantly alter the crystal structure or unit cell dimensions in this specific system.

Rietveld refinement of the 25 mol% Sm-substituted Bi_2O_3 sample annealed for 15 hours (Figure 3.11b) revealed a predominantly rhombohedral phase, with a good fit to the R$\bar{3}$m structure. However, the presence of unidentified peaks in the diffraction pattern, such as those observed near 40° and 60°, indicated the presence of impurity phases. Attempts to identify these impurities using Rietveld refinement with potential phases such as monoclinic ($P2_1/c$), cubic (Fm$\bar{3}$m), and tetragonal ($P42_1/c$) were unsuccessful. The 15-hour annealed sample also exhibited lower crystallinity compared to samples annealed for shorter durations (5 and 10 hours). The presence of impurity phases in a sample annealed for an extended period is unexpected and suggests a potential issue during sample preparation or with the furnace and heat treatment. To confirm the origin of these impurity phases, repeating the measurement would be necessary. These measurements could not be repeated during this project, which would be a suitable starting point for future work. With that being said, the experimental results propose that annealing duration may not have a significant influence on desired phase formation and crystallinity, which would reduce the long hours of uninterrupted electricity supply required for this synthetic method. Therefore, this finding could be advantageous in a country like South Africa that experiences regular power outages.

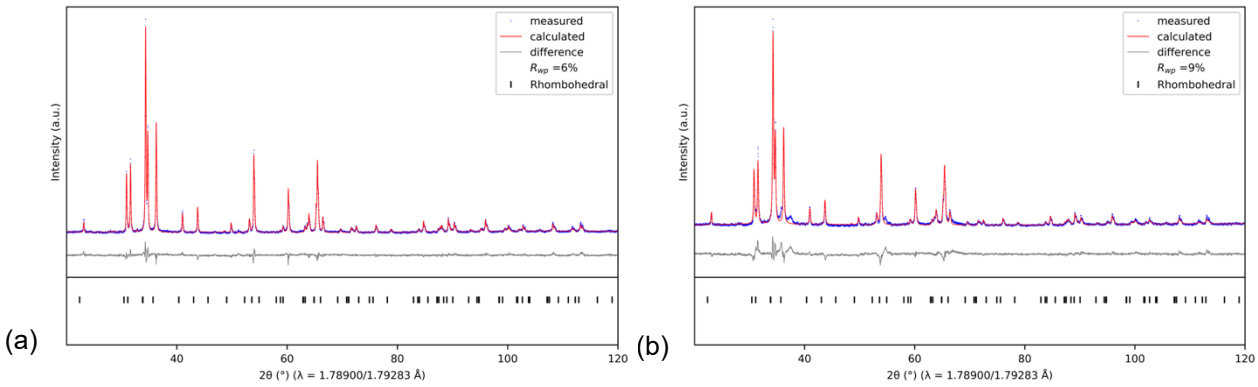


Figure 3.11: Rietveld Refinement of the laboratory XRD pattern of $Bi_{0.85}Sm_{0.25}O_{1.5}$ annealed for (a) 10 hours and (b) 15 hours

3.2.1.4 Annealing temperature

The final parameter examined using laboratory x-ray diffraction is the annealing temperature. Two different annealing temperatures were selected to assess its suitability to produce the rhombohedral phase specifically. According to various literature sources, the desired rhombohedral phase forms around 650 °C during cooling from the cubic ($Fm\bar{3}m$) phase. Therefore, temperatures were selected above and below the proposed phase transition temperature to confirm this phase behavior. The laboratory diffraction patterns of $Bi_{0.75}Sm_{0.25}O_{1.5}$ that were annealed for 5 hours at 610 °C and 750 °C are compared in Figure 3.12. The XRD pattern of the 750 °C annealed material is characterized by sharp, well-resolved peaks that were assigned to the rhombohedral phase using Rietveld analysis. On the other hand, the pattern for the 610 °C annealed material has broad, overlapping peaks and contains more peaks which indicates a phase mixture.

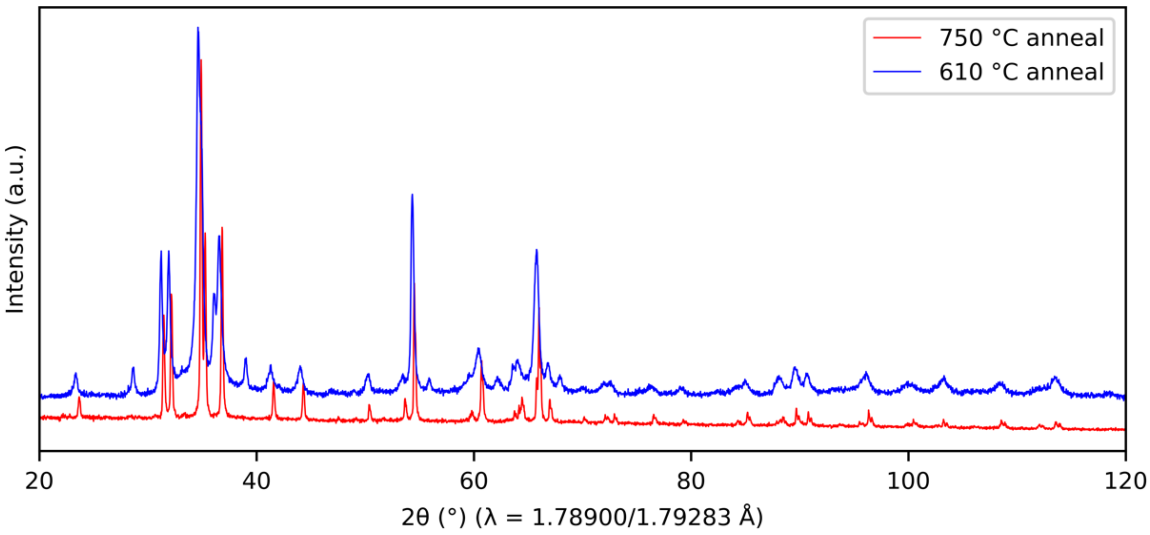


Figure 3.12: Superimposed laboratory XRD patterns of $Bi_{0.75}Sm_{0.25}O_{1.5}$ subjected to annealing at 610 °C and 750 °C

Rietveld refinement of the XRD patterns revealed that both 610°C and 750°C annealed 25 mol% Sm-substituted Bi_2O_3 samples form substituted oxides with identical unit cell dimensions of 432 Å³ (Table 3.9). However, a significant difference lies in their crystallinity. The sample annealed at 610°C exhibited low crystallinity with a crystallite size of 27.2 nm, while the sample annealed at 750°C demonstrated high crystallinity with a crystallite size of 116 nm.
This suggests that increasing the annealing temperature from 610°C to 750°C promotes the formation of larger, more crystalline domains in the 25 mol% Sm-substituted Bi_2O_3 material.

Table 3.9: The refined lattice parameters of $Bi_{0.75}Sm_{0.25}O_{1.5}$ subjected to annealing temperatures of 610 °C and 750 °C

Sample	**a lattice parameter (Å)**	**c lattice parameter (Å)**	**Unit cell volume ($Å^3$)**	**Metal IDPs ($Å^2$)**	**Oxygen IDPs ($Å^2$)**	**Crystallite size (nm)**
610 °C annealed	3.973(3)	27.428(4)	432	1.83	4.37	27.2(2)
750 °C annealed	3.9721(2)	27.3689(9)	432	3.86	5.60	116.(2)

Visual inspection of the 610 °C annealed sample alongside the 750 °C annealed sample (that is purely rhombohedral) shows that the material is mostly rhombohedral in phase composition (Figure 3.13). The refinement of the XRD data for the 610 °C annealed material confirmed the mixture of rhombohedral and cubic phases. Although a single rhombohedral phase was not obtained at this annealing temperature, it is interesting to note that the rhombohedral phase did form below 650 °C. Lower temperature formation of the desired phase contributes to its suitability as a potential solid electrolyte as lower temperatures would require less energy. The annealing treatment could be modified by annealing for longer durations to possibly remove impurity phases and improve its crystalline nature.

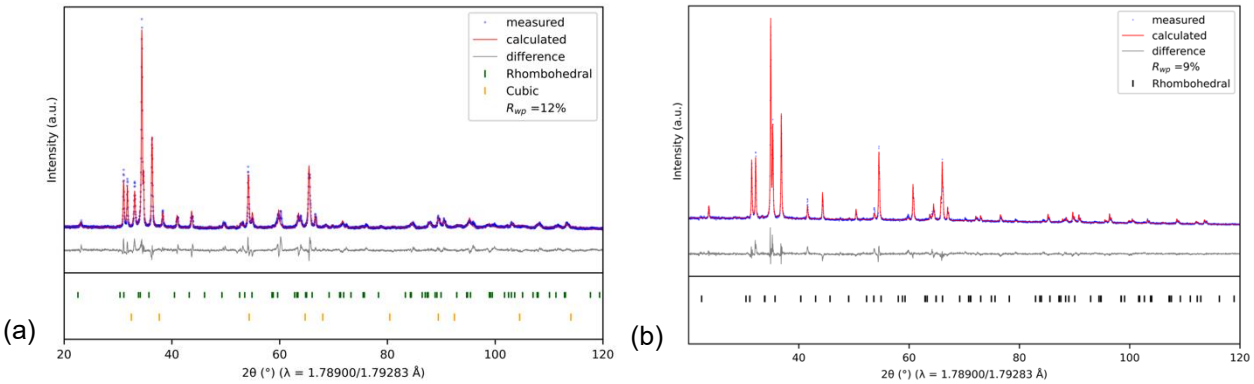


Figure 3.13: Rietveld Refinement of the laboratory XRD pattern of $Bi_{0.75}Sm_{0.25}O_{1.5}$ annealed at (a) 610 °C and (b) 750 °C

3.2.2 Synchrotron powder X-ray Diffraction

Synchrotron X-ray diffraction (at ESRF Beamline ID31) was used to measure the diffractions patterns of materials having the composition ($Bi_{0.75}Ln_{0.25}O_{1.5}$), where the lanthanide substituent (Ln) was varied as lanthanum, samarium and gadolinium.These three materials were studied in the laboratory and synchrotron X-ray diffraction sections. However, freshly prepared samples were used for the synchrotron measurements, thus it was not the exact same sample that was analysed using the two techniques.

Although their diffraction patterns (compared in Figure 3.14) are similar to each other having the same peaks with comparable peak widths, the pattern for the La-substituted material is downward shifted on the 2θ axis as compared to that for the Sm- and Gd-substituted materials. This shift is indicative of larger lattice parameters for the La-substituted material, which is expected when considering the relative lanthanide sizes that are substituted in the bismuth oxide materials. The pattern for the La-substituted sample also contains minor peaks that are not observed for the Sm- and Gd-substituted materials. Examples of these peaks can be found at approximately 1 and 10° (Figure 3.14). The Sm- and Gd-substituted materials have mostly the same XRD patterns, despite a difference in intensities. These materials were analysed further using Rietveld refinement to confirm these structural properties.

The relative lattice parameters show that the lattice expands slightly with increasing substituent size, as expected (Table 3.10). The IDPs had reasonable values, as the metal IDPs varied from 1.5 to 2 which are acceptable as metal IDPs should have values of approximately 1 (Table 3.10). The same can be said for the oxygen IDPs that are roughly 5, which is expected according to Dinnebier et al.[13] The refinements of the synchrotron XRD data are thus reliable, and all three materials are very similar.

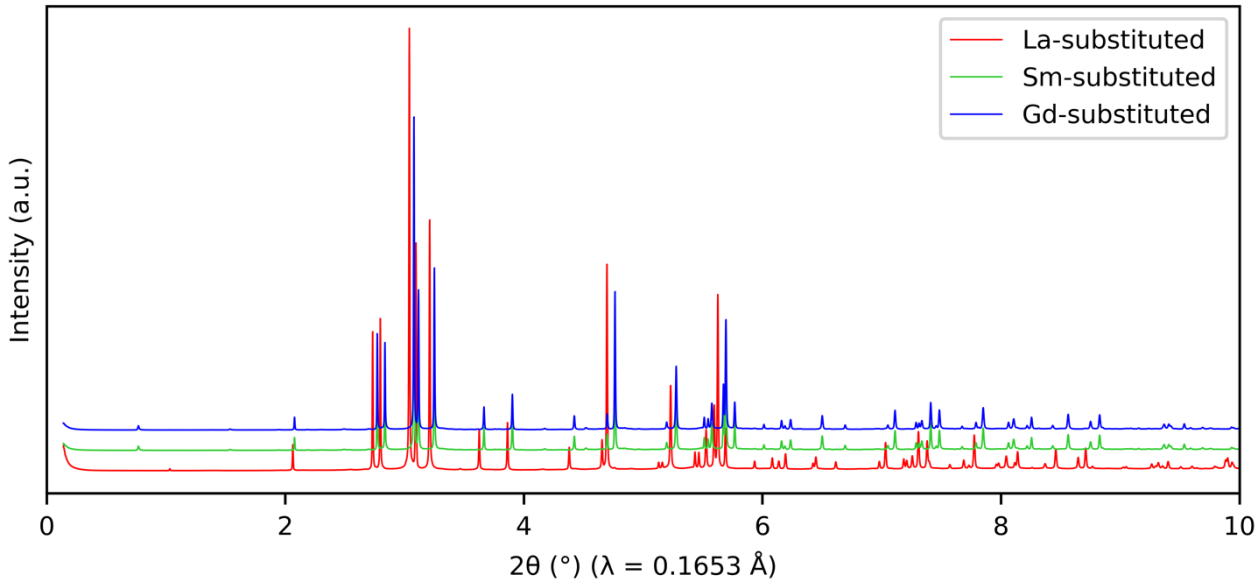


Figure 3.14: Superimposed synchrotron XRD patterns of $Bi_{0.75}Ln_{0.25}O_{1.5}$ materials where Ln = La, Sm or Gd

Table 3.10: Parameters obtained from Rietveld refinements for the $Bi_{0.75}Ln_{0.25}O_{1.5}$ materials.

Sample	a lattice parameter (Å)	c lattice parameter (Å)	Unit cell volume ($Å^3$)	Metal IDPs ($Å^2$)	Oxygen IDPs ($Å^2$)	Crystallite size (nm)
$Bi_{0.75}La_{0.25}O_{1.5}$	4.0342(5)	27.5392(5)	447	2.35	4.58	157.(1)
$Bi_{0.75}Sm_{0.25}O_{1.5}$	3.9770(0)	27.351(8)	434	1.54	5.46	182.(2)
$Bi_{0.75}Gd_{0.25}O_{1.5}$	3.965(7)	27.3136(5)	430	2.16	5.25	125.(1)

Synchrotron XRD analysis of the 25 mol% La-substituted Bi_2O_3 sample revealed a predominantly rhombohedral phase, with all Bragg peaks fitting well to the $R\bar{3}m$ structure (Figure 3.15a). However, a significant intensity mismatch is observed, resulting in a notable difference curve. Nevertheless, the phase formation aligns with literature reports on the rhombohedral phase formation in La-substituted Bi_2O_3 at this composition. However, the most intense peak just after 3° shows an unresolved peak base, which may indicate peak overlap (Figure 3.15a). Despite this, the sample displays high crystallinity, characterized by sharp Bragg peaks and a crystallite size of 157 nm, as determined by synchrotron XRD. The unresolved peak base is most prominent in the La-substituted material, suggesting the potential presence of additional phases not detected with the current instruments or sample composition. While the unit cell volumes of Sm- and Gd-substituted samples differ by only 4 Å between each other (Figure 3.14), the La-substituted sample exhibited a significantly larger unit cell volume, 17 Å greater than the Gd-substituted sample.

Rietveld analysis of the 25 mol% Sm-substituted Bi_2O_3 sample measured at a synchrotron revealed a well-defined rhombohedral phase with no evidence of additional phases (Figure 3.15b). The sample displayed the highest crystallinity among the three materials studied, with a crystallite size of 182 nm. This high crystallinity is reflected in the sharp, well-resolved Bragg peaks at the detection level of synchrotron radiation. The sample shows a significant intensity mismatch, as seen in all materials discussed above. The 25 mol% Sm-substituted material displays many structural similarities with the 25 mol% Gd-substituted material, with a minor difference in their ionic radii (0.026 Å).

The Rietveld refinement for the $Bi_{0.75}Gd_{0.25}O_{1.5}$ sample showed that most of the Bragg peaks in the diffraction pattern are owed to the $R\bar{3}m$ rhombohedral phase (Figure 3.15c). No other peaks were detected in the material, even at the low detection limit of the synchrotron. However, there was a significant intensity mismatch between the observed and calculated patterns, where the observed pattern had greater intensities than the structure model. With that being said, the average structure of the 25 mol% Gd material can be confidently described as purely rhombohedral. This was not expected as the laboratory diffraction data of the same material appeared to form a phase mixture of rhombohedral and cubic on an average length scale. The laboratory XRD pattern was measured within a day after

completed synthesis, while the synchrotron XRD pattern was measured weeks after the materials were prepared. This may suggest that the minimal cubic phase (3%) present converted to the more stable rhombohedral phase over time. Since the resolution of synchrotron x-ray diffraction is higher than that for lab instruments, it is certain that some phase conversion must have occurred, indicating that the cubic phase is only metastable at room temperature.

Despite this discrepancy in the $Bi_{0.75}Gd_{0.25}O_{1.5}$ material, there is a significant similarity between the synchrotron and laboratory XRD data for all three samples, as indicated by the refined lattice parameters. This provides confidence in the subsequent refinements of laboratory XRD data.

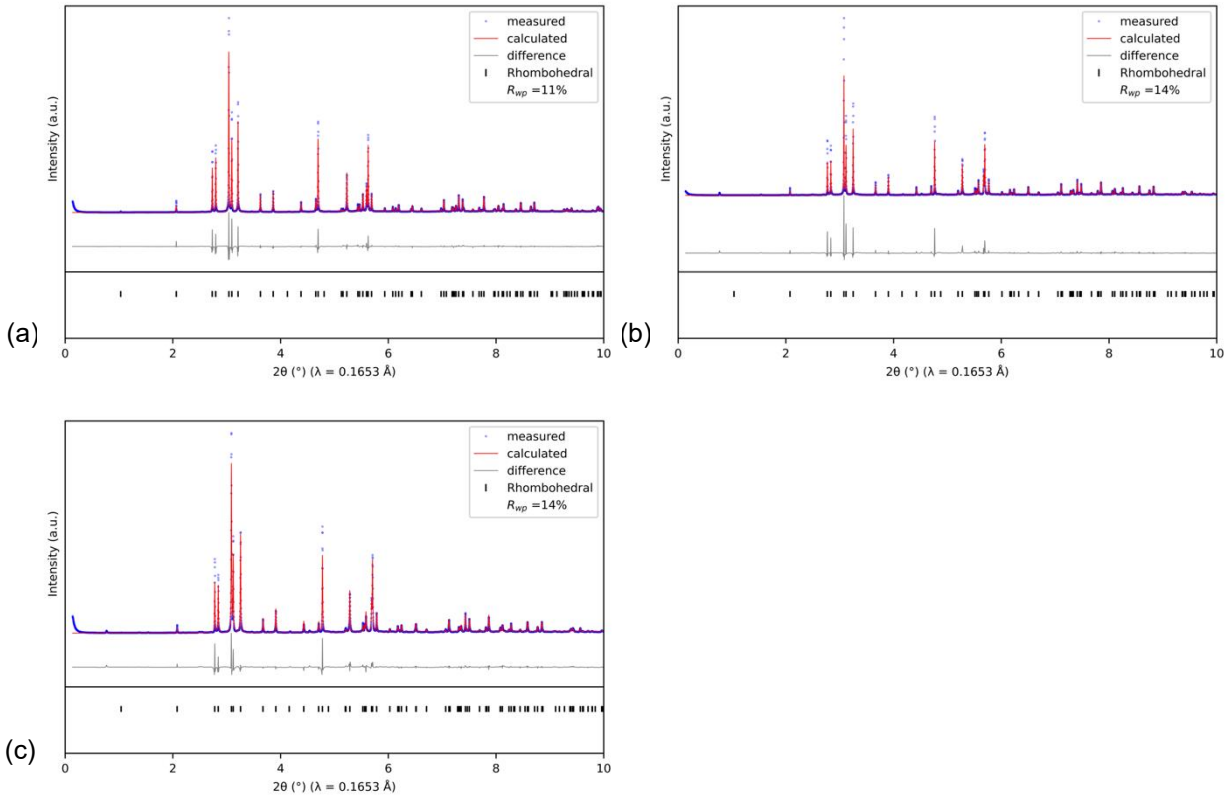


Figure 3.15: Rietveld Refinement of the synchrotron XRD patterns of (a) $Bi_{0.75}La_{0.25}O_{1.5}$, (b) $Bi_{0.75}Sm_{0.25}O_{1.5}$ and (c) $Bi_{0.75}Gd_{0.25}O_{1.5}$.

3.2.3 Pair Distribution Function (PDF)

Selected samples underwent total scattering measurements and synchrotron XRD measurements at the ESRF. Materials with composition $Bi_{0.75}Ln_{0.25}O_{1.5}$ were subjected to PDF measurements, where Ln was varied as lanthanum, samarium and gadolinium. Laboratory and synchrotron XRD measurements shared many

similarities, as all measurements revealed the rhombohedral phase as the dominant phase on an average scale. Certain samples did show distinct differences, such as the $Bi_{0.75}Gd_{0.25}O_{1.5}$ measured by laboratory XRD that contained a phase of mixture of rhombohedral and cubic. However, this sample's composition was quantified as 97% rhombohedral phase, showing that all the materials of interest predominantly formed the rhombohedral phase. The PDFs of the 25 mol% substituted materials are compared in Figure 3.16 to examine their local structure. A qualitative inspection shows similarity between the three functions, with mostly similar peak positions and peak intensities. Notably, an upward shift is observed in the La-substituted material at high.r values, and less so in the Sm-substituted sample. Nevertheless, the similar PDFs suggest that all 25 mol% substituted materials have comparable atom-atom pairs in the same unit cell for both the local and average structure. The proposed structure is the $R\bar{3}m$ rhombohedral phase, as the phase accurately describes the materials average structure. The rhombohedral unit cell is comprised of atoms on its corners, so the unit cell lengths should be the simplest interatomic distances to identify in a PDF. The a and c lattice parameters in 25 mol% lanthanide substituted bismuthate are approximately 4 and 27 Å, respectively. Inspection of the PDFs reveal an intense peak at approximately 4 Å (Figure 3.16), which would correspond to metal – metal distances between corners in the rhombohedral unit cell. The high intensity of this peak supports the possibility of its origin as metal – metal distances, as the high scattering of the bismuth metal would explain the significant peak intensity. Less intense peaks occur for metal – oxygen distances, as oxygen has relatively low scattering lengths compared to bismuth and the lanthanides. There is also a peak around 27 Å (Figure 3.16), which could account for the metal – metal distance along the c-axis of the rhombohedral cell. The experimental PDF of $Bi_{0.75}Sm_{0.25}O_{1.5}$ has been compared to partial PDFs to confidently associate atom pairs with peaks in the function.

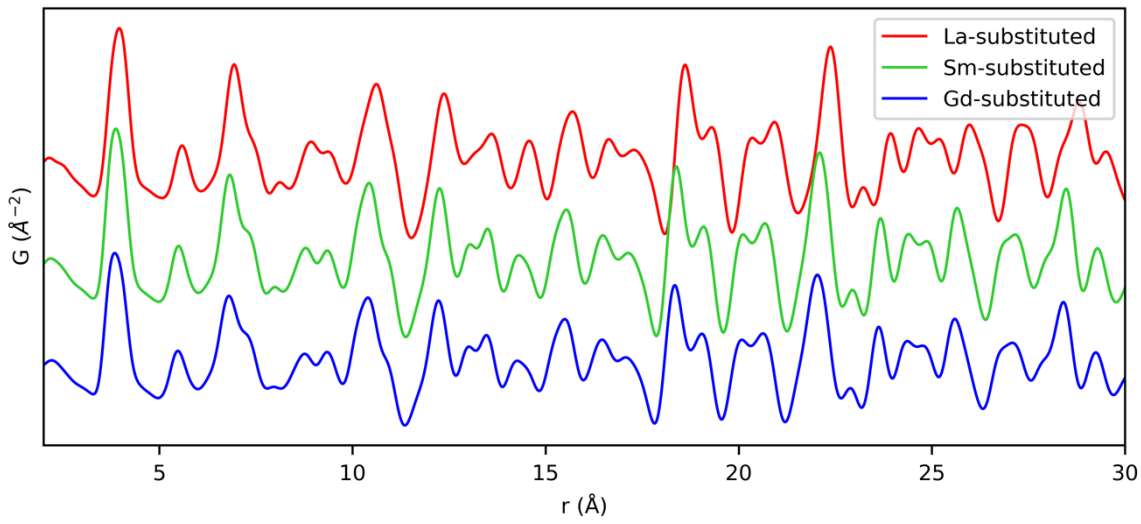


Figure 3.16: Superimposed PDFs of $Bi_{0.75}Ln_{0.25}O_{1.5}$ materials where Ln = La, Sm and Gd

The experimental PDF of $Bi_{0.75}Sm_{0.25}O_{1.5}$ was compared to the calculated partial PDFs of the R$\bar{3}$m rhombohedral structure (Figure 3.17). The calculated structure was obtained from the powder neutron diffraction study by Obbade et al. [7]. The experimental PDF is compared to the calculated partials in the low-r range from 1 to 10 Å to confidently associate atom pairs with peaks in the function (Figure 3.17). The metals in the structure were generalized to the dominant metal, bismuth. The intense peak around 4 Å is clearly owed to Bi – Bi atom pairs. The most intense peaks in the low-r range are all owed to the Bi – Bi pairs as indicated by the partial functions. The peak around 2.4 Å represents Bi – O atom pairs, and it can be seen that all Bi – O distances produce low intensity peaks. The O – O atom pairs may also contribute to the peaks that have been associated to other atom pairs, but the low scattering power of oxygen makes this correlation difficult to confirm. Nonetheless, the partial functions of the rhombohedral pattern suggest the local structure of 25 mol% substituted materials is rhombohedral.

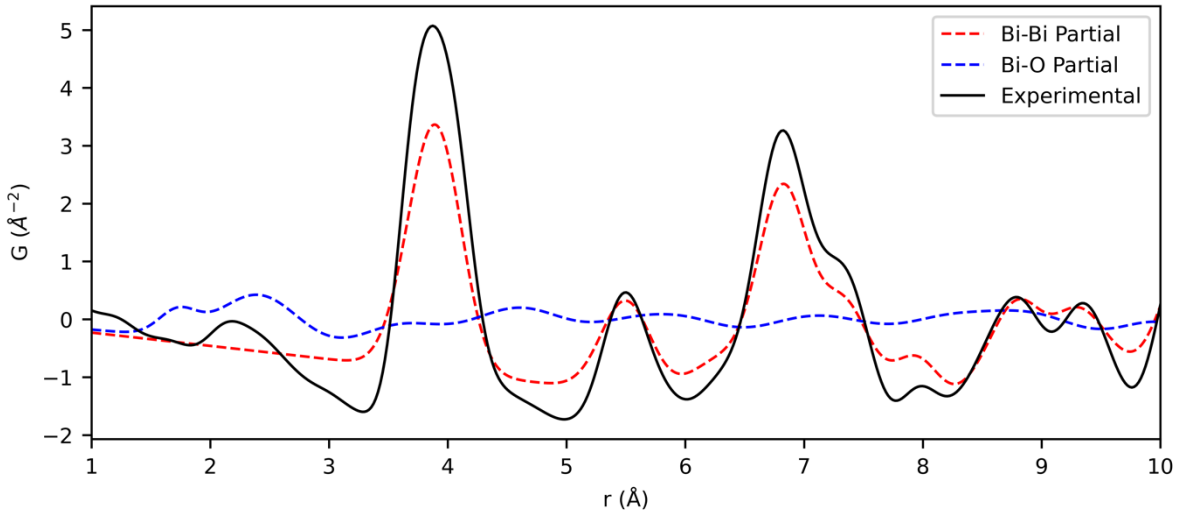


Figure 3.17: Experimental PDF of $Bi_{0.75}Sm_{0.25}O_{1.5}$ superimposed on the calculated partial PDF functions of the R$\bar{3}$m rhombohedral structure.

Since all three 25 mol% substituted materials have very similar PDFs, the refinement of one representative sample has been included for discussion. The refinement was preceded by a calibration of silicon and LaB_6 reference standards using PDFGui. The refinement of the standards verified the real-space data quality and provided instrumental parameters that are required for experimental data refinements. These instrumental parameters include Q_{damp} and Q_{broad} effects. The Q_{damp} parameter is introduced in modeling to account for the exponential dampening of the PDF peaks, which is a result of limited Q-resolution. The Q_{broad} parameter accounts for peak broadening at high Q, because of increased intensity noise. These parameters are refined during the standard calibration and used in the experimental refinements. The Q_{max} value is an experimental parameter that is determined during the Fourier

transformation of the PDF data. The finite data range used in the Fourier transform may introduce termination ripples in the PDF. In this experiment, the Q_{max} was determined as 22 $Å^2$ which accounts for the ripples in the function. The parameters that were refined during the calculation include the lattice parameters, scale factor, delta2 and anisotropic thermal displacement (ATP) factors. The delta2 parameter is a coefficient for the $1/r^2$ contribution to peak sharpening in the function. The delta2/r^2 factor describes the low temperature behavior, while the delta1/r factor defines the high temperature component. These two parameters are strongly related so only one factor needs to be refined.

The refined PDF of $Bi_{0.75}Sm_{0.25}O_{1.5}$ is shown in Figure 3.18 against the $R\bar{3}m$ rhombohedral pattern. In good agreement between the observed and calculated PDF is observed, providing a R_w value of 17%. In PDF refinements, an indicator of a strong fit is a R_w value of 10%. In Figure 3.18 there are minor peaks in the observed PDF, at 12 and 16 Å for example, where the intensities were not well-matched by the rhombohedral pattern used. This could suggest a very minor impurity phase, such as the $Fm\bar{3}m$ cubic phase noted in some XRD patterns, is present on the local scale. It could also simply be some disorder in the structure that will only be picked up at a local level. Irrespective of the cause, it can be confidently proposed that the 25 mol% samarium substituted material predominantly formed the rhombohedral phase on a local scale.

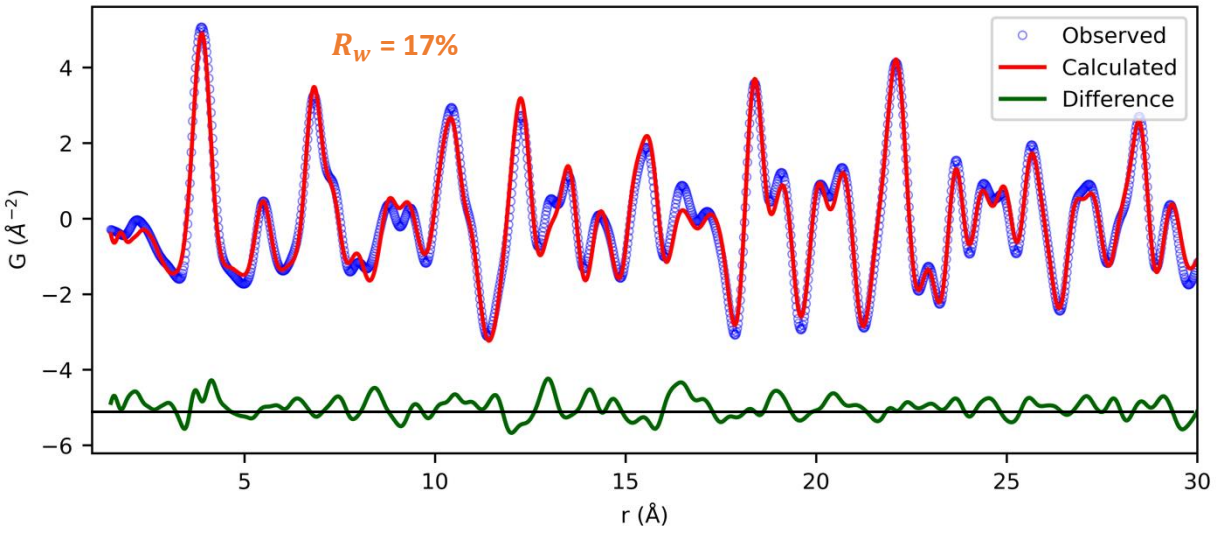


Figure 3.18: Refinement of the PDF data for $Bi_{0.75}Sm_{0.25}O_{1.5}$.

3.3 Conclusion

In summary, this study has comprehensively investigated the structural properties of $Bi_{0.75}Ln_{0.25}O_{1.5}$ materials with varying lanthanide (Ln) substitutions (La, Sm, Gd) using a combination of experimental techniques, including X-ray diffraction (XRD) and pair distribution function (PDF) analysis. The results have demonstrated that while all materials predominantly adopt the desired rhombohedral phase, subtle variations in structural parameters and the presence of minor impurity phases are observed depending on the nature and concentration of the lanthanide substituent. This study provides valuable insights into the structure-property relationships of these materials, which are crucial for understanding their functional properties and guiding future materials design efforts.

The influence of lanthanide (Ln) substitution on the structural properties of $Bi_{0.75}Ln_{0.25}O_{1.5}$ materials was investigated using laboratory and synchrotron X-ray diffraction (XRD) and pair distribution function (PDF) analysis. Lanthanum, samarium, and gadolinium were selected as substituents to examine their effects on phase formation and structural parameters. Laboratory XRD analysis revealed that all materials predominantly crystallized in the rhombohedral phase, with minor variations observed between compositions. Interestingly, laboratory XRD measurements of the gadolinium-substituted sample indicated the presence of an impurity phase corresponding to the Fm3m cubic structure. This observation contradicted the synchrotron XRD data for the same material, which showed a single rhombohedral phase. Given the lower detection limits of synchrotron XRD, the presence of an additional phase would have been detectable if it existed. Considering that the laboratory XRD data was collected shortly after synthesis and the synchrotron XRD data was measured several weeks later, it is hypothesized that the cubic phase may have transformed into the more stable rhombohedral phase over time. The lanthanum-substituted sample exhibited poorly resolved peaks and significant peak overlap in the laboratory XRD pattern, suggesting the potential presence of multiple phases. While the high-resolution synchrotron XRD data did not reveal any additional peaks, the broad peak bases still hints at the possibility of underlying impurity phases in this material. In contrast, the samarium-substituted material demonstrated the best fit to the calculated rhombohedral pattern in both laboratory and synchrotron XRD. Additionally, the samarium-substituted sample exhibited high crystallinity compared to the other two materials. Based on these findings, the samarium-substituted sample was selected for further in-depth investigation.

The influence of samarium substituent concentration on the phase formation in Bi_2O_3 was investigated within the range of 15 mol% to 25 mol% using laboratory X-ray diffraction (XRD). XRD analysis revealed that a 15 mol% Sm substitution was insufficient to form the single rhombohedral phase. The 15 mol% Sm sample produced a predominantly rhombohedral phase (77%), with a minor cubic phase

(23%) alsopresent. On the other hand, samarium substitution levels between 20 mol% and 25 mol% appeared to successfully format the single rhombohedral phase.

To optimize the synthetic route towards the desired phase, the annealing treatment of the samples was investigated using laboratory X-ray diffraction (XRD). Initially, the annealing duration was varied between 5, 10, and 15 hours. While longer annealing times are typically expected to improve crystallinity and remove impurity phases, XRD analysis revealed a contrary trend where crystallinity decreased with increasing annealing duration. This unexpected observation suggests the presence of other factors influencing the impact of annealing time. Subsequently, the annealing temperature was varied to examine its effect on phase formation. Two annealing temperatures were selected: 610 °C and 750 °C. Both temperatures resulted in the formation of the desired rhombohedral phase, however, only the samples annealed at 750 °C were free of impurity phases. Furthermore, the 750 °C annealed material exhibited sharp, well-defined peaks in its diffraction pattern, indicative of high crystallinity. In contrast, the 610 °C annealed samples displayed broad peaks and additional peaks characteristic of the cubic phase. These results suggest that heating at the lower annealing temperature (610 °C) would require significantly longer annealing durations to achieve comparable levels of crystallinity and eliminate the cubic phase.

To determine the local atomic structure of selected materials, pair distribution function (PDF) analysis was conducted on materials with the composition $\mathrm{Bi_{0.75}Ln_{0.25}O_{1.5}}$. In this compound, Ln represents lanthanum, samarium, or gadolinium. The PDFs of the 25 mol% lanthanide-substituted materials revealed comparable peak profiles, with the most notable difference being an upward shift in peak positions for the La-substituted sample, and to a lesser extent, for the Sm-substituted sample. Given that the average structure of these materials was determined to be rhombohedral using X-ray diffraction, a rhombohedral model structure was used for PDF refinement. The experimental PDF of the samarium-substituted material showed strong agreement with the rhombohedral model structure, as confirmed by the figures of merit. However, minor discrepancies were observed, suggesting the presence of an impurity phase or localized regions with oxide formation. Despite these minor deviations, it is evident that the 25 mol% lanthanide-substituted materials predominantly adopt the desired rhombohedral phase on both local and average length scales.

3.4 References

1. Ahi, A., Mellergård, A. & Eriksson, S.-G. Local and average atomic order of ion-conducting Bi0.775La0.225O1.5 studied by neutron scattering and reverse Monte Carlo simulations. Solid State Ionics **177**, 289–297 (2006).
2. Drache, M., Roussel, P. & Wignacourt, J.-P. Structures and Oxide Mobility in Bi−Ln−O Materials: Heritage of Bi $_2$ O $_3$. Chem. Rev. **107**, 80–96 (2007).
3. Jolley, A. G., Jayathilake, R. & Wachsman, E. D. Optimizing rhombohedral Bi2O3 conductivity for low temperature SOFC electrolytes. Ionics **25**, 3531–3536 (2019).
4. Drache, M., Obbade, S., Wignacourt, J. P. & Conflant, P. Structural and Conductivity Properties of Bi0.775Ln0.225O1.5Oxide Conductors (Ln=La, Pr, Nd, Sm, Eu, Gd, Tb, Dy) with Rhombohedral Bi–Sr–O Type. Journal of Solid State Chemistry **142**, 349–359 (1999).
5. Richter, W. & Becker, C. R. A Raman and far-infrared investigation of phonons in the rhombohedral V2–VI3 compounds Bi2Te3, Bi2Se3, Sb2Te3 and Bi2(Te1−xSex)3 (0 <x < 1), (Bi1−ySby)2Te3 (0 <y < 1). Phys. Stat. Sol. (b) **84**, 619–628 (1977).
6. Sammes, N. M. & Tompsett, G. A. Bismuth Based Oxide ElectrolytesÐ Structure and Ionic Conductivity.
7. Obbade, S. Powder Neutron Diffraction and TEM Investigations of Bi0.775Ln0.225O1.5 Oxide Conductors (Ln=La, Pr, Nd, Sm, Tb, Dy) with Rhombohedral Bi–Sr–O type: Structural Relationships with Monoclinic ε-Bi4.86La1.14O9 Form. Journal of Solid State Chemistry **168**, 91–99 (2002).
8. Sears, V. F. Neutron scattering lengths and cross sections. Neutron News **3**, 26–37 (1992).
9. Iwahara, H., Esaka, T. & Sat, T. Formation of High Oxide Ion Conductive Phases in the Sintered Oxides of the System B&O3 -Ln,O, (Ln = La -Yb).
10. Datta, R. K. & Meehan, J. P. The System Bi2O3–R2O3 (R=Y, Gd). Zeitschrift für anorganische und allgemeine Chemie **383**, 328–337 (1971).
11. Takahashi, T., Esaka, T. & Iwahara, H. High oxide ion conduction in the sintered oxides of the system Bi2 Gd20 3.
12. Dislich, H. Sol-gel: Science, processes and products. Journal of Non-Crystalline Solids **80**, 115–121 (1986).
13. Dinnebier, R. & Scardi, P. X-ray powder diffraction in education. Part I. Bragg peak profiles. J Appl Crystallogr **54**, 1811–1831 (2021).

Chapter 4 – The local structure of rhombohedral substituted bismuth oxide using Raman Scattering

Raman spectroscopy provides valuable insights into the local structure of solid solutions, such as lanthanide-substituted bismuth oxide, by probing the vibrational modes of the material.[1] This technique is highly sensitive to changes in bond lengths, bond angles, and local environments of atoms within the crystal lattice.[1,2] While X-ray diffraction (XRD) provides average crystallographic information, Raman spectroscopy offers a complementary perspective by revealing subtle structural distortions and local disorder that may not be readily apparent from diffraction data.[3] By combining Raman spectroscopy with XRD, researchers can gain a more comprehensive understanding of the structural intricacies within these complex materials, including the effects of lanthanide substitution on the local atomic arrangements and the resulting impact on their functional properties.

4.1 Literature Review

This review explores the various methods available for interpreting Raman data. Furthermore, it investigates Raman spectroscopy studies based on materials related to the rhombohedral phase of bismuth oxide. This provides essential background information for the results section, where the Raman scattering of rhombohedral $R\bar{3}m$ substituted bismuth oxide will be interpreted.

4.1.1 Group Theory and Selection rules

Richter et al.[4] studied solid solutions with $R\bar{3}m$ symmetry using Raman and infrared active modes to assess the accuracy of a lattice dynamical model. The materials studied were Bi_2Se_3, Bi_2Te_3, Sb_2Te_3, prepared using the solid-state reaction to form solid solutions. These materials have gained interest due to their thermoelectric and topological insulator properties. The Raman activity of these materials was assigned using Group Theory and is the focus of this review.

These crystalline materials belonging to the $R\bar{3}m$ space group, have an atomic arrangement described by hexagonal close-packed layers along the c-axis. Atoms are arranged according to their group number, in the pattern described below:

$$A_{VI}^{(1)} – B_V – A_{VI}^{(2)} – B_V - A_{VI}^{(1)}$$

In this pattern, A and B represent different atoms, and the subscripts VI and V refer to the group in the periodic table in which the atom is found. This notation is shown in relation to the materials being studied in Table 4.1. The superscripts 1 and 2 correspond to the position of the atom within the five-atom layer, where 1 represents atoms on the external parts of the layer and 2 indicates the middle atom.

Table 4.1:Key to the representative pattern arrangement for the materials studied by Richter et al. [4]

	Bi_2Se_3	**Bi_2Te_3**	**Sb_2Te_3**
A_{VI}	Se	Te	Te
B_V	Bi	Bi	Sb

The Raman spectra of Bi_2Se_3, Bi_2Te_3 and Sb_2Te_3 were examined according to the point group (D^5_{3d}) deduced from its space group ($R\bar{3}m$). According to the point group, the twelve optical modes are classified into $2A_{1g}$, $2E_g$, $2A_{1u}$ and $2E_u$ modes. As the rhombohedral structure has a center of inversion, these modes are exclusively either Raman or IR active according to selection rules. A_{1g} and E_g are Raman-active modes, due to their change in polarizability, and their frequencies were determined using a lattice dynamical model shown in Figure 4.1.

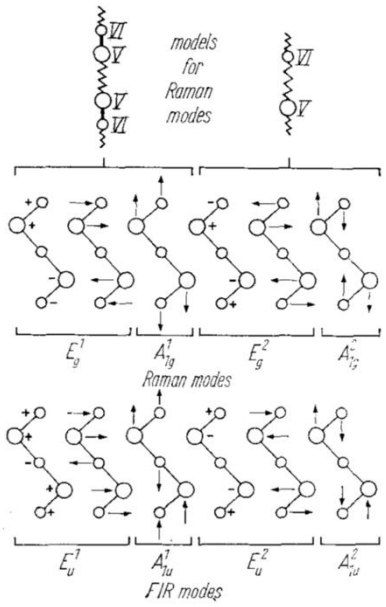


Figure 4.1: Linear chain model illustrating the Raman and FTIR modes.[4]

The Raman spectrum, measured under polarizing conditions, for the binary compound Bi_2Se_3 is shown in Figure 4.2. The upper curve is the xx component of the Raman tensor, and the lower curve is the xy component. The upper curve has three peaks, while the lower curve only has one. Using the polarization conditions showed that the peak present in both components is an E_g mode, while the other two peaks in the upper curve are consequently assigned as A_{1g} modes. Group theory predicts $2A_{1g}$ and $2E_g$ modes, so one of the E_g modes is missing from the spectrum. This observation is also present in the Raman spectra of the mixed Bi-Sb-Te and Bi-

Te-Se systems, which suggests that this scattering behaviour is inherent with related materials of the same space group.

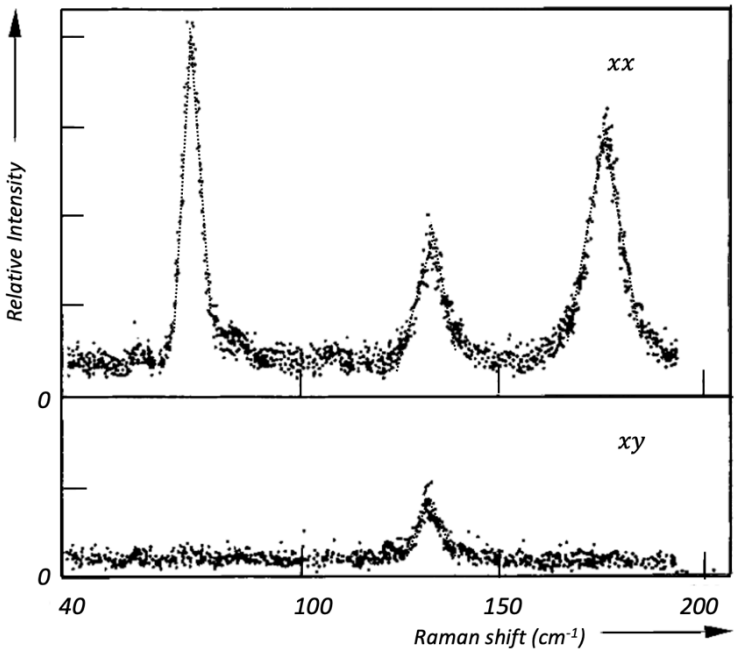


Figure 4.2: Raman spectrum, measured under polarizing conditions, of pure Bi_2Se_3. The upper trace is the xx Raman tensor component and the lower trace is the xy Raman tensor component. [4]

While the study by Richter et al.[4] focuses on the space group of interest in this project, the unit cells between the two structures vary significantly. Firstly, the unit cell of this paper has five atoms, while the structure of interest in this project has nine. Additionally, this study in the paper has a five-atom layer in the unit cell, and this project the structure has three-metal layers with anions occupying interstitial sites. A comparison of atomic sites could not be directly conducted as the paper does not provide information on the atom positions.

Nevertheless, the study by Richter et al.[4] has contributed valuable insights into the Raman scattering of the $R\bar{3}m$ structure. It showed that Group Theory is a reliable method to assign the Raman-active bands their respective Mulliken symbols in the D^5_{3d} point group. This work also compared the observed phonon frequencies in Raman spectra to calculated values obtained from a lattice dynamical model. This provides valuable guidance when examining Raman scattering data in this project.

4.1.2 Empirical relation – Raman stretching frequencies and bond lengths

A method was developed by Hardcastle and Wachs[5] that determined Raman stretching frequencies using bond lengths. An empirical relation between bismuth – oxide (Bi – O) bond lengths, bond strengths and Raman stretching frequencies were developed to characterize Raman spectra.

Firstly, the empirical relations between the metal – oxygen bond lengths and Raman stretching frequencies were found for several transition metal oxide systems such as vanadium, molybdenum, and tungsten-oxygen bonds. The exponential relation is expressed by Equation 4.1, where υ is the Raman stretching frequency (cm^{-1}), *A* and *B* are fitting parameters and *R* are metal – oxygen bond lengths (Å). It was found that this equation could also fit the relation for bismuth oxide reference compounds. The fitting parameters for bismuth – oxide bonds were determined from a nonlinear least-squares function, using 38 Bi – O stretching frequencies. The resulting equations relating Bi – O bond lengths to Raman stretching frequencies are shown in Equation 4.1 and Equation 4.2 and illustrated in Figure 4.3.

Equation *4.1:* $\upsilon = A^{(BR)}$

Equation 4.2: $\upsilon = 92{,}760^{(-2.511R)}$

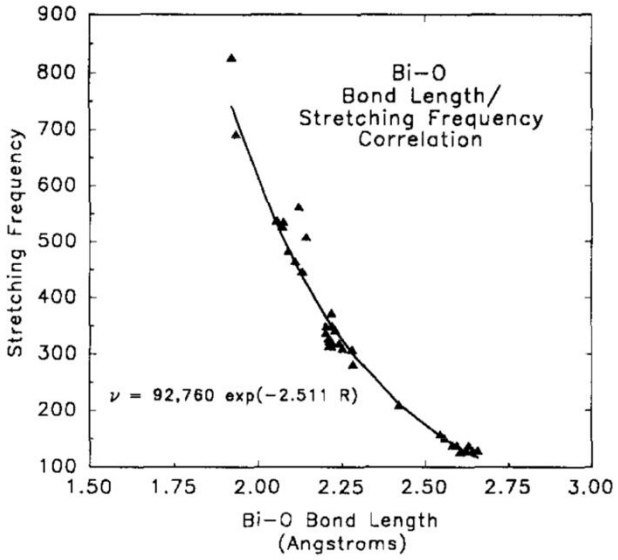


Figure 4.3: The empirical correlation between bismuth – oxygen bond lengths and Raman stretching frequencies.[5]

Brown and Wu[6] developed a general relationship between the metal – oxygen bond valence (*s*) to its bond length *R*, shown in Equation 4.3. The Pauling bond strength, measured in valence units, indicates the relative distribution of valence electrons among the covalent bonds of a metal oxide species. By combining the bond valence and bond length empirical relationship of Brown and Wu [6], with the relation between

Raman stretching frequency and bond lengths, a correlation is established between the Pauling bond strength and Raman stretching frequency. This relation is expressed in Equation 4.4 and plotted in Figure 4.4.

Equation 4.3: $s(Bi_2O_3) = (R/2.010)^{-5.0}$

Equation 4.4: $s(Bi_2O_3) = \{0.198\ ln\left(\frac{92{,}760}{\upsilon}\right)\}^{-5.0}$

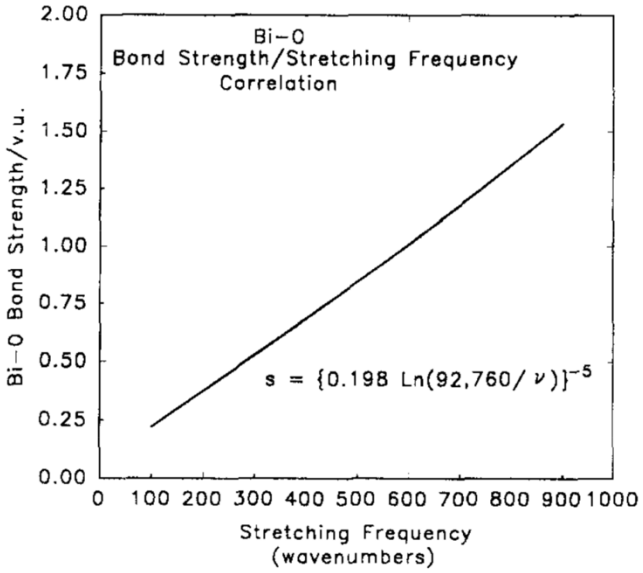


Figure 4.4: The empirical correlation between Pauling bond strength and Raman stretching frequencies.[6]

These empirical relations can be applied to an ideal BiO_x unit that has an even valence distribution throughout the x Bi – O bonds. In a $Bi^{3+}O_6$ octahedron, each Bi – O bond has 3.0 valence units per six Bi – O bonds or 0.5 valence units per Bi – O bond. This valence can be used to determine the bond length (2.309 Å) and a stretching frequency (281 cm^{-1}) using Equation 4.3 and Equation 4.4 above. It should be noted that these estimated stretching frequencies for the perfect BiO_x polyhedra represent the lowest frequency values for a given coordination. The Bi – O stretching mode shifts to higher wavenumbers as the structure becomes increasingly distorted.

Even though these empirical relations represent ideal polyhedra, the structure of the material can still be confirmed while the amount of distortion in the structure is inferred. These empirical relations have advanced the analysis of Raman spectra beyond qualitative methods and may be applied to the bismuth oxide material in this project to gain a deeper understanding of the structure probed with Raman scattering.

4.1.3 Raman scattering of bismuth oxide materials

Rubbens et al.[7] characterized doped Bi_2O_3 structures using ambient Raman scattering spectrometry. This work investigated the orthorhombic, triclinic and δ-cubic structures of bismuth oxides that are doped with various lanthanides.

In $Bi_xLn_{(1-x)}O_{1.5}$ systems, the face-centered cubic (fcc) δ-phase is metastable and progressively transforms into various room temperature stable phases, which include the $R\bar{3}m$ rhombohedral β_1/β_2 layered form, the monoclinic ε-phase, and the orthorhombic and triclinic phases. The Raman spectra of orthorhombic and triclinic phases are shown in Figure 4.5 and Figure 4.6, respectively. For both phases a slight shift to greater stretching frequencies was seen when substituting with smaller lanthanides, such as lutetium, however, the spectra are mostly similar for the same phase. The more notable differences are observed between the orthorhombic and triclinic phases. For example, the bands are better resolved for the triclinic structure [7], even for the external lattice modes located in the low frequency range (> 200 cm^{-1}). The intense band close to 600 cm^{-1} (597 cm^{-1} for the orthorhombic phase and 639 cm^{-1} for the triclinic phase) has been attributed to the Bi – O bond in both cases in previous studies [5,8]. These values reflect the difference in Bi – O bond lengths in the two phases; the triclinic has a shorter bond than the orthorhombic form.

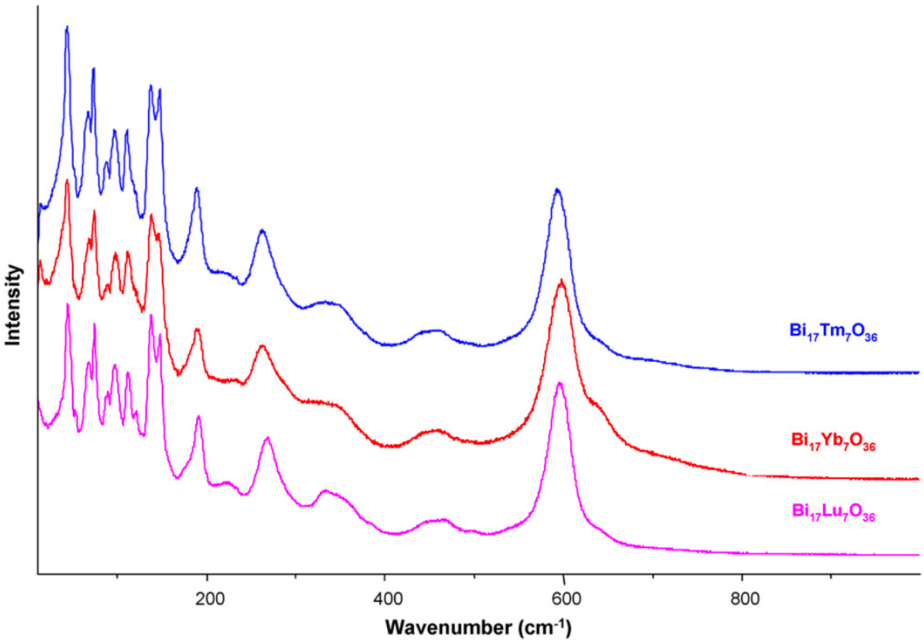


Figure 4.5: Raman spectra of orthorhombic $Bi_{17}Ln_7O_{36}$ (Ln = Tm, Yb, Lu). [7]

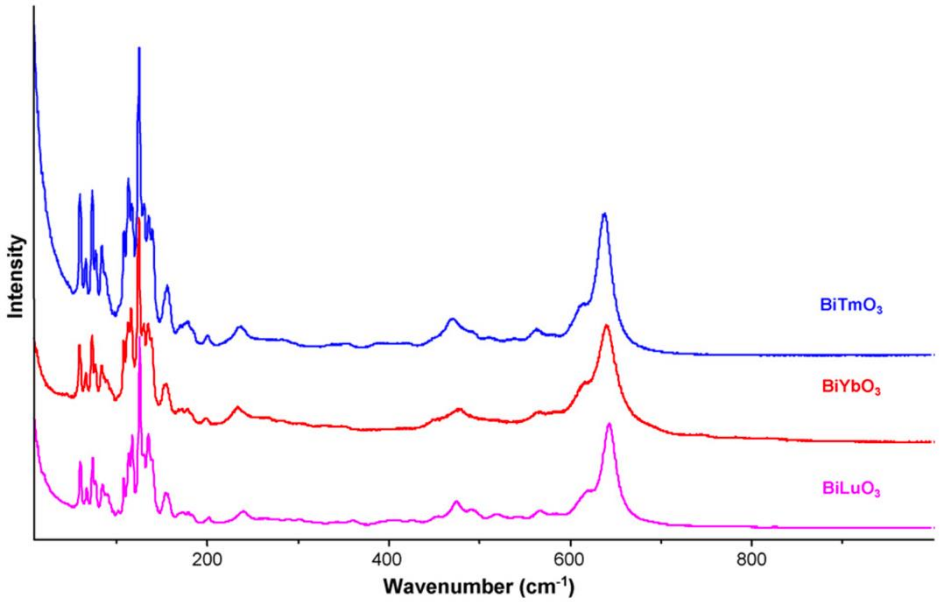


Figure 4.6: Raman spectra of triclinic $BiLnO_3$ (Ln = Tm, Yb, Lu). [7]

The cubic phase is characterized by broad, intense bands in the Raman spectrum that reflect the disorder in the crystalline cell. This is seen in the Raman spectrum in Figure 4.7, as well as the characteristic band at 635 cm^{-1} for a Bi – O bond.

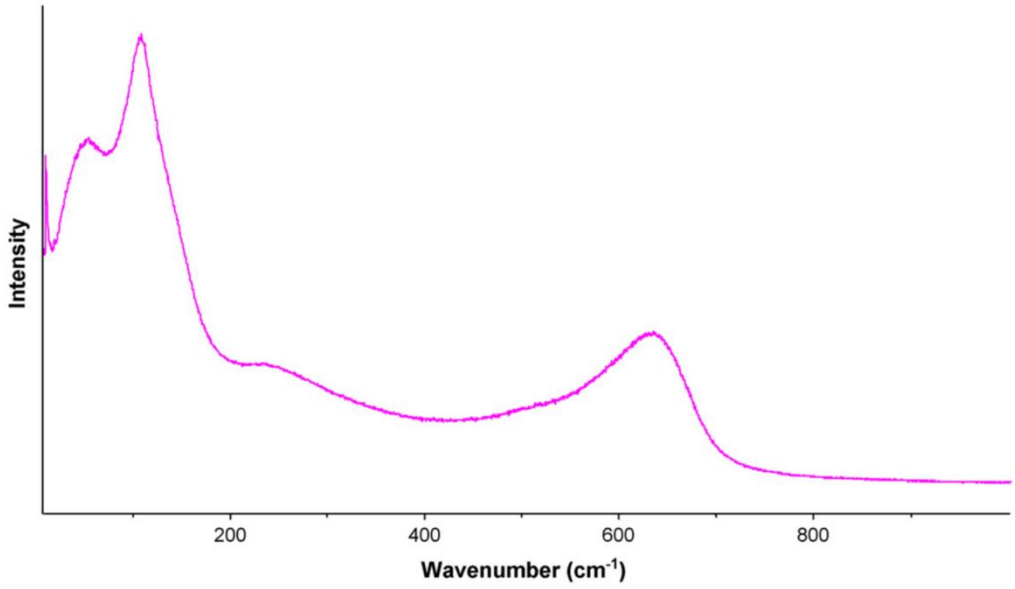


Figure 4.7: Raman spectrum of cubic $Bi_{0.7}Yb_{0.3}O_{1.5}$. [7]

As previously mentioned, the orthorhombic and triclinic structures are closely related to the δ-cubic form. The broad bands in the low frequency region (0 to ~350 cm^{-1}) of the cubic system were deconvoluted to examine this relation (Figure 4.8). This region shows the lattice vibration modes and internal vibration modes. In the cubic

spectrum there are two main maxima at 55 and 108 cm^{-1}, also present in the triclinic structure at ~77 and ~123 cm^{-1}. While this structural relationship between these phases has been established, one can also clearly distinguish between the cubic and triclinic Raman spectra. There is an upward frequency shift by 15 to 20 cm^{-1} in the triclinic spectra and improved there band resolution as compared to the cubic form.

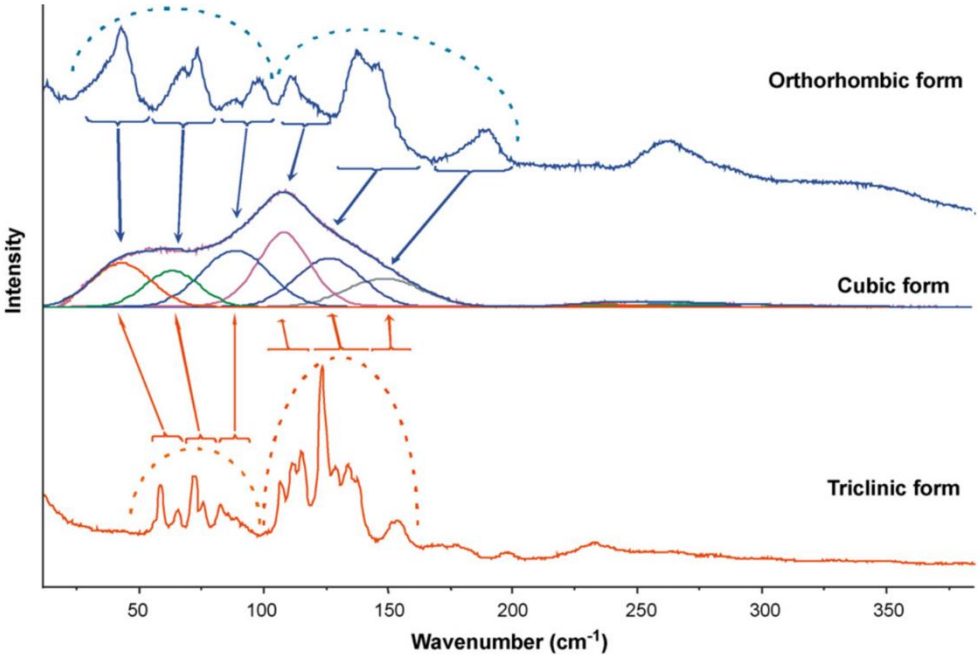


Figure 4.8: Raman spectra showing the low frequency range (0 – 350 cm^{-1}) for ytterbium substituted bismuth oxides. [7]

The Raman scattering analysis of mixed bismuth oxides provided insight into the vibrational modes of $Bi_xLn_{(1-x)}O_{1.5}$ systems. While this study did not focus on the desired rhombohedral ($R\bar{3}m$) phase, background information on the mixed bismuth-lanthanide oxides was gained regarding their vibrational spectra. Deconvolution of the less resolved cubic phase revealed correlations between this metastable phase and the room temperature forms.

4.2 Results and Discussion

A comprehensive review of literature relevant to the experimental work on Raman spectroscopy was conducted. This review highlighted the expected Raman scattering behaviour from rhombohedral ($R\bar{3}m$) materials, providing a theoretical context to the experimental observations. Furthermore, the literature survey extensively explored the various methods available for analysing Raman spectroscopy data, offering a valuable guide for interpreting the experimental results and forming meaningful conclusions.

Like the previous chapter that studied X-ray diffraction (XRD), the current section investigates the phase formation and stability of substituted Bi_2O_3 materials by systematically varying four key parameters: substituent size, substituent concentration, annealing duration, and annealing temperature. XRD analysis revealed the average structure of the materials, providing key insights into phase formation. For example, XRD data indicated the phase mixture of rhombohedral and cubic phases in 25 mol% Gd- and 15 mol% Sm-substituted Bi_2O_3. Interestingly, the 25 mol% Sm-substituted material exhibited significant rhombohedral phase formation, which was unexpected given its relatively low size. While XRD provides valuable information about the average crystal structure, Raman spectroscopy offers a complementary perspective by probing the local atomic arrangements and vibrations within the material. These techniques will be compared, to provide a more comprehensive understanding of the structural properties and phase behaviour of these substituted Bi_2O_3 materials.

Samples were prepared using the citrate sol-gel method described in the Experimental Methodology chapter. Heating treatments comprised of calcination at 500 °C for 12 hours and annealing at 750 °C for 5 hours. Once the powdered samples were pressed into pellets, the pellets underwent sintering at 750 °C for 12 hours.

4.2.1 Substituent Type

The effects of substituent type on the structure of 25 mol% substituted Bi_2O_3 were investigated by examining the Raman scattering of materials that differed only in lanthanide substituent (Figure 4.9). These materials were subjected to the preparation method described above. General inspection of the spectra of the different lanthanides, indicates that mostly the same characteristic peaks are present in their respective Raman spectra. Furthermore, the peaks were fitted using a least squares minimization that showed the best fit with a Gaussian-Lorentzian function. These results confirmed the different peak characteristics of the La- substituted sample compared to that for the Sm- and Gd-materials. In the low frequency range, there are two peaks at approximately 90 and 116 cm^{-1} in the Sm and Gd spectra (Table 4.2). Unlike the other two substituents, the peak around 116 cm^{-1} in the La-

substituted sample could not be fitted using the Gaussian-Lorentzian function due to it's significantly lower intensity. The broadest band of the spectra is present in the Sm- and Gd- substituted materials around 270 cm^{-1}, while it is present at 254 cm^{-1} in the La sample. This upward shift in the Sm- and Gd-substituted material is observed again when comparing lanthanum's band around 355 cm^{-1} to very low intensity bands between 390 and 400 cm^{-1} in samarium and gadolinium. A characteristic peak around 620 cm^{-1} is present in all three materials, and each have a shoulder located around 570 cm^{-1}. The La- substituted material is once again set apart from the other two materials in that the spectra for the Sm- and Gd- substituted materials have an additional shoulder located around 650 cm^{-1}.

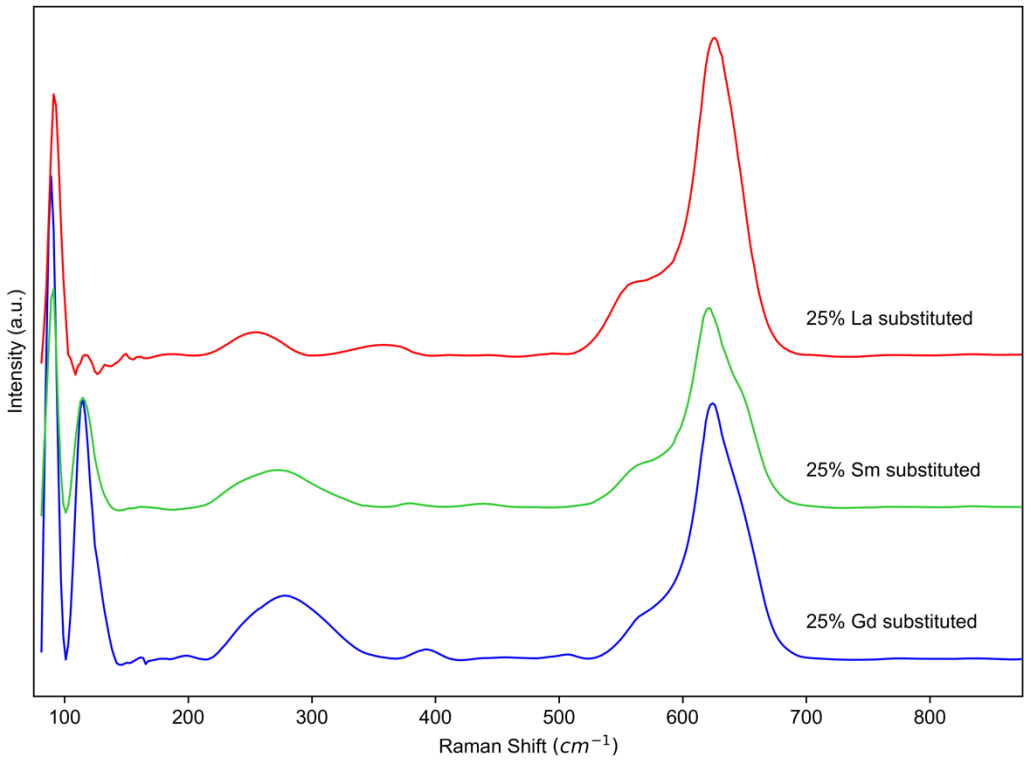


Figure 4.9: Raman Spectra of $Bi_{0.75}Ln_{0.25}O_{1.5}$ where Ln = La, Sm, Gd.

Table 4.2: Positions of Raman bands of the spectra in Figure 4.9 that were determined by fitting with a Gaussian-Lorentzian function.

	Raman bands (cm^{-1})		
	Lanthanum-doped	Samarium-doped	Gadolinium-doped
1.	92.04	89.98	89.6
2.	(not fitted) ~117.0	116.0	116.1
3.	254.5	271.6	278.1

4.	355.1	(not fitted) ~390.0	(not fitted) ~395.0
5.	566.3	577.8	571.3
6.	627.8	620.6	623.0
7.	(not fitted)	647.9	650.4

The $R\bar{3}m$ space group falls under the D^5_{3d} point group, and its character table is shown in Table 4.3. As shown in the character table, the Raman active modes are A_{1g} and E_g. Based on their multiplicity, there are 7 Raman-active modes for this point group. The Raman spectra above (Figure 4.9) shows a maximum of seven bands for a spectrum except for the La-sample, and two of those are classified as external lattice vibration modes. The external lattice vibration modes are usually located around 100 cm^{-1} and so are classified as the peaks at 90 and 116 cm^{-1} in the spectra. This means five bands are left to be assigned to the seven Raman-active modes of the relevant point group. There may be additional bands below 100 cm^{-1}, however the spectrometer can not detect below this frequency because of the filter used. The broad bands could also be deconvoluted into overlapping peaks that are not currently visible. Two very low intensity peaks were identified by visual inspection between approximately 450 and 510 cm^{-1}, that also could be the missing 2 bands. While these may be plausible explanations, the experiment would require lower detection levels to confirm the position of the additional bands.

Table 4.3:Character table of the D_{3d} point group.

D_{3d} $(3m)$	E	$2C_3$	$3C_2$	i	$2S_6$	$3\sigma_d$	Linear, rotation	quadratic
A_{1g}	1	1	1	1	1	1		$x^2 + y^2, z^2$
A_{2g}	1	1	-1	1	1	-1	R_z	
E_g	2	-1	0	2	-1	0	(R_x, R_y)	$(x^2 - y^2, xy)$ (zx, yz)
A_{1u}	1	1	1	-1	-1	-1		
A_{2u}	1	1	-1	-1	-1	1	z	
E_u	2	-1	0	-2	1	0	(x, y)	

The peaks can be assigned to Raman-active modes according to their response to polarization conditions [1]. However, this could not be completed during this project as the instrumentation required was not available, so the corresponding results in literature will be referred to instead. Richter and co-authors [4] studied the Raman

scattering of Bi_2Se_3 that belongs to the relevant space group ($R\bar{3}m$) and the consequent Raman spectra had three assigned peaks [4]. The bands at 72 cm^{-1}, 131.5 cm^{-1} and 174.5 cm^{-1} are assigned to the A_{1g}, E_g and A_{1g} modes, respectively. The interatomic distances of Bi_2Se_3 are slightly larger than those of the structure being investigated here, but the largest difference in interatomic distance between the two structures is relatively small at less than 1 Å. Larger interatomic distances would translate to lower stretching frequencies, so the bands for Bi_2Se_3 would occur at lower frequencies compared to those in this work. Despite accounting for the frequency shift, none of the peaks in Figure 4.9 could be readily assigned to the work of Richter and co-authors. Consequently, the Raman active bands could not be assigned using a combination of Group theory and previous studies.

One could also assign the Raman-active bands by using the empirical relation of bond length and stretching frequency developed by Hardcastle and Wachs [5]. The direct correlation between Raman stretching frequency, bond valence and bond length was established for ideally symmetric bismuth oxide polyhedra. This empirical method was applied to a rhombohedral $R\bar{3}m$ reference model [9], where the Bi – O bond lengths were used to estimate the stretching frequencies (Table 4.4).

Table 4.4:The estimated stretching frequencies for the $R\bar{3}m$ rhombohedral phase determined using the empirical relation of Hardcastle and Wachs [5].

	Bond length (Å)	**Estimated frequency (cm^{-1})**
Bi1/Ln – O1	2.5025	173
Bi1/Ln – O2	2.5779	143
Bi2– O1	2.0686	515
Bi2– O2	2.3615	247
Bi2– O3	2.3246	270
Bi2– O4	2.6541	118

The distortion in the real structure must be considered, as the empirical relation holds the assumption that the BiO_x polyhedral are ideal. An upward frequency shift is consequently expected in the actual frequencies. The comparison of the estimated and actual stretching frequencies is shown in Table 4.5, and no direct correlation is shown. The limitation of the empirical relation is highlighted here, as this method was not really relevant for interpreting Raman spectra. By employing various techniques, it has been established that interpreting Raman spectra of the rhombohedral structure is quite complex. Group theory, limited relevant literature and the empirical relation methods could not provide a reliable analysis. A better approach to analyse Raman spectra could be comparing experimental results to a calculated spectrum, that would be determined using structural data of a reference $R\bar{3}m$ model structure.

Comparison to XRD results of the 25 mol% substituted samples showed similar behaviour when comparing the La-sample to the Sm- and Gd-sample. While samarium and gadolinium had very similar Bragg rhombohedral peaks, La had an underlying phase that could not be detected. This difference could account for the non-fitting or non-detecting of expected Raman bands (Figure 4.9). It must be noted that Gd had 3% of the cubic phase present in it's XRD results, however the presence of cubic was not detected in the representative Raman measurement. The cubic phase is characterized by broad Raman bands, however the Gd sample has sharper bands than Sm (Figure 4.9). While some of the data between XRD and Raman measurements correlate like the distinct behaviour of the La-sample, the different scale of measurements is highlighted when interpreting the Gd-sample.

Table 4.5:Comparison of the actual stretching frequencies in the Raman spectra to the estimated frequencies from the empirical relation.

	Actual frequencies (cm^{-1})	**Estimated frequencies (cm^{-1})**
1.	89 – 92	
2.	116	118, 143, 173
3.	254 – 278	247, 270
4.	355	
5.	566 – 577	515
6.	620 – 627	
7.	647 – 650	

4.2.2 Substituent concentration and annealing duration

The influence of substituent concentration and annealing time (at 750 °C) was investigated with Raman spectroscopy under the same preparation conditions as the samples described above. It was found that the $\mathrm{Bi}_x\mathrm{Sm}_{(1-x)}\mathrm{O}_{1.5}$ system has the best rhombohedral phase formation and stability on an average scale using XRD, and this system was thus selected for further investigations. As shown in Figure 4.10(a) and (b), there are notable changes observed for both parameters. The Raman spectra have the characteristic peaks that were identified and listed in Table 4.5. However, it is shown in Figure 4.10a that Sm concentrations lower than 25 mol% have additional Raman bands, that are labelled with a star. These results correspond with powder XRD work, which showed evidence of impurities in the 20 mol% and 15 mol% Sm samples. The 15 mol% Sm sample contained 23% cubic phase according to Rietveld refinements. While the impurity phase could not be detected using XRD in the 20 mol% Sm material, it's similarity in Raman scattering to the 15 mol% Sm sample suggests that there are trace amounts of cubic in the 20 mol% Sm material too. In Figure 4.10b, all spectra display the same Raman bands. However, these peaks become sharper and more resolved as heating is increased which is indicative of

improved crystallinity. Powder XRD results of these samples showed no correlation between annealing duration and crystallinity, which contrasts with the Raman scattering measured. As proposed in the XRD section of this work, the annealing duration influence on lanthanide substituted Bi_2O_3 requires further investigation to better understand experimental results.

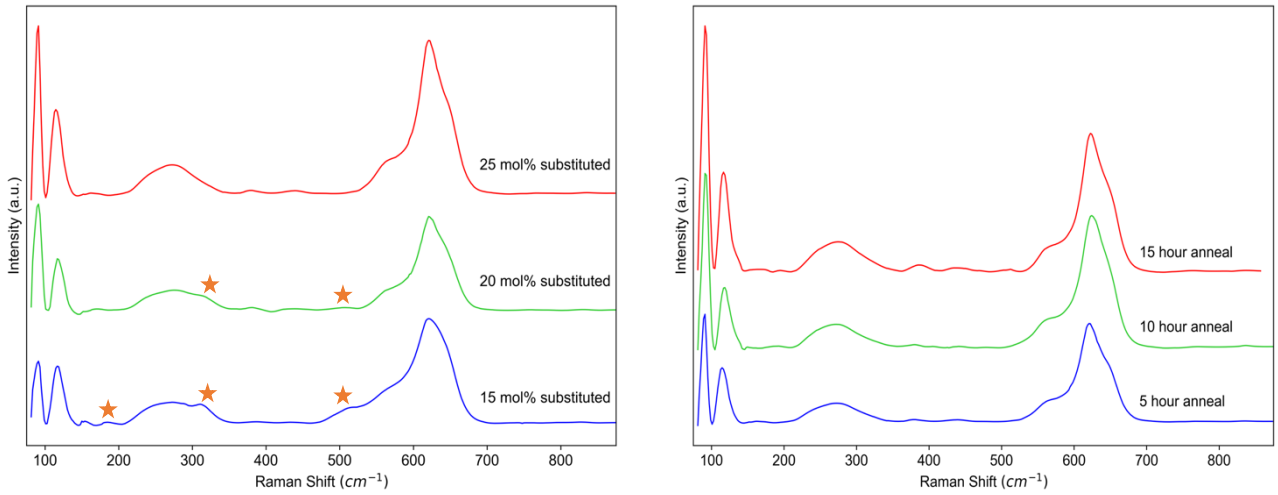


Figure 4.10: Raman spectra of (a) $Bi_xSm_{(1-x)}O_{1.5}$ with x ranging between 0.15 and 0.25 and (b) $Bi_{0.75}Sm_{0.25}O_{1.5}$ with varying annealing durations.

4.2.3 Annealing temperature

The effects of annealing temperature were also investigated with a Raman probe. The Raman spectra of $Bi_{0.75}Gd_{0.25}O_{1.5}$ materials annealed at 610 °C and 750 °C for 5 hours were measured and are shown in Figure 4.11. The Raman bands for both annealing temperatures were compared in Table 4.6, and the strong agreement between the two materials is evident. Visual inspection of the Raman spectra showed an additional peak at approximately 398 cm^{-1} that could not be fitted with a Gaussian-Lorentzian function. The most significant discrepancies between the two materials is that the Raman bands of the 750 °C annealed sample has significantly greater intensity, and the 610 °C annealed material has an additional Raman band at 514.7 cm^{-1}. Other than that, the two materials show great similarity and rhombohedral ($R\bar{3}m$) phase formation on a local scale.

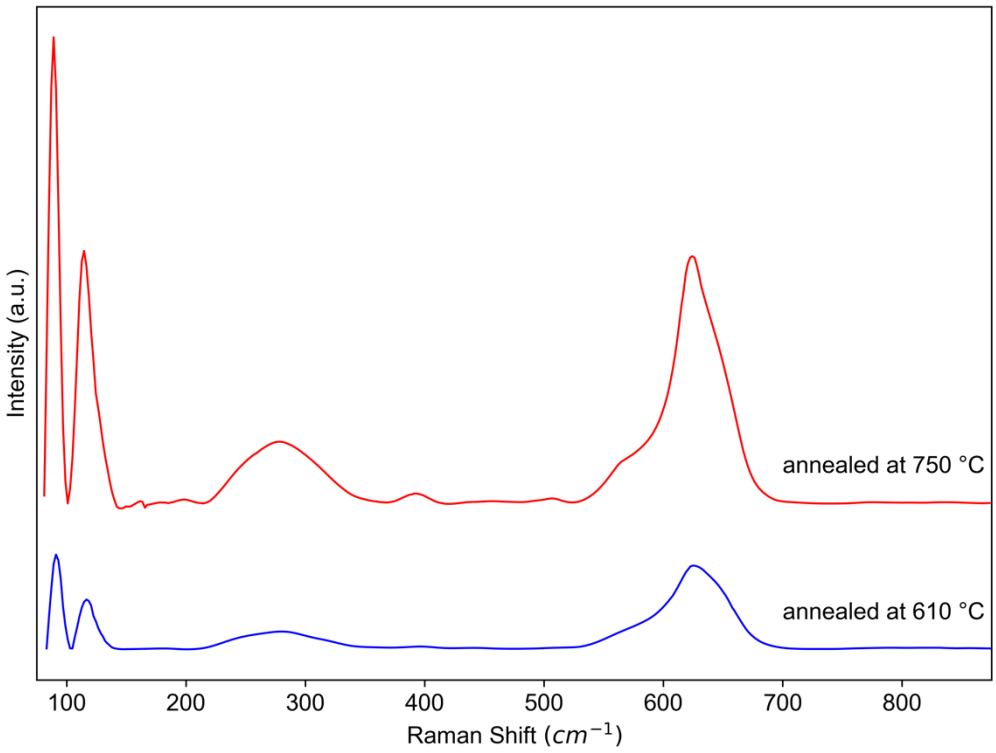


Figure 4.11: Raman spectra of $Bi_{0.75}Gd_{0.25}O_{1.5}$ annealed at different temperatures for 5 hours each; 610 °C and 750 °C.

Table 4.6: The Raman bands of the spectra in Figure 4.11 that were fitted with a Gaussian-Lorentzian function.

Raman bands (cm^{-1})	
Annealed at 610 °C	Annealed at 750 °C
91.53	89.61
117.7	116.1
277.7	278.1
(not fitted) ~ 398.0	(not fitted) ~ 398.0
514.7	(not fitted)
571.9	571.3
630.5	623.0
(not fitted) ~ 660.0	650.4

This Raman scattering behaviour corresponds in some ways with the results of powder XRD. The improved crystallinity with higher annealing temperatures was

observed in both techniques, as well as the rhombohedral phase forming as the dominant phase. However, the Rietveld refinement of the 610 °C annealed material's XRD results detected trace levels of the cubic phase that could not be confirmed in the Raman spectra.

A significant challenge in Raman spectroscopy of powdered samples lies in the small sampling volume, which may not accurately reflect the bulk properties of the material. Also, powder samples may exhibit inhomogeneity or lack of uniformity. To address this, a multipoint Raman mapping technique was employed on the sample after annealing at 610 °C under ambient conditions.

A sample square was created by selecting 8 x 8 points over an area of 500 μm x 500 μm (Figure 4.12). Each point was averaged over two measurements of 15 seconds. All 64 points showed the same characteristic Raman bands of the rhombohedral ($R\bar{3}m$) phase at ambient conditions (Figure 4.13), although some spectra do have slightly different band shapes. This particularly occurs at the Raman band around 620 cm^{-1}, that may have underlying peaks present. Nonetheless, the multipoint measurement confirms that the powdered sample is mostly homogeneous throughout its area, and that the rhombohedral phase is prevalent throughout the sample. It can be concluded that the Raman and XRD techniques do not provide fully complimentary results, and this highlights the differences between the two probes. Raman spectroscopy is more sensitive to the local structural changes, while powder XRD is known to probe the overall average long range order. [10] Also, differences between Raman and powder XRD appear to be common in materials where order, disorder and phase transition processes are known to occur.[10]

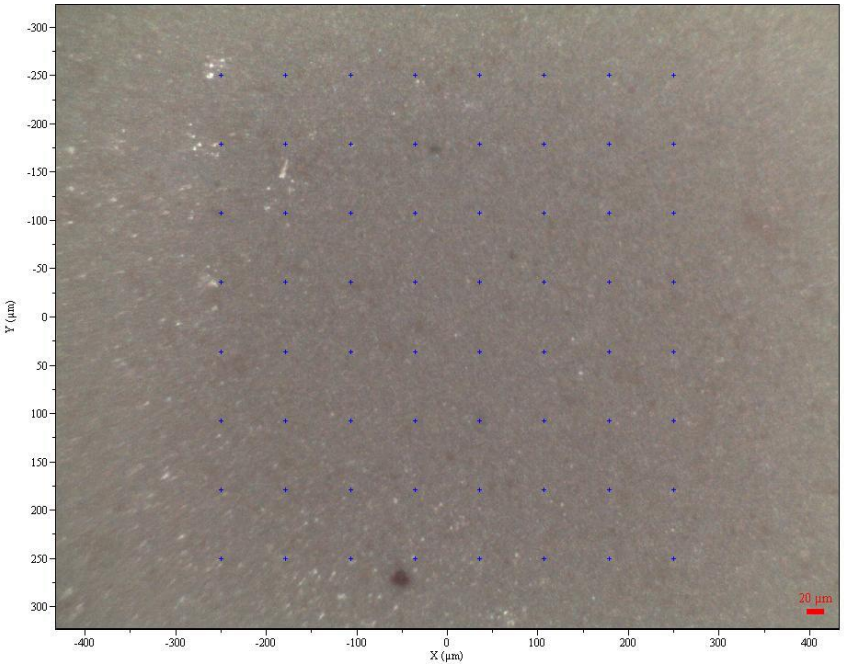


Figure 4.12: Multi-point sample square created on $Bi_{0.75}Gd_{0.25}O_{1.5}$ powder sample annealed at 610 °C by selecting 8 x 8 points over an area of 500 μ x 500 μ. The blue dots represent the 64 sample points.

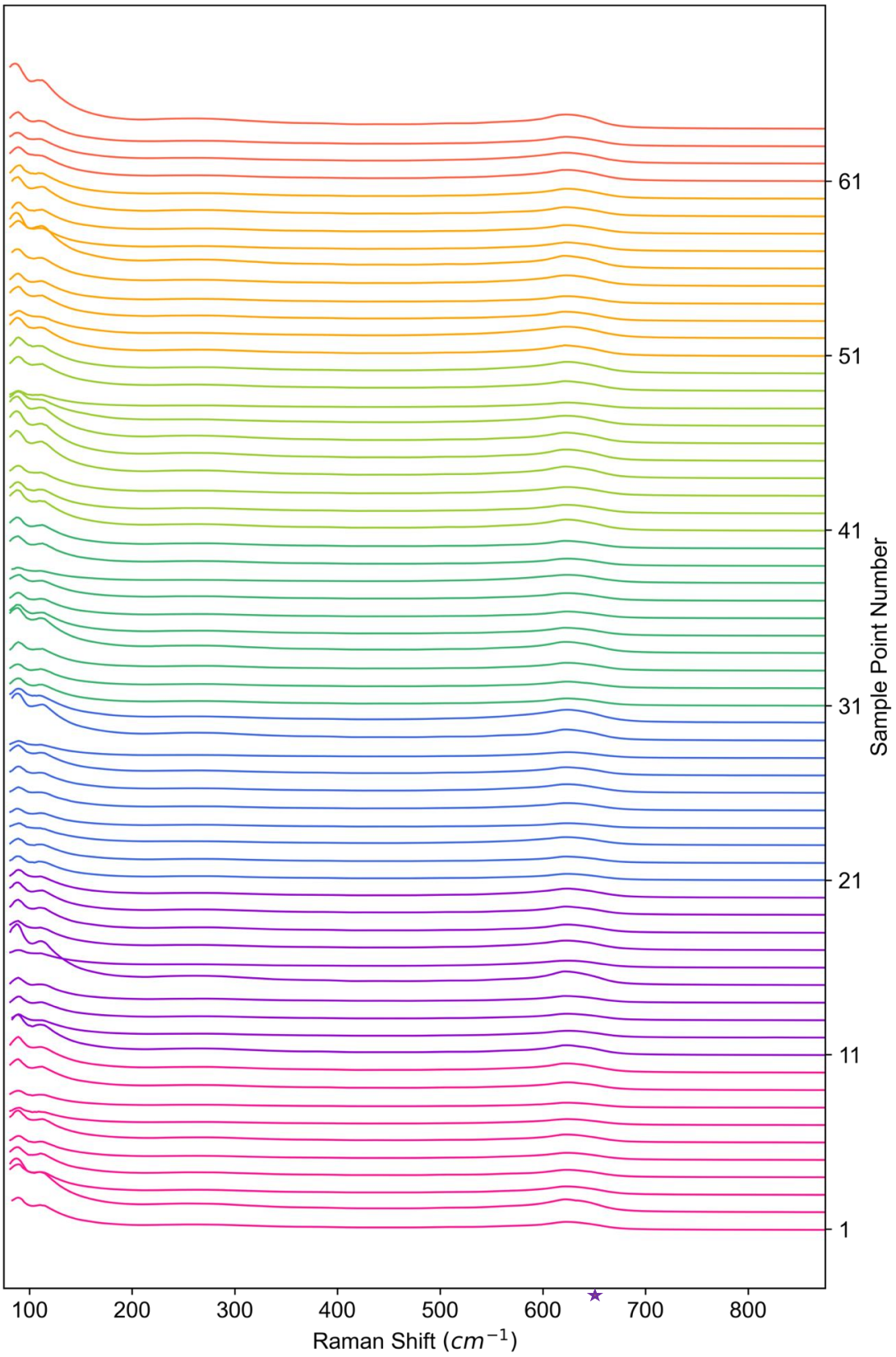


Figure 4.13: Raman spectra of the multipoint measurement of $Bi_{0.75}Gd_{0.25}O_{1.5}$, sample points 1 – 64.

4.2.4 Variable temperature Raman measurements

The material with composition $Bi_{0.75}Sm_{0.25}O_{1.5}$ showed the best rhombohedral R$\bar{3}$m phase formation according to the Rietveld refinement of powder x-ray diffraction results at ambient conditions. This material was thus a reliable starting point to measure Raman scattering with varying temperature. The first measurement at 23 °C had the characteristic Raman bands of the rhombohedral phase that were identified in other ambient spectra (Figure 4.14). As temperature increased, the band at around 640 cm^{-1} undergoes a downward shift, especially from 23 °C to 350 °C. This shift is indicative of a lattice expansion, which is expected upon heating. Another change as temperature increased is the significant decrease in peak intensity, that is clearly observed in the rescaled spectra in Figure 4.15. This is an instrument-related effect that can not be overcome. However, even with the lowered band intensities, a transformation is observed around 550 °C. The band around 640 cm^{-1} transforms to a broader, more symmetrical band which is a feature of the Fm$\bar{3}$m cubic phase [5,7]. This symmetrical band that is prevalent in spectra above 550 °C reflects the loss of the shoulder that was present around 570 cm^{-1} in the rhombohedral phase. The loss of the broad band around 270 cm^{-1} from 550 °C confirms that there is a phase change that occurs from R$\bar{3}$m rhombohedral to Fm$\bar{3}$m cubic. The cubic phase is persistent up the highest temperature measured; 750 °C. After reaching 750 °C, the material was cooled to 30 °C. A final spectrum was measured at this stage, and the spectra had all the characteristic bands of the rhombohedral phase (Figure 4.16). This suggests that the cubic phase may have transformed back to the R$\bar{3}$m rhombohedral phase during cooling, and that the phase change is reversible.

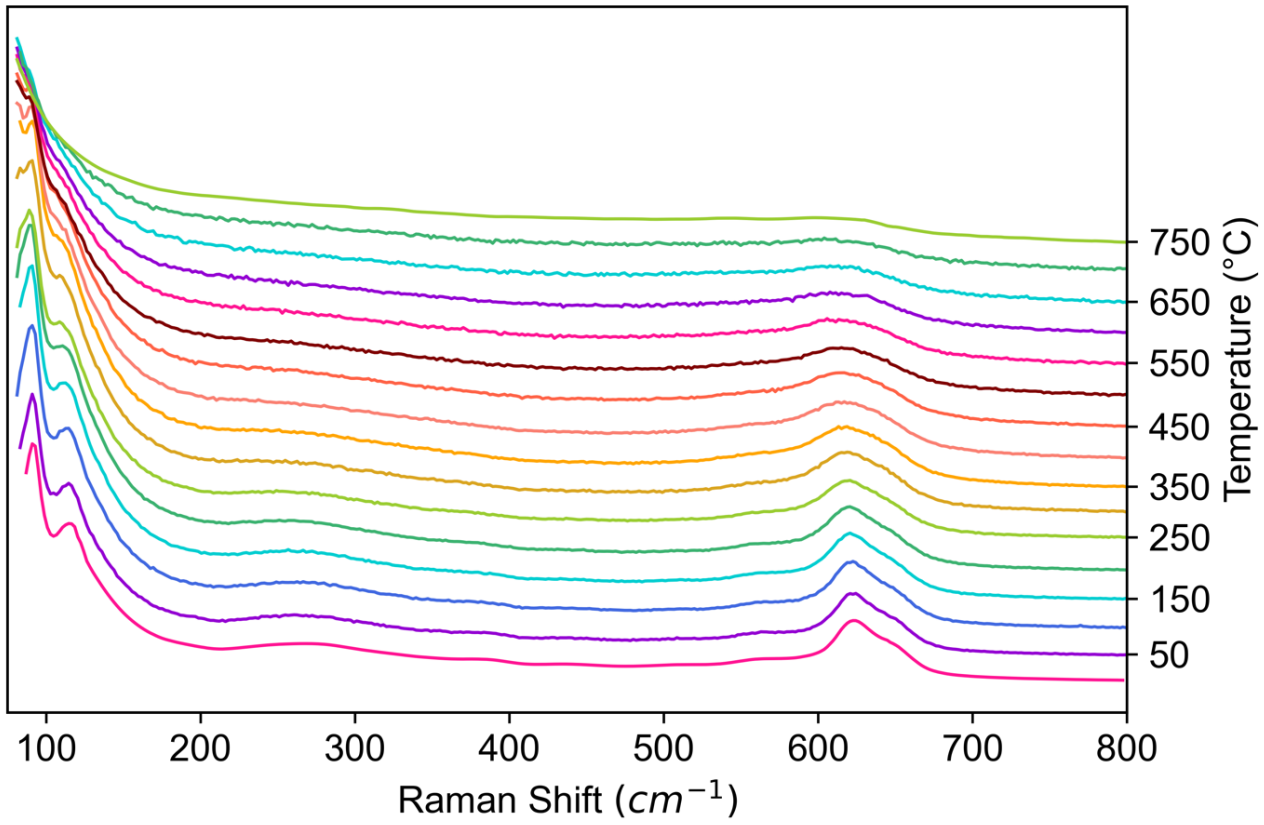


Figure 4.14: Variable temperature Raman spectra of $Bi_{0.75}Sm_{0.25}O_{1.5}$ annealed at 750 °C for 5 hours.

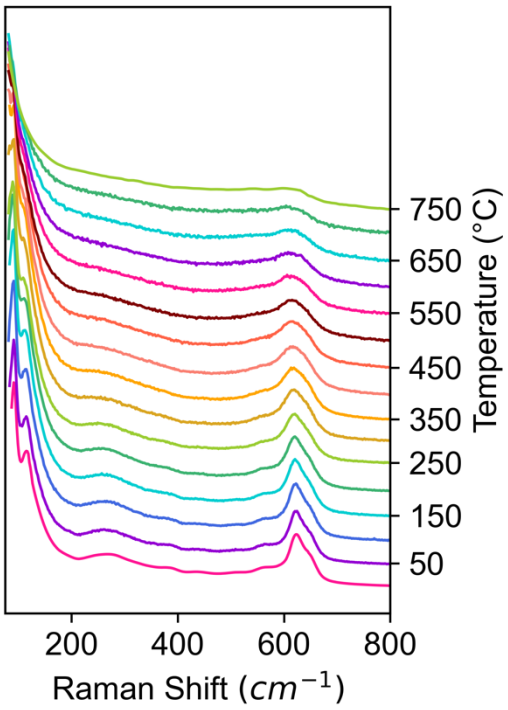


Figure 4.15: Rescaled view of the variable temperature measureent Raman spectra in Figure 4.14

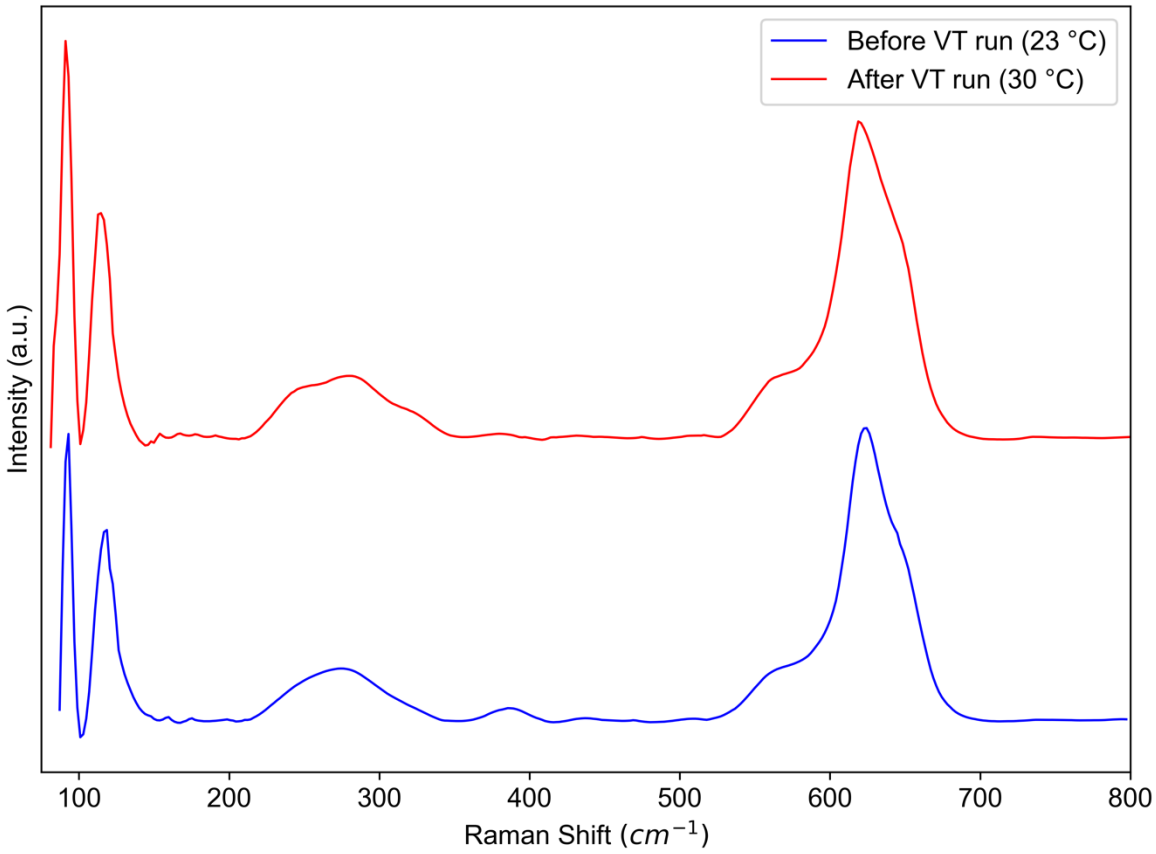


Figure 4.16: Comparison between Raman spectra of $Bi_{0.75}Sm_{0.25}O_{1.5}$ before and after the variable temperature measurement, at 23 °C and 30 °C respectively.

4.3 Conclusion

Ambient Raman scattering measurements were conducted to examine the impact of various parameters, including substituent type, substituent concentration, annealing time and annealing temperature on structural properties on a local scale. The analysis of substituent type using ambient Raman spectra indicated a significant distinction in the lanthanum-substituted sample compared to the samarium and gadolinium substituted materials. In terms of Raman scattering, three notable differences were observed between the lanthanum-substituted materials and the others. Specifically, the lanthanum-substituted materials lacked a Raman band at approximately 650 cm^{-1}, which were present in the other materials. Additionally, the lanthanum-substituted material had an additional band at around 350 cm^{-1} that was too weak to be fitted in the other materials.

Group theory predicts seven Raman active bands for materials with the $R\bar{3}m$ space and D^5_{3d} point group. However, when analyzing the ambient Raman spectra, only six Raman bands were observed in the La-substituted sample and could be fitted with a Gaussian-Lorentzian function. Seven Raman bands were detected in the Sm- and

Gd- substituted materials. The two low-frequency bands, which appeared around 100 cm^{-1}, were identified as external lattice vibration modes and do not correlate to symmetry within the structure. This means that four of seven Raman bands have been successfully identified through peak fitting. The Raman-active modes in this point group are A_{1g} and E_g. which can be assigned in Raman spectra based on their different polarization conditions. However, due to a lack of instrumentation availability in this study, a comparison with previous studies was used instead. Richter and co-authors [4] studied the Raman scattering of a similar structure (Bi_2Se_3), and three bands were identified in the Raman spectrum. The bands at 72 cm^{-1}, 131.5 cm^{-1} and 174.5 cm^{-1} were assigned to the A_{1g}, E_g and A_{1g} modes respectively. Unfortunately, bands with similar frequencies could not be identified in the measured Raman spectra, preventing the assignment of bands using relevant previous studies. Consequently, the use of Group theory did not provide an approach that is suitable for interpreting the Raman spectra for the rhombohedral ($R\bar{3}m$) structure in this project.

The empirical relation between bond length and stretching frequency established by Hardcastle and Wachs [5] was employed to potentially interpret the Raman scattering results. However, the estimated frequencies based on the reference $R\bar{3}m$ structure's bond lengths did not correlate with the actual frequencies. Therefore, the empirical relation was not successful in interpreting the Raman scattering of the rhombohedral phase materials too.

This work highlights a great need for an alternative method to compare and interpret the Raman scattering of materials. This method should not rely on estimations or comparison to previous studies. One possible approach is to calculate Raman spectra based on the structure determined using complementary techniques such as x-ray and neutron diffraction. By comparing the observed and calculated Raman spectra, a qualitative or quantitative analysis can be performed, ensuring consistency and reliability.

Investigating the influence of substituent concentration and annealing time was completed by analyzing the Raman scattering of relevant materials. All Raman spectra exhibited the characteristic bands of the $R\bar{3}m$ rhombohedral phase, however the 15 mol% and 20 mol% Sm-substituted materials also displayed additional peaks. Based on the Rietveld refinements of the 15 mol% Sm substituted material, these additional peaks could be attributed to the cubic phase. Beside rhombohedral phase formation, increased annealing time showed improved crystallinity with increased annealing times. It can be concluded that the Raman scattering behaviour of the substituent concentration and annealing duration parameters compliment the corresponding XRD results.

The last parameter examined was the annealing temperature. The Raman scattering results produced largely similar spectra when annealing at 610 °C and 750 °C. The 610 °C annealed sample displayed an additional Raman band, which could indicate a minor impurity phase. To ensure that the Raman spectra was an accurate representation of the material, a multipoint mapping measurement was conducted on the 610 °C annealed material. A total of 64 points were measured, resulting in 64 ambient Raman spectra. All these spectra displayed the expected characteristic bands of the rhombohedral phase. There were no significant differences between the spectra, indicating that the powder sample is homogeneous throughout its dimensions.

An in-situ variable temperature Raman measurement was completed on the $Bi_{0.75}Sm_{0.25}O_{1.5}$ material ranging from 23 °C to 750 °C. The spectrum obtained at the intial temperature of 23 °C comprised of Raman bands that are indicative of the rhombohedral phase ($R\bar{3}m$). A transformation occurred at around 550 °C that appear to be a phase change from rhombohedral to cubic. This cubic phase persisted in the material up to the highest temperture measured, at 750 °C. After completing the variable temperature measurement and allowing the instrument to cool, a final measurement was taken at 30 °C. Both the spectra obtained before and after the variable-temperature measurement, at 23 °C and 30 °C respectively, displayed the same characteristic bands of the rhombohedral phase. This suggests that the phase change is reversible, and the material transformed back to the $R\bar{3}m$ rhombohedral phase upon cooling.

4.4 References

1. Kudelski, A. Analytical applications of Raman spectroscopy. *Talanta* **76**, 1–8 (2008).
2. Cialla-May, D., Schmitt, M. & Popp, J. Theoretical principles of Raman spectroscopy. *Physical Sciences Reviews* **4**, (2019).
3. Coates, J. Vibrational Spectroscopy: Instrumentation for Infrared and Raman Spectroscopy∗. *Applied Spectroscopy Reviews* **33**, 267–425 (1998).
4. Richter, W. & Becker, C. R. A Raman and far-infrared investigation of phonons in the rhombohedral V2–VI3 compounds Bi2Te3, Bi2Se3, Sb2Te3 and Bi2(Te1−xSex)3 (0 <x < 1), (Bi1−ySby)2Te3 (0 <y < 1). *Phys. Stat. Sol. (b)* **84**, 619–628 (1977).
5. Hardcastle, F. D. & Wachs, I. E. The molecular structure of bismuth oxide by Raman spectroscopy. *Journal of Solid State Chemistry* **97**, 319–331 (1992).
6. Brown, I. D. & Wu, K. K. Empirical parameters for calculating cation–oxygen bond valences. *Acta Cryst B* **32**, 1957–1959 (1976).
7. Rubbens, A., Drache, M., Roussel, P. & Wignacourt, J. P. Raman scattering characterization of bismuth based mixed oxides with Bi2O3 related structures. *Materials Research Bulletin* **42**, 1683–1690 (2007).
8. Ermakova, L. V., Strekalovskii, V. N., Vovkotrub, É. G. & Bamburov, V. G. Structural transformations in a Bi2O3 crystal and solid solution. *Journal of Applied Spectroscopy* **69**, 152–154 (2002).
9. Obbade, S. Powder Neutron Diffraction and TEM Investigations of Bi0.775Ln0.225O1.5 Oxide Conductors (Ln=La, Pr, Nd, Sm, Tb, Dy) with Rhombohedral Bi–Sr–O type: Structural Relationships with Monoclinic ε-Bi4.86La1.14O9 Form. *Journal of Solid State Chemistry* **168**, 91–99 (2002).
10. Lekgoathi, M. D. S. & Kock, L. D. Effect of short and long range order on crystal structure interpretation: Raman and powder X-ray diffraction of LiPF6. *Spectrochimica Acta Part A: Molecular and Biomolecular Spectroscopy* **153**, 651–654 (2016).

Chapter 5 - The ionic conductivity of rhombohedral substituted bismuth oxide using Electrochemical Impedance Spectroscopy

Material properties are owed to their structure on an atomic scale. As a result, the previous chapters have examined the R$\bar{3}$m structure extensively to gain a deep understanding of the structure, by using multiple probes as characterizing techniques. This was done to contribute to a larger aim of improving the conductive properties of rhombohedral Bi_2O_3-based electrolytes. Now that the effects of selected dopants, their composition and synthetic effects on the R$\bar{3}$m structure of the Bi_2O_3 system is better understood, the conductivity properties of the structure will be investigated.

5.1 Literature Review

5.1.1 Conductivity Mechanism

Previous work by Mercurio and co-workers[1] studied the crystal structure of the rhombohedral (R$\bar{3}$m) $Bi_{0.75}Sr_{0.25}O_{1.375}$ phase, using single crystal neutron diffraction (neutron wavelength = 1.043 Å) at varying temperatures. The temperatures selected for measurements were 300 K, 600 K and 1050 K. The crystal structure was determined by completing refinement calculations using SHELLX76 and the scattering lengths.

The starting model for refinements was the $Bi_{0.765}Sr_{0.235}O_{1.383}$ structure obtained by Conflant *et al*.[2] (Figure 5.1). The structure is comprised of:

- 2.25 Sr and 0.75 Bi on the M(1) site : 3a (0, 0, 0)
- 6 Bi on the M(2) site : 6c (0, 0, 0.22)
- 6 O on the O(1) site : 6c (0, 0, 0.29)
- 6 O on the O(2) site : 6c (0, 0, 0.10)

The refinements showed a strong convergence between model and experimental structures. Thereafter, difference Fourier syntheses were performed. This revealed the presence of three additional anionic sites with partial occupancy in the structure:

- The O(3) site: 6c (0, 0, 0.44)
- The splitting of O(2) and O(3) sites respectively:
    1. The O(2)' site: 18h (x, $2x$, z)
    2. The O(3)' site: 18h (x, $2x$, z)

Structure information from refinements such as occupancies, thermal parameters and interatomic distances were collectively used to propose a R$\bar{3}$m structure (Figure 5.1). The refined parameters showed that the structure at all temperatures measured is the regular repetition of three fluorite-like sheets shifted with respect to one

another by a vector μ = 2($\frac{a}{3}$ + $\frac{b}{3}$ + $\frac{c}{3}$). The fluorite-like sheet is composed of three hexagonal metal layers; two external layers of Bi on the M(2) site and an internal layer of Bi and alkaline earth metals on the M(1) site (Figure 5.1). The repetition of fluorite-like sheets occurs along the c-axis where each sheet is separated by an intersheet space.

The comparison of structures at different temperatures showed a change in anion occupancy, sheet and intersheet size and interatomic distances (Table 5.1). While there are five different anionic sites present in the structure, a general trend was identified with regards to their occupancy as a function of temperature. The anions were classified into two general subsets; sheet anions and intersheet anions. As the name suggests, the sheet anions and intersheet anions are described by their location in the structure. As temperature was increased, there was a decrease in occupancy of sheet anions with a simultaneous increase in occupancy of intersheet anions (Table 5.1 and Figure 5.2), suggesting a migration of anions from the fluorite-like sheet to the intersheet as temperature increases. A significant outlier to this general trend is the O(1) anions which maintain a full occupancy of their site at all temperatures. The O(1) anions are the only anions located near the internal Bi/Sr layer which suggests that any anion migration from the fluorite-like sheet is a result of anions located along the external Bi layers (Figure 5.1). With these results, this work acknowledges a migration pathway where the motion of anions occurs along the c-axis (Figure 5.1). The oxide ion occupancy determined in this study is quite reliable, as a neutron probe is more sensitive to lighter elements compared to x-rays, especially when heavy elements such as Bi are present in the sample.

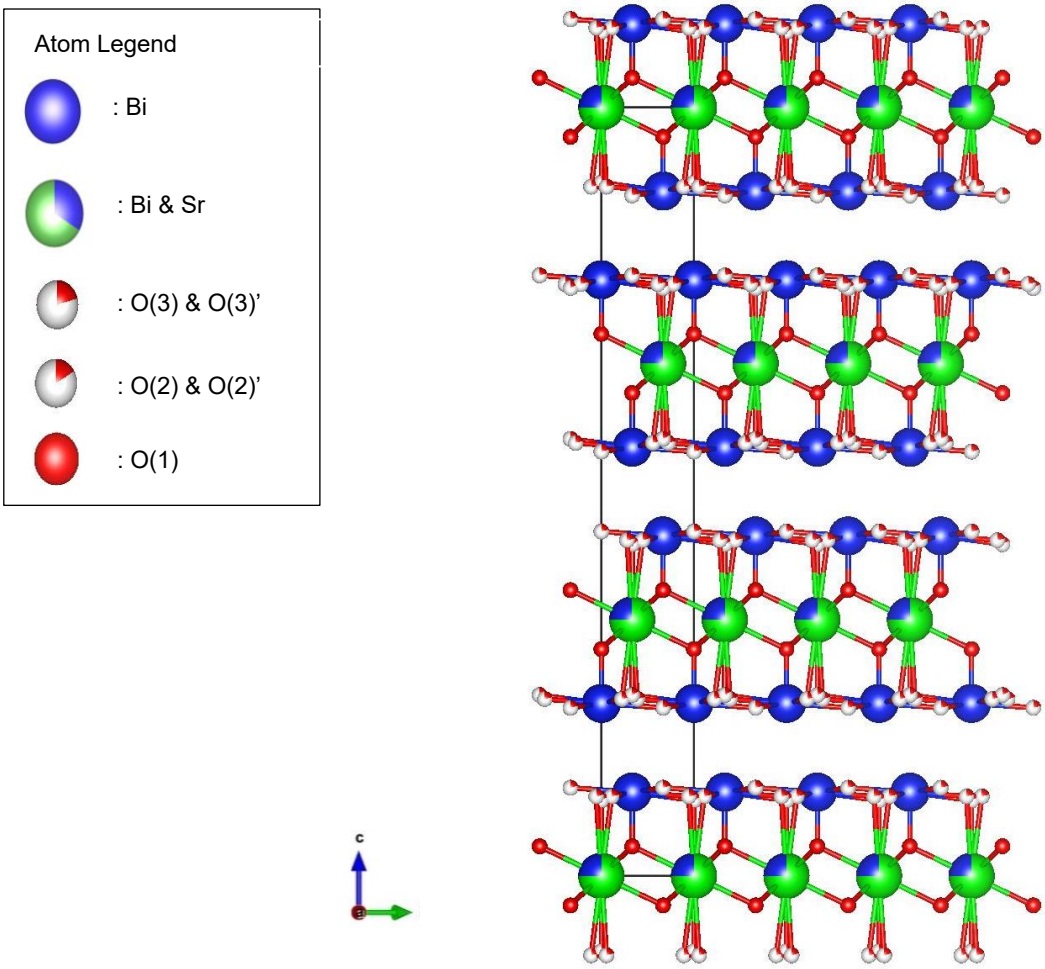


Figure 5.1: The $R\bar{3}m$ structure: CIF obtained from the measurement of $Bi_{0.765}Sr_{0.235}O_{1.383}$ at 300K.[2]

Table 5.1: The oxide ions occupancies determined by single crystal neutron diffraction at 300 K, 600 K and 1500 K.[1]

	Oxygen ions	**Occupancy at 300K**	**Occupancy at 600K**	**Occupancy at 1500K**
Sheet anions	O(1)	1	1	1
	O(2)	0.16(8)	0.18(5)	0.1(2)
	O(2)'	0.21(8)	0.16(2)	0.15(7)
Intersheet anions	O(3)	0.22	0.37	0.35(5)
	O(3)'			0.04(2)

Although the results from work of Mercurio and co-authors[1] seemed to suggest the direction of oxide conductivity in the structure as parallel to the c-axis, they acknowledged work done by Conflant *et al*[2] which showed the R$\bar{3}$m structure has more than one direction of anion diffusion. The study by Conflant and co-workers[2] showed the motion of anions occurs perpendicular to the c-axis too (along the ab-plane), and conductivity in this direction is greater by 2 orders of magnitude than conductivity parallel to the c-axis.

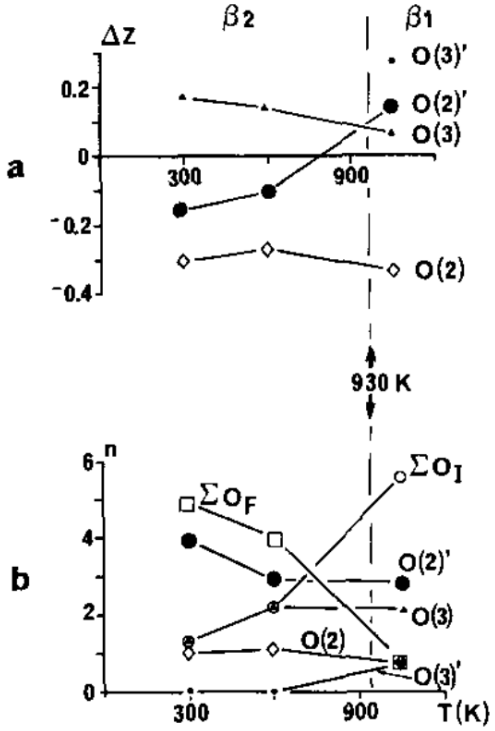


Figure 5.2: (a) Thermal evolution of the position of oxide ions with respect to the M(2) layers (positive Δz values correspond to ions within the intersheet space and negative Δz values correspond to ions within the fluorite-like sheets, where Δz represents the displacement of anions from their original positions). (b) The occupancies of oxide ions with increasing temperature. $\sum O_I$ refers to the sum of intersheet oxide ions and $\sum O_F$ refers to the sum of fluorite-like sheet oxide ions.[1]

The results obtained in this study[1] together with the work of Conflant et al.[2] allowed authors to propose migration pathways that give rise to the ionic conductive property of the R$\bar{3}$m structure of substituted Bi_2O_3. The first pathway involves anions moving along the external Bi layer, within the fluorite-like sheet (Figure 5.3). The direction of anion migration in this pathway is perpendicular to the c-axis. This pathway is highly unlikely, as it would require a much smaller size of the fluorite–fluorite window (shown in Figure 5.4) than what has been determined using interatomic distances from refinement calculations. The second pathway also involves anions moving perpendicular to the c-axis and along the external Bi layer, however, this motion occurs within the intersheet space (Figure 5.3). This pathway is more probable than the first because it requires large intersheet–intersheet and fluorite–intersheet

windows (shown in Figure 5.4), which is present in the structure according to calculated interatomic distances. The last pathway involves anions moving across the intersheet space from one external Bi layer to the next (Figure 5.3). Unlike the first two cases, this pathway is parallel to the c-axis. This proposed migration is highly probable as it would need a large size of fluorite–intersheet windows (Figure 5.4) that is confirmed in the structure by refinement calculations. This pathway also correlates with the change in anion occupancies as temperature is increased. This pathway is even more likely for lanthanide substituted Bi_2O_3 as these structures have the exclusive presence of partial occupancies of oxide ions in the intersheet space. While it is convenient to separate the possible pathways in theory, it is more realistic that anions migrate using a combination of pathways.

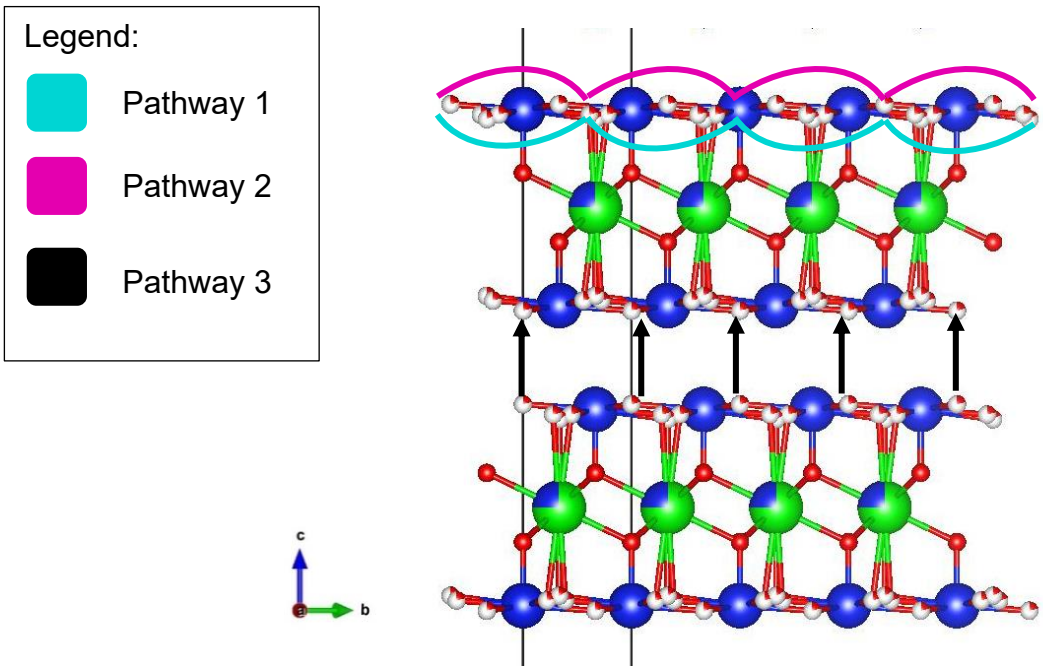


Figure 5.3: An illustration of the proposed migration pathways in the R$\bar{3}$m structure measured at 300K.

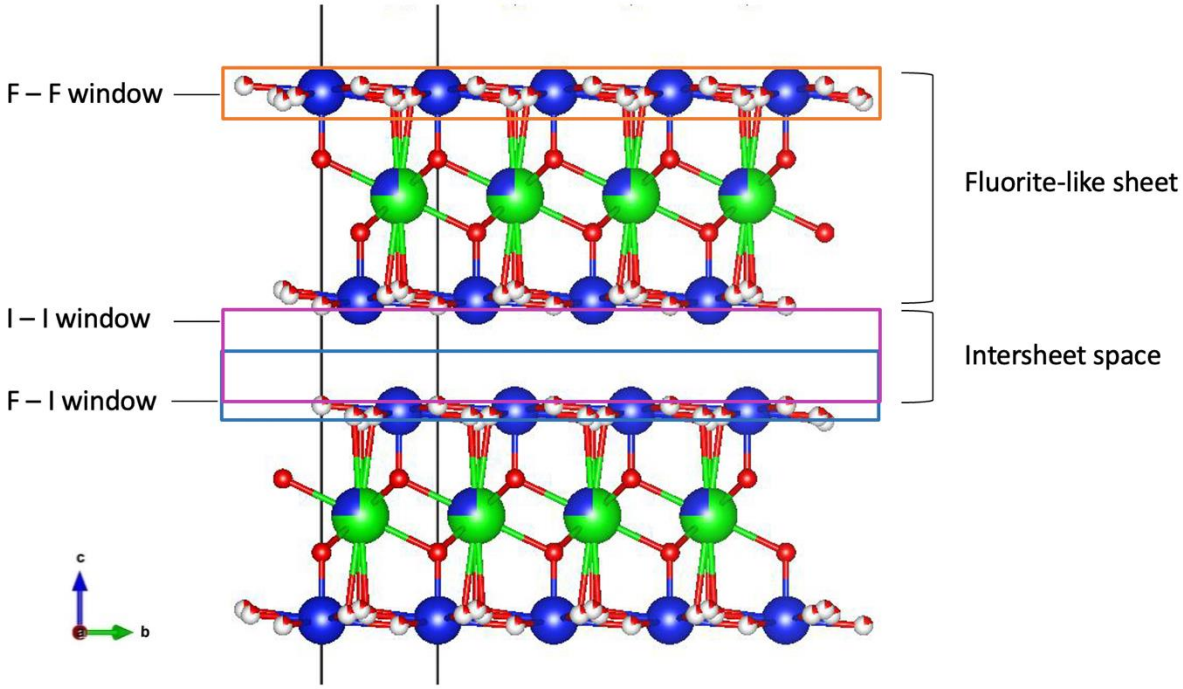


Figure 5.4: Graphical representation of the components of the R$\bar{3}$m structure used to describe anion pathways.

In the next study under review, Ahi and co-workers[3] investigated the $Bi_{0.775}La_{0.225}O_{1.5}$ structure using powder x-ray diffraction, variable temperature powder neutron diffraction, electrochemical impedance spectroscopy (EIS) and Reverse Monte-Carlo (RMC) simulations. This work aimed to study the ion-conducting nature of $Bi_{0.775}La_{0.225}O_{1.5}$ having a rhombohedral crystal structure analogous to that of $Bi_{0.851}Sr_{0.149}O_{1.425}$.

The migration pathways proposed by Mercurio *et al.*[1] were assessed in this study using variable temperature neutron powder diffraction and RMC simulations. The diffraction results were refined with the R$\bar{3}$m structure determined by Obbade *et al.*[4] Once structural refinements were completed, a RMC model was constructed based on neutron diffraction measurements at 10 K and the simulations performed confirmed additional sites present in the structure. The O(2) and O(3) 6c crystallographic sites are split into 18h sites, denoted O(2)' and O(3)' respectively, as observed in the work of Mercurio and co-workers.[1] Atomic density distributions were then determined using RMC simulations. The oxygen atomic distributions showed holes at the centre of both O(2) and O(3) sites, and the valence sum drops well below the nominal valence of 2. So Rietveld refinements were completed with the inclusion of the O(2)' and O(3)' sites, which showed an improvement in fitting experimental data. Unlike the work of Mercurio *et al.*[1], the structure determined by Obbade and co-workers[4] did not show splitting of O(2) or O(3) sites at ambient conditions. However, their anisotropic thermal parameters indicated larger displacements in the ab-plane.

As temperature was increased, a decrease in occupation of O(3)' sites was observed (Figure 5.5). This corresponds to a transfer of O(3)' ions to positions halfway between O(2) and O(3) sites, as indicated by its new z coordinate values that are close to 0.42 or equivalent. These results support migration pathway 1 (Figure 5.3), where ions in the O(2) sites migrate to the O(3) site through the fluorite sheet. This work contradicts that of Mercurio et al.[1], which concluded pathway 1 to be highly unlikely.

Additionally, Obbade *et al*.[4] considered an oxygen site is present in the intersheet space, referenced as "O(4)". However, the inclusion of O(4) sites in structural refinements led to unreliable results. The presence of an oxygen site in the intersheet space was further opposed by atomic density distributions. While there were distinct concentrations found at other oxygen sites, there was no distinct localization to the O(4) sites observed. Migration pathway 3 proposes that anions move through the intersheet space from one external Bi layer to the next using the partially occupied oxygen sites in the intersheet site. However, the absence of oxygen sites in the intersheet space, or O(4) sites, provide evidence to suggest that this pathway is not a plausible conductivity mechanism. If this pathway is active, the conductivity mechanism could have a jumping character. This migration pathway was considered highly possible by Mercurio *et al*.[1] due to the average anion migration from the fluorite sheet to the intersheet space observed in experimental data. While the same trend was present in this study, upon closer inspection it was revealed that this overall motion corresponds to displacement of O(3) ions along the c axis towards neighbouring O(3) sites. The movement in between O(3) pairs does not contribute significantly to the system's conductivity. Therefore, the anionic migration from the fluorite sheet to the intersheet space through the external metal boundary does not appear to contribute to the conductivity in $\mathrm{Bi_{0.775}La_{0.225}O_{1.5}}$.

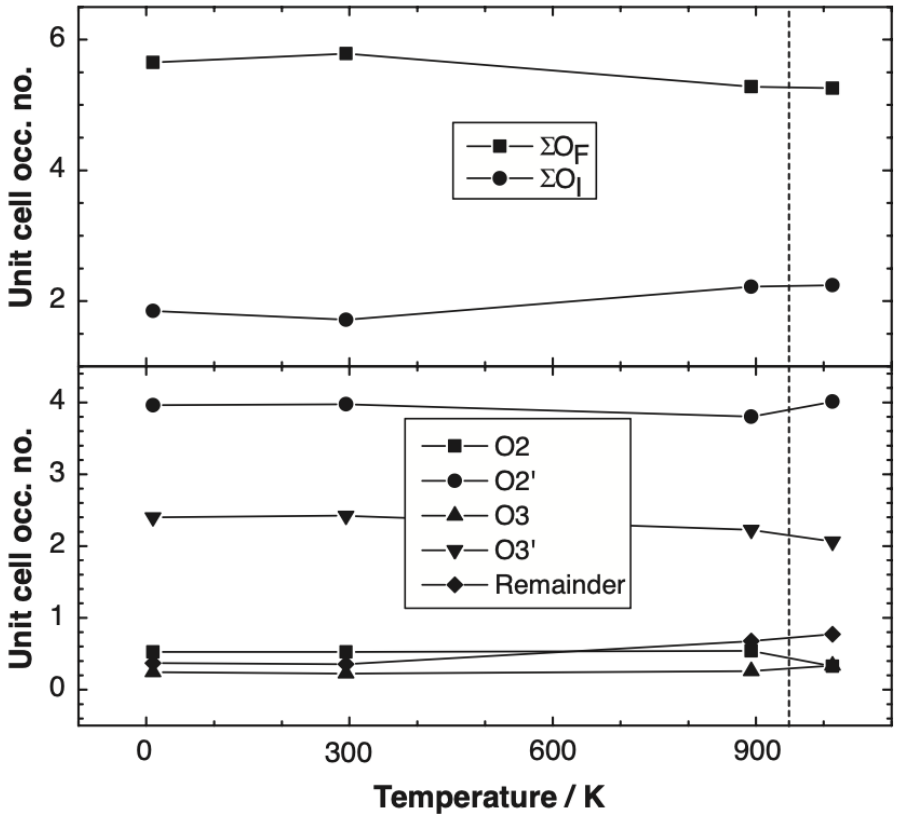


Figure 5.5: Unit cell occupation numbers for oxide ions as a function of temperature. $\sum O_I$ refers to the sum of intersheet oxide ions and $\sum O_F$ refers to the sum of fluorite-like sheet oxide ions.[10]

The separate accounts of work done on the conductive nature of the rhombohedral $R\bar{3}m$ phase are not in agreement with one another. Even though high-end techniques such as single crystal neutron diffraction were used to investigate the oxygen ions within the structure as a function of temperature, it is clear that the data can be interpreted in different ways. Therefore, one cannot confidently confirm the ionic conductivity mechanism within the rhombohedral $R\bar{3}m$ phase. It should be noted that the two studies in this review used different types of metal substituents; Mercurio *et al*.[1] substituted Bi_2O_3 with an alkaline earth metal (strontium), while Ahi and co-authors[3] used a rare earth metal (lanthanum). It has been reported that the kind of substituents as well as the quantity added to the system has a significant influence on its properties.[5,6]

5.1.2 Structural and Synthetic effects

Drache and co-workers[7] studied the structural and conductivity properties of $Bi_{0.775}Ln_{0.225}O_{1.5}$ oxide conductors, where Ln was La, Pr, Nd, Sm, Eu, Gd, Tb and Dy. The range of lanthanide substituents added to the Bi_2O_3 system enabled a conductivity study as a function of dopant type and size. Conductivity measurements were completed on pelletised samples using impedance spectroscopy in the frequency range of 1 – 10^6 Hz. The thermal investigation of conductivity was

completed with two treatment cycles, the first was from 300 to 600 °C and the second from 300 to 800 °C. All the samples showed a linear range between 300 and ~700 °C, followed by a sharp increase in conductivity above ~700 °C (Figure 5.6).

This work[7] has proposed that the rhombohedral phase has two temperature-dependent forms that are very similar in structure. The β_2 form is present at room temperature and transforms to the β_1 form at high temperatures (~700 °C). The Arrhenius plot for Bi_2O_3 substituted with 25% of the largest lanthanide, La, showed the β_2 to β_1 transformation occurs at 700 °C with the step increase in conductivity (Figure 5.6). On the other hand, substituting with 25% of the smallest lanthanide in this study, Dy, showed different behaviour in its Arrhenius plot (Figure 5.6). While the room temperature phase is hexagonal, it undergoes a phase change to the cubic ($Fm\bar{3}m$) δ-type phase after 700 °C. The $Fm\bar{3}m$ phase persists in the material after cooling, and so the conductivity values were not reproducible between heating and cooling cycles. As expected, the conductivity during heating was less than that during cooling where the more conductive cubic phase was still present. This comparison reveals that when substituting with larger lanthanides, the material tends to transform to the rhombohedral β_1 form, while for smaller lanthanides the material is converted to the cubic phase at high temperatures.

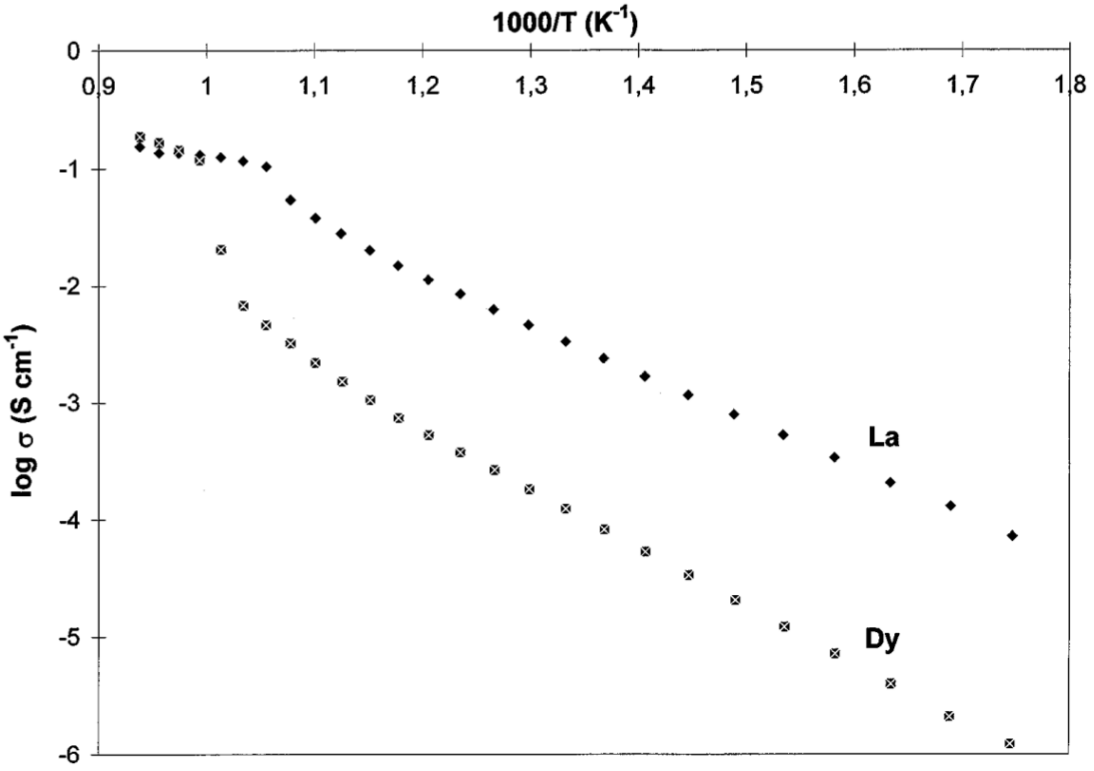


Figure 5.6: Arrhenius plot for $Bi_{0.775}La_{0.225}O_{1.5}$ and $Bi_{0.775}Dy_{0.225}O_{1.5}$ (during the second heating regime).[7]

The isothermal conductivity at 400 °C was reported as a function of Ln^{3+} radius (Figure 5.7). A general trend observed was that ionic conductivity increased as the lanthanide ion size increased. This overall increase occurs in two domains, the first is from La to Eu and the second includes Gd, Tb and Dy (Figure 5.7b). The lattice parameters and thermal expansion coefficients show linear behaviour as a function of La^{3+} radius, however, this occurs in the same two ranges of lanthanide size too. From this data, a slight difference in structure when the ionic radius is less than 0.94 Å is shown, which this is reflected in conductivity behaviour. In the discussion of the proportional relationship between lanthanide ion size and ionic conductivity, Drache and co-authors[7] suggested that the La^{3+} size influences the bond strength between mobile oxide ions and the cationic sheets. Smaller lanthanide ions result in thinner cationic sheets, and thus greater charge density. This higher charge density then leads to stronger bonds between the mobile oxide ions and the cationic sheet, and so lowers the mobility of oxide ions.

As expected, an inverse relationship exists between activation energy and La^{3+} radius (Figure 5.7a), meaning as the size of lanthanide ions increase, the activation energy decreases. This occurs within the same two size domains observed for the conductivity values. It was proposed that the activation energy is related to the motion of oxide ions from the sheet to the intersheet space. This rationale is justified by the proportional relationship between the pathway window size and the “a” lattice parameter, and is also supported by the work of Mercurio et al.[1] that proposed anion migration from the sheet to the intersheet space (i.e. pathway 3 in Figure 5.3). Therefore, the relative ease of migration for larger lanthanide ions is owed to their larger pathway windows.

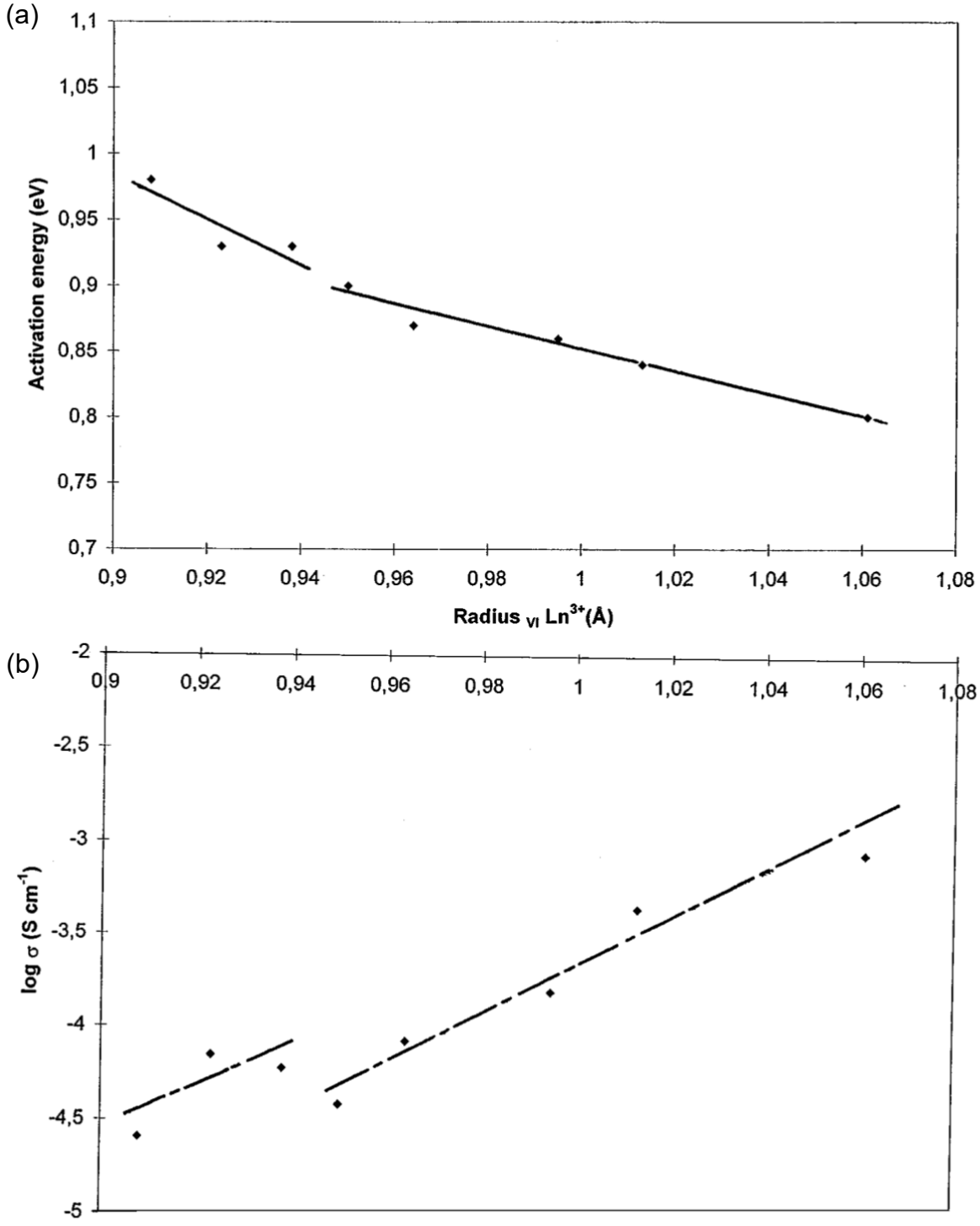


Figure 5.7: Evolution of Ln^{3+} radius with (a) activation energy and (b) isothermal conductivity at 400 °C.[7]

The oxide ion conduction of the Bi_2O_3-Ln_2O_3system with varying lanthanides was also studied by Iwahara et al.[6] While studying sintered disks of the Bi_2O_3-Ln_2O_3 system, the Ln_2O_3 content was varied to study its influence on ionic conductivity. The ionic conduction of samples was measured by recording the electrical conductivity and emf of oxygen gas concentration cells, where sample disks were used as electrolytes. The oxide ion conductivity of the Bi_2O_3-Sm_2O_3system was studied as a function of varying Sm_2O_3concentration (Figure 5.8). The broken line (1), representing pure Bi_2O_3, shows an abrupt jump in conductivity around 730 °C that is associated with the monoclinic ($P2_1/c$) to cubic ($Fm\bar{3}m$) phase change. The Arrhenius plots labelled 2, 3 and 4 show a more gradual jump in conductivity that possibly represents the phase change from rhombohedral ($R\bar{3}m$) to cubic. This is supported by the x-ray diffraction pattern of $Bi_{0.7}La_{0.3}O_{1.5}$, that shows the material is purely rhombohedral in phase content. Differential thermal analysis (DTA) measurements showed an endothermic change at these temperatures, further supporting the idea of a phase change. The Arrhenius plots marked 5 and 6 are fairly linear throughout the temperature range, which shows that materials substituted with 40-50% Sm_2O_3 have the cubic phase stabilized at room temperature up to the highest temperature measured; 900 °C (Figure 5.8).

The isothermal conductivity of the Bi_2O_3-Ln_2O_3system at 600 °C is shown (Figure 5.9b). A similar decreasing trend is identified between conductivity and extent of substitution in the system for all the lanthanides, all with similar conductivity values. These results suggest that the most significant effect on ionic conductivity is lanthanide (substituent) concentration rather than the identity of the lanthanide.

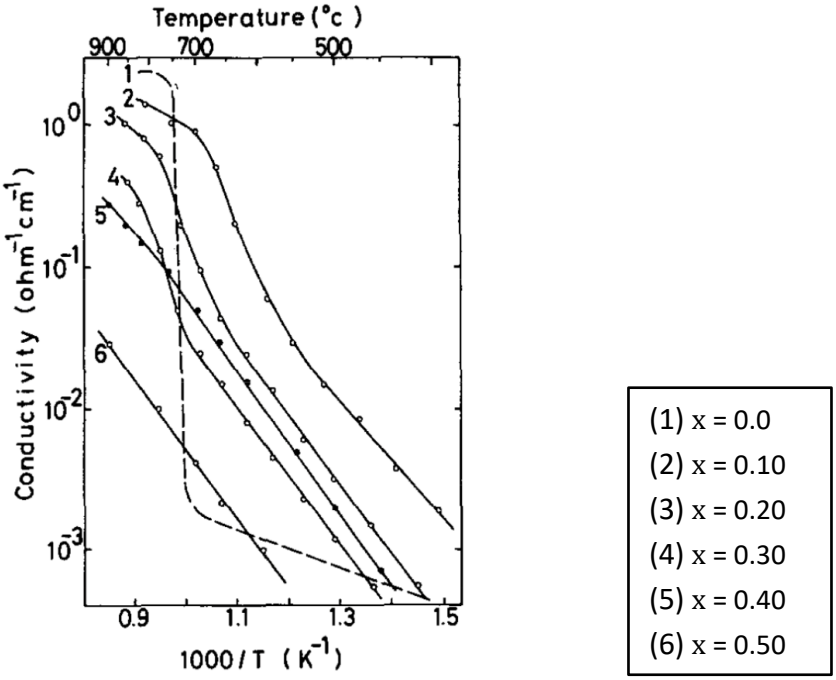


Figure 5.8: Arrhenius plots of sintered disks of the $Bi_{(1-x)}La_xO_{1.5}$ system.

The review of previous work regarding the influence of structural type and concentration on ionic conductivity in the rhombohedral R$\bar{3}$m system, has provided insight into what can be expected from the conductivity measurements of materials synthesised in this project. It was shown that larger lanthanides substituted into the rhombohedral bismuth oxide system should result in higher conductivity than the substitution of smaller lanthanides.[8] It is also implied that a lower amount of metal substitution generally tends to higher conductivities, depending on the varying structure produced. These parameters among others are investigated in the rhombohedral phase using impedance spectroscopy.

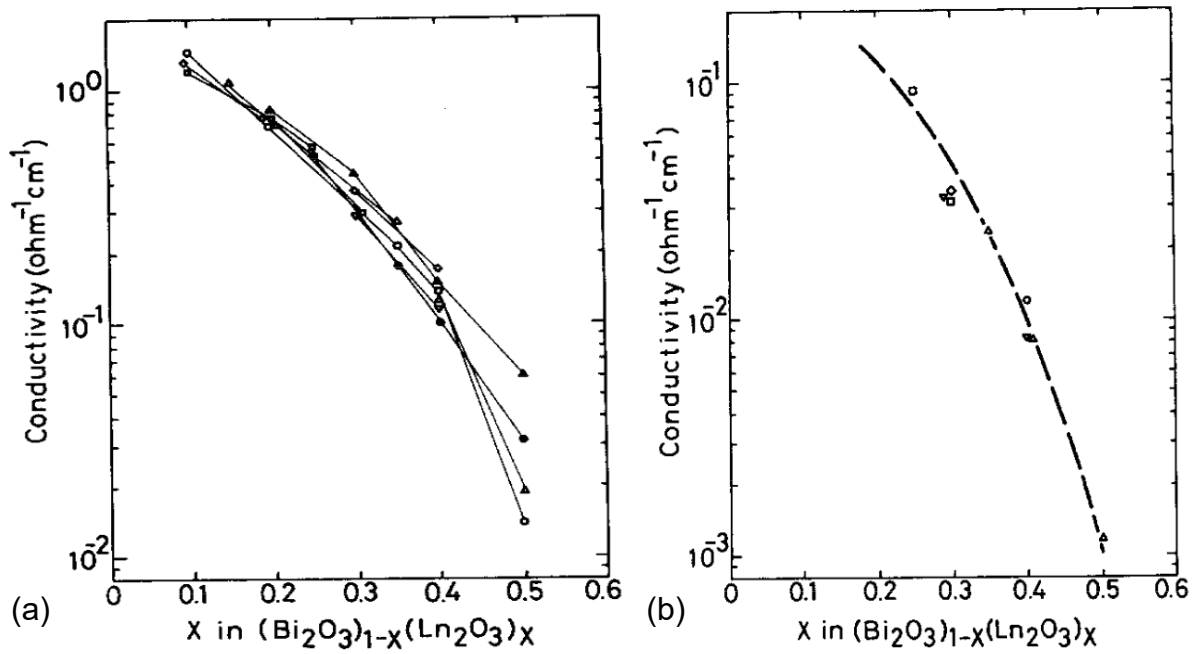


Figure 5.9: Isothermal conductivity of the $Bi_{(1-x)}La_xO_{1.5}$ system at (a) 800 °C and (b) 600 °C.

● = La ▲ = Nd ○ = Sm △ = Gd ▽= Dy □= Er ◇ = Yb

5.2 Results and Discussion

In a standard air environment, the electrical conductivity of bismuth-based electrolytes primarily arises from oxide ion movement.[9] Nyquist plots from the impedance measurements were fitted using equivalent electrical circuits, to provide physical meaning to the impedance data.[10] By varying the frequency, different processes occurring in the material can be separated in impedance measurements and thereafter examined.[10,11] The relative contributions of these various processes change with temperature. It follows that the same equivalent circuit was able to accurately fit the Nyquist plots of measurements within a temperature range for the range of materials studied. Consequently, a representative equivalent circuit is used to fit the impedimetric data within each temperature range. To interpret the impedimetric behaviour of rhombohedral (R$\bar{3}$m) bismuth oxide materials, the

impedance measurements of the $Bi_{0.75}Sm_{0.25}O_{1.5}$ material were examined in detail in the following section. All materials were prepared using the citrate sol-gel method described in the experimental methodology chapter, which involved calcination at 500 °C for 12 hours and annealing at 750 °C for 5 hours.

5.2.1 EIS of $Bi_{0.75}Sm_{0.25}O_{1.5}$ at low temperatures (250 °C – 400 °C)

The semicircle at high frequencies in the Nyquist plot for $Bi_{0.75}Sm_{0.25}O_{1.5}$ at 250 °C (Figure 5.10b) would normally correspond to a Randles circuit.[10,12] However, a constant phase element is added in parallel to the resistor instead of a capacitor. This is represented in as Q1 and R1 in the equivalent circuit (Figure 5.10a). This is necessary due to the non-ideal behaviour of the electrode and solid electrolyte. The bulk conduction and dielectric processes in solid electrolytes are represented by the high frequency semicircle. [9] This is supported by the Q1 value, which falls within the range typical for conductivity in the bulk material of 10^{-10} – 10^{-12} F $s^{(a-1)}$ (Table 5.2). It is also evident that there is no separate region representing the grain boundary, that is typically characterized with a capacitance 10^{-11} – 10^{-8} F. Therefore, the bulk and grain boundary resistances have very similar time constants and are not separable. In the lower frequency region of the Nyquist plot, a curved line is observed (Figure 5.10b). This region represents the mass transfer of species to the surface in contact with the electrode.[9] However, if this was the only process occurring at lower fre (b) cies, a straight line at 45° to the axes would be present and represented by the Warburg element in the equivalent circuit.[10,14] The combination of processes occurring is represented in the equivalent circuit by a constant phase element (Q2) in parallel to the series arrangement of a resistor (R2) and Warburg element (W2) (Figure 5.10a), which was able to fit the observed data quite well. The value of Q2 (10^{-5} – 10^{-7} F $s^{(a-1)}$) (see Table 5.2) corresponds to processes at the sample-electrode interface in this study.[15] The large size of the high-frequency semicircles and the relatively short "tail" at lower frequencies indicate that the kinetics of the charge transfer reaction dominates at low temperatures in this range and there is minimal electrode interfacial resistance.[9]

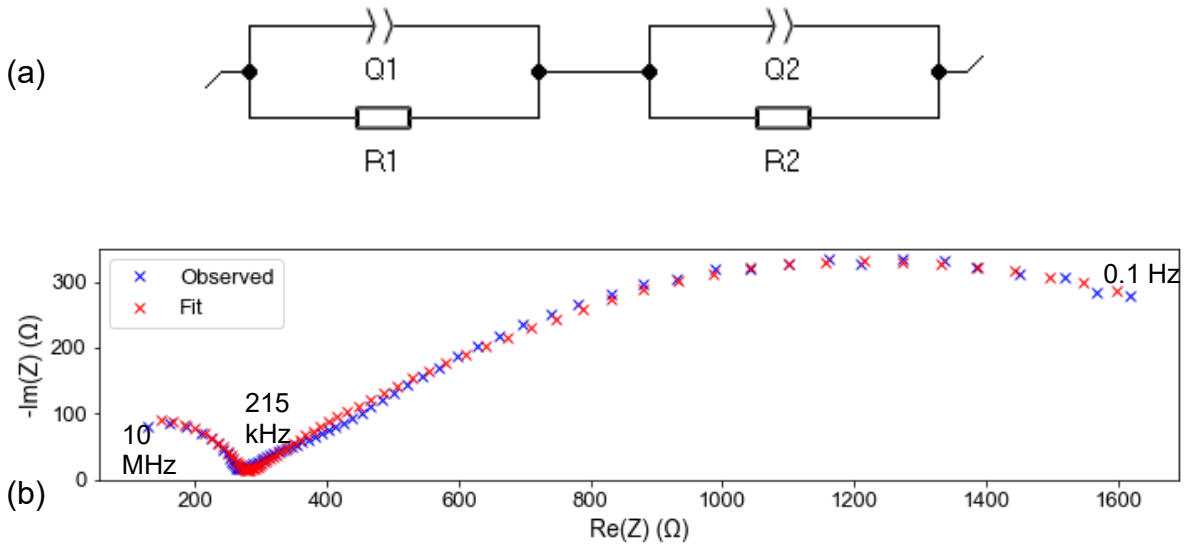


Figure 5.10: (a) The equivalent electric circuit and (b) the Nyquist plot for $Bi_{0.75}Sm_{0.25}O_{1.5}$ at 250 °C.

5.2.2 EIS of $Bi_{0.75}Sm_{0.25}O_{1.5}$ at low – intermediate temperatures (450 °C – 600 °C)

As temperature is increased, the size of the high frequency semicircle decreases (Figure 5.11b) and is still represented with a Randles circuit, labelled as Q1 and R1 in the equivalent circuit (Figure 5.11a). This means that the electrolyte resistance becomes smaller with increasing temperature. The large, curved arc at low frequencies, indicates that the diffusion of oxide to the electrode surface becomes increasingly dominant with increasing temperature.[9,11] The increased curvature suggests that diffusing species are approaching a boundary[10], and the Warburg impedance, which implies semi-infinite diffusion no longer accurately represents the process.[9,10] Even though diffusion processes are still occurring, the lower frequency region was just represented with a Randles circuit, as the kinetics of the reaction still contribute to the resistance at lower frequencies.

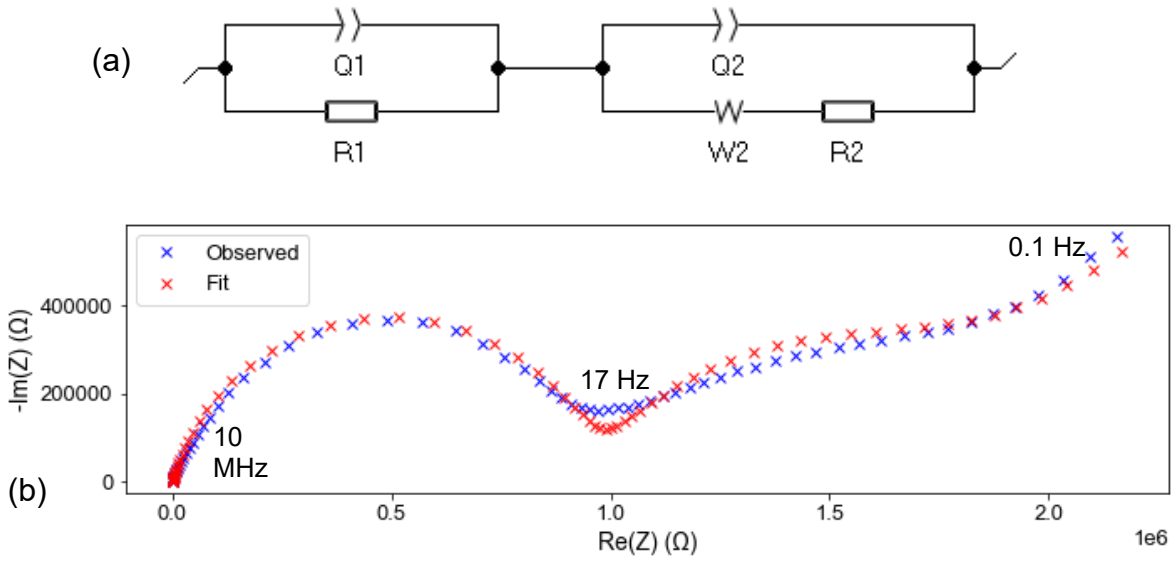


Figure 5.11: (a) The equivalent electric circuit and (b) the Nyquist plot for $Bi_{0.75}Sm_{0.25}O_{1.5}$ at 550 °C.

5.2.3 EIS of $Bi_{0.75}Sm_{0.25}O_{1.5}$ at intermediate - high temperatures (650 °C – 700 °C)

At intermediate to high temperatures, only half of the semicircle can still be observed at high frequencies (Figure 5.12b). This observation is explained by considering the relative time constants of the different processes occurring in the system[5,10,13], where the maximum frequency for the process (ω_{max}) is 1/RC.[16] The time constants of the bulk and grain-boundary impedance are lower compared to those of the electrode interface. For lower resistances at a capacitance representing processes in the bulk material, only measurements at extremely high frequencies would be able to access further data to complete the semi-circle, but this is not possible with available equipment. At lower frequencies, a distorted semicircle emerges as the temperature is increased (Figure 5.12). The first portion of the semicircle appears as a straight line, while the second portion displays more curvature. This distorted semicircle at lower frequencies indicates that the diffusion of the species is now restricted by a finite length diffusion, which is represented in the equivalent circuit as Wd2 (Figure 5.12a).[10]

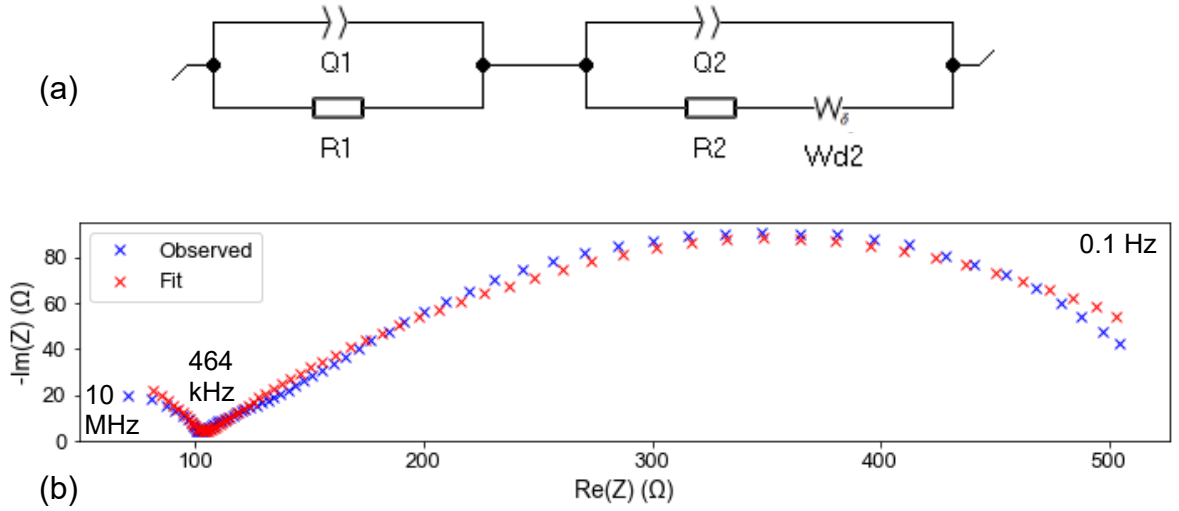


Figure 5.12: (a) The equivalent electric circuit and (b) the Nyquist plot for $Bi_{0.75}Sm_{0.25}O_{1.5}$ at 600 °C.

5.2.4 EIS of $Bi_{0.75}Sm_{0.25}O_{1.5}$ at high temperatures (750 °C)

The material's impedimetric behaviour at high temperatures (750 °C) is displayed as a single arc that relates to the finite length diffusion process (Figure 5.13b). Since the high frequency semicircle is no longer present, the use of a Randles circuit becomes impossible when modelling the high frequency data. Instead, the high frequency region is represented by a single resistor in series denoted as R1 in the equivalent circuit (Figure 5.13a) which represents the resistance of the bulk electrolyte. The finite length diffusion dominates the low frequency region, which is represented in the equivalent circuit used to fit the impedance measurement.

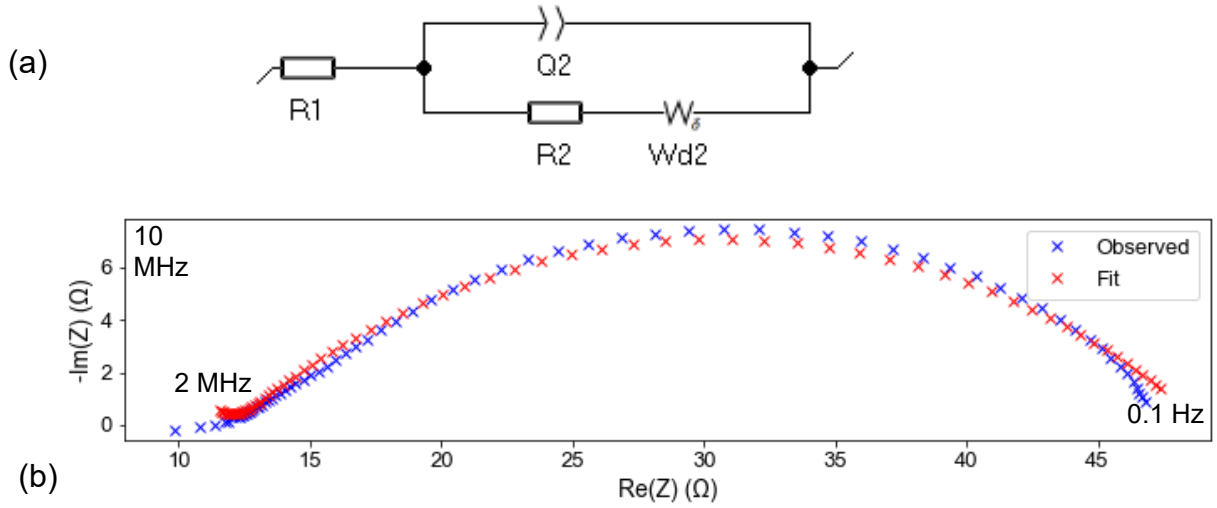


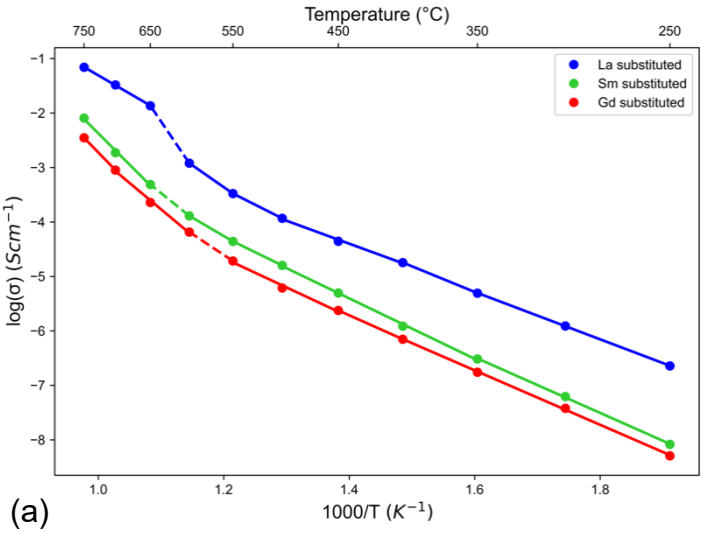
Figure 5.13: (a) The equivalent electric circuit and (b) the Nyquist plot for $Bi_{0.75}Sm_{0.25}O_{1.5}$ at 750 °C.

Table 5.2: The values of electrical elements obtained by fitting Nyquist plots with a calculated fit.

	250 °C	**550 °C**	**600 °C**	**750 °C**
Q1 (F s$^{(a-1)}$)	0.29×10^{-10}	3.7×10^{-9}	17×10^{-9}	
a1	0.83	0.76	0.68	
R1 (ohm)	9.6×10^{5}	268	102	12
Q2 (F s$^{(a-1)}$)	0.15×10^{-6}	0.28×10^{-3}	0.65×10^{-3}	2.1×10^{-3}
a2	0.68	0.42	0.42	0.47
R2 (ohm)	9.4×10^{5}	1.8×10^{3}	421	37
s2 (ohm$^{-1/2}$)	3.6×10^{5}	----------	----------	----------
Rd2 (ohm)	----------	----------	73	1.8
td2 (s)	----------	----------	0.072	0.015

5.2.5 Effect of substituent type on oxide conductivity

The heating curves of the bismuth oxide materials containing 25 mol% of different lanthanides are displayed in Figure 5.14. Upon initial inspection, it is clear that the material substituted with lanthanum behaves differently than the materials substituted with samarium and gadolinium. The La substituted material appears to maintain its structural stability as the temperature increases from 250 °C up to 600 °C. A significant increase in conductivity at 600 °C, of approximately an order in magnitude, suggests that a phase change occurs in the material at this temperature. It is common for the rhombohedral phase to transition to the $Fm\bar{3}m$ cubic phase around 600 °C, with the cubic phase being more conducting, so this could be the presumed transition occurring in the La substituted material. However, according to multiple sources, the cubic phase tends to be favoured for smaller substituents.[3,5–7] Lanthanum is the largest lanthanide with an ionic radius of 1.17 Å, making it highly unlikely for this material to transform into the cubic phase at higher temperatures.



(a)

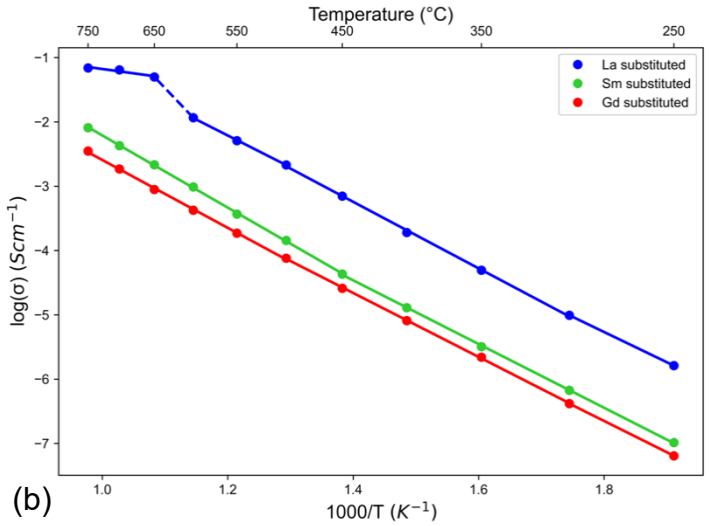


Figure 5.14: The Arrhenius plots of $Bi_{0.75}Ln_{0.25}O_{1.5}$, $Bi_{0.75}Sm_{0.25}O_{1.5}$ and $Bi_{0.75}Gd_{0.25}O_{1.5}$ displayed as their corresponding (a) heating curves and (b) cooling curves.

Previous research by Drache et al.[7] suggests that the rhombohedral bismuth oxides with larger lanthanide substituents, especially La, undergo a change to the closely-related β1 form at higher temperatures. This change was observed from around 650 °C for $Bi_{0.775}Sm_{0.225}O_{1.5}$ [7], while the transition in this study occurs at 600 °C for $Bi_{0.75}La_{0.25}O_{1.5}$. This structural transition was also reversible as the cooling curve in Figure 5.14b demonstrates the La substituted material experiences a significant decrease in conductivity at 650 °C. Unfortunately, structure determination with varying temperature was not possible in this work, as it could have confirmed the high temperature phase. Despite having similar compositions, the conductivities of these materials were different, with that for $Bi_{0.775}La_{0.225}O_{1.5}$ measured as ~0.16 S cm^{-1} at 750 °C [7], and for $Bi_{0.75}La_{0.25}O_{1.5}$ in this work being about half that, at 0.0693 S cm^{-1} at 750 °C (Table 5.3). This difference could suggest that the two materials do not convert to the same high temperature form, or the different synthetic methods produce products with different morphologies which could affect the conductivity, or that the extent of sintering was different. It is worth noting the XRD results of the $Bi_{0.75}La_{0.25}O_{1.5}$ sample discussed in Chapter 3, which exhibited an underlying phase that could not be identified with Rietveld refinements. This impurity phase could also influence the impedimetric behavior of the material.

The Sm and Gd substituted materials exhibit similar behaviour to each other during their heating and cooling cycles. These materials show structural stability during the heating process until 600 °C for the Sm substituted material and 550 °C for the Gd substituted material based on the linear Arrhenius plots. Although there is an increase in the slope of these plots above the mentioned temperature, there is no step function to correspond to a clear phase change in the temperature range

studied. According to laboratory XRD measurements, the Gd substituted material did contain a small amount (3%) of the $Fm\bar{3}m$ cubic phase. Hence, the slight increase in conductivity may be attributed to a partial conversion to the cubic phase (with full conversion only occurring at higher temperatures). However, this proposed mechanism may not be able to explain the change in activation energy in the Sm substituted material. According to laboratory XRD results, this material consists of the rhombohedral phase only. Since Sm is also a relatively small substituent ion, conversion to the cubic phase is still plausible at high temperatures. However, the cooling curves show that this change is not reversible, which proves the cubic formation change unlikely (Figure 5.14b). The high temperatures involved in sample preparation, such as annealing and sintering at 750 °C, could also affect the starting structure of the material used in EIS measurements. However, the starting structures of selected pellets were measured using laboratory XRD, which were confirmed to be rhombohedral. Another plausible explanation is the β_2 to β_1 transition, however this would require variable temperature structure analysis to confirm. A more plausible explanation is a structural ordering change. Nonetheless, it can be confidently concluded that this change in slope does not indicate an overall phase change within the material. Whatever transformation occurs in these materials is not reversible, as there is no observed structural change upon cooling

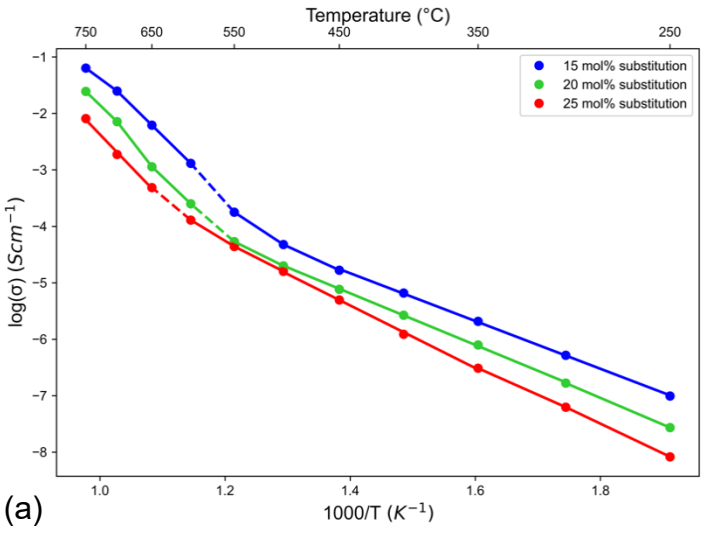
The behaviour of the Gd substituted material was not expected, as the rhombohedral phase appears to persist up to high temperatures (Figure 5.14a). The small size of gadolinium should favour the material's conversion to the cubic (fcc) phase when heated [6,17]. This phase change from rhombohedral to cubic was observed in a similar material; $Bi_{0.775}Gd_{0.225}O_{1.5}$ in the work of Drache and co-workers[7] in 1998. The study by Takahashi and co-authors[18] also showed that materials containing 10 – 30 mol% Gd form the rhombohedral phase at room temperature and the fcc structure at high temperatures. Therefore, the impedimetric behaviour of the Gd substituted material does not correspond with previous studies. Similarly, a previous study[6] proposed Sm substituted materials in the composition range of 20 – 30 mol% will also form the rhombohedral phase at room temperature and then transition to the cubic (fcc) phase at higher temperatures. However, this is not observed in the Sm substituted material shown in Figure 5.14. The similarity in outcomes between these materials may suggest that the synthetic method used results in greater stability of the rhombohedral phase, however this would need to be confirmed by other variable temperature techniques.

The 25 mol% substituted materials exhibit a consistent trend in conductivity across the temperature range measured, with larger substituents resulting in higher ionic conductivities. The La, Sm and Gd substituents have ionic radii of 1.17 Å, 1.079 Å and 1.053 Å, respectively. Their respective conductivities at 750 °C are 0.0693 S cm^{-1}, 0.00812 S cm^{-1} and 0.00325 S cm^{-1} (Table 5.3). The La substituted material does have a significantly larger conductivity, not only due to its somewhat larger size, but

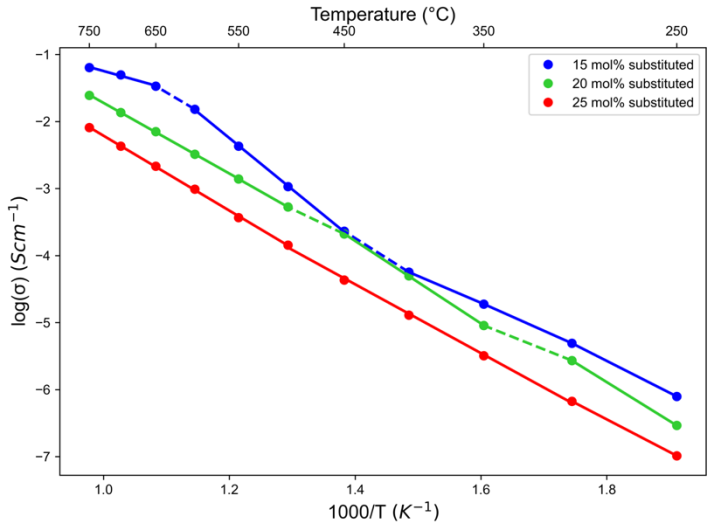
also since this material undergoes a phase change to a more conductive form at high temperatures. However, at temperatures before the phase change occurs, the La substituted material is still significantly more conductive. Since the predominant structure in the Sm and Gd substituted materials is rhombohedral, their conductivities at 750 °C serve as a reliable range of conductivities for the rhombohedral phase at high temperatures.

5.2.6 Effect of substituent concentration on oxide conductivity

The relationship between ionic conductivity and substituent concentration was investigated for the samarium substituted bismuth oxide materials, and the Arrhenius plots are presented in Figure 5.15. The main finding was that a lower substituent concentration results in higher ionic conductivity. At 750 °C, the 15 mol% substituted material has the highest conductivity at 0.064 S cm^{-1}, while the 25 mol% substituted material has the lowest conductivity of 0.0081 S cm^{-1} (Table 5.3). Despite having the highest conductivity, it is important to note that the material with 15 mol% substitution does not appear to be structurally stable during the heating and cooling regimes. From 550 °C, a significant increase in conductivity is observed during the heating cycle, indicating a structural transition (Figure 5.15a). Based on laboratory XRD refinements that showed the 15 mol% Sm sample contained a phase mixture of rhombohedral (77%) and cubic (23%), this transition is most likely further conversion from the rhombohedral to cubic phase. The combination of a lower dopant amount and the smaller Sm size (1.079 Å) makes the material highly susceptible to transforming into the cubic phase upon heating.[5,19,20] This is also supported by the slight flattening of the heating curve at high temperatures, which is indicative of a transition ending. The material underwent a structural change during the cooling cycle at 650 °C (Figure 5.15b). This is most likely the reversible phase transformation observed during heating, which suggests a conversion from the cubic phase back to the rhombohedral phase. Another slope change is observed at 450 °C during cooling, which is not commonly observed for the rhombohedral phase. This slight slope change is likely noise in the data at lower temperatures.



(a)



(b)

Figure 5.15: The Arrhenius plots of $Bi_{0.85}Sm_{0.15}O_{1.5}$, $Bi_{0.8}Sm_{0.2}O_{1.5}$ and $Bi_{0.75}Sm_{0.25}O_{1.5}$ displayed by their corresponding (a) heating curves and (b) cooling curves.

The 20 mol% Sm material showed similar trends to the 15 mol% Sm material. During the heating cycle, it undergoes a slope change at 550 °C (Figure 5.15a). This transition could be a rhombohedral to cubic phase transition. However, this transition does not result in a significant increase in conductivity, which could be explained as only a portion of the material undergoing this change. Interestingly, the material with 20 mol% Sm experiences another transition at 650 °C during heating, which could be another partial conversion to the cubic phase since there is no notable increase in conductivity (Figure 5.15a).

The cooling curve reveals that the 20 mol% Sm material remains structurally stable until 500 °C, at which point a structural change occurs as depicted by the slope change in Figure 5.15b. This may represent the same reversible transition observed in the 15 mol% Sm sample during heating, whereby the cubic phase converts back to the rhombohedral phase. Notably, this transition occurs at a temperature 50 °C higher than in the 15 mol% Sm material. Another slope change occurs during cooling at 350 °C, that can be regarded as noise data due to the low temperature of measurement.

As discussed earlier, the 25 mol% substituted material experiences a structural change during the heating cycle at 650 °C, which has been proposed as the β_2 to β_1 transition, which is most likely as this change is not reversible upon cooling (Figure 5.15b). However, this would require a complimentary variable temperature measurement to confirm.

Varying the Sm substituent concentration in the $Bi_{1-x}Sm_xO_{1.5}$ material has supported the fact that the lower the substitution, the higher the conductivity. However, lower amounts of substituents do not stabilize the rhombohedral phase fully as seen from the XRD data discussed in a previous chapter, and phase transition to the cubic phase readily occurs at high temperatures in the $Bi_{1-x}Sm_xO_{1.5}$ system. In general, the 25 mol% substituted material appears to provide the best phase stability despite having a slightly lower conductivity.

5.2.3 Structure - property relationship

5.2.3.1 Temporal effects of heating

The 25 mol% Sm material was used as a representative sample to investigate the influence of annealing duration (at 750 °C) during the synthesis on the material's conductive properties. Three materials, all having the same composition, were prepared and subjected to different annealing durations of 5, 10, and 15 hours (Figure 5.16). All materials predominantly formed the rhombohedral phase according to XRD measurements, with the 5 hour and 10 hour annealed samples forming the single rhombohedral phase. The 15 hour annealed sample did exhibit a minor impurity phase, that could not be identified using Rietveld refinements of XRD data. Furthermore, the 5 and 10 hour annealed samples shared other structural similarities such as identical unit cell volumes of 432 $\text{Å}^3$and similar crystallinities of 116 and 110 nm respectively. On the other hand, the 15 hour annealed sample had a unit cell volume of 434 Å^3 and crystallinity of 72.8 nm. The structural properties revealed that the 5 hour and 10 hour annealed samples are closely related, which was not observed in the impedimetric behaviour data. In both the heating and cooling curves, the 5 hour and 15 hour curves have a strong overlap with almost identical conductivity values. At 750 °C, the 15 hour sample had a conductivity of 0.0076 S cm^{-1}, and the 5 hour sample had a conductivity of 0.0081 S cm^{-1}. Both materials have a slope change during heating from 550 °C to 650 °C, which is not observed in the cooling curve, The 10 hour sample follows similar behaviour, but at lower conductivities than the other two materials. This material had the lowest conductivity of 0.0034 S cm^{-1} at 750 °C. The XRD and EIS measurements did not show any correlation, which may suggest that these measurements should be completed several times and inspected for reproducibility. It is common for EIS measurements to be repeated and the average of results are recorded.

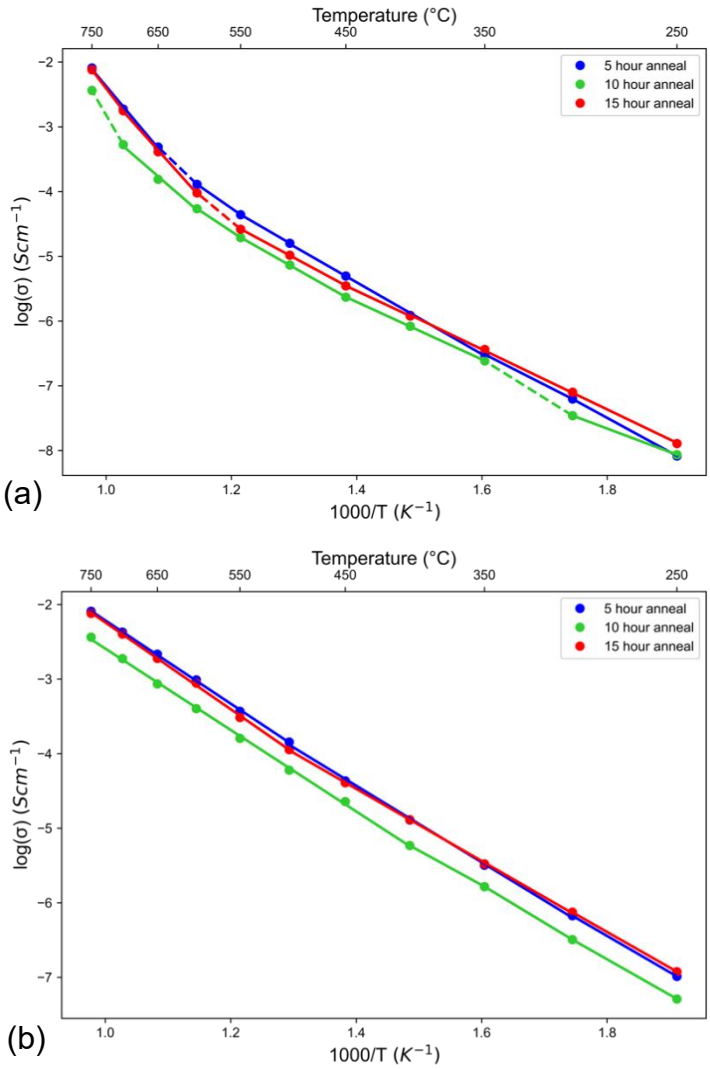
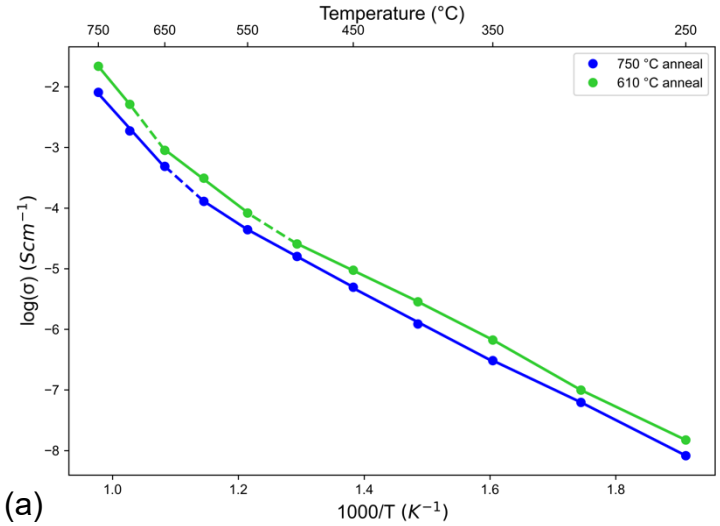


Figure 5.16: The Arrhenius plots of $Bi_{0.75}Sm_{0.25}O_{1.5}$ that were subjected to 5, 10 and 15 hour annealing time as displayed by their (a) heating curves and (b) cooling curves.

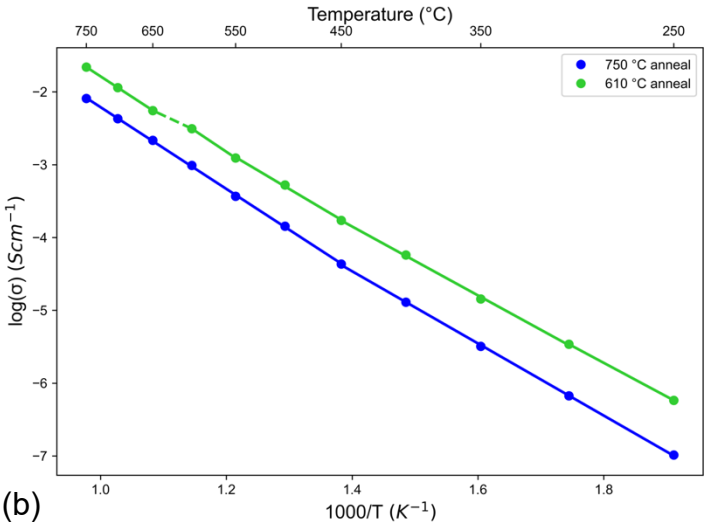
5.2.3.2 Effect of annealing temperature

Once again, the representative sample used is the 25 mol% Sm material and was prepared by annealing either at 610 °C or 750 °C for 5 hours. The pellets of these materials were sintered at the same temperature as their respective annealing temperatures to keep the temperature variable fixed. The material that was annealed at 610 °C displayed a phase mixture of rhombohedral and cubic in XRD measurements, and exhibited higher conductivities throughout the heating and cooling process in EIS measurements (Figure 5.17). In particular, the conductivities at the 750 °C point of measurement for the 610 °C and the 750 °C annealed samples were 0.0219 S cm^{-1} and 0.00812 S cm^{-1}, respectively (Table 5.3). This disparity is quite large, which could possibly be better understood by examining the structural stability of the two materials. During heating, the 610 °C annealed sample appears to

undergo two transitions corresponding to the change in slopes of the Arrhenius plot, one at 500 °C and another 650 °C (Figure 5.17a).



(a)



(b)

Figure 5.17: The Arrhenius plots of $Bi_{0.75}Sm_{0.25}O_{1.5}$ that were subjected to annealing at 610 °C and 750 °C as displayed by their (a) heating curves and (b) cooling curves.

However, these are relatively small slope changes that do not correspond to notable step increases in conductivity. The 750 °C annealed material also undergoes a slope change during heating at 600 °C, that is not reversed upon cooling (Figure 5.17

Figureb). While these changes occur at different temperatures, the most likely explanation of this behaviour is the β_2 to β_1 transition observed in rhombohedral materials from previous work.[1,7] These results showed the expected behaviour of the dominant rhombohedral phase in both materials, as well as the increased

conductivity in the 610 °C annealed material due to the low amounts of $Fm\bar{3}m$ cubic phase present.

5.3 Conclusion

The review of relevant literature allowed for the interpretation of the conductivity mechanism in the $R\bar{3}m$ structure. Two widely referenced accounts of work were used as starting points to understand the oxide ion motion in the layered structure. Mercurio and coworkers [1] proposed that oxide ions move in a direction parallel to the c-axis, as evidenced by the oxygen occupancies at increasing temperatures determined by single crystal neutron diffraction. They acknowledged the preceding work of Conflant *et al.*[2] that proposed the bidimensional character of oxide ion diffusion, determined by single crystal x-ray diffraction. It was concluded that the most likely ion migration involves a combination of ions moving along the c-axis and ab plane.

The structural effects on conductivity were also reviewed using reliable sources in literature. Drache and co-workers [7] studied the effect of substituent type and size by varying the lanthanide in the $Bi_{0.775}Ln_{0.225}O_{1.5}$ system. Their results showed that substituent size and conductivity have a largely proportional relationship, and that the lanthanides appear to behave in two domains according to size. It was proposed that structural behaviour of the lanthanides can be categorized into two domains; those with larger and smaller than 0.94 Å ionic radii. This work also showed how larger lanthanides (Sm and Gd) tend to form the high-temperature rhombohedral ($\beta 1$) form at 700 °C, while smaller lanthanides (La) transform to the cubic phase at high temperatures for the $Bi_{0.75}Ln_{0.25}O_{1.5}$ system. The Bi_2O_3-Ln_2O_3 system was also examined by Iwahara *et al.*[6] to see how lanthanide concentrations affect the conductivity of the system. This study was conducted with various lanthanides, and it was found that all seem to follow a general trend as the Ln_2O_3 amount is varied. There is an inverse relationship between the substituent concentration and conductivity. The similar values across the lanthanides measured suggests that substituent concentration may be the dominant structural influence on conductivity.

The influence of substituent type, substituent concentration, sample annealing durations and annealing temperature on the rhombohedral structure's ionic conductivity were investigated using variable-temperature electrochemical impedance spectroscopy. After the impedimetric behaviour was measured within the frequency range of 10 MHz and 0.1 Hz, the Nyquist plots were modelled with equivalent electric circuits to provide physical meaning to the impedance data. At high frequencies, the bulk resistance is exhibited, while diffusion of the species to the electrode interface occurs at low frequencies. The high-frequency semicircle, representing the bulk behaviour of the material, gradually disappeared as the measurement's temperature increased. The Nyquist plots at high frequencies can be modelled with a modified Randles circuit, consisting of a constant phase element and resistor in parallel. The Nyquist plots in the low-frequency region constitute a combination of processes with the mass diffusion to the electrode surface taking place and possibly some charge transfer processes too. Consequently, both

processes are used in equivalent circuits to represent the low frequency behaviour. The mass diffusion is described using the Warburg element. At intermediate temperatures, the ions begin approaching the electrode boundary, and the diffusion is no longer semi-infinite as described by the Warburg element. The diffusion of ions between intermediate and high temperatures is defined by a finite diffusion element.

The effect of substituent type on the conductivity was performed on materials that mostly formed the rhombohedral phase at room temperature. The Arrhenius plots of materials containing 25 mol% of lanthanum, samarium and gadolinium were compared. It was clear that conductivities increase as the substituent size increased. The La substituted material had the highest conductivity of 0.0693 S cm^{-1} at 750 °C. However, the La-containing material displayed a significant jump in conductivity at 700 °C, representing an unexpected structural change. The most likely reason for this structural transition is the conversion to the high-temperature β_1 form of the rhombohedral phase, as this was reported to occur in similar structures at approximately the same temperature. The Sm and Gd containing materials do experience a minor structural change upon heating as reflected by the increasing slopes in the Arrhenius plot, but show structural stability throughout the cooling cycle. It has been proposed that there may be a minor conversion of some material to the cubic phase. This may be especially true for the Gd substituted material, as gadolinium's small size favours the conversion to the cubic phase at elevated temperatures, and trace amounts of the cubic phase were identified in the sample using XRD measurements. However, additional variable temperature measurements are required to confirm the proposed phase behaviour with heating.

The effect of substituent concentration on conductivity was studied for the $Bi_{1-x}Sm_xO_{1.5}$ system. A lower substituent concentration results in higher conductivity, with the 15 mol% substituted material having the highest conductivity of 0.064 S cm^{-1} at 750 °C. This significant conductivity was influenced by the phase mixture of rhombohedral (77%) and cubic (23%) identified present. While the lower substituted materials may have higher conductivities, they are not structurally stable throughout the heating and cooling regime as materials with a higher substituent amount.

Lastly, the relationship between structure and property was further explored by examining the temporal effects of heating and the influence of annealing temperature. The EIS results of temporal effects of heating did not correlate with XRD results, and required further investigating to understand. On the other hand, the EIS results of annealing temperature complimented the XRD measurements. Since the 610 °C material contained trace amounts of the cubic phase, this sample had higher conductivities. It is worth noting that since the rhombohedral phase was dominant in both materials, both samples displayed similar behaviour during heating and cooling cycles.

Among the materials investigated, $Bi_{0.75}La_{0.25}O_{1.5}$ and $Bi_{0.85}Sm_{0.15}O_{1.5}$ exhibited the highest conductivities. However, the presence of impurity phases detected in their XRD patterns at room temperature likely influenced their variable temperature conductivity measurements. Conversely, $Bi_{0.75}Gd_{0.25}O_{1.5}$ and 10-hour annealed $Bi_{0.75}Sm_{0.25}O_{1.5}$ displayed the lowest conductivities. The low conductivity of $Bi_{0.75}Gd_{0.25}O_{1.5}$ was unexpected, considering the trace amounts of the highly conductive cubic phase at room temperature. While the low conductivity of the 10-hour annealed $Bi_{0.75}Sm_{0.25}O_{1.5}$ was anticipated due to its single rhombohedral phase, it deviates significantly from other materials with the same phase. Comparison with literature values revealed significantly higher conductivities in previous work, which could be influenced by factors such as differences in coating and measurement techniques. Another potential influence is the highly conductive cubic phase being the dominant phase at ambient temperature. Common solid electrolytes like 25YSB (25 mol% yttria-stabilized bismuth oxide), where yttrium, with its relatively small ionic radius of 1.019 Å were included for comparison. These values show the conductive differences between commonly cited solid electrolytes and the $R\bar{3}m$ rhombohedral phase of substituted bismuth oxide.

Table 5.3: Conductivities of materials at 750 °C in this work in comparison to commonly used solid electrolytes.

Material	σ /S cm^{-1}	Coating	Phase (Ambient temp.)	Phase (750 °C)	Technique	Ref
$(La_2O_3)_{0.25}(Bi_2O_3)_{0.75}$	0.0693	Gold	Rhombohedral	Unconfirmed	Potentiostatic EIS in air	This work
$(Sm_2O_3)_{0.25}(Bi_2O_3)_{0.75}$	0.00812	Gold	Rhombohedral	Unconfirmed	Potentiostatic EIS in air	This work
$(Gd_2O_3)_{0.25}(Bi_2O_3)_{0.75}$	0.00325	Gold	Rhombohedral & cubic	Unconfirmed	Potentiostatic EIS in air	This work
$(Sm_2O_3)_{0.15}(Bi_2O_3)_{0.85}$	0.0637	Gold	Rhombohedral & cubic	Cubic	Potentiostatic EIS in air	This work
$(Sm_2O_3)_{0.20}(Bi_2O_3)_{0.80}$	0.0246	Gold	Rhombohedral	Cubic	Potentiostatic EIS in air	This work
$(Sm_2O_3)_{0.25}(Bi_2O_3)_{0.75}$ ■	0.0219	Gold	Rhombohedral	Unconfirmed	Potentiostatic EIS in air	This work
$(Sm_2O_3)_{0.25}(Bi_2O_3)_{0.75}$ ∝	0.00366	Gold	Rhombohedral	Unconfirmed	Potentiostatic EIS in air	This work
$(Sm_2O_3)_{0.25}(Bi_2O_3)_{0.75}$ †	0.0076	Gold	Rhombohedral	Unconfirmed	Potentiostatic EIS in air	This work
$(La_2O_3)_{0.225}(Bi_2O_3)_{0.775}$	~ 0.16	Gold	Rhombohedral β2 form	Rhombohedral β1 form	Potentiostatic EIS	[7]
$(Sm_2O_3)_{0.20}(Bi_2O_3)_{0.80}$	~ 0.5	Silver	Rhombohedral/cubic	Cubic	Oxygen concentration cell	[6]
$(Sm_2O_3)_{0.30}(Bi_2O_3)_{0.70}$	~ 0.06	Silver	Rhombohedral	Cubic	Oxygen concentration cell	[6]
$(Gd_2O_3)_{0.10}(Bi_2O_3)_{0.90}$	~ 0.95	Silver	Rhombohedral	Cubic	Oxygen concentration cell	[17]
$(Gd_2O_3)_{0.20}(Bi_2O_3)_{0.80}$	~ 0.09	Silver	Rhombohedral	Cubic	Oxygen concentration cell	[17]
25YSBi	~ 0.22	Platinum	Cubic	Cubic	Complex admittance	[21]
8YSZ	~ 0.02		Cubic	Cubic	Oxygen concentration cell	[22]
25YSBi	0.398		Cubic	Cubic	Oxygen concentration cell	[23]
GDC (10GdC)	~ 0.07		Cubic	Cubic	Wet oxygen (3 vol% H2O)	[22]

■ = 610 °C anneal ∝ = 10 hour anneal † = 15 hour anneal

5.4 References

1. Mercurio, D., Champarnaud-Mesjard, J.C. & Frit.B. Thermal Evolution of the Crystal Structure of the Rhombohedral $Bi_{0.75}Sr_{0.25}O_{1.375}$ Phase: A Single Crystal Neutron Diffraction Study. *Journal of. Solid State Chemistry.* **112**, 1–8 (1994).
2. Conflant, P., Boivin, J.-C. & Thomas, D. Etude structurale du conducteur anionique $Bi_{0.765}Sm_{0.235}O_{1.383}$. *Journal of Solid State Chemistry* **35**, 192–199 (1980).
3. Ahi, A., Mellergård, A. & Eriksson, S.G. Local and average atomic order of ion-conducting $Bi_{0.775}La_{0.225}O_{1.5}$ studied by neutron scattering and reverse Monte Carlo simulations. *Solid State Ionics.* **177**, 289–297 (2006).
4. Obbade, S., Huve, M., Suard, E., Drache, M. & Conflant, P. Powder Neutron Diffraction and TEM Investigations of $Bi_{0.775}Ln_{0.225}O_{1.5}$ Oxide Conductors (Ln=La, Pr, Nd, Sm, Tb, Dy) with Rhombohedral Bi–Sr–O type: Structural Relationships with Monoclinic ε- $Bi_{4.86}La_{1.14}O_9$ Form. *Journal of Solid State Chemistry.* **168**, 91–99 (2002).
5. Sammes, N. M., Tompsett, G. A., Nafe, H. & Aldinger, F. Bismuth Based Oxide Electrolytes Structure and Ionic Conductivity. *Journal of the European Ceramic Society.* **19**, 1801 - 1826 (1999).
6. Iwahara, H., Esaka, T. & Sato, T. Formation of High Oxide Ion Conductive Phases in the Sintered Oxides of the System Bi_2O_3 -Ln_2O_3 (Ln = La -Yb). *Journal of Solid State Chemistry*. **39**, 173 - 180 (1981).
7. Drache, M., Obbade, S., Wignacourt, J. P. & Conflant, P. Structural and Conductivity Properties of $Bi_{0.775}Ln_{0.225}O_{1.5}$ Oxide Conductors (Ln=La, Pr, Nd, Sm, Eu, Gd, Tb, Dy) with Rhombohedral Bi–Sr–O Type. *Journal of Solid State Chemistry* **142**, 349–359 (1999).
8. Takahashi, T., Esaka, T. & Iwahara, H. Conduction in Bi_2O_3 -based oxide ion conductor under low oxygen pressure. II. Determination of the partial electronic conductivity. *Journal of Applied Electrochemistry*. **7**, 303 - 308 (1977).
9. Huang, K., Feng, M. & Goodenough, J.B. Bi_2O_3 - Y_2O_3 - CeO_2 solid solution oxide-ion electrolyte. *Solid State Ionics.* **89**, 17–24 (1996).
10. Lazanas, A. Ch. & Prodromidis, M. I. Electrochemical Impedance Spectroscopy—A Tutorial. *ACS Measurement Science Au.* **3**, 162–193 (2023).
11. Boukamp, B. A. A Linear Kronig-Kramers Transform Test for Immittance Data Validation. *Journal of Electrochemistry Society.* **142**, 1885–1894 (1995).
12. Schönleber, M. & Ivers-Tiffée, E. Approximability of impedance spectra by RC elements and implications for impedance analysis. *Electrochemistry Communications.* **58**, 15–19 (2015).
13. Abrahams, I., Krok, F., Malys, M. & Wrobel, W. Phase transition studies in BIMEVOX solid electrolytes using AC impedance spectroscopy. *Solid State Ionics.* **176**, 2053–2058 (2005).

14. Wu, Y. C., Chang, Y. W. & Wang, S. F. Electrical Properties and Microstructural Analysis of Aliovalent-Ion (Y^{3+}, Nb^{5+})–Doped Bismuth-Based Solid-Oxide Electrolyte. *Ferroelectrics.* **455**, 123–128 (2013).
15. Irvine, J. T. S., Sinclair, D. C. & West, A. R. Electroceramics: Characterization by Impedance Spectroscopy. *Advanced Materials.* **2**, 132–138 (1990).
16. Irvine, J. T. S & Connor, P. *Solid Oxide Fuels Cells: Facts and Figures: Past Present and Future Perspectives for SOFC Technologies.* (Springer London, London, 2013).
17. Takahashi, T., Esaka, T. & Iwahara, H. High oxide ion conduction in the sintered oxides of the system Bi_2O_3 - Gd_2O_3 . *Journal of Applied Electrochemistry.* **5**, 197 - 202 (1975).
18. Takahashi, T., Iwahara, H. & Nagai, Y. High oxide ion conduction in sintered Bi_2O_3 containing SrO, Ca O or La_2O_3 . *Journal of Applied Electrochemistry.* **2**, 97 - 104 (1972).
19. Jiang, N. & Wachsman, E. D. Structural Stability and Conductivity of Phase-Stabilized Cubic Bismuth Oxides. *Journal of the American Ceramic Society.* **82**, 3057–3064 (2004).
20. Watanabe, A. The dependence of polymorphism on the ionic radius of Ln^{3+} (Ln = La-Er, Y) in the oxide ion conductors $Bi_{0.775}Ln_{0.225}O_{1.5}$. *Solid State Ionics.* **67**, 25 - 28 (1993).
21. Fung, K. Z. & Virkar, A. V. Phase Stability, Phase Transformation Kinetics, and Conductivity of Y_2O_3 -Bi_2O_3 Solid Electrolytes Containing Aliovalent Dopants. *Journal of the American Ceramic Society.* **74**, 1970–1980 (1991).
22. Mahato, N., Banerjee, A., Gupta, A., Omar, S. & Balani, K. Progress in material selection for solid oxide fuel cell technology: A review. *Progress in Material Science.* **72**, 141–337 (2015).
23. Watanabe, A. & Kikuchi, T. Cubic-Hexagonal transformation of Yttria-Stabilized δ-Bismuth Sesquioxide, $Bi_{2-2x}Y_{2x}O_3$ (x = 0.215 - 0.235). *Solid State Ionics*. **21**, 287 - 291 (1986).

Chapter 6 – General Conclusion

The overall aim of this project was to investigate the formation and conductive properties of the R$\bar{3}$m rhombohedral phase of doped Bi_2O_3. The aim was systematically approached by individually examining parameters that may influence phase formation and properties. These structural and synthetic parameters comprised of substituent type, substituent concentration, annealing duration and annealing temperature. These parameters were investigated using a range of techniques that included synchrotron and laboratory x-ray diffraction, total scattering measurements, Raman scattering and Electrochemical impedance spectroscopy. Therefore, the influence of these factors on the rhombohedral phase of substituted bismuthate were extensively examined in this work.

6.1 Substituent type

The potential contribution of the lanthanide substituent to rhombohedral phase behaviour was explored by studying three lanthanide substituted systems. These lanthanides were lanthanum, samarium and gadolinium. Their compositions in the bismuth oxide system were 25 mol% in their respective compounds, such that each material had the chemical formula $Bi_{0.75}Ln_{0.25}O_{1.5}$. Rietveld refinements of synchrotron XRD measurements revealed that 25 mol% of lanthanum, samarium or gadolinium substituted in Bi_2O_3 predominantly formed the rhombohedral phase. Similarly, laboratory XRD data exhibited the same major rhombohedral phase formation, with underlying phases that could not be identified. The lanthanum substituted material was distinctly different from the other two in both synchrotron and laboratory XRD measurements. The La-substituted sample displayed a significant downward shift, that is quite large to be attributed to it's relatively large ionic radii. The gadolinium substituted material also displayed distinct behaviour. Laboratory XRD measurements revealed a phase mixture of rhombohedral and Fm$\bar{3}$m cubic, that was not detected in synchrotron XRD measurements. This difference in behaviour was owed to the time of measurements, where laboratory XRD was measured shortly after synthesis, and synchrotron XRD was measured only weeks thereafter. The minority cubic phase may have transformed to the more stable rhombohedral phase during the interim. Nevertheless, both data sets confirm that all three lanthanide substituents with a 25 mol% concentration in Bi_2O_3 form an average structure of mainly rhombohedral. Total scattering measurements were completed to probe the local structure using the PDFs of the 25 mol% lanthanide substituted materials. The qualitative inspection of the PDFs showed almost no difference between each other. Refinements were completed on the functions by fitting the experimental data to a rhombohedral model structure. These refinements had a strong match with good figures of merit. There were minor peaks that weren't accounted for by the rhombohedral model, however the local structure can be confidently described as mainly rhombohedral. Since minor cubic traces were

identified in the XRD patterns of some samples, it was deduced that this may be the probable impurity phase on the local scale too.

The ambient Raman scattering of the 25 mol% lanthanide substituted materials was measured to investigate the local structure too. The qualitative analysis of the Raman spectra showed a distinct difference between the lanthanum-substituted sample and the other two materials (samarium and gadolinium substituted). While the lanthanum-substituted sample lacked a few characteristic bands, all three spectra shared significant similarity. The conductive properties of the 25 mol% substituted materials were measured using Electrochemical impedance spectroscopy between 200 and 750 °C. Once again, the lanthanum substituted material behaves quite differently than the other two. The lanthanum-containing sample displayed a significant conductivity jump around 600 °C. The cause of this behavior could not be confirmed, but it has been proposed that the rhombohedral phase converts to its high temperature form, that has been reported in previous work. The samarium and gadolinium containing materials do undergo a slight structural change upon heating, at 600 and 550 °C respectively. This change is not reversed in the cooling cycle, and is not large enough to correspond to a general phase change. The most likely cause of this structural change is a minor conversion of some material to the $Fm\bar{3}m$ cubic phase. This is supported by the small size of gadolinium, that favors the conversion to the cubic phase at elevated temperatures. A general trend was observed between substituent type and ionic conductivity; where conductivity increases with increasing lanthanide size. Therefore, the lanthanum substituted sample was the most conducting and gadolinium containing material was the least conductive. The only other variable temperature measurement in this project was completed using Raman spectroscopy. The Raman scattering of 25 mol% samarium was measured from 23 °C to 750 °C. The first spectrum collected at 23 °C was indicative of the rhombohedral phase, based on the other spectra measured. At 550 °C, a transformation occurred and the new Raman scattering behaviour persisted up to the highest temperature measured (750 °C). The Raman spectrum corresponded to the cubic phase identified in multiple literature sources. This phase transition appears to be reversible, as the final Raman spectrum collected after cooling related to the rhombohedral phase. The impedance and Raman measurements both suggest that the 25 mol% samarium sample undergoes a structural change around 550 to 600 °C. The Raman scattering confirmed that a rhombohedral to cubic phase change occurred, however this was not confirmed in impedimetric measurements as the structural change was not reversable upon cooling. It can be concluded that additional variable temperature probes are required to confidently confirm the variable temperature behaviour of the rhombohedral phase. Nevertheless, it is certain that the lanthanum substituent behaves quite differently than the other lanthanides (samarium and gadolinium), but all lanthanides mainly form the desired rhombohedral phase at 25 mol% concentration in Bi_2O_3.

6.2 Substituent concentration

The influence of substituent concentration was studied by varying the amount of samarium substituted in bismuth oxide. Laboratory XRD results revealed that 15 mol% substituted samples form a phase mixture of rhombohedral (77%) and cubic (23%). Samarium compositions from 20 mol% in the Bi_2O_3 system seem to mainly form the rhombohedral phase. Rietveld refinements also showed that the 15 mol% substituted material had a significantly larger unit cell volume of 437 Å³ compared to the 20 mol% and 25 mol% substituted materials that had volumes of 432 Å³. The 15 mol% substituted material also had significantly lower crystallite size (68 nm) compared to the other two materials (131 and 166 nm). It can be inferred from this work that a minimum of 20 mol% lanthanide is required to predominantly form the rhombohedral phase, most certainly for medium sized lanthanides such as samarium (1.079 Å). While the lower limit of lanthanide concentration has been established for desired phase formation, the upper limit must still be investigated. The ambient Raman scattering of substituted Bi_2O_3 was measured for materials containing 15 mol%, 20 mol% and 25 mol% samarium. These results showed that as Sm concentrations were lowered, additional Raman bands were identified. This coincides with XRD results that confirmed a phase mixture in the 15 mol% substituted material, and a single rhombohedral phase in the 25 mol% samarium sample. The impedimetric behavior of the three materials ~~of interest~~ revealed that substituent concentration does influence the conductivity of rhombohedral bismuth oxide. The least substituted material, 15 mol% Sm, had the highest conductivity of 0.064 S cm^{-1} at 750 °C. While the 15 mol% ASm sample was the most conductive, it was not structurally stable throughout the heating and cooling regimes. The materials with higher substituent concentrations were more stable throughout the heating and cooling cycles. It can be concluded that to successfully form and stabilize the rhombohedral phase of bismuth oxide, the system should be substituted within the composition range of 20 to 25 mol%. These compositions may not be as conductive as materials with less substituent, but they can withstand heating and cooling cycles as desired by a suitable solid electrolyte.

6.3 Annealing Duration

The heat treatment during synthesis was investigated in efforts of optimizing the synthetic route to the desired phase. Materials with composition $Bi_{0.75}Sm_{0.25}O_{1.5}$ were annealed for 5-, 10- or 15-hours at 750 °C. The laboratory XRD results of the 25 mol% samarium material annealed for the respective durations produced similar diffraction peaks. The XRD patterns all comprised of sharp Bragg peaks with no relative shifts along the 2θ axis. The Rietveld refinements of diffraction data showed that all three materials have similar lattice parameters and displacement parameters, however the crystallite sizes exhibited an unexpected trend. The 5- and 10-hour annealed samples had similar crystallite sizes of 116 and 100 nm respectively, while the 15-hour annealed sample had a smaller crystallite size of 72.8 nm. It was predicted that as annealing is continued, materials would have improved crystallinity. These materials require further examination to understand the structural behaviour

during annealing. The ambient Raman scattering of these materials was measured, which showed that the characteristic Raman bands remained consistent as annealing duration was varied. The most significant difference with increased annealing time was the Raman bands becoming sharper and more resolved, which is indicative of improved crystallinity. These results contradict the XRD refinements, however it is worth noting that the XRD is measuring the average structure of the material and Raman scattering measures the local structure. The electrochemical impedance of the 5-, 10- and 15-hour annealed samples showed no direct relationship between annealing duration and ionic conductivity. The 5- and 15-hour annealed samples shared a strong overlap with almost identical conductivities in both heating and cooling cycles. On the other hand, the 10-hour annealed sample had slightly lower conductivity. These results do not correlate with XRD measurements that showed a strong structural similarity between the 10- and 15-hour annealed samples. The relationship between annealing duration and ionic conductivity could be more accurately determined by investigating additional annealing durations. The investigation of this synthetic parameter revealed that annealing time does not seem to have a significant influence on phase behavior. In an energy conscious society, annealing rhombohedral phase materials for 5 hours has proven to be sufficient.

6.4 Annealing Temperature

The temperature-dependent behaviour of the rhombohedral phase was investigated by annealing substituted bismuth oxide at different temperatures. Based on various literature sources, the rhombohedral phase converts from the high temperature $Fm\bar{3}m$ cubic phase at approximately 650 °C during cooling. Therefore, two temperatures were selected for the annealing step; one below and the other above the proposed phase transition temperature. 25 mol% samarium substituted bismuthate was subjected to annealing at either 610 °C or 750 °C for 5 hours. The laboratory XRD results of annealing at 750 °C was characterized by sharp, well-resolved peaks that could all be assigned to the desired rhombohedral phase. On the other hand, the average structure of the 610 °C annealed sample produced broad, overlapping peaks in its XRD pattern. This was indicative of a phase mixture that was confirmed by a Rietveld refinement of the XRD results. The 610 °C annealed sample seems to form a rhombohedral-cubic phase mixture, however the major phase is rhombohedral. It is interesting to note that the rhombohedral phase is stable around 610 °C, and may require longer annealing durations to remove impurity phases and potentially improve crystallinity. The desired phase formation at lower temperatures contributes to the phase suitability as a SOFC electrolyte. The ambient Raman scattering of the different annealing temperatures in the 25 mol% gadolinium substituted material produced largely similar spectra. The only notable difference between the two spectra was the heightened intensities of Raman bands in the 750 °C annealed sample, compared to that of the 610 °C annealed material. While different substituents were used in XRD and Raman scattering measurements,

the XRD results indicate significant structural differences from the two annealing temperatures, which does not complement the Raman scattering data. Even though Raman scattering probes the local structure, similarity between the two techniques is expected. A multipoint mapping measurement of the 610 °C annealed gadolinium sample was completed to ensure the homogeneity of the sample throughout its dimensions. The mapping did not reveal any significant differences between all 64 points measured. This confirmed the accuracy of the closely related Raman spectra of the 610 °C and 750 °C annealed materials. The impedimetric behavior of the two samples revealed a correlation with XRD data. Interestingly, the 610 °C annealed sample displayed higher conductivity throughout the heating and cooling regime. This could be explained by the rhombohedral – cubic phase mixture identified in XRD results, leading to further conversion to the highly conductive cubic phase upon heating. The 610 °C annealed material underwent two structural changes during heating, while the 750 °C annealed sample just had one. This work showed that the 750 °C annealed sample forms the desired rhombohedral phase with structural stability upon heating, even though it does not display higher conductivities.

In closing, this project has made several strides to its aim of investigating the formation of rhombohedral doped Bi_2O_3. This work provided a thorough analysis of phase behaviour when composition or synthesis is varied. The conductivity properties of the rhombohedral phase have also been extensively examined, which provided evidence for the widely referenced stability of the $R\bar{3}m$ rhombohedral phase. The continuation of this work can be implemented by investigating co-substituted Bi2O3 systems as well as exploring the long-term stability of rhombohedral materials. In other phase types, like the cubic phase, lower concentration of dopants is needed to stabilise the phase when co-doping occurs compared to single doping. A lower extent of doping also improves the conductivity. The question is if the same trends are seen for the rhombohedral phase. This can be explored further in future work. The challenges with interpreting Raman spectra can also be explored by investigating the use of computational Density Functional (DFT) analysis and polarised Raman measurements. Based on this work, it can be confidently stated that rhombohedral doped Bi_2O_3 has many properties of an acceptable solid electrolyte. This project contributes to the knowledge of the solid oxide electrolyte known as rhombohedral substituted bismuth oxide.